Intravascular Ultrasound Elastography

The studies presented in this dissertation were financially supported by the Dutch Technology Foundation (RGN 3462).

ISBN : 90-9012664-3

Intravascular Ultrasound Elastography

Intravasculaire Ultrageluids Elastografie

PROEFSCHRIFT

ter verkrijging van de graad van doctor
aan de Erasmus Universiteit Rotterdam
op gezag van de rector magnificus
Prof.dr. P.W.C. Akkermans M.A.
en volgens het besluit van het College voor Promoties

De openbare verdediging zal plaatsvinden op
woensdag 23 juni 1999 om 15.45 uur

door
Christoffel Leendert de Korte
geboren te Sint Maartensdijk

PROMOTIECOMMISSIE

PROMOTOR:	Prof.dr.ir. N. Bom
OVERIGE LEDEN:	Prof.dr. C. Borst
	Prof.dr. J.R.T.C. Roelandt
	Prof.dr. P.W. Serruys
CO-PROMOTOR:	Dr.ir. A.F.W. van der Steen

Financial support by the Netherlands Heart Foundation (NHS) and the Interuniversity Cardiology Institute of the Netherlands (ICIN) for the publication of this thesis is gratefully acknowledged.

The financial contributions of EndoSonics Europe B.V, Dutch Technology Foundation (STW), and Pfizer are gratefully acknowledged.

Ter nagedachtenis aan mijn grootvader
Christoffel Leendert de Korte

Voor Pé

Contents

Chapter 1

Introduction

1.1 Heart diseases

The pumping action of the heart is fundamental to adequate nutrition of cells and maintenance of the internal environment (Miller & Leavell, 1972). Without this pumping action, cells would starve, waste products would build up and life of the cell and of the individual would cease. The heart consists of two pumps in series: one to propel the blood through the lungs for exchange of oxygen and carbon dioxide (the pulmonary circulation) and the other to propel blood to all other tissues of the body (the systemic circulation). The heart itself also needs oxygen to fulfill its function. This is accomplished by the coronary arteries. A problem arises when these arteries are narrowed due to a stenosis: blood flow is diminished and the heart muscle nourished by these arteries is not able to function properly anymore. A larger problem occurs when the artery is totally blocked. A total occlusion can arise slowly by a growing stenosis but also acutely due to thrombosis. The result will be an infarction.

1.1.1 The atherosclerotic plaque

The normal vessel wall consists of three layers: the intima, media and adventitia (Becker, 1988).

The intima is a layer containing endothelial cells and is separated from the media by the internal elastic lamina. The layer is selectively permeable resulting in the possibility of materials to pass through this layer.

The media is the middle layer. In elastic arteries this layer contains smooth muscle cells, collagen and small elastic fibers. In muscular arteries the media consists only of smooth muscle cells.

The adventitia contains mainly smooth muscle cells intermixed with fibrous connective tissue.

The formation of atherosclerotic lesions starts already in early adolescence. Three groups of lesions can be distinguished (Becker, 1988):

Fatty streaks are normally asymptomatic and the development starts already in the early adolescence. Especially, low-density lipoproteins play an important role in the formation of fatty streaks. A low shear-stress at the lumen-intima boundary results in

an increased exchange of these lipoproteins (Krams et al., 1997; Kornet et al., 1998). These fatty streaks cause no stenosis and contain intra- and intercellular lipid deposits and smooth muscle cells that have proliferated and migrated from the media into the intimal layer.

Elevated plaques are plaques causing moderate stenoses. The development of these types of plaque normally takes 15 to 20 years in human beings. The plaque consists of fibrotic material or a fibrotic cap covering a core containing free extra-cellular lipids, cell debris, calcium crystals and fibrotic material. These plaques show a great diversity of material composition.

The complicated lesion is an elevated lesion of which the cap has ruptured. Due to the rupture and ulceration of the plaque, thrombus is formed. Since this thrombus can be formed rapidly, rupture of the plaque is considered an important mechanism for acute coronary syndromes.

1.1.2 Vulnerable plaque

Acute coronary syndromes are caused by an occlusion of the lumen by coronary thrombi (Falk, 1991; Fuster et al., 1992; Fuster, 1994; Kragel et al., 1991). Thrombus formation will only occur in arteries with atherosclerotic plaques (Constantinides, 1990). There are two major mechanisms underlying plaque disruption (Burke et al., 1997; Davies, 1996): rupture of a fibrous cap of a lipid-rich plaque (Falk et al., 1995) and denudation and erosion of the endothelial surface (Farb et al., 1996; Fishbein & Sighel, 1996).

There are several morphological features that characterise an unstable plaque, including a thin fibrous cap overlying an eccentric plaque with a large necrotic core of lipid and cellular debris (Lee & Libby, 1997)(Fig. 1.1). The instability of these plaques is mainly caused by the large mechanical stresses that will develop in the thinnest part of the fibrous cap (Richardson et al., 1989; Loree et al., 1992). Since the soft lipid core is unable to bear these mechanical forces, all the stress is concentrated in the fibrous cap. Rupture of the cap (Fig. 1.2) may also be caused by local weakening of the fibrous cap due to macrophages: an increased density of macrophages was found in caps of ruptured plaques compared to caps of intact plaques (Lendon et al., 1991). This is why the vulnerability of a plaque is not only determined by the geometrical features of the cap and the lipid core. Furthermore, macrophage-rich areas were more prevalent in plaque tissue from patients with acute coronary syndromes than with stable angina (Moreno et al., 1994). A major problem is the diagnosis of vulnerable plaques: identification of plaque vulnerability *in vivo* is still limited. Using coronary angiography, advanced lesions, thrombosis and calcifications may be revealed, but other qualitative features of the plaque cannot be assessed with this imaging technique (Falk et al., 1995). It is now widely accepted that the propensity of a lesion to rupture is poorly predicted by coronary angiography (Lee & Libby, 1997) since vulnerability of plaques is not directly related to plaque size (Topol & Nissen, 1995; Ambrose et al., 1988; Fishbein & Sighel, 1996) or lumen size (Pasterkamp et al., 1998). The composition of the plaque is a major determinant (Davies, 1996; Lee & Libby, 1997).

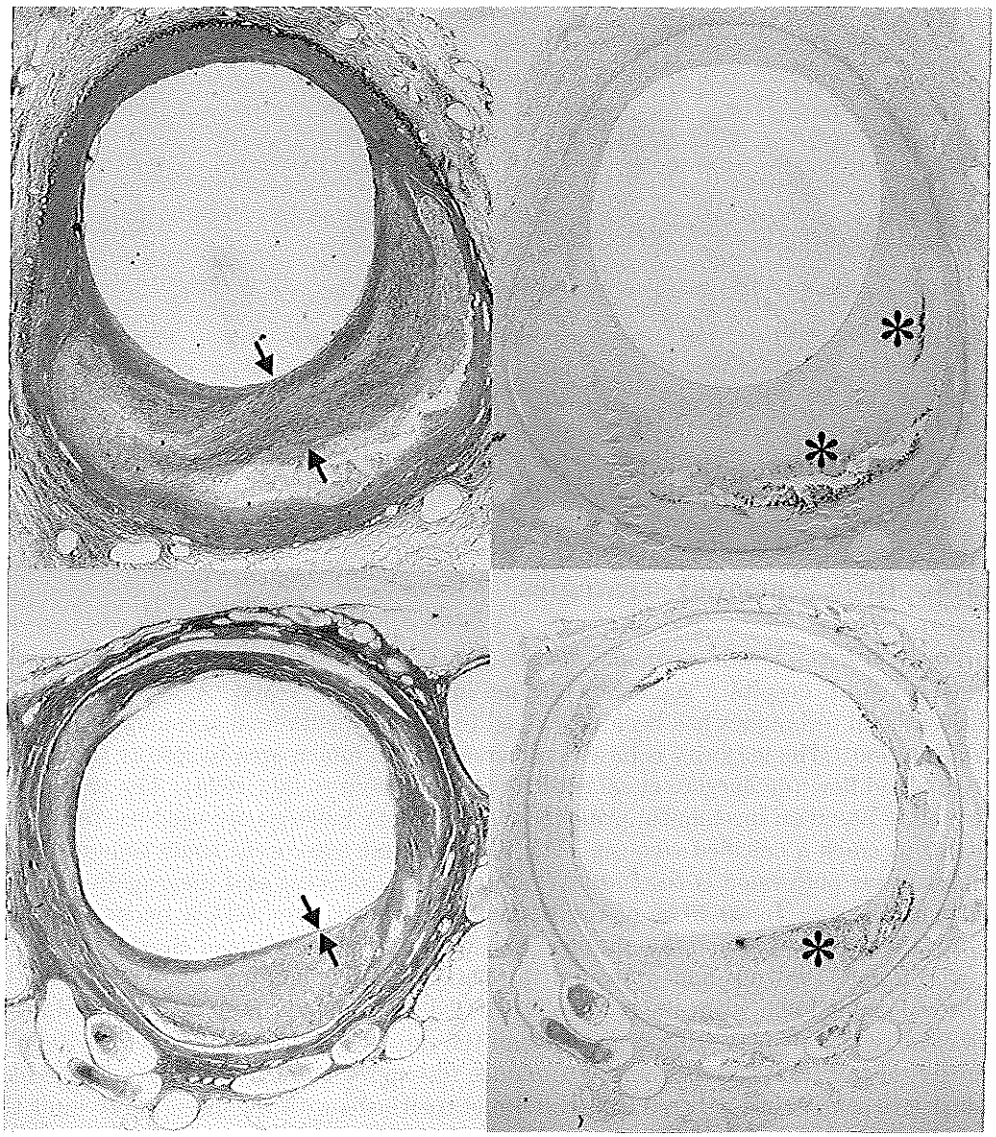

Figure 1.1 Examples of histological features of a stable and a vulnerable plaque. The left images show the picro-Sirius red stain. This stain reveals the collagen. The right images show the anti-CD68 antibody stain that reveals the presence of macrophages. The stable plaque (upper panel) has a atheromatous core (left panel) with macrophages present deep in this core (* in right upper panel). The core is covered by a stabilising thick fibrous cap (arrows in upper left panel). The lower panel shows the features of a vulnerable plaque. An atheromatous core is covered by a thin fibrous cap that is almost totally absent at the location indicated by the arrows. Macrophages are observed in the core and the cap (* in lower right panel) (Pasterkamp et al. 1998)

Figure 1.2 Picro-Sirius red staining of a cross-section with a large atheromatous plaque (arrow) with a rupture in the center of the fibrous cap (Courtesy G. Pasterkamp)

1.1.3 Interventional strategies

Currently, atherosclerotic coronary disease remains the leading cause of death in the Western World, despite a significant decline in the last 25 years. A whole arsenal of interventional techniques has been developed to treat patients with coronary syndromes (Waller, 1989). The majority is based on increasing the lumen area to restore the appropriate blood flow (de Jaegere et al., 1994; van Beusekom et al., 1994). The techniques are mainly based on mechanical principles. Angioplasty balloons are used to stretch the area or to crack a calcified stenosis. The problem that may occur some time after angioplasty was performed is restenosis. The stenosis is growing and may again obstruct the luminal area. In 20-40 % of the patients, restenosis after PTCA occurs (Serruys et al., 1998). To overcome this problem, stents have been developed. Stents are metallic wire-frames that are folded around the balloon. With inflation of the balloon the stent will expand and when the balloon is deflated the stent will keep its expanded form. However, restenosis may still occur although the rate of restenosis is lowered to 10-30 % (Serruys et al., 1998). A possibility to reduce restenosis is brachytherapy, where sealed radioactive sources are inserted near the site of treatment with the intention to limit the pathologic process by irradiation (King III et al., 1998). Additionally, radioactive stents can be used as source to irradiate the tissue (Hehrlein & Kubler, 1997).

With other techniques, the stenosis is not pushed away, but the obstruction is removed. For this purpose, several techniques have been developed. Laser techniques are used to evaporate the obstruction (van Leeuwen et al., 1993; Hamburger et al., 1997). Atherectomy scrapes or cuts the obstruction from the arterial wall. Since the scraped particles can cause an obstruction distal from this side, the particles are collected and removed through the catheter. With spark-erosion, the obstruction is removed by applying a high electric power differential (Slager et al., 1985). The major feedback mechanism and a key factor for decision making during these intravascular procedures is imaging.

1.2 Medical ultrasound

Ultrasound imaging is based on transmitting and receiving high frequency sound waves. The transmitted wave propagates through a medium until it hits a reflecting object. The reflected wave is in return received by the transducer. The time between transmission and reception of the wave is directly related to the distance between source and reflector. In nature, this principle is used by several animals to estimate their position or to locate possible preys. A dolphin uses ultrasound to determine its position and bats use high frequency ultrasound to locate insects and possible obstructions.

The advantage of ultrasound is that it can travel through water and soft tissue. Additionally, ultrasound is harmless for soft tissue at the energy levels used for imaging. Therefore, ultrasound gives the opportunity to image structures noninvasively in the body. For the development of ultrasound imaging, the discovery of the piezoelectric effect by Pierre and Jacques Curie was essential (Curie & Curie, 1880). They discovered that an electric charge is produced by materials like ceramics and quartz when a force is applied on it. On the other hand, these materials are mechanically deformed if a voltage is applied. So, applying a voltage on a piezoelectric material results in a deformation that can be used to transmit a sound wave. Conversely, a sound wave impinging on a piezoelectric material causes a mechanical force and deformation resulting in a voltage.

The first practical applications of ultrasound were related to detection of submarines during World War I and II. The first publication seems to be that of Firestone (1945). After World War II, the first medical application of ultrasound was performed by Dussik et al. (1947). He imaged his own skull by a transmission based technique. In 1949, the first pulse-echo technique for medical imaging was described by Ludwig and Struthers.

Different imaging modalities have been developed since then. In A-mode, the amplitude of echo is displayed as a function of the time (and thus echodepth) (Wild & Reid, 1952). In M-mode, the amplitude of the echo is transformed into a grey level. The positions of the echo dots are recorded as a function of time. This allows study of motion of reflecting structures (Edler & Hertz, 1954a). Especially for moving objects as the beating heart this imaging mode is useful. A B-mode image is build if the sound beam is swept through the scanning plane. This can be done with a pivoting transducer. For each soundbeam, the amplitude of the echo is plotted in greyscale. Combining all lines obtained at the different positions results in a 2-dimensional image. Another possibility to obtain a 2-dimensional image is using a linear array transducer. This transducer contains several acoustic elements in line. By rapid electronic switching, 2-dimensional images can be obtained without moving the transducer, and therefore allowing real time imaging. This was first described in 1971 (Bom et al., 1971; Lancée et al., 1975).

The resolution of an ultrasound image is directly related to the frequency used: The higher the frequency used, the better the resolution. However, increasing the frequency results directly in an increased attenuation of the ultrasound wave and thus limiting the penetration depth. The frequency used for imaging is therefore a trade-off between optimal resolution and desired penetration depth. A typical frequency of 5 MHz is used to image large organs in the body. The resolution obtained with this frequency is in the order of a millimeter. When the organ that has to be imaged is small and the transducer can be placed close to the region of interest, the frequency can be increased.

Typical frequencies for eye-scanners are 10 MHz and intravascular transducers operate at frequencies between 20 and 50 MHz. The best known application of ultrasound is imaging the unborn fetus. Using a transducer placed on the body of a pregnant woman, 2-dimensional and 3-dimensional images can be obtained. Given the advantages of ultrasound, many applications have been developed in the past, especially for detection of tumors.

1.2.1 Imaging and analysis of organs

Because different organs have different sizes, are located in different parts of the body and may have motion, dedicated transducers, frequencies and scanning sequences have been developed.

- *Liver scanner.* Ultrasound is routinely used to detect tumors in the liver. Since the liver is a relative large organ and is located in the abdomen, typical frequencies used are 3-5 MHz. Since tumors are not always identifiable using the echo-intensity, several methods have been developed. These tissue characterisation methods are mainly based on spectral analysis (Kuc & Schwartz, 1979; Oosterveld et al., 1991; Thijssen et al., 1993) and statistical parameters of the speckle pattern (Garra et al., 1987).

- *Breast scanner.* The breast was one of the first organs imaged with ultrasound (Wild & Reid, 1954). The principal application of ultrasound is to differentiate between solid and fluid-filled (cystic) lesions. For characterisation of solid lesions, a good spatial and contrast resolution is required, since the characterisation is based on the shape of the lesion boundary and evidence of acoustic shadowing. Additionally, ultrasound is nowadays used as a 'screening' technique for early signs of breast cancer.

- *Eye scanner.* The eye is a relative small structure that is easily accessible from outside the body. Typical used frequencies are in the order of 10-15 MHz resulting in a resolution of 500 μm. Ultrasound is mostly used to detect melanomas. For characterisation of these melanomas different spectral characterisation methods have been developed (Romijn et al., 1991).

1.2.2 Imaging the heart

The first ultrasound M-mode registrations of the heart were produced by Edler and Hertz (1954b). They described a technique to visualise moving structures in the heart. In 1968, Somer constructed the first phased array for intracranial imaging. The technique was refined by Thurstone and von Ramm (1974) and is still the most widespread technique used in cardiac ultrasound. Using this technique, 2-dimensional images of a cross-section of the heart could be viewed using a "small footprint" probe. Currently, there is a tendency to 3-dimensional imaging of the heart using ultrasound. For this purpose, off-line and real-time applications have been developed or are currently under development.

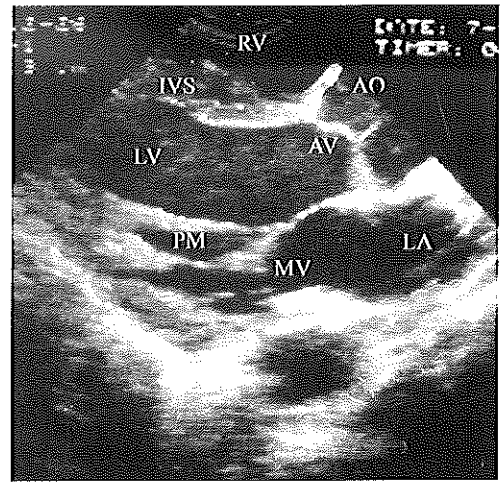

Figure 1.3 Anatomic view of the heart obtained with a TTE probe. RV=right ventricle, IVS= intraventricular septum, LV=left ventricle, LA=left atrium, AV=aortic valve, AO=aorta, MV=mitral valve and PM=papilary muscle

2-Dimensional approaches. 2-Dimensional imaging techniques are commonly based on phased array transducers. Using electronic steering, the beam scans a 2-dimensional plane. When the transducer is placed on the thorax (Trans-Thoracic Echocardiography or TTE)(Fig. 1.3) the sound waves have to pass the ribs and the lungs. Since the heart is not located near the transducer, relative low ultrasound frequencies have to be used to obtain enough penetration. These problems are circumvented when the transducer is placed in the esophagus (Trans Esophageal Echocardiography or TEE, Fig. 1.4) (Djoa et al., 1996).

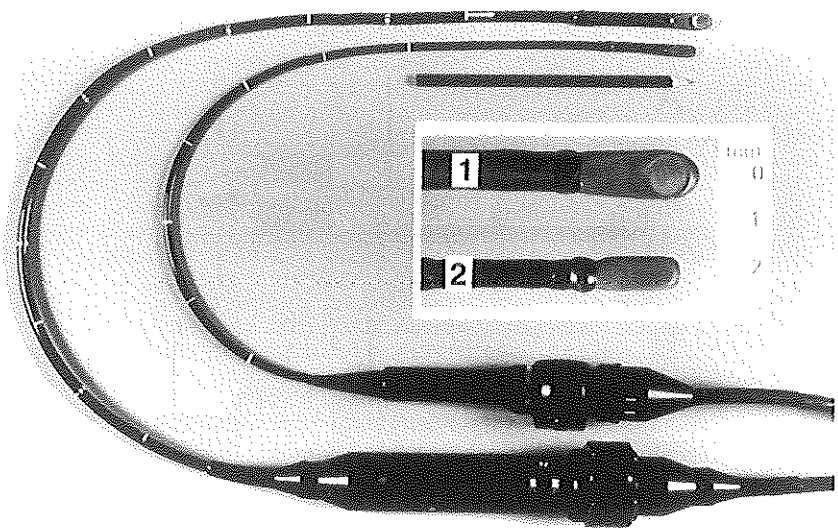

Figure 1.4 A pediatric high frequency (7.5 MHz) single plane TEE probe (probe 2) and a pediatric varioplane TEE probe (probe 1).

3-Dimensional approaches. 3-Dimensional images are obtained when 2-dimensional arrays are used or when the 1-dimensional array is rotated or moved. A real-time phased array system was developed at Duke University (von Ramm & Bashford, 1991). This scanner relies on 2-dimensional arrays operating at 3 MHz to scan volumes at rates of 18-40 volumes per second. At the Erasmus University, a fast rotating probe has been developed (Djoa et al., 1999; de Jong et al., 1999). The 64 element, 3.75 MHz phased array is rotated at 450 revolutions per minute. In this way, 15 3-dimensional volumes per second are acquired.

Tissue characterisation. A lot of effort has been put in myocardial tissue characterisation. The main goal is to differentiate normal from injured tissue, to identify abnormal myocardial tissue and to quantify the extent of the injury. The underlying principle is that the backscattered ultrasound signal changes with changes in the microscopic structure of the cardiac muscle. A large part of the pioneers work has been accomplished by the group of Miller and Pérez (Miller et al., 1985). Although ultrasonic tissue characterisation has been studied for several years by many groups (Pérez et al., 1988; Rijsterborgh et al., 1993; Sagar et al., 1987; van der Steen et al., 1997) many phenomena are still not explained to a satisfactory level.

1.2.3 Imaging arteries

Arteries can be imaged from outside the body or from inside the lumen. Carotid arteries are located just underneath the skin and can be imaged from outside the body. Using 5 MHz transducers, quantitative information of the free lumen and plaque can be obtained (Pignoli et al., 1986). At slightly higher frequencies (around 7.5 MHz), the intima media thickness of the distal wall of the carotid can be measured, which can be very useful for

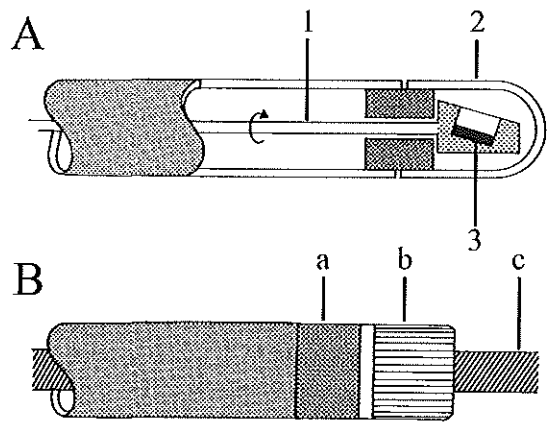

Figure 1.5 (A) Mechanical rotating single-element catheter tip consisting of rotating shaft (1), transparent dome (2) and transducer element (3). (B) Electronically switched phased array catheter tip consisting integrated circuitry for reduction of the number of wires (a), multi-element transducer (b) and guide wire (c).

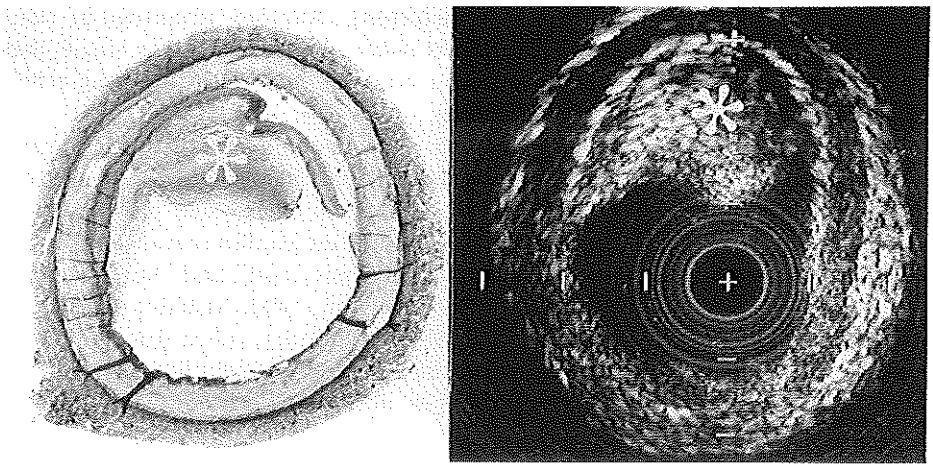

Figure 1.6 Cross-sectional ultrasound image (right) and corresponding histology (left) of a muscular femoral artery, obtained *in vitro*, showing an eccentric obstructive atherosclerotic plaque ($*$) (Gussenhoven et al. 1989).

monitoring the effect of lipid lowering drugs (de Groot et al., 1998; Kornet et al., 1998). Additionally, Doppler techniques were developed to determine blood flow (Hocks et al., 1992). This flow information is also used to investigate the shear rate at the lumen-vessel wall boundary.

Other arteries can not be imaged from outside the body with sufficient resolution. Intravascular ultrasound (IVUS) is a technique to acoustically survey arteries from within the lumen. Cross-sectional images of a vessel are generated by sweeping the ultrasound beam sequentially in a 360° scan angle. Early approaches have been described for the mechanical rotation by Wells (1966) and for electronic beam rotation by Bom (1972). Although the latter system was developed for intracardiac use, application in arteries was suggested as well. Current systems are still based on these two principles (Fig. 1.5). More recently, this group developed a single element catheter for intravascular purposes. This catheter has a transducer in the tip of the catheter that is rotated by means of a flexible axis. With this technique, real-time cross-sectional images of the vessel wall and plaque are obtained (Gussenhoven et al., 1989) (Fig. 1.6). This in contrary to the projection of the lumen that is provided with classical angiography. Therefore, IVUS is more and more routinely used during interventional procedures for diagnosis, guiding the procedure and investigation of the chances for restenosis.

By now, a 64 element catheter has been developed by EndoSonics Corp. in close collaboration with O'Donnell and co-workers (1992, 1997). The tip of this catheter contains 64 elements folded around it. Using Synthetic Aperture Focusing Techniques (SAFT), an image containing 512 angles is formed. The advantage of this technique is that rotational artifacts are not present. In single element catheters, the axis that rotates the element may get stuck if the catheter is positioned in a curved vessel. Since

the catheter can not rotate, the images are deformed. Another advantage is, that the catheter is advanced over the guidewire that is inside the catheter. For single element catheters the guidewire is outside the catheter and this introduces a strong reflection with distal shadowing in one part of the image.

IVUS has potential to characterise different plaque components. Calcified areas can be identified by their high echogenicity. The reflection of ultrasound waves on calcified tissue components is very strong. Therefore, almost no energy can pass the calcified region and shadowing distal to the region will result. Some studies reveal that "soft" and "hard" echoes correspond to soft and hard material where "soft" and "hard" correspond to regions with low and high echogenicity (Potkin et al., 1990; Nishimura et al., 1990; Gussenhoven et al., 1996; Barzilai et al., 1987). In contrary, other studies reveal that only calcified and non-calcified tissue can be identified since identification of lipid and mixed fibro-fatty tissue remains difficult (Hori et al., 1997; Yock & Linker, 1990).

1.3 Imaging of plaque components and vulnerability

1.3.1 Electrical impedance imaging

Electrical impedance imaging is based on the hypothesis that the electrical impedance of material is related to its main components. The catheter used to determine the electrical impedance contains 3 sensors at the tip. A current field is created by the combination of one excitation electrode proximal to the catheter and one electrode distal from the catheter (Konings et al., 1997). An *in vitro* validation study revealed that increasing amounts of lipid in the intima corresponds with increasing impedance in most cases (Bouma, 1998). An *in vivo* study in Yucatan pigs revealed that the relation between lipid content and impedance is present but only a small correlation was found. The disadvantage of the technique is that no cross-sectional images are obtained so the technique should be combined with IVUS or OCT imaging.

1.3.2 Angioscopy

Angioscopy is a technique based on visualising the arterial wall and plaque with light. The development started in 1924, when Rhea et al. described a system containing a rigid metal tube with a distal lens. However, blood corrupted proper imaging of the surface. The technique was further developed in the 80's. The optical system was incorporated in flexible catheters, small enough to image most vessels of interest. By flushing the lumen with saline or using a transparent balloon, the blood was removed from the plane of sight.

The technique allows an improved diagnosis of thrombus, atheroma and ulcerated plaque (Cortis et al., 1984). Angioscopy is especially suitable to detect thrombus (Siegel et al., 1991). Red thrombus can be differentiated from plaque by the colour and the texture, where this is not always possible for white thrombus (White et al., 1996). The disadvantages of the technique include the need to flush the lumen to obtain proper results and the lack of depth dependent information. Only the surface of the lumen is

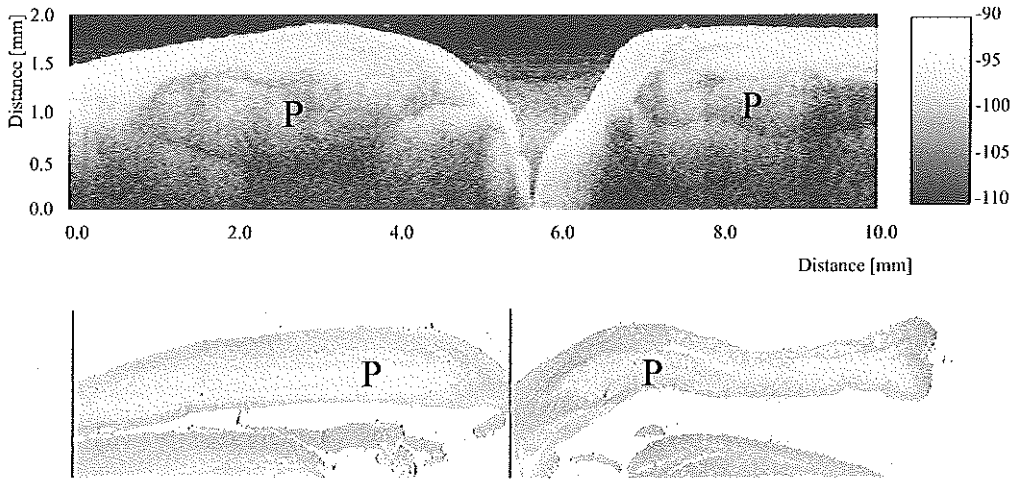

Figure 1.7 In vitro OCT image (top) with corresponding histology (Elastic van Gieson stain, bottom) of human thoracic aorta segment with plaques hidden in the media of the arterial wall on both sides of a side branch (center of the image). The resolution of the OCT system was 15 micrometer. The greyscale is plotted in dB. The image consists of 500 by 2048 datapoints. (Courtesy T.G. van Leeuwen)

visualised and especially for detection of plaque vulnerability, characterisation of plaque components behind the surface is important.

1.3.3 Optical Coherence Tomography

Optical Coherence Tomography (OCT) is a new technique that uses laser light to image biological tissues (Tearney et al., 1997). It is based on similar principles as ultrasound imaging: Laser light is emitted and will reflect on surfaces and small particles. However, the delay between transmitting and receiving the light cannot be directly used to represent the depth, since the speed of light is far to high. To overcome this problem, interferometry is used to determine the depth of the tissue under investigation. The resolution of OCT is very high: depending on the used wavelength of the laser light, a resolution in the order of 10 μm is achievable. *In vitro* studies on aorta specimens (Fig. 1.7) demonstrated the potential of the technique (Brezinski et al., 1997). The high resolution, broad dynamic range and ability to be delivered through intravascular catheters makes it a promising technique.

1.3.4 Raman spectroscopy

Raman spectroscopy is a technique to characterise the chemical composition of biological tissue. The technique was named after C.V. Raman, who discovered the effect (Raman, 1928a; Raman & Krishnan, 1928b). Raman spectroscopy was applied on viruses (ThomasJr & Agard, 1984), eye lenses (de Korte et al., 1994; Yaroslavsky et al., 1994),

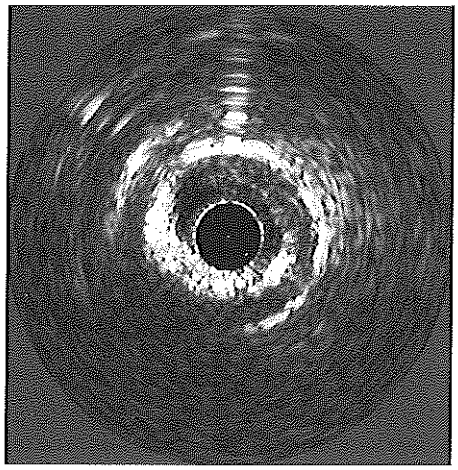

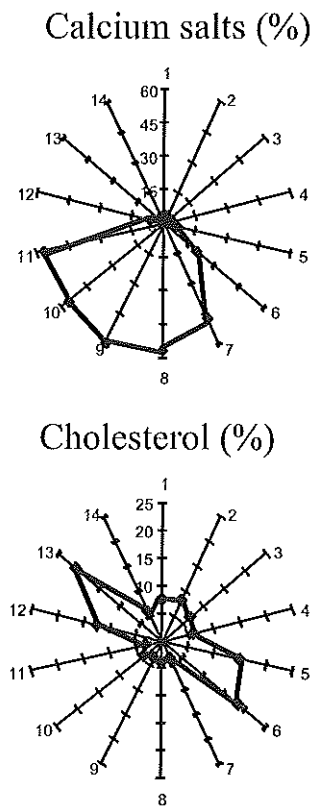

Figure 1.8 IVUS image of a calcified coronary artery (left), and the relative weights of calcium salts (top) and total cholesterol (bottom) in the same artery plane determined by Raman spectroscopy. IVUS images were obtained from an intact artery segment, which were marked by a needle (12 o'clock). Raman spectra were obtained from the artery after the artery was opened. The IVUS image shows a calcification, in agreement with the calcium salts detected with Raman spectroscopy. In addition, cholesterol is detected with Raman spectroscopy but cannot be seen in the IVUS image. (Courtesy T.J. Römer)

teeth (Tsuda et al., 1996), etc. Currently, the technique is applied on arterial tissues (Brennan III et al., 1997; Römer, 1999). *In vitro* experiments revealed that the chemical composition can be accurately quantified with the technique. Raman spectroscopy is especially powerful to detect cholesterol and calcium salts (Römer et al., 1998)(Fig. 1.8). A disadvantage of the technique is the relative long acquisition time which makes it difficult to implement for *in vivo* applications. Additionally, Raman spectroscopy is currently a 1-dimensional technique since it has no depth dependent information. Therefore, no cross-sectional images can be produced with the technique. For clinical applications, the technique may be powerful when it is combined with an imaging technique like IVUS or OCT.

1.3.5 Thermal detection

Thermal detection is based on the principle that the temperature in a vulnerable plaque is increased due to macrophage infiltration. This hypothesis was tested by Casscells et al. (1996) using living samples (n=50) of carotid arteries taken at endarterectomy. The temperature correlated positively with the macrophage cell concentration. Based on these findings it could be useful to develop a catheter based temperature sensor to identify plaque at high risk of rupture or thrombosis.

1.4 Elastography

Elastography is based on the following principle : "When a force is applied on tissue, the response of the tissue will be a function of its mechanical properties." For example, when the same force is applied on a stone and a sponge, the deformation of the sponge will be much larger than the deformation of the stone, since the sponge is much softer. In clinical practice, this technique is often applied by palpation: the clinician used his hands to palpate the body of a patient to detect hard inclusions.

For ultrasound applications, two different strategies have been developed. Sonoelasticity imaging (Parker et al., 1990, 1996; Parker & Lerner, 1992) uses a low frequency vibration field (100-500 Hz) as a mechanical excitation. The propagation of these waves through the tissue is a function of its mechanical properties. The power of the technique is that detection of the vibration patterns is feasible with commercial available echo systems, equipped with Doppler modes. The weakness of the technique is that the vibration pattern can not be directly converted to the mechanical properties of the tissue.

Elastography (Céspedes, 1993a; Ophir et al., 1991, 1996) is a static approach. The tissue is imaged at two or more different levels of static compression. Next, the two images are compared to determine the local compression of the tissue. Using this strain image (elastogram), information of the local mechanical properties can be obtained. For quantitative information, the distribution of the Young's modulus has to be reconstructed using finite element modelling algorithms (Skovoroda et al., 1995). This reconstructive approach is called the inverse problem and the obtained image is called modulus elastogram.

1.4.1 Non-vascular applications

The first applications of elastography were developed for detection of carcinomas in breast. These carcinomas are often not detectable with ultrasound since the echogenicity of the tumor and the surrounding tissue is the same. However the difference in Young's modulus is often large: tumors are an order of magnitude harder than healthy breast tissue. Using phantom studies, the feasibility of the technique was demonstrated. The technique was applied *in vivo* (Céspedes et al., 1993b) and it was demonstrated that tumors could be detected with elastography where they remained undetectable in the echogram.

More recently, ultrasound elasticity imaging was used for renal applications. Emelianov et al. (1995) demonstrated *in vitro* that kidney elasticity changes with renal damage and

that these changes could be identified using elastography. These changes were not detectable with traditional diagnostic techniques. Using additional processing techniques, the sensitivity of the technique was improved resulting in the possibility to detect early states of kidney transplant rejection with elastography (Emelianov et al., 1997).

1.4.2 Vascular applications

Ryan et al. (1992, 1997b) described a method to track vessel wall displacement. 1-Dimensional correlation was used to determine time shifts between sequentially acquired rf-echo signals collected in M-mode. In images of a phantom with a soft and hard part they demonstrated that the displacement in the soft part was larger. In addition, grey-scale displacement images of an *in vitro* iliac artery specimen were presented. These images were obtained using a 2-dimensional search technique on video echo images obtained at different static pressures.

Talhami et al. (1994) developed a technique for 1-dimensional strain assessment in the vessel wall by special processing of video signals. They stated that radio frequency (rf) based techniques were not applicable since the decorrelation of signals from a vessel wall was to large. The chirp Z-transform was used to estimate changes of the mean scatterer spacing that result from vessel wall compression. The chirp Z-transform is based on the scaling property of the Fourier transform. This technique computes an average strain estimate for the entire vessel wall at each angular position of the scan; radial strain estimates are colour coded and displayed as a ring overlaid on the original echo image. Preliminary results from a tissue-mimicking test object and *in vivo* vessels were reported.

Using a computer simulation, O'Donnell et al. (1991) demonstrated the feasibility of using a speckle tracking technique to estimate axial and azimuthal wall displacement. Based on this approach, Shapo et al. (1996a, 1996b), reported on a displacement and strain imaging technique using an array-transducer catheter. The technique operates in conjunction with a fluid-filled balloon used to expand the vessel (Sarvazyan et al., 1993). They presented grey-scale strain images from a computer simulation and plots of averaged displacement and strain from a uniform phantom experiment. A probable weakness of this technique in the intravascular application is that estimation must be performed over a number of echo images in a system of intense dynamics (e.g., seven pushes were used in the reported phantom experiment). Other problems arise due to the expansion of the balloon. First, the transducer in the balloon will move during inflation. Shapo et al. (1996b) described the geometrical center algorithm to overcome this problem. Secondly, the balloon used is a non-compliant angioplasty balloon. This kind of balloon will have a round shape while inflated and correct deformation of the vascular tissue will only occur for vessels with a round shaped lumen.

Soualmi et al. (1997, 1998) presented work on the forward and inverse problem in intravascular elastography. Using computer simulation and finite element models, they determined intravascular strain elastograms of a vessel with lesion. With this strain image given as input, they were able to calculate a Young's modulus elastogram. However, additional boundary conditions were needed to generate a useful modulus elastogram.

1.5 Outline of the thesis

The aim of this study was to develop elastography for intravascular purposes. The feasibility of the technique was investigated using phantom studies. Phantom materials with different ultrasound and mechanical properties were constructed (Chapter 2) to identify the potential of intravascular elastography to characterise soft and hard material (Chapter 3). The dependence of the elastographic results on the echographic information was evaluated.

Next the technique was advanced to *in vitro* applications. A dedicated filter was developed that uses the peak of the correlation function (Chapter 4). The dependence of the technique on catheter position was investigated (Chapter 5). Additionally, a robust and fast implementation of the technique will be discussed (Chapter 6). Validation of intravascular elastography was performed using an *in vitro* study on diseased human arteries (Chapter 7). The potential of the technique to characterise different plaque components was investigated (Chapter 8). Additionally, the possibility to detect vulnerable plaque is demonstrated.

Finally, preliminary results of *in vivo* experiments are presented to demonstrate that it is possible to obtain elastographic images during an intervention in the catheterisation laboratory (Chapter 9).

Chapter 2

Elastic and Acoustic Properties of Vessel Mimicking Material

abstract

The mechanical and acoustic properties of agar-gelatin gels, used to construct vessel mimicking phantoms for ultrasonic elasticity studies, were investigated. Gels with varying compression moduli were made using a gelatin solution (8% by weight) with a variable amount of agar (1%-3% by weight). Carborundum particles were added as scattering material. The compression modulus was determined using a dynamic mechanical analyser. The dependence of the compression modulus and the acoustic parameters on the agar concentration, as well as on the age and the temperature of the samples was investigated. The results show that the compression modulus is strongly influenced by these factors, while the effect on the acoustic parameters is less. Compression moduli spanning a useful range for vascular phantom construction with realistic acoustic parameters can be achieved by varying the amount of agar. Phantoms constructed from these gels are well suited to serve as a model for plaque containing vessels.

2.1 Introduction

Ultrasound elasticity imaging has proven to be a technique able to detect differences in tissue stiffness to obtain information that is unavailable or inconclusive from ultrasonic imaging alone (Chapter 3),(Ophir et al., 1991, 1996; Céspedes et al., 1993b; Shapo et al., 1996a; O'Donnell et al., 1994; Rubens et al., 1995; Lerner et al., 1990). In intravascular applications, plaque remodelling and removal procedures are predominantly mechanical in nature (Waller, 1989; van Leeuwen et al., 1991, 1993). Therefore, knowledge about the local mechanical properties (assessed with ultrasound elasticity imaging) may be a useful tool to assist in the selection of the most adequate interventional procedure (Tobis et al., 1991).

based on the Publication : "Elastic and Acoustic Properties of Vessel Mimicking Material for Elasticity Imaging" by Chris L. de Korte; E.Ignacio Céspedes; Anton F.W. van der Steen; Ben Norder and K. te Nijenhuis. *Ultrasonic Imaging* 19(2):112-126; 1997

For evaluation of ultrasound elasticity techniques, it is useful to have test objects with elastic and acoustic properties similar to those of tissue. For intravascular applications, obvious choices like tubes made of rubber or silicon are unsuitable since these materials are highly attenuating at typical intravascular ultrasound frequencies (20-40 MHz) (Bom et al., 1993; Foster et al., 1993; Nissen & Gurley, 1991). Therefore, other materials were needed for this investigations. Water based gels containing gelatin and/or agar have been widely used as tissue mimicking materials in a variety of ultrasound tissue characterisation applications (Céspedes et al., 1993b; van den Aarssen et al., 1989; Yamakoshi et al., 1990; de Jong et al., 1991).

Some acoustic parameters of these materials are described in the literature. Reported values for the ultrasound velocity c depend on the amount of gelatin and agar used. Values for the ultrasound velocity between 1550 and 1650 m/s at room temperature are reported for gels containing more than 15% gelatin (Madsen et al., 1982a). Lower values of the ultrasound velocity for gels with agar are reported: 1500-1600 m/s at $22°C$ (Madsen et al., 1982a). The velocity in these gels can be increased by adding an amount of n-propanol (Madsen et al., 1978) or decreased by adding olive or castor oil (Madsen et al., 1982a). The velocity is also dependent on the gelatin concentration: Ryan (1997a, 1997b) described a higher ultrasound velocity for a 30% gelatin gel (1601 m/s) than for a gel containing 15% gelatin (1549 m/s). Since gelatin gels with less than 15% gel concentration can be formed, a lower value than 1550 m/s for the speed of sound must be achievable. The ultrasound velocity in gels is also dependent on the temperature. Madsen et al. (1978) described a 25 m/s increase in c from $15°C$ to $25°C$ for a gelatin-water-alcohol gel, but also a decrease on the order of 15 m/s between $22°C$ and $34°C$ for several oil-gelatin-water gels (Madsen et al., 1982a). The attenuation of these materials is also dependent on the gel and concentration used.

Assuming the attenuation α can be described by $\alpha = \alpha_0 \cdot f^n$ (Wells, 1977) where α_0 and n are constants and f is the frequency, Ryan (1997a, 1997b) reported values for 15% gelatin gels of 0.18 dB/cm.MHz and 1.4 for α_0 and n respectively and 0.42 and 1.35 for α_0 and n respectively for a concentration of 30% gelatin. Madsen et al. (1978) added powdered graphite to raise the attenuation: by increasing the graphite concentration from 0.049 to 0.187 g/cm^3 α_0 is increasing from 0.368 to 1.453 dB/cm.MHz and n is decreasing from 1.24 to 0.99. The temperature dependency was also investigated by Madsen and co-workers: There is only a minor influence of the temperature but, both the values for α_0 and n tend to decrease with increasing temperature (Madsen et al., 1978, 1982a).

Although there is a wealth of data concerning the ultrasonic velocity and attenuation, only a few measurements of the mechanical properties of water based gels are available in the context of ultrasound elasticity assessment. Ryan (1997a, 1997b) reported values of 420kPa and 1.3MPa for the circumferential Young's modulus of vessel phantoms made with 15% and 30% gelatin, respectively. Parker and co-workers used a mixture of gelatin and agar for their elasticity imaging technique (Parker et al., 1990; Lerner et al., 1990). A Young modulus of 10 kPa for mixture of 1.5% agar and 1.5% gelatin and a modulus of 100 kPa for a 3% agar and 3% gelatin mixture were reported. O'Donnell and co-workers performed elasticity imaging techniques on gelatin gels using a 5.5% solution as soft and 12 % as hard material (O'Donnell et al., 1993; Lubinski et al., 1996).

Te Nijenhuis (1981a, 1981b) described some mechanisms influencing the storage modulus in shear of gelatin gels. The storage modulus determines the elastic part of the stress,

according to the storage of mechanical energy. In the first paper, the dependency of the storage modulus in shear on the gelatin concentration and the ageing (i.e. the time between gelling and measuring) of gelatin gels was described. For gelatin concentrations between 2% and 25%, the storage modulus is approximately proportional to the square of the concentration. A strong dependency of the storage modulus on the age of the samples was found : the modulus is an ever increasing value as a function of the age of the sample. Next, the temperature at which the samples were gelled and aged influences the storage modulus. At a low temperature ($-1.2°C$), the storage modulus increased much faster with age than at room temperature ($25°C$). In the second paper, ageing with a temperature history was discussed. A higher value for the storage modulus was obtained when the gelatin is pre-aged at $17.4°C$ for some time and subsequently aged at $-1.2°C$ than when the samples were immediately put at $-1.2°C$. When the gelatin was returned to $17.4°C$, the storage modulus quickly decreased and followed the ageing curve of $17.4°C$.

Since knowledge of the mechanical properties is necessary for constructing realistic vessel mimicking phantoms for ultrasound elasticity imaging studies, we investigated the compression modulus of water-based gels in this study. Using a dynamic mechanical analyser, the compression moduli of different mixtures were investigated. Next, we investigated the linearity of the elastic modulus of the gel samples, the temperature dependency and the influence of the age of the samples. The temperature and age dependency of the ultrasound velocity, the attenuation at 25 MHz and the slope of the attenuation spectrum between 20 and 30 MHz of the samples were investigated. Finally, these acoustic parameters of samples with different agar concentrations were determined.

2.2 Methods

2.2.1 Materials

The tissue mimicking material used in this study is a combination of gelatin and agar-agarose. Pure gelatin gels are strong but a high concentration (15-30 %) of gelatin is needed to obtain a manageable material (Ryan et al., 1993). However, attenuation at high gelatin concentrations is prohibitively high (at 30 MHz) and sample manageability at room temperature is low. On the other hand, pure agar-agarose gels are firmer at much lower concentrations (1-3%), but tend to tear or crack easily.

To overcome the individual disadvantages of these materials, we have utilised a mix of porcine skin gelatin (Type I, approximately 300 bloom, No.G-2500, Sigma Chemical company, St Louis, USA) and agar (Agar Agar CMN, Boom, Meppel, The Netherlands). Using a mixture of these two materials, we obtained easily manageable gels (strong, consistent, with tear strength) with the consistency caused by the gelatin and a variable stiffness dominated by the agar concentration. Agar concentrations of 1%, 2% and 3% by weight were used to span a range of desired hardnesses. 0.5% to 1% by weight carborundum powder (SiC crystals) with a particle size in the range of 3-10 μm was used to add ultrasonic scattering to the otherwise echolucent gel. By varying the carborundum concentration, the echogenicity of the material could be manipulated.

Batches of 100 g of the different gels were made. Distilled water produced by a Milly-Q plus (Millipore SA, Molsheim, France) was mixed with 8 g of gelatin and the desired amount of agar and carborundum. These batches were heated in a microwave oven at an

output power of 900 Watt for 2 minutes, positioned at the edge of a rotating tray. The batches were stirred at 30 s intervals to prevent the forming of hot-spots. A portion of the batch was poured in a petri dish until a layer with a thickness of approximately 7 mm was formed. To control the gelling temperature, the petri dish was placed on melting ice and after 5 minutes of gelling, samples with a diameter of 10 mm were cut using a punch.

2.2.2 Compression modulus assessment

Equipment: The elastic modulus is the ratio of a stress to a strain that indicates how the test object (sample) reacts to a mechanical energy. This modulus can be measured in flexure, tensile or compression geometry. The elastic modulus of the samples was estimated using a dynamic mechanical analyser DMA 7e (Fig. 2.1, Perkin Elmer, Norwalk CT, USA). This instrument determines the mechanical properties of materials in compression mode by applying an oscillating force and measuring the response of the material. The device is able to characterise materials with a compression modulus from 1 kPa to 1000 GPa. In this study, the experiments were performed in the controlled strain mode. A sinusoidal oscillating "dynamic" strain was applied, and the force needed for applying this strain was measured (This in contrary to the controlled stress mode were a constant sinusoidal stress is applied and the strain is measured). The resolution of the applied force is 1 mN and the amplitude of vibration encompasses 3 decades from 1 to 1000 μm with a 0.2 μm sensitivity. In this study, only the real part of the elasticity modulus (storage modulus) is measured since the elastic part of the gels is always more than 10 times larger than the viscous part. Since the measurements were performed in compression, we utilise the term compression modulus.

For the experiments, we used a strain with a amplitude of 0.5 %. The samples were positioned between two parallel plates with a diameter of 15 mm. Using this method, the measured compression modulus is closely related to Young's modulus since the plates were larger than the samples (Chen et al., 1996). To achieve free-slip conditions the samples were lubricated with water and measured under water. Since the samples were not fixed to the plates, the samples were precompressed with a "static" strain with a value of 120 % of the dynamic strain (which is 0.6% strain) to ensure continuous contact with the plates. A personal computer was used to program the experiments and to store the measured data.

Acquisition: Before the modulus of a sample was measured, the device performed a calibration step: A run without sample was performed to be able to compensate for the weight of the plate and the water environment. Next, the sample was put between the two parallel plates and the measurements were performed under water. The temperature was controlled using a Tamson TC9 circulating water-bath (Tamson Inc. Zoetermeer, The Netherlands). Several factors that are supposed to influence the compression modulus were investigated, before the compression moduli of samples with different agar concentrations were determined.

Initially, the influence of the used vibration frequency of the DMA on the compression modulus of the material was investigated. We performed a frequency scan (0.1 Hz to 5 Hz) on a sample of 8% gelatin, 1% agar and 1 % SiC at constant temperature of $25°C$. Next the linearity of the compression modulus was determined by measuring the stress-strain curve for strains in the 0-2% range on an 8% gelatin, 2% agar and 1% SiC sample.

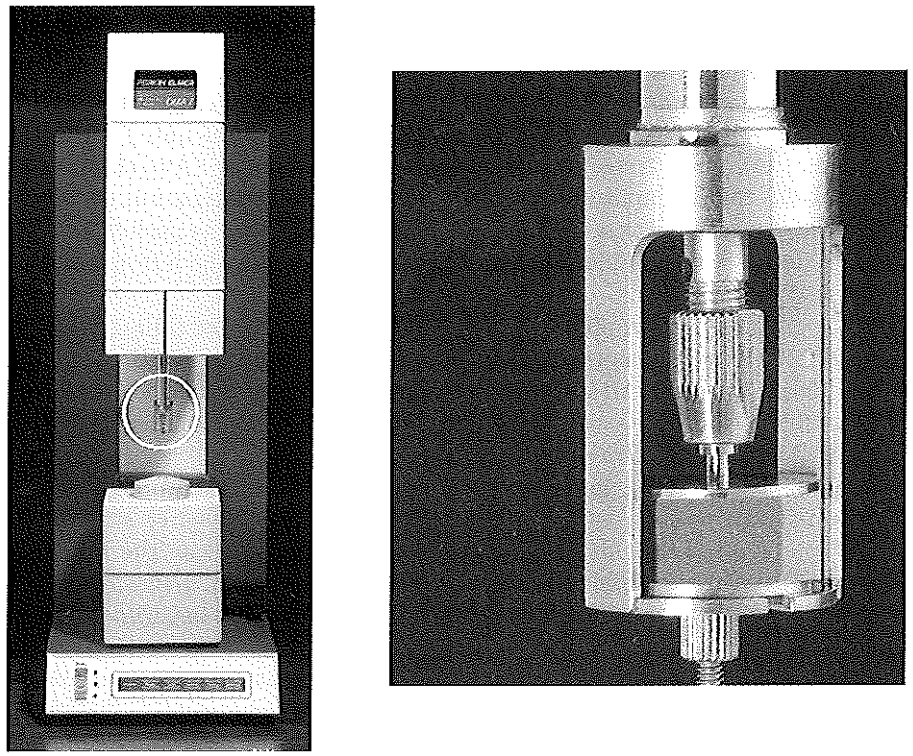

Figure 2.1 The dynamic mechanical analyser

Since the compression modulus of gels is not only determined by the concentration of gelatin and agar but also by some physical factors during the preparation and measurement of the materials, we investigated these factors. The age of the material, which is the time between gelling and measurement of the samples, was investigated by measuring the compression modulus at a constant temperature of $25°C$ for 240 minutes after gelling time. To prevent confounding of the age and temperature dependency, the temperature dependence was investigated using a sample aged for 6 days at temperatures between 5 and $40°C$. At this time, changes of the modulus during the scan are negligible, since the full temperature scan took 35 minutes.

The reproducibility of the measurements was investigated using 4 samples with 1% agar gels (with 8% gelatin and 0.5% carborundum) obtained from a single batch. These samples were measured 45 times within a five minutes period after 4 hours of ageing at room temperature. The mean and standard deviation of the compression modulus estimation were determined. Next the variability between the four samples (SD_{intra}) and within the samples (SD_{inter}) were calculated (Armitage, 1973). Since the modulus is dependent on the temperature during the ageing process (te Nijenhuis, 1981a), the age of the samples and the temperature during the actual measurement of the compression modulus, these parameters were kept constant for the samples. We allowed gelling and ageing of the samples to take place in iced water. After four hours of ageing, the modulus of 1%, 2% and 3% agar samples was measured at $20°C$.

2.2.3 Acoustic parameter assessment

Equipment: The acquisition set-up consists of a water tank with a transducer mounted in a fixed holder. The custom made transducer assembly houses a 25 MHz acoustic element (1 mm ⌀) with a -6dB bandwidth between 20 and 30 MHz mounted on a stainless steel rod (5mm ⌀). The transducer was excited with a pulser (Avtech AVL-2-PS-P, Toronto, Canada) (pulse amplitude 40V, duration 40ns) and immersed in water with the phantoms placed at the bottom of the water tank. The pulser was excited by a custom made trigger device with an output pulse that is in phase with the internal clock of the digital oscilloscope.

The rf-signals were pre-amplified (gain 40 dB) using a receiver (Miteq AU-3A-0120, Hauppage NY, USA) after passing a custom-made high pass filter (-6dB, 10 MHz). The signals were digitised at 100 MHz, 8 bit by a digital oscilloscope (LeCROY 9400, Spring Valley NY, USA). The rf-data was transported using an IEEE-488 interface to an IBM compatible PC for off-line processing.

Acquisition: The acoustic parameters were measured with the protocol also used in the acoustic microscopes of Foster et al. (1984) and van der Steen et al. (1994). The transducer was placed 2 mm above the material, which is placed on the bottom of the water tank and 10 rf-traces (tissue signal) were acquired. Next the material was removed and again 10 traces (reference signal) were acquired. During the experiments the water temperature was $20°C$.

Data processing: Three acoustic parameters were calculated as described by van der Steen et al. (1991): the velocity of ultrasound and two which characterise the attenuation spectrum: The value at 25 MHz (central frequency of the transducer) and the slope of the spectrum between 20 and 30 MHz. The mean value and the standard deviation of the parameters were calculated.

Similarly to the compression modulus studies, the temperature dependency of the acoustic parameters was investigated between 5 and $40°C$ using one sample. At each temperature, a tissue and reference signal were acquired and the parameters were calculated using the reference ultrasound velocity determined by Del Grosso and Mader

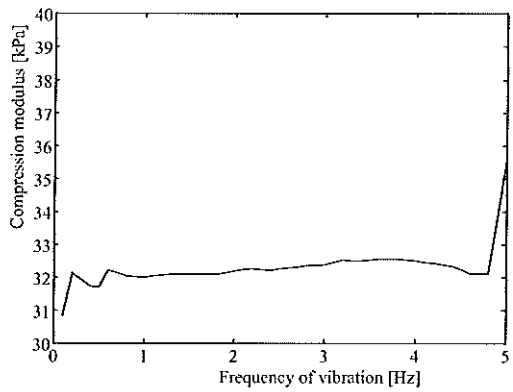

Figure 2.2 Dependency of the compression modulus on the frequency of the dynamic mechanical analyser vibration.

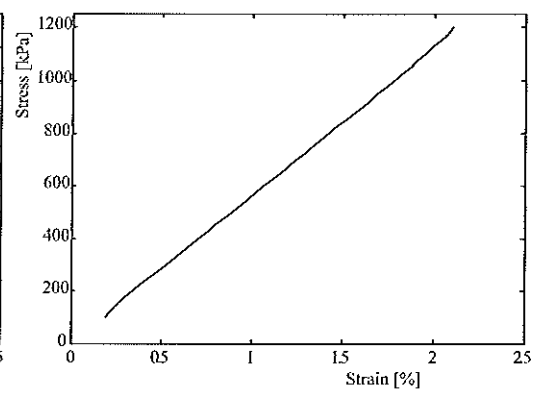

Figure 2.3 Relation between the stress and the strain measured with the dynamic mechanical analyser. Monitored stress is plotted as a function of applied strain (0-2%).

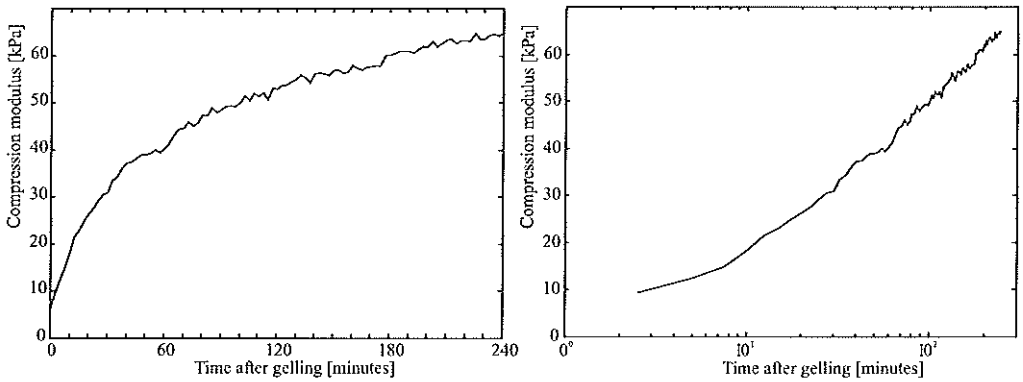

Figure 2.4 Relation between the compression modulus and the age of a 1% agar, 8% gelatin and 1% SiC sample measured with the dynamic mechanical analyser. a) linear time scale, b) logarithmic time scale.

(1972). The effect of ageing was investigated during 4 hours at a constant temperature of $20.3°C \pm 0.1$ using one sample for each data point. All samples were taken from one batch. Finally the acoustic parameters were measured for the samples with different agar concentrations. For each concentration, a batch was made and 20 samples were taken from each batch.

2.3 Results

2.3.1 Compression modulus

The influence of the frequency of vibration on the compression modulus is presented in figure 2.2. It is shown that the modulus was practically independent of the frequency in the range of 0.1 - 5 Hz; A frequency of 0.5 Hz was chosen for conducting the rest of the experiments. The stress-strain curve (Fig. 2.3) shows a linear behaviour of the compression modulus of the gel.

The influence of ageing on the compression modulus of the sample is illustrated in figures 2.4a and 2.4b. It is shown that the compression modulus increased with ageing time. A linear behaviour of the modulus as function of the logarithm of the time is observed. When the modulus is plotted versus a linear time scale, it can be seen that after 240 minutes of ageing the rate of increase drops substantially. By that time, a ten-fold increase in the modulus occurs. In figure 2.5, the result of the temperature scan is shown. The compression modulus behaves almost constant between 5 and $20°C$, but an order of magnitude decrease in the modulus is observed between 20 to $40°C$.

Table 2.1 Reproducibility measurements of the compression modulus with 1% agar, 8% gelatin, 1% SiC samples (n=4) each sample measured 45 times.

Mean	SD	SD_{inter}	SD_{intra}
25.01	0.44	0.34	0.32

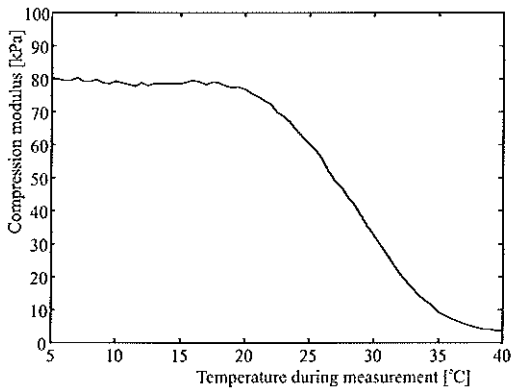

Figure 2.5 Temperature dependency between 5 and 40°C of the compression modulus of a 1% agar, 8% gelatin and 1% SiC sample measured with the dynamic mechanical analyser. The sample had aged for 6 days and the scan took 35 minutes.

The reproducibility of the measurement was tested on 4 samples, obtained from a single batch (Table 2.1). The standard deviation is less than 2% and the intersample variability (SD_{inter}) and intrasample variability (SD_{intra}) are less than 1.5%. The compression moduli of the samples with different agar concentrations are presented in Table 2.2. The mean values are 36 kPa, 56 kPa and 123 kPa for the 1%, 2% and 3% agar samples (8% gelatin, 1% SiC) respectively, with a standard deviation that is in the order of 1.5%.

2.3.2 Acoustic parameters

The results of the influence of ageing on the acoustic parameters are presented in figure 2.6. A linear regression line is fitted through the data. At a constant temperature ($20.35 \pm 0.05°C$) the ultrasound velocity increases significantly (p=0.025) with time, the attenuation at 25 MHz decreases ($p < 0.01$) and the slope of the attenuation spectrum shows no significant age dependency (p=0.31).

The temperature dependency of the parameters is presented in figure 2.7. The ultrasound velocity has an overall tendency to increase with temperature. For comparison, the ultrasound velocity in water is also plotted (del Grosso & Mader, 1972). Both attenuation parameters increase between 5 and 10°C and then decrease between 10 and 40°C.

The values for the velocity and attenuation as a function of different agar concentrations are presented in figure 2.8. All the parameters increase with an increase in agar concentration. The ultrasound velocity increases from 1512 to 1518 m/s with a standard deviation of 0.5 m/s. The attenuation at 25 MHz shows an increase from 6 to 9 dB/cm with a standard deviation of 1 dB/cm. The mean value of the slope of the attenuation spectrum increases from 0.35 to 0.55 dB/(cm.MHz) with a standard deviation of 0.1 dB/(cm.MHz).

Table 2.2 Compression moduli of gel samples at 20°C, 4 hours after gelling in iced water (8% gelatin 1% SiC). Each sample was measured 30 times.

	1% agar	2% agar	3% agar
Mean (kPa)	35.58	55.91	122.55
SD (kPa)	0.54	1.02	1.76

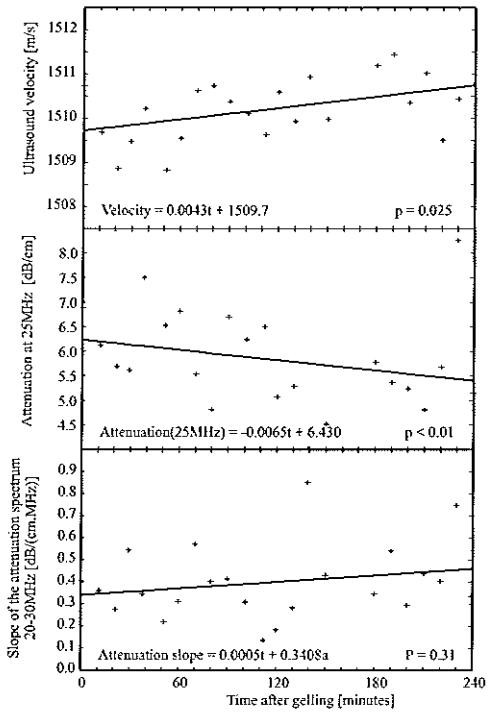

Figure 2.6 Dependency of the acoustical parameters on the age of the samples measured at $20°C$. a) Ultrasound velocity b) Attenuation at 25 MHz c) Slope of the attenuation spectrum between 20 and 30 MHz.

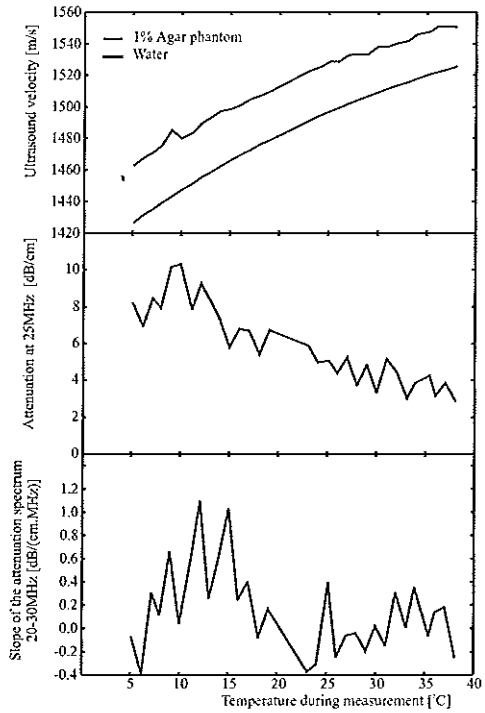

Figure 2.7 Relation between the measuring temperature and the acoustical parameters. a) Ultrasound velocity b) Attenuation at 25 MHz c) Slope of the attenuation spectrum between 20 and 30 MHz.

2.4 Discussion and Conclusions

In this study, we have investigated the compression modulus, the ultrasound velocity and the attenuation coefficient of a tissue mimicking material of interest for intravascular elasticity imaging. Using a mixture of water, agar-agar, and gelatin we were able to make manageable materials with desirable mechanical and acoustical properties.

The dependence of the compression modulus of agar-gelatin gels on age of the sample and actual temperature is investigated. The results show that the compression modulus increases by an order of magnitude during the first 4 hours. When the modulus is plotted versus the logarithm of the time, the relationship is nearly linear. A similar relationship was also observed by te Nijenhuis (1981a) for the storage modulus, measured in shear. The storage modulus measured in compression is 3 times the storage modulus measured in shear for materials with a Poisson's ratio in the order of 0.5. It can be seen that the influence of the time on the modulus has decreased substantially after 4 hours of gelling, with respect to the time needed for performing an experiment. Thus, for elasticity experiments, it looks useful to start the measurements no earlier than after 4 hours of gelling of the material.

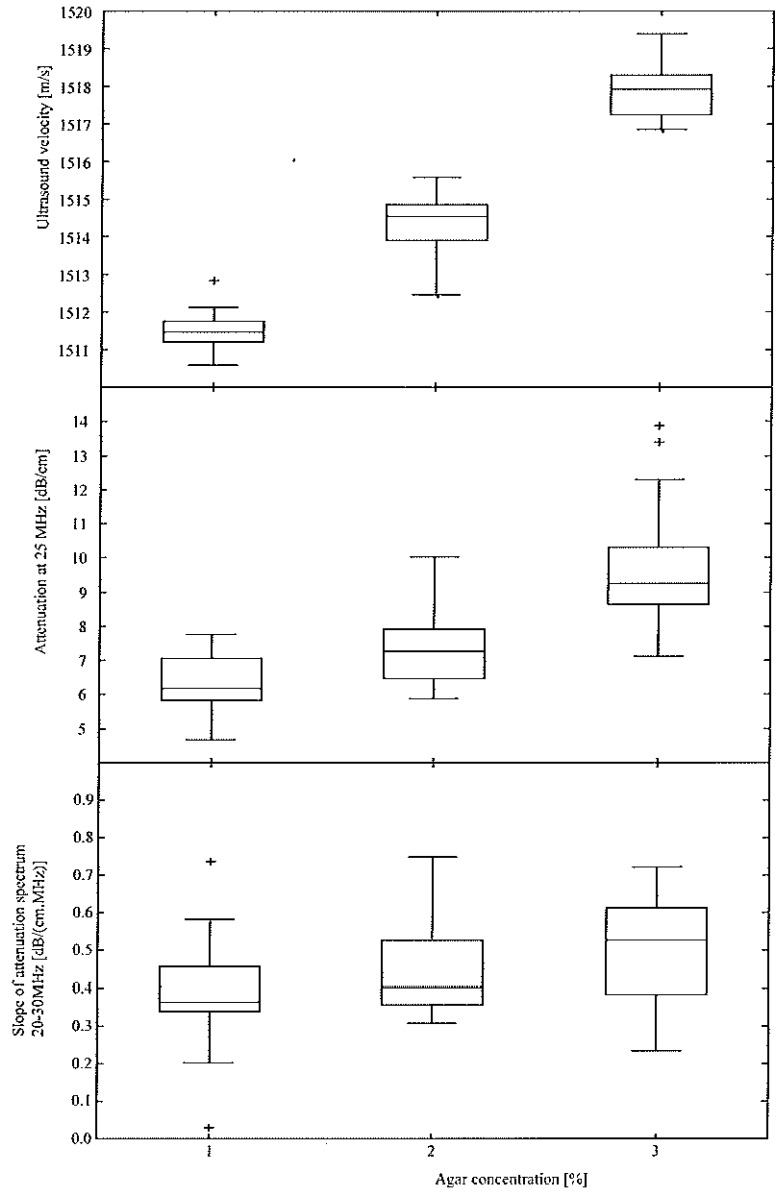

Figure 2.8 Acoustical parameters at 20°C of samples (n=20 for each concentration) containing different amounts of agar presented as box and whisker plot (lines of the box represent lower quartile, median and upper quartile and the whiskers show the extend of the rest of the data (+ is an outlier)). a) Ultrasound velocity b) Attenuation at 25 MHz c) Slope of the attenuation spectrum between 20 and 30 MHz.

The compression modulus is also strongly influenced by the temperature: Between 5 and 20°C the modulus is almost constant, but between 20 and 40°C an order of magnitude decrease of the modulus is observed. Therefore, while performing experiments with these materials at room or body temperature, the temperature needs to be well controlled. The melting points of agar and gelatin gels are 78°C and 32.5°C respectively (Madsen et al., 1982a). The melting point of agar-gelatin mixtures was not studied but it is interesting to note that the rapid decrease of the compression modulus occurs just before the melting point of gelatin.

The reproducibility study using four equally aged samples (Table 2.1) revealed that a good estimate could be made using a DMA when the temperature is constant. The compression modulus of the samples can be easily modified by adjusting the amount of agar. Using agar concentrations between 1% and 3%, compression moduli between 35 and 120 kPa were found. Values for Young's modulus for different vascular tissues reported by Fung (1993) are in the range between 5 and 500 kPa. Lee et al (1992) report static stiffness values for different atherosclerotic material. A value of 41 kPa for non-fibrous material, 82 kPa for fibrous specimens and 355 kPa for calcified deposits. Therefore, the mixtures investigated in this study span a useful range of compression moduli.

A different value for the compression modulus is found for the 1% agar samples used in the concentration dependency study (Table 2.2) and the reproducibility experiment (Table 2.1). Since we were interested in the reproducibility, no care was taken to measure the samples at exactly 20°C. However, also the different amount of carborundum particles used (0.5% and 1.0%) can influence the compression modulus. The measurements on the samples with varying agar concentrations were all performed with a 1% carborundum concentration.

Contrary to the compression modulus, the ultrasound velocity is hardly influenced by the ageing of the samples. An increase of 1.0 m/s in the velocity is observed during the 4 hours of ageing. The attenuation at 25 MHz has decreased 1.5 dB/cm and the attenuation slope increase 0.12 dB/(cm.MHz). These changes are in the same order as the standard deviation of the acoustic parameter estimation (Fig. 2.8).

The acoustic parameters are highly dependent on temperature. The ultrasound velocity shows a significant ($p < 0.001$) increase of 90 m/s when the temperature changes from 5 to 40°C. Since the main component is water this increase could be expected. The ultrasound velocity in pure water (del Grosso & Mader, 1972) increases 100 m/s in the same temperature range. The same trend was also observed by Madsen et al. (1978) for gelatin-water gels with alcohol added as preservative. Between 16 and 28°C, a 25 m/s increase in velocity was observed. This increase was in the same order as our observations. The attenuation first increases from about 7 to 10 dB/cm, but then decreases to 3 dB/cm at 40°C. A linear regression line fitted through this data shows a significant temperature effect ($p < 0.001$). Attenuation measurements on gelatin-water gels by Madsen et al. (1978) showed a decrease of 1.5 dB/cm at 5 MHz between 16 and 28°C. Although this decrease is in accordance with the results from this study, a comparison can not be made since the frequencies used are different. The slope of the attenuation spectrum has a similar temperature dependency as the attenuation at 25 MHz, indicating a high correlation between these two parameters. A high correlation between these two parameters was also found in biological tissue (Romijn et al., 1991; Oosterveld et al., 1991; de Korte et al., 1994). A linear regression fit reveals no significant relationship between temperature and attenuation slope ($p = 0.21$). It can be concluded that not only the compression modulus, but also the acoustic parameters of the gels are highly

influenced by the temperature. Thus, during the experiments, temperature needs to be well controlled.

The measured acoustic parameters are dependent on the agar concentration used. The ultrasound velocity shows a 6 m/s increase, when the agar concentration changes from 1% to 3%. The influence of this 0.4% increase will be of minor influence on the echograms. The attenuation at 25 MHz increases 3 dB/cm. This corresponds to a 50% increase and is large compared to the increase in the ultrasound velocity. The effect of a 50% increase of the attenuation must be taken into account, when multilayer phantoms (composed out of gels with varying agar concentration) are used.

Several papers can be found containing values for the ultrasound velocity of vascular tissue and plaque material. Greenleaf et al. (1974) reported values for arterial tissue with several lesions between 1501 and 1532 m/s at $20°C$. Lockwood et al. (1991) reported values for arterial specimens between 1579 and 1628 m/s at $37°C$. Comparison of the ultrasound velocity at a temperature of $20°C$ in biological tissue and in this phantom material reveals that the values are in the same range.

Reported values for the attenuation range between 6 and 15 dB/cm at 10 MHz (Greenleaf et al., 1974). At 30 MHz, an attenuation of 40 dB/cm is reported (Lockwood et al., 1991). It can be concluded that the attenuation of the agar gels is lower than the attenuation in arterial tissue. When material is needed with an attenuation coefficient similar to biological tissue, the amount of scattering material could be increased. Note that increasing the amount of scattering material also can affect the compression modulus.

Compression moduli spanning the values found in the literature for intravascular tissue can be achieved by varying the agar concentration. Since the acoustic parameters of the mixtures described in this study are in the range of values found in literature for these tissues, these mixtures are well suited for phantom preparation for intravascular elasticity measurements. Using these mixtures, we constructed phantoms mimicking intravascular morphologies to evaluate the effectiveness of intravascular elasticity imaging (Chapter 3). Since we found various and strong dependencies of the gel properties on various factors, we suggest that these phantoms are best suited for relative elasticity measurement.

Chapter 3

Feasibility Studies in Phantoms

abstract

A technique is described for measuring the local hardness of the vessel wall and atheroma using intravascular ultrasound. Strain images were constructed using the relative local displacements, which are estimated from the timeshifts between gated echo signals acquired at two levels of intravascular pressure. Time shifts were estimated using 1-dimensional correlation with band-limited interpolation around the peak. Tissue mimicking phantoms with the typical morphology and hardness topology of some atherosclerotic vessels were constructed. Hard and soft regions could be distinguished on the strain image, independently of their contrast in echogenicity. Thus, the potential of ultrasonic hardness imaging to provide information that may be unavailable from the echogram alone was demonstrated. The strain images of the homogeneous and layered phantoms showed some artifacts that need to be corrected for, to obtain images of the modulus of elasticity. For in vitro and in vivo experiments the spatial resolution of the technique needs to be improved. Furthermore 2-dimensional correlation techniques may be necessary in case of non radial expansion and an off-centre catheter position.

3.1 Introduction

Several catheter-based vascular interventional techniques for treating symptomatic atherosclerotic disease (dilating balloons, laser ablation, atherectomy devices, stents) palliate luminal encroachment based on either plaque remodelling (angioplasty, stenting) (de Jaegere et al., 1994; van Beusekom et al., 1994) or recanalisation by plaque removal (lasers, atherectomy) (Waller, 1989). Because these procedures are predominantly mechanical in nature, the outcome of the intervention is largely influenced by the morphology and composition of the atheromatous plaque. Identification of plaque types associated with dissections, fractures or complications may provide the rationale for the selection of alternative revascularisation devices (Baptista et al., 1996; Linker et al., 1991). Intravascular ultrasonography (IVUS) has made it possible to study the plaque

based on the publication: "Intravascular Elasticity Imaging using Ultrasound: Feasibility Studies in Phantoms" by Chris L. de Korte; E. Ignacio Céspedes; Anton F.W. van der Steen and Charles T. Lancée. *Ultrasound in Medicine and Biology* 23(5): 735-746; 1997

morphology; however, ultrasonic distinction between some plaque types is difficult (di Mario et al., 1992). Using IVUS, calcified plaques are correctly classified in most cases (Potkin et al., 1992); conversely, lipid-filled and mixed (fibrous, lipid, calcified) plaques are not as easily identified (Yock & Linker, 1990). Thus, while plaque morphology is well defined by IVUS imaging in most cases, plaque composition remains undefined in some situations (di Mario et al., 1992).

The availability of IVUS images has lead to interest in the development of ultrasonic characterisation techniques to assess the mechanical properties of the vessel wall and atherosclerotic depositions to obtain clinically relevant information that is not always available from IVUS alone (Linker et al., 1991). Due to the mechanical action of dilatation techniques, a different response of tissue components with different mechanical properties can be expected. For example, lesions with calcification would be expected to be more rigid and therefore prone to fracture in response to the biomechanical stress of balloon dilation compared to a softer, non-calcified atheroma which might stretch but not crack (Honye et al., 1992; Lee et al., 1991). Conversely, lesions with low modulus of elasticity stretch easily in response to angioplasty but, being relatively soft and elastic, may tend to recoil recovering their shape before dilation. Therefore, knowledge about the local mechanical properties of plaque may be a useful tool for identifying the most appropriate and efficient interventional procedure (Tobis et al., 1991).

In this chapter, we investigated the possibility for determination of the mechanical properties of intravascular tissue using ultrasound. Tissue mimicking phantoms containing hard or soft regions were made. Local strain imaging using a modified intravascular ultrasound scanner is investigated and some artifacts inherent to this technique are described.

3.2 Previous related work

3.2.1 Mechanical testing of tissues

Although there is a wealth of data in the literature on the mechanical properties of normal arteries (for example see Fung (1993)), data on the mechanical properties of atherosclerotic plaque are limited. Studies of the mechanical properties of vessels date back to the 1800s and have continued until recently (Fung, 1993). Such measurements concentrate on the evaluation of vessel distensibility, *viz*, the fractional change of lumen area in response to a intraluminal pressure differential (Reneman et al., 1986; The et al., 1995). Many of these studies were aimed at the characterisation of vessel hardening with age.

Although distensibility is affected by all components of the vessel wall, it only provides a global measure of vessel elasticity. Reported measurements of the elasticity of local vessel components are scarce. However, the data available suggest that there are significant differences between the elastic moduli of normal vessel wall, fibrous and non-fibrous plaques, and even larger differences between the moduli of these and that of calcified plaque (Lee et al., 1993; Loree et al., 1994a). These elasticity differences are in the range that can be assessed using ultrasound elasticity imaging techniques (Ophir et al., 1991).

3.2.2 Tissue elasticity assessment and imaging techniques

In the past, several techniques have been developed for estimating tissue elasticity and motion using ultrasound (Dickinson & Hill, 1982; Krouskop et al., 1987; Ophir et al., 1991; Parker et al., 1990; Ryan et al., 1992, 1993; Shapo et al., 1996a, 1996b; Talhami et al., 1994; Tristam et al., 1986, 1988; Wilson & Robinson, 1982; Yamakoshi et al., 1990). Most techniques use mechanical excitation of the tissue under examination and subsequent measurement of tissue displacement or velocity using 1- or 2-dimensional crosscorrelation, optical flow, or Doppler velocimetry techniques. By computing the elastic modulus as the ratio of estimated local stress and measured strain, images of the elastic modulus can be obtained. The source of mechanical excitation can originate from blood pressure or respiratory forces, or from externally applied static or cyclic modes of deformation. Reviews of these techniques are available in the literature and are not discussed here (Hein & O'Brien, 1993; Céspedes et al., 1993b; Ophir et al., 1996). Extensions of these techniques have been applied more recently to the field of intravascular ultrasound.

Foster et al. (Foster et al., 1993) and Ryan et al. (Foster et al., 1993; Ryan et al., 1992; Ryan & Foster, 1997b) described a method where 1-dimensional correlation was used to determine time shifts between sequentially acquired radio frequency (rf) echo signals collected in M-mode format to track net vessel wall displacement. In addition, they used a 2-dimensional search technique on video echo images obtained at different static pressures to obtain grey-scale displacement images of an *in vitro* iliac artery specimen.

Talhami et al (1994) developed a technique for 1-dimensional strain assessment in the vessel wall by special processing of video signals. Based on the Fourier scaling property, they use chirp Z-transforms to estimate changes of the mean scatterer spacing that result from vessel wall compression. This technique computes an average strain estimate for the entire vessel wall at each angular position of the scan; radial strain estimates are colour coded and displayed as a ring overlaid on the original echo image. Preliminary results from a tissue-mimicking test object, *in vitro* and *in vivo* vessels were reported.

Using a computer simulation, O'Donnell et al. (1991) demonstrated the feasibility of using a speckle tracking technique to estimate axial and azimuthal wall displacement. Based on this approach, Shapo et al. (1996a, 1996b) reported on a displacement and strain imaging technique using an array-transducer catheter. The technique operates in conjunction with a fluid-filled balloon used to expand the vessel (Sarvazyan et al., 1993). Shapo et al. (1996a) present grey-scale strain images from a computer simulation and plots of averaged displacement and strain from a uniform phantom experiment. A probable weakness of this technique in the intravascular application is that estimation must be performed over a number of echo images in a system of intense dynamics (*e.g.*, seven pushes were used in the reported phantom experiment).

3.2.3 Displacement and strain in a uniform vessel

The measured data for the displacement and the strain can be checked when a theoretical model of the radial motion in the vessel can be derived. Ryan et al. (1992, 1997b) and Shapo et al. (1996a) derived relations for the radial motion. Shapo et al. (1996a) presented a 1/r decay of the displacement based on geometrical considerations. Consequently, the strain has a $-1/r^2$ relation with radial depth. Ryan et al. (1992, 1997b) described theoretical functions for the displacement and the strain using a plane strain

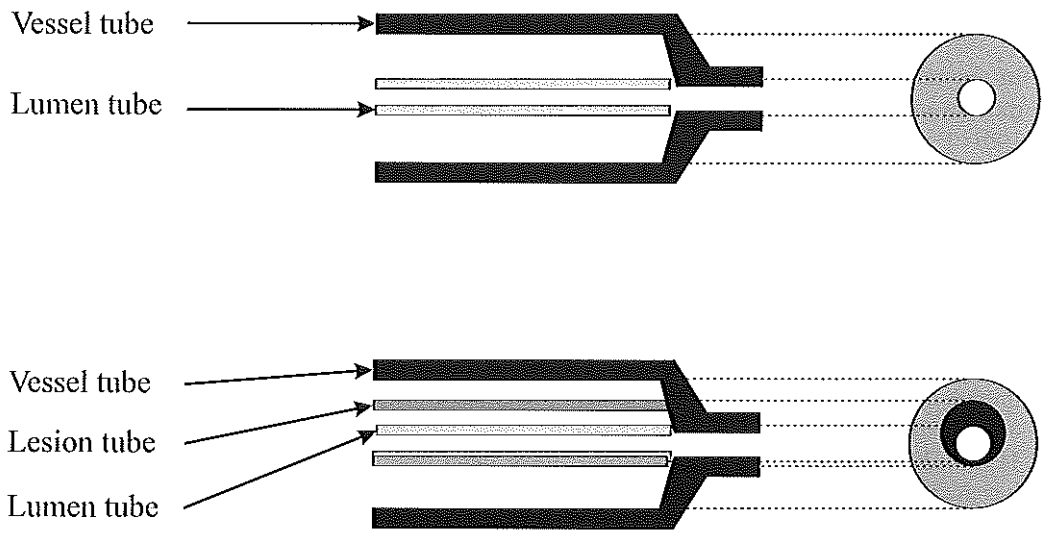

Figure 3.1 Tube system for creating phantoms *top)* Tube system for creating homogeneous phantoms. *bottom)* Tube system for creating layered phantoms.

model based on solid mechanics principles.

In this study, relations for the radial displacement and strain versus the radial distance in the vessel wall were derived using plane stress and plane strain models (Appendix A). In the plane stress model, the stress along the vessel wall is independent along the z-direction. In this case, the length of the vessel can change. The plane strain model assumes, that the length of the vessel does not change, since the strain in the z-direction is zero. The phantoms in this study are isotropic, causing changes in the z-direction when the phantom vessel is deformed in the radial direction. The displacement and strain in these phantoms are best described by the plane stress model. However, due to the anisotropy of real vessels (Poisson's ratio in z-direction is smaller than in the angular (θ) direction (Patel & Janicki, 1970a; Cheng et al., 1993), the displacement and strain are better described by the plane strain model.

3.3 Methods

3.3.1 Material

Vessel phantoms were made from a solution of agar (agar agar powder CMN, Boom BV, Meppel, The Netherlands) and gelatin (G 2500 porcine skin, Sigma, St.Louis, MO, USA) in water. Both agar and gelatin and combinations of them have been widely used for tissue equivalent ultrasound phantoms (de Jong et al., 1991; Madsen et al., 1978, 1982b, 1982a; Lerner et al., 1990; Parker et al., 1990; Yamakoshi et al., 1990). Values reported for the ultrasound velocity and attenuation of these materials are in the same range as the values in human tissue. At a fixed concentration of gelatin (8% by weight), gels with different hardness were made by varying the agar concentration. A solution of 1% agar and 8% gelatin was used as soft material (Young's modulus=30 kPa). Hard material

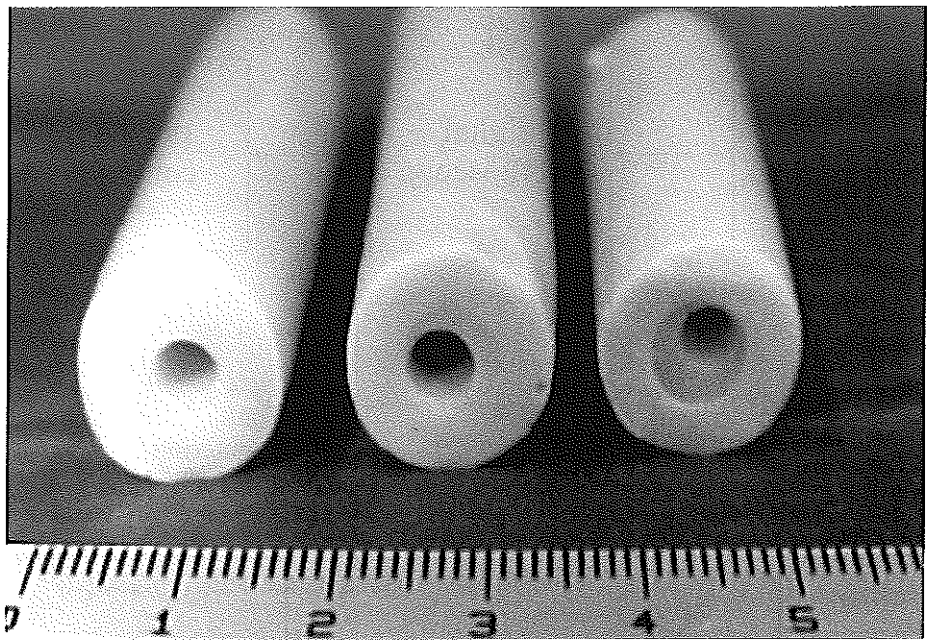

Figure 3.2 Morphology of three vessel phantoms *left)* Homogeneous phantom *middle)* Hard vessel wall with soft isoechoic plaque *right)* Hard hyper-echoic vessel wall with soft hypoechoic plaque.

(with a Young's modulus of 120 kPa) was made using 3% agar and 8% gelatin (Chapter 2). Carborundum (Silicon-Carbide (SiC), ranging from 3-10 μm) particles were used for scattering. Hypo- and hyperechoic materials were formed using different carborundum concentrations (0.5% to 2% SiC). The ultrasound velocity for these materials is approx. 1515 m/s at 20°C and are in the same range as values for the ultrasound velocity in vascular tissues (Chapter 2). The attenuation is 6 dB/cm and 9 dB/cm at 25 MHz for the soft and hard material respectively. These values are lower than the attenuation in vascular tissue, but did not interfere with the purpose of this study.

A homogeneous vessel was made using a 'vessel tube' (the outer body of a syringe with an inner diameter of 15 mm) (Fig. 3.1 *top*). A soft vessel phantom was made using a solution with 1% agar, 8% gelatin and 1.5% SiC. After the solution was poured in the tube it was shaken until the solution almost reached the gelling point to prevent the carborundum particles from sinking. A 'lumen tube' (outer diameter 4 mm) was inserted in the syringe to create the lumen. After gelling (approx. 5 minutes), the lumen tube was heated by running warm water (60°C). When the lumen tube was loosened from the gel, the water flow was stopped and the tube was removed and immersed in melting ice for 2 minutes. Using water streaming along the outside of the vessel tube, the phantom (Fig. 3.2 *left*) was loosened from the vessel tube and put in the water tank for measurements.

Layered vessels were made in a similar way (Fig. 3.1 *bottom*). Three different phantoms were created. These were a hyperechoic hard vessel with a hypoechoic soft lesion, a hypoechoic soft vessel with a hyperechoic hard lesion and a hard vessel containing a

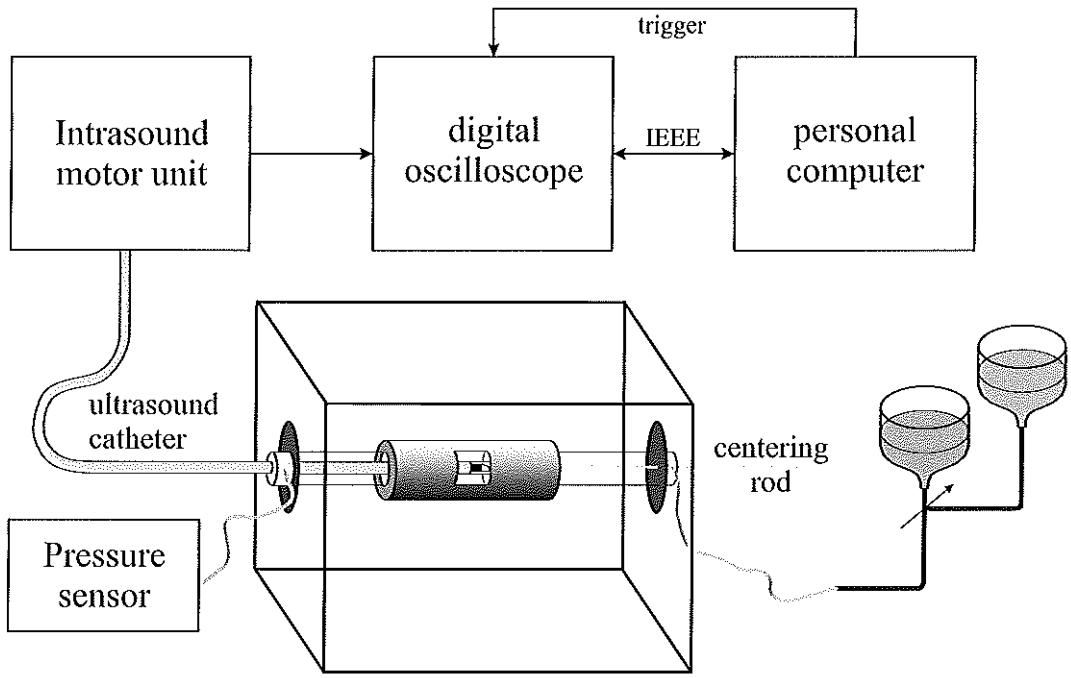

Figure 3.3 Instrumental set-up for performing strain measurements

soft lesion with no echo contrast between the two regions. First, the vessel was created using the vessel tube (a syringe with 15 mm inner diameter). To obtain an eccentric lesion phantom, first an initial larger lumen was created (using a 'lesion tube' with an outer diameter of 7 mm). This lesion tube was removed using warm water. Afterwards, the smaller lumen tube was used to create the final lumen by filling the space with gel representing the lesion material. The same procedures as for the homogeneous phantom were performed to loosen the vessel phantom from the tubes. The phantoms (Fig. 3.2 *middle & right*) were measured at $20°C$ and after 4 hours of ageing to diminish changes in the mechanical properties of the materials during the experiments (Chapter 2).

3.3.2 Experimental set-up

The vessel phantoms were scanned in a water tank (Fig. 3.3) at room temperature ($23°C$). The water tank is equipped with sheaths (8 F) at both sides. At the proximal side, an intravascular catheter (Princeps® 4.3F, Endosonics/DuMed, Rijswijk, the Netherlands) is inserted through the proximal sheath into the lumen of the phantom. The catheter is connected to an IVUS system (IntraSound®, Endosonics/DuMed, Rijswijk, the Netherlands). At the distal side, a steel rod is inserted and connected to the tip of the catheter to align it in the centre of the phantom lumen. The distal sheath is connected to a water column system for pressurisation. Pressure is monitored using a custom pressure sensor, connected to the proximal sheath. Two static pressure levels are used for endoluminal expansion of the vessels. Local compression on the order of

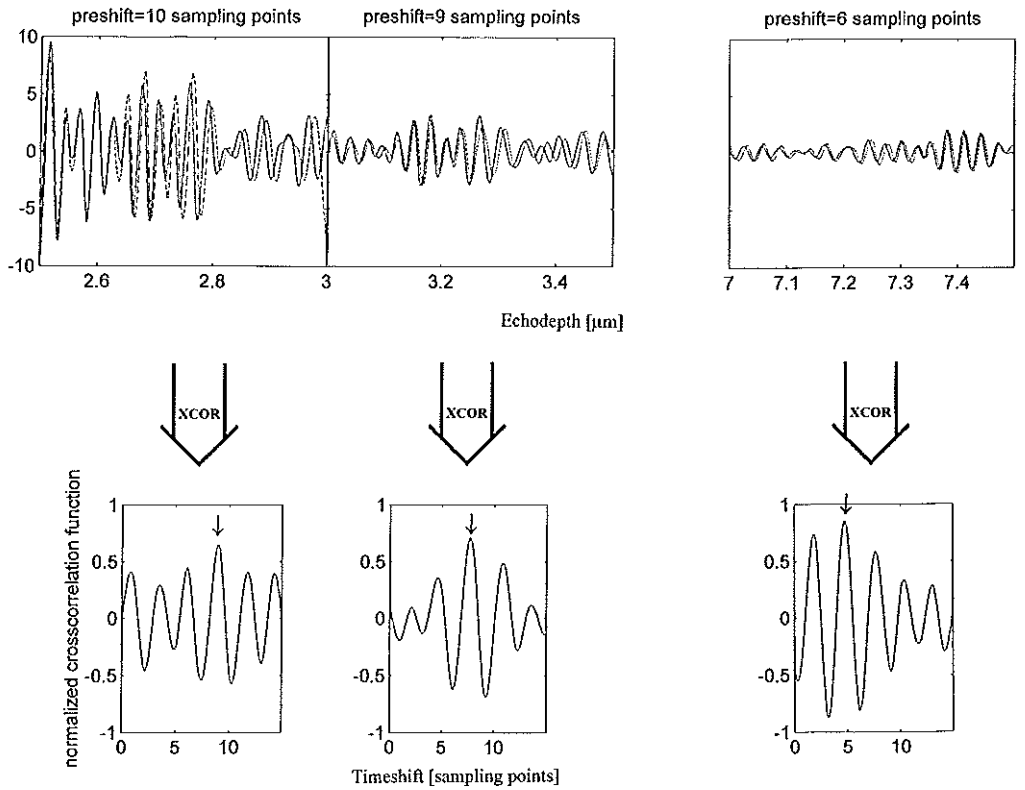

Figure 3.4 Principle of time-delay estimation using the peak of the crosscorrelation function. In the upper part, both traces (with the second trace pre-shifted for better visual comparison) are shown for windows with increasing echo depth. In the lower part, the corresponding crosscorrelation coefficient function for each window is plotted, showing a decreasing position of the peak with increasing echodepth.

1% is applied. A scan of 400 angles was performed at each pressure. The environmental pressure during the experiments was approx. 760 mmHg and the endoluminal pressure was measured with respect to this reference. The first scan was made at a 4 mmHg overpressure and the second scan at 8 mmHg overpressure. This pressure differential is smaller than the variation that will occur in the human body.

Rf data were obtained using a custom made acquisition system. The catheter with the transducer (f_c = 30 MHz, BW = 20 MHz) was connected to a modified motor unit of the DuMed IntraSound® machine equipped with a stepper motor to scan the vessel at 400 angles/revolution. Triggering of the rf-system and sampling of the data was phase-synchronised with the acquisition set-up using the external clock output of the digital oscilloscope. At each angle, 30 traces of 1000 points, were acquired. The 1000 points represent an echodepth of 7.5 mm. After passing through a limiter/pre-amplifier and a band-pass filter (10 - 40 MHz), the rf data are digitised at a sampling frequency of 100 MHz in 8 bits using a digital oscilloscope (LeCROY 9400) and stored for off-line processing.

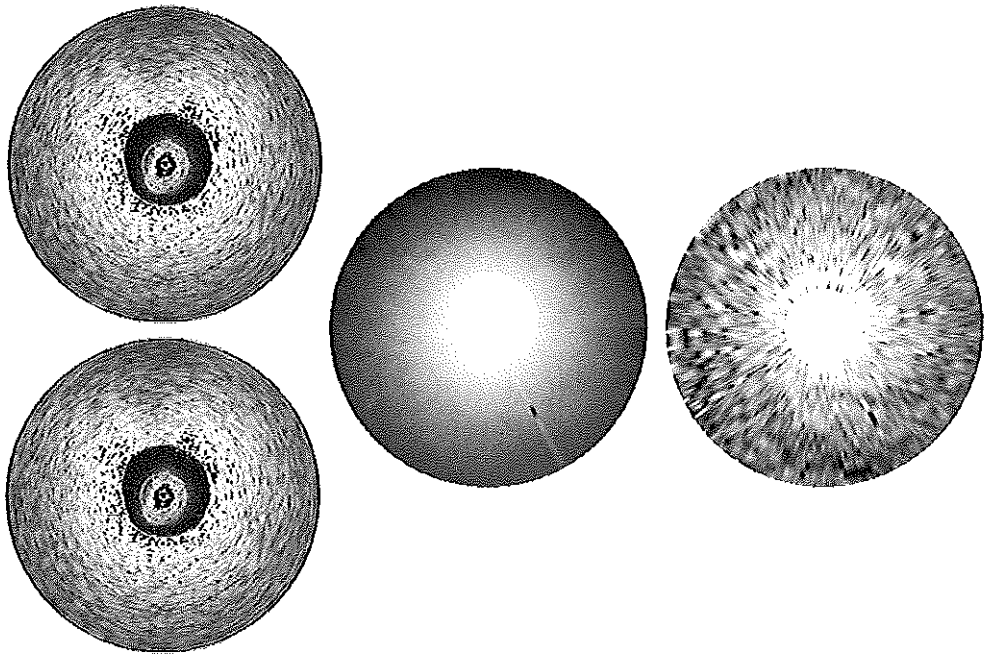

Figure 3.5 Schematic representation for deriving the strain images. left) Both the echo images at the low *(upper part)* and high *(lower part)* pressurisation level. *middle)* Time shift image between the pairs of rf-traces. *right)* Strain image.

3.3.3 Data processing and imaging

Time delay between the two traces can be determined using a correlation function. Due to the finite observation time available, the correlation function is estimated using the correlation coefficient function (Dickinson & Hill, 1982; Tristam et al., 1986; Trahey et al., 1988) and an interpolation algorithm on the rf data (Céspedes et al., 1995a; de Jong et al., 1990; de Korte et al., 1997).

After averaging the 30 traces, acquired at one angle, the first 200 data points of each mean rf signal, containing the echoes from the dome of the catheter and a part of the lumen, are excluded. Nonoverlapping windows of 50 points are used. For each window, the time delay is determined by detection of the position of the peak of the correlation coefficient function. The correlation coefficient function is upsampled by a factor of 40 using the low-pass interpolation Algorithm 8.1 (IEEE, 1979), to obtain the required resolution for the time shift estimation. The calculation of the time delay as a function of echodepth is illustrated in figure 3.4. In the upper part of the figure, subsequent windows of 50 sampling points of both the rf traces are shown. In this figure both traces are interpolated and the second scan is preshifted for improved visual inspection of the shape of the signals. Comparison of the 2 signals, before and after compression, shows that the correlation between the signals is high, thus allowing use of the proposed technique. The crosscorrelation function was estimated using these windows of the two traces and are shown in the bottom part of the figure. Comparison of the subsequent

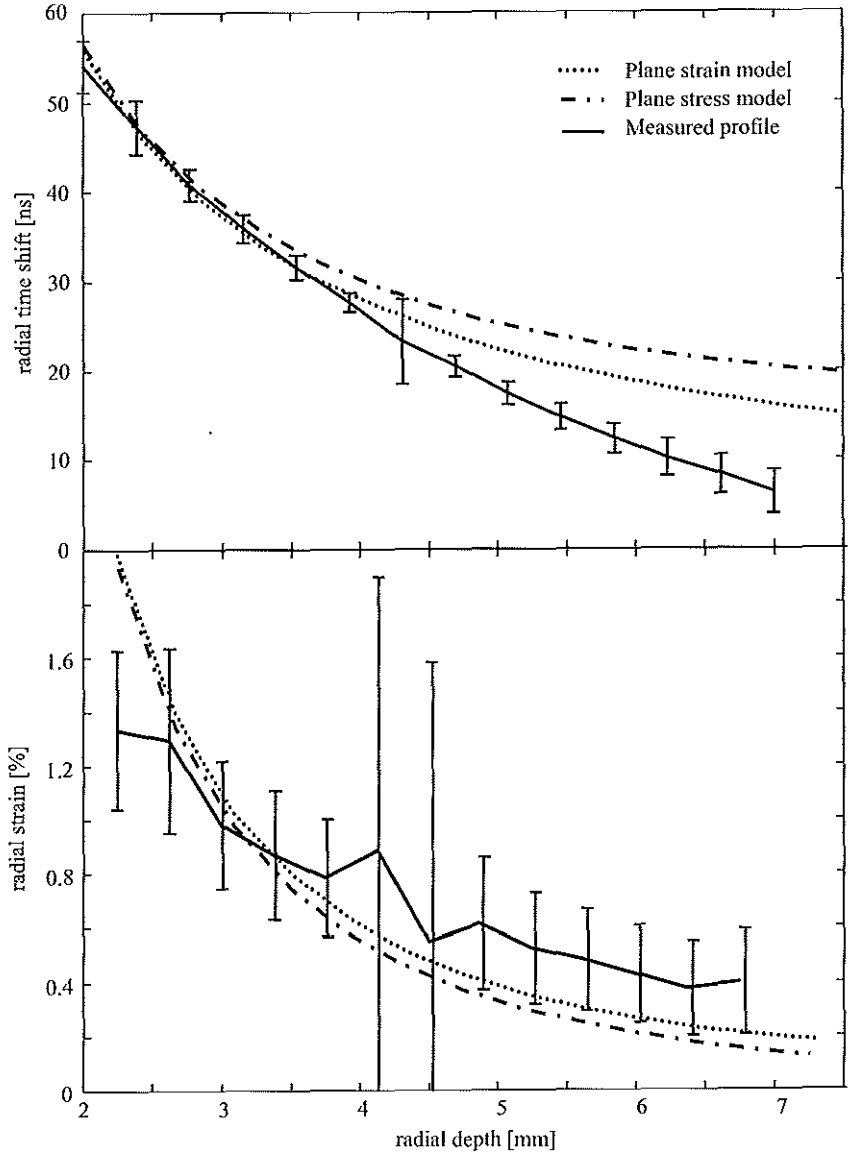

Figure 3.6 Mean and standard deviation calculated over all 400 angles of the homogeneous soft phantom for *top)* time shift between the pairs of traces and *bottom)* strain.

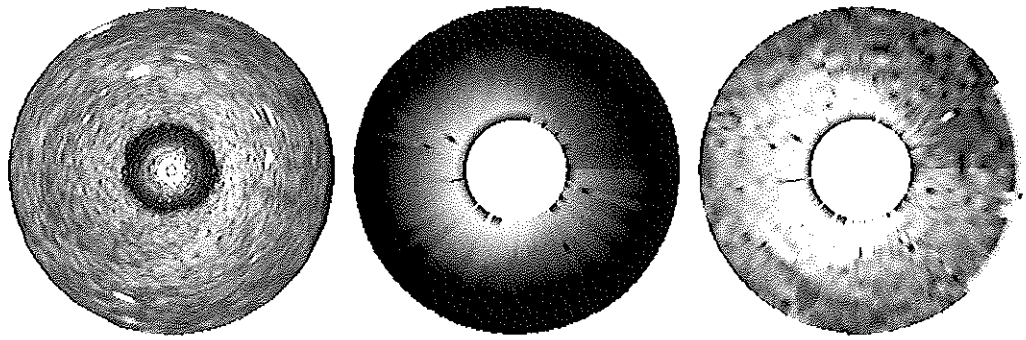

Figure 3.7 Hypo-echoic soft lesion in a hyper echoic hard vessel. *left)* Echogram of vessel with dark lesion. *middle)* Time shift image *right)* Strain image with a bright lesion in a dark vessel (border between lesion and vessel wall is clearly visible).

crosscorrelation function windows in echodepth shows a decreasing position of the peak of this function, due to the compression of the material. The radial strain profile is calculated using a 1-dimensional finite difference algorithm (Ophir et al., 1991) This profile contains 15 points.

Echo images (envelope of the rf-signal) and images of the time delay and strain of the vessel phantoms are generated using a software scan converter program. Strain values are filtered using a five-point sliding median filter in the angular direction. The values are plotted as a grey level using a bilinear interpolation. A mean profile of the time shift and the strain is calculated of the homogeneous phantom. These profiles are compared to the theoretical strain profiles using the plane stress and plane strain model.

3.4 Results

The described protocol for calculating the strain images of the vessel phantoms is visualised in figure 3.5. Using a homogeneous phantom, a time shift image (Fig. 3.5 *middle*) is calculated out of two echoscans (Fig. 3.5 *left*), acquired under different levels of endoluminal expansion. The difference between the two echograms is hardly visible, since the maximum displacement is less than 100 microns. The time shift image shows a decreasing brightness from the centre. The mean and standard deviation of the time shift over all angles is presented together with the theoretical profiles (with $E = 50$ kPa, $\nu = 0.495$) of the plane stress and plane strain model (Eqs. A.6 and A.9 resp.) in figure 3.6 *top*. The strain image (Fig. 3.5 *right*), calculated from the time shift signals, also shows a decreasing brightness with the distance to the centre, as predicted by equations A.6 and A.9. Figure 3.6 *bottom* shows the mean value and standard deviation of the strain image over all angles with both the theoretical strain curves.

The results of the experiment with the vessel phantom containing the hypoechoic eccentric soft lesion are presented in figure 3.7. In the echogram, the hypoechoic region from 6 to 12 o'clock is clearly visible. In the displacement image there is only a small effect visible at the inner part of the phantom, but the soft region is not distinguishable. Conversely, the strain image shows a white region between 6 and 12 o'clock, which

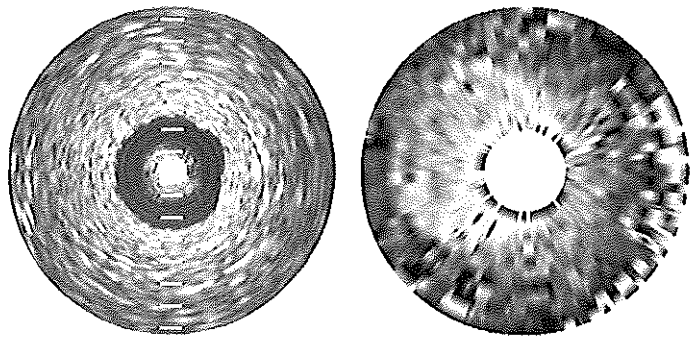

Figure 3.8 Soft lesion in a hard vessel with no echo contrast. *left)* Echogram with no lesion visible (calibration is 1 mm.) *right)* Strain image with a bright lesion in a dark vessel.

matches well with the hypoechoic region in the echogram. In this region, the strain is higher than in the surrounding part, indicating the presence of softer material. The border between the softer 'lesion' and the harder 'vessel' is also well delineated.

A similar phantom is measured with an eccentric soft lesion, but no echocontrast. With this phantom we demonstrate that a region, having a different hardness than the surrounding tissue but with no echocontrast can be detected with elastography although it will be invisible in the echogram. As expected, the echogram (Fig. 3.8) of this phantom shows no lesion while the strain image shows a bright region similar to the bright region in figure 3.7.

In the echogram of the vessel with the hyperechoic hard lesion (Fig. 3.9), the region representing the lesion can be easily recognised. A minor influence of this region is found in the displacement image. The dark area in the strain image corresponds with the hard lesion. This region is less apparent than the soft regions in figures 3.7 and 3.8. At 9 o'clock, where the lesion has the largest diameter, the brightness behind the lesion is similar to the brightness in the lesion itself. In general, the border between the lesion and the vessel is weakly delineated.

3.5 Discussion

In this study, we described a method for assessment of the local strain in vessel-like phantoms using different levels of endoluminal expansion. Strain images show the possibility of differentiation between 'harder' and 'softer' tissue regions.

Vessel phantoms were made using solutions of agar and gelatin. The hardness of the solution is mainly determined by the concentration of both the substances. The hardness is also affected by a series of other factors such as the gelling temperature, ageing of the material (*i.e.*, time between preparation and moment of measuring) and the measurement temperature (te Nijenhuis, 1981a, 1981b), (Chapter 2). In the process of making phantoms, we prepared the solutions each time using an identical protocol. In this way, the influence of other factors on the hardness is kept equal for all solutions, and the differences in hardness are mainly determined by the concentrations of the material used.

The time shifts between pairs of traces in the homogeneous soft phantom decrease with increasing echodepth (Fig. 3.6), which is characteristic for elastography experiments using compression. The standard deviation of this parameter is larger in the beginning and at the end of the trace (Fig. 3.6 *top*). (The large standard deviation at an echodepth of 4.25 mm is caused by an outlier). This effect can be explained by the higher compression of the signal at a small echodepth, causing decorrelation effects and by the decreased SNR towards the end of the trace, due to attenuation.

The theoretical values for the time shift (using plane stress and plane strain models) are plotted together with the measured profile. For the theoretical curves a Young's modulus of 50 kPa and a Poisson's ratio of 0.495 are chosen, so starting values for these curves are approximately the same as the measured curve. The difference between the plane stress and plane strain models is only apparent for large distances from the transducer. The measured time shift is smaller than the theoretical time shift. A hypothesis for this discrepancy is the protocol for the phantom preparation: the vessel phantoms are separated from the vessel tube (Fig. 3.1) using hot water, causing different mechanical properties of the outer layer due to differences in gelling time and gelling temperature. The simple theoretical model described by Shapo et al. (Shapo et al., 1996a) differs from the theoretical expressions derived in appendix A, since a linear term is missing.

As can be seen in figure 3.6, the standard deviation of the strain is larger than the standard deviation of the time shift. This is inherent to the method used for calculating the strain profile, since a finite difference algorithm is used (note that the outlier in the time shift causes two large values for the standard deviation in the strain). The theoretical strain profile values are in the same range as the calculated values. The theoretical values for the time shift and strain calculated using equations A.6 and A.9 are only valid for a homogeneous phantom. Theoretical local displacements in inhomogeneous layered phantoms can be estimated using finite element methods.

The strain images made of the phantoms with a lesion illustrate several phenomena. In the soft eccentric lesion (Figs. 3.7 and 3.8), the regions at the beginning of the phantom at 6 and 12 o'clock are brighter than the region at 9 o'clock. This effect is caused by the geometry of the lesion. At 6 and 12 o'clock the soft region is small compared to the region at 9 o'clock. The small regions are more compressed than the larger region, causing higher values for the strain. This effect is also described by Ophir et al. (Ophir et al., 1991) and is called 'elastic enhancement'. Another phenomenon is that the hard lesion (Fig. 3.9) is less apparent than the soft lesion, although the contrast in hardness is the same. This is caused by an effect we call 'mechanical shadowing'. With respect to the intravascular situation, an interesting case is soft tissue covered by a hard cap, for example a fatty lesion with a fibrous or calcified cap. The soft tissue behind this cap will be less compressed, than similar tissue that is not behind a region of hard material. This effect occurs parallel with the acoustic shadowing, that appears behind a region that is highly attenuating or reflecting. A calcium deposit in a vessel will both be hard and highly attenuating, so acoustic and elastic shadowing will both occur. Note that the mechanical shadowing is mainly caused by it's geometry and not by the hardness of the region. A thin ring will cause more shadowing than a hard spot surrounded by soft tissue. Understanding of artifacts apparent in this morphologies can be increased using finite element modelling.

During the experiments described in this chapter, special care was taken to position the catheter near the centre of the lumen. Since tissue motion due to the different pressurisation levels is mainly in the radial direction, the local compression can simply

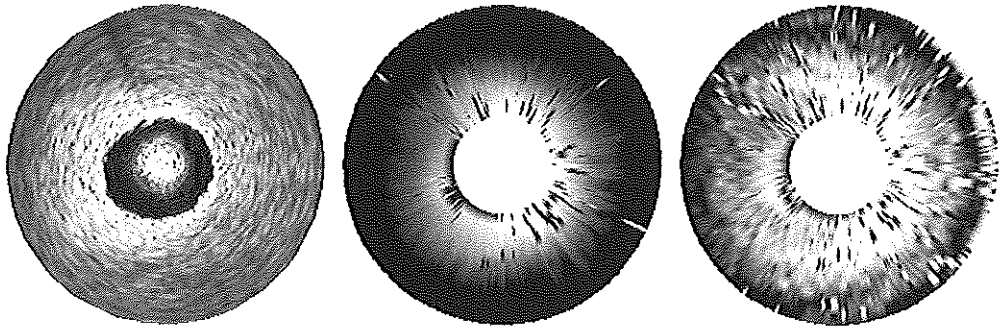

Figure 3.9 Hyper-echoic hard lesion in a hypo-echoic soft vessel.*left)* Echogram of vessel with dark lesion (calibration is 1 mm.) *middle)* Time-shift image *right)* Strain image with a dark lesion in a brighter vessel (border between lesion and vessel wall is not clearly visible).

be determined by calculating the time shift between the gated pairs of rf-traces. *In vivo*, the position of the catheter in the lumen is normally off-centre and the geometry of the lumen is generally not circular when atheroma is present. In these cases, tissue displacements may be misaligned with the ultrasound beam, introducing decorrelation errors when 1-dimensional displacement estimation techniques are used. To overcome this problem 2-dimensional correlation techniques may be required, which compare not only pairs of rf-traces but also rf-traces at subsequent angles. The window size used in the experiments will cause another problem when this methods are applied on real vessels. The vessel wall will be thinner than the wall of the phantoms prepared, causing a limited amount of estimated time shifts. The spatial resolution of the technique needs to be improved for adequate imaging of the morphology of the vessel wall and its pathology.

3.6 Conclusions

A technique is proposed for measuring the local hardness of the vessel wall and atheroma. We developed a method for making tissue mimicking gels with differences in hardness and constructed phantoms with the morphology of atherosclerotic vessels. The feasibility of this technique is demonstrated using vessel mimicking phantoms. Using these phantoms, hard and soft plaques can be identified, independently of the echogenicity contrast between the plaque and the vessel wall. Thus, the images show the potential of ultrasonic hardness imaging to obtain information that is inconclusive or unavailable from intravascular ultrasonic imaging alone.

The image artifacts that can occur due to the approximate nature of this technique, must be corrected to obtain images of the modulus of elasticity. In simple pathologies compensation for the artifacts is possible, but complex morphologies require complex compensation. In these cases finite element modelling can be useful.

Improvement of the spatial resolution is required to advance the technique to *in vitro* and *in vivo* experimentation. For example: An improved rf acquisition system will increase the SNR allowing to decrease the window size. The decorrelation effects of the vessel expansion when the catheter is off-centre and the non-radial expansion due to the geometry of the vessel must be investigated.

Chapter 4

Echo Decorrelation from Compressed Tissue

abstract

Several ultrasonic techniques for the estimation of blood velocity, tissue motion and elasticity are based on the estimation of displacement through echo time-delay analysis. A common assumption is that tissue displacement is constant within a short observation time used for time delay estimation (TDE). The precision of TDE is mainly limited by noise sources corrupting the echo signals. In addition to electronic and quantisation noise, a substantial source of TDE error is the decorrelation of echo signals because of displacement gradients within the observation time.

We present a theoretical model that describes the mean changes of the crosscorrelation function as a function of observation time and displacement gradient. The gradient is assumed to be small and uniform within the observation time; the decorrelation introduced by the lateral and elevational displacement components are assumed to be small compared to the decorrelation due to the axial component. The decorrelation model predicts that the expected value of the crosscorrelation function is a low-pass filtered version of the autocorrelation function (i.e., the crosscorrelation obtained without gradients). The filter is a function of the axial gradient and the observation time. This theoretical finding is corroborated experimentally. Limitations imposed by decorrelation in displacement estimation and potential uses of decorrelation in medical ultrasound are discussed.

4.1 Introduction

Useful additions to conventional ultrasonic imaging have been proposed and implemented in relation to the capability of this modality to provide information in real time and consequently assess tissue dynamics. A major contribution to modern ultrasonic instrumentation has resulted from the incorporation of blood flow measurement and imaging. In general, blood flow estimation is based on the assessment of the evolution of echo

based on the publication: "Echo decorrelation from displacement gradients in elasticity an velocity estimation" by E. Ignacio Céspedes; Chris L. de Korte and Anton F.W. van der Steen. *IEEE Transaction on Ultrasound, Ferroelectrics and Frequency Control*: in press; 1999

signals over time. Although flow measurement techniques based on the Doppler effect are dominant, other emerging techniques measure the time delay and/or decorrelation of subsequent echo signals obtained in M-mode (Ferrara et al., 1996; Foster et al., 1990; Loupas et al., 1995; Adler et al., 1995; Li et al., 1997).

Ultrasound-based tissue motion measurement and elasticity imaging for medical diagnosis have become fields of increasing research during the past 15 years (Gao et al., 1996; Céspedes et al., 1997a; Ophir et al., 1996; Parker et al., 1996; Shapo et al., 1996a). In brief, these techniques measure local displacement or velocity of tissue based on the evolution or dynamics of received echo signals. For example, tissue strain may be computed by finite difference of local tissue displacements measured at subsequent compression levels; displacements may be estimated from the relative time delays (or shifts) between pre- and post-compression echo signals. Note that although tissue is practically volumetrically incompressible, the term "compression" is used to mean 1-dimensional compression.

Common to both, elasticity and blood velocity estimation, is the presence of displacement gradients. In elasticity assessment, the local displacement of tissue varies in space: the displacement gradient along a given direction is by definition the strain component along that direction. In blood velocity assessment, common flow conditions give rise to velocity gradients usually quantified by the "shear rate" (i.e., the rate of velocity change in the vessel lumen (Milnor, 1982, page 53)). Velocity gradients result in corresponding displacement gradients that increase the variance of velocity estimators (Foster et al., 1990; Bonnefous, 1989). Recent work has demonstrated that displacement gradients due to blood velocity gradients impose constraints on the choice of observation window in intravascular ultrasound flow assessment (Li et al., 1997). Although in general strain and velocity gradients vary in space, a piece-wise constancy approximation is reasonable within a small ultrasonic sample volume of interest. Thus, in the remainder of this chapter we will assume constant strains and velocity gradients.

When all scattering particles within a backscattering object displace a small and equal amount, and noise is absent, an exact estimation of time delay, or time shift, is possible by ultrasound means. However, in practice the precision of time delay estimation (TDE) is limited by various sources of echo signal corruption. In addition to electronic and quantisation noise, a main source of error in ultrasonic TDE is the decorrelation of the echo signal because of the aforementioned displacement gradients (termed decorrelation noise). Under the effect of displacement gradients, scattering particles change their relative positions along the axial direction, with concomitant warping of the corresponding echo signals. The decorrelation effect of displacement gradients is illustrated in figure 4.1, which shows two echo signal pairs: one obtained from flowing blood (Fig. 4.1, top) and another one obtained from an artery wall undergoing compression (Fig. 4.1, bottom). The signals from blood correspond to the region near the vessel wall where velocity gradients are typically the highest. These signals illustrate that in addition to an overall temporal compression, also there are regions of localised high and low decorrelation within the signal segment. In addition to displacement along the ultrasound beam, scattering particles may move in the lateral and elevational directions; the decorrelation effects due to these motions are ascribed to a different physical mechanism and are outside the scope of this chapter.

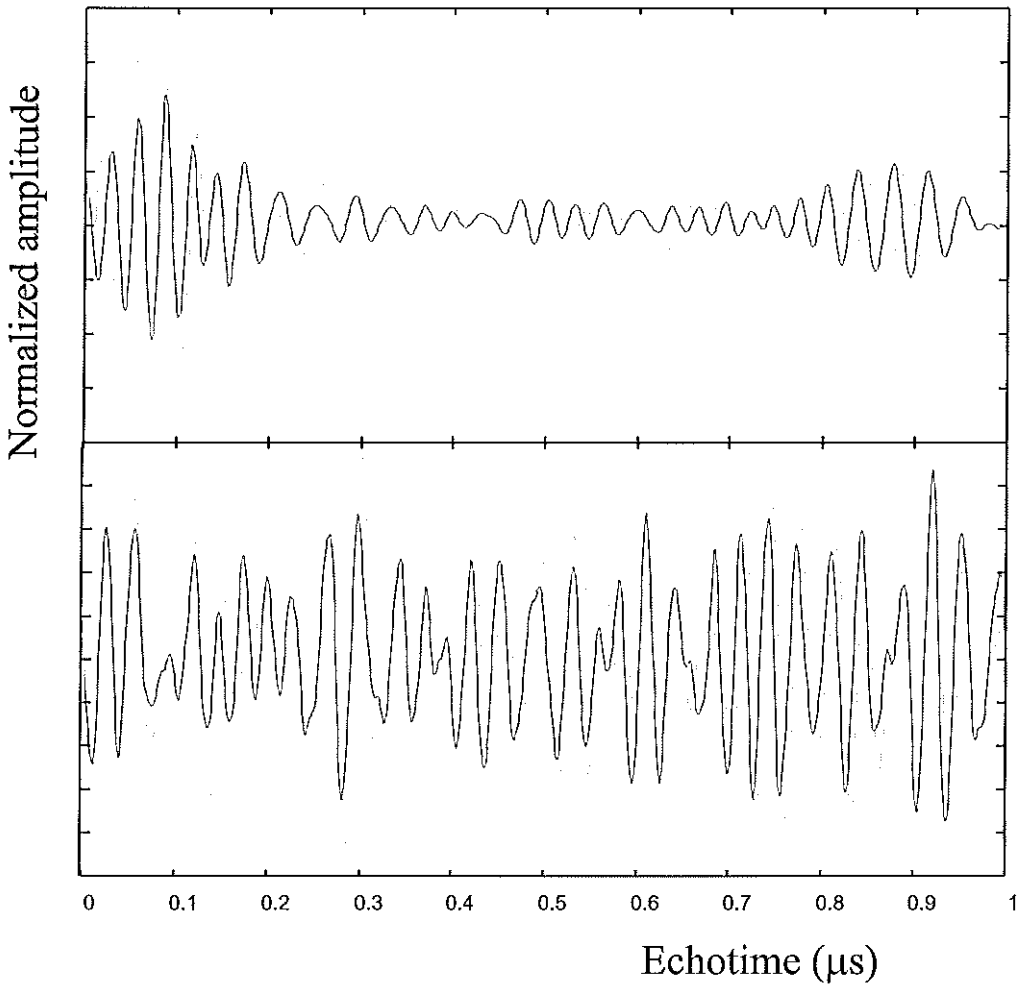

Figure 4.1 Echo signal pairs (30 MHz center frequency) illustrating the effect of a displacement gradient within the observation time (i.e., a nonstationary time shift). *(top)* two intravascular rf signals from flowing blood near the carotid artery wall in a live pig (the time interval is approximately 128 ms). *(bottom)* rf signals from an iliac artery specimen obtained before (dashed line) and after (solid line) compression with a 4 mmHg increase in intraluminal pressure.

The goal of this chapter is to obtain a theoretical model for the decorrelation process (i.e., the mean changes of the crosscorrelation coefficient function) induced by an axial displacement gradient and to corroborate the theory experimentally. We also seek to obtain practical formulas for calculation of decorrelation from strain and vice versa.

4.2 Previous related work.

The limitations imposed by random noise (electronic noise, quantisation noise, etc.) on TDE are described by known expressions of precision bounds such as the Cramér-Rao lower bound (CRLB) (Knapp & Carter, 1976; Quazi, 1981). Decorrelation noise can be introduced in these expressions by means of the equivalent signal-to-noise ratio expressions (Céspedes et al., 1997b) (Friemel, 1994). To that same effect, Walker and Trahey developed an expression of the CRLB that includes an additional term for decorrelation noise (Walker & Trahey, 1994, 1995). In (Walker & Trahey, 1994), an expression was derived that yields the correlation coefficient based on the strain and the data length, for the special case of signals with flat bandlimited spectra. In the limit of small strains, the expression in (Walker & Trahey, 1994) is similar to a preliminary version (Céspedes, 1993a) of the development presented here. A precision bound for axial strain estimation has been derived on the basis of stationary random noise, which on first approximation can also be utilised with decorrelation noise (Céspedes et al., 1995b). Varghese and Ophir (1996) describe an estimate of strain from decorrelation and show that their model of decorrelation yields a biased estimator of strain. Alam and Ophir (1997) investigated rf and envelope signal decorrelation as tissue strain estimators and concluded that the bias of their estimate is affected by the center frequency and the signal-to-noise ratio. Finally, the decorrelation between pre- and post-strain signals when the post-strain signal is temporally scaled to match the pre-strain signal has been investigated (Varghese & Ophir, 1996; Bilgen & Insana, 1996; Kallel et al., 1997).

In the context of blood flow assessment, Foster et al. (1990) investigated the error introduced by velocity gradients (separation) on velocity estimates. The jitter of the velocity estimates was obtained from simulations and they report on gradient related errors that can exceed all other sources in some situations. Bonnefous (1989) derived an expression of the correlation coefficient that includes decorrelation effects due to velocity dispersion within the observation window. The theoretical model agreed with simulation results. Li et al. (1998a) performed simulations to investigate the effect of velocity gradients on decorrelation-based estimation of flow by intravascular ultrasound; their results compared favorably with predicted values obtained with the expression in (Bonnefous, 1989). None of these investigators corroborated the theoretical or simulation results experimentally.

Wear and Popp (1987) investigated the correlation properties of ultrasonic echoes from moving tissue for the measurement of myocardial contractile velocity. The dispersion of the scattering particles in time was studied using a 1-dimensional model consisting of scatterers arranged on an elastic band. An increasing stretch of the elastic band was used to simulate increased velocity dispersion. They showed that the normalised correlation function can be obtained from the characteristic function of the displacement probability-density function (pdf). For a uniform displacement pdf, the theory and experiment showed overall agreement; however, the theoretical estimates of the correlation function fell within three to four standard deviations from the experimental estimates. A disadvantage of the approach taken by Wear and Popp is that it does not provide a direct expression for the crosscorrelation function of the compressed scatterers (unknown) in terms of the autocorrelation function of the system (which can be estimated).

Meunier and Bertrand (1995) have investigated the changes of ultrasound images when tissue undergoes rotation, translation and biaxial deformation. In (Meunier &

Bertrand, 1995), expressions were derived for the decorrelation of radiofrequency (RF) and demodulated echo signals when these signals are previously compensated for the motion and the point spread function is Gaussian; simulation results obtained using large strains (1-10%) showed good agreement with the theory.

Hence, to date a modest amount of research has been done to model or simulate the effect of displacement gradients on the correlation coefficient. Most of these efforts have concentrated on specific signal models and lack experimental validation. In this study, we take a more general approach to the investigation of decorrelation as a function of strain that includes substantial experimental corroboration. Additional insight into the mechanism underlying decorrelation would improve our understanding of decorrelation as a limiting factor or as a potential estimator in elasticity and blood flow imaging applications.

4.3 Theory

An estimate of the time delay between a broad-band signal and a delayed replica of the signal, in the presence of additive noise, is commonly obtained by crosscorrelation techniques. The use of these techniques was introduced for sonar applications where the crosscorrelation is usually performed between a signal and a time-scaled version of the signal (due to Doppler shifts) in the presence of additive noise (Remley, 1963); by definition, such signals are jointly nonstationary. Estimates of differential Doppler and relative time-delay are obtained with time-companding crosscorrelators and appropriate signal filtering (Betz, 1984; Chan et al., 1981). The effect of uncompensated time-scaling on the correlation has been investigated in sonar applications (Betz, 1984, 1985; Adams et al., 1980; Remley, 1963).

In ultrasound applications, displacement gradients also lead to echo signals that are jointly nonstationary as a result of an essentially different situation from Doppler, however. In this case, the location of the scatterers, rather than the frequency of the signal, is scaled. Consequently, the crosscorrelation between echo signals is generally a distorted version of the autocorrelation function; the dominant feature of this distortion is a decrement of the peak value (i.e., decorrelation).

The validity of the analysis presented here is restricted to small, 1-dimensional displacement gradients such that the fundamental shape of the correlation function is maintained. For larger gradients, the analysis of time delay in the presence of correlation peak ambiguities is fundamentally different and requires considerations that deviate from the objective of this chapter. Furthermore, we assume that the decorrelations introduced by lateral and elevational components of displacement are small compared to the decorrelation due to the axial component. This is a reasonable assumption in typical ultrasound imaging conditions where the axial resolution is considerably better than the transverse counterpart. When these assumptions are not valid, the lateral and elevational decorrelation must also be considered and it may be possible to extend the approach developed here for axial decorrelation to transverse decorrelation. For example, in elasticity imaging, transverse decorrelation may be neglected when the target is compressed with a compressor that is large compared to the transducer (Ponnekanti et al., 1992). In such situation, the imparted strain results in lateral and elevational displacements that are small compared to the spatial resolution of the ultrasound system in the corresponding directions.

In this chapter, we develop an analytical expression of the mean crosscorrelation function as estimated from finite-length observation windows in terms of the autocorrelation function when displacement gradients are present. In practice, the autocorrelation function can be estimated or obtained empirically. The analysis is similar to the work of Betz (1984) for sonar signals that are temporally scaled due to the Doppler effect. However, in Doppler-based velocity estimation, time compression or expansion (termed companion) occurs *in addition* to the decorrelation effect from gradients; the contribution of Doppler companion is negligible for short data lengths (Ferrara & DeAngelis, 1997) and thus not considered in this work. The decorrelation model for an axial displacement gradient predicts that the expected value of the crosscorrelation function is a low-pass filtered version of the autocorrelation (i.e., the crosscorrelation obtained without a displacement gradient). The filter is a function of the axial gradient and the observation window length.

4.3.1 Definitions: strain, velocity gradient, echo signal model and correlation functions

Deformation of a solid object can be described in terms of the engineering *strain*, ε, or the *stretch ratio*, α, which are defined as the following dimensionless ratios

$$\varepsilon = \frac{L - L_0}{L_0} \tag{4.1}$$

$$\alpha = \frac{L}{L_o} = 1 + \varepsilon \tag{4.2}$$

where L_0 is the original observed length and L is corresponding length after (Fung, 1993; Dobrin, 1978). In this chapter, we are interested in small strains $\varepsilon < 0.025 (< 2.5\%)$ with corresponding stretch ratios close to unity. Note that strain can be positive or negative. We are interested in the absolute value of the strain since the definition of the original length could be reversed without influencing the decorrelation mechanism and effect.

Strain also can be defined in terms of local displacements. Since we are involved with ultrasonic assessment of displacements, we establish the relationship between echo time shift, τ, and displacement, d, given by $\tau = \frac{2}{c}d$, where c is the speed of sound in the medium and the factor of two accounts for round trip travel. Thus, we obtain

$$\varepsilon = \frac{\tau_p - \tau_d}{T} \tag{4.3}$$

where τ_p and τ_d are the local axial displacement in the proximal and distal regions of the observation window and T is the separation between them.

A similar analysis to the above applies to the case of blood flow when we consider axial velocity gradients. Consider a continuous and monotonous gradient of axial velocity occurring from the proximal to distal parts of an observation window of length T. The local time shift due to the axial velocity component, v, is $\tau = \frac{2}{c}d = \frac{2}{c}\Delta t$, where Δt is the time interval between echo signal acquisitions.

A quantity describing the velocity gradient that resembles strain is

$$\varepsilon_v = \frac{v_p - v_d}{\frac{c}{2}T} = \frac{\tau_p - \tau_d}{T}\Delta t = \varepsilon\,\Delta t \tag{4.4}$$

where v_p and v_d are the local axial velocities in the proximal and distal regions of the observation window, T is the separation between them, and t_p and t_d are the corresponding local axial displacements occurring during the time interval Δt. Thus, a velocity gradient can be interpreted as a hypothetical *"strain"* occurring during the time interval Δt. Therefore, axial strain and axial velocity gradients can be analysed simultaneously based on the similitude of the above equations. We will proceed with the analysis based on a single parameter, ε, which applies to both situations.

4.3.2 Echo signal models and correlation functions

The pre- and post-compression echo-signals, $r_1(t)$ and $r_2(t)$, are modeled as zero mean, bandpass signals with additive noise as follows:

$$r_1(t) = s_1(t) * p(t) + n_1(t) = s(t) * p(t) + n_1(t) \quad \textit{and} \tag{4.5}$$

$$r_2(t) = s_2(t) * p(t) + n_2(t) = s(\alpha t - t_o) * p(t) + n_2(t) \tag{4.6}$$

where $s_1(t)$ and $s_2(t)$ are the pre- and post-compression backscatter functions representing the tissue, $p(t)$ is the impulse response of the stationary, bandpass ultrasonic system, $n_1(t)$ and $n_2(t)$ are zero-mean, uncorrelated random noises, t_0 is a fixed time delay, α is the stretch ratio and $*$ denotes convolution. For illustration purposes, the post-compression backscatter function in equation 4.6 can be expressed as $s_2(t) = s(\alpha t - t_0) = s(t - ([1-\alpha)t - t_0])$, which evidences the displacement gradient by expressing the total time shift of s(t) as composed by the two terms inside the square brackets: a time dependent term, $(1-\alpha)t$, and a constant term, t_o.

In general, the crosscorrelation function between two *stationary* signals, $x_1(t)$ and $x_2(t)$, that are jointly stationary is defined by

$$R_{12}(\tau) = \lim_{T \to \infty} \int_0^T x_1(t)\, x_2(t+\tau)\, dt \tag{4.7}$$

(Altman, 1994), p.146. When signal and noise are zero mean, the crosscorrelation and crosscovariance functions are identical, $R_{12}(\tau) = C_{12}(\tau)$.

The correlation coefficient function is defined by

$$\rho_{12}(\tau) = \frac{R_{12}(\tau)}{\sigma_1(\tau).\sigma_2(\tau)} \tag{4.8}$$

where $\sigma_1(\tau)$ and $\sigma_2(\tau)$ are the standard deviations of the correspondingly indexed signal amplitudes (Bendat & Piersol, 1986, page 118). We define the correlation coefficient, ρ_{12}, as the peak value of the correlation coefficient function $\rho_{12} = \rho_{12}(\tau_{peak})$.

When using finite length echo signals (finite observation window), the crosscorrelation function can be estimated with the following,

$$\hat{R}_{12}(\tau) = \frac{1}{T} \int_{-T/2}^{T/2} r_1(t)\, r_2(t+\tau)\, dt \tag{4.9}$$

where T is the observation time and $\hat{R}_{12}$ denotes the estimate of R_{12} (Bendat & Piersol, 1986, page 270). Because of the finite integration time, the crosscorrelation function estimate in equation 4.9 varies for each pair of signals: it is in effect a random variable and must be described statistically. The mean crosscorrelation function is defined as the expected value (mean) of the estimates $\hat{R}_{12}(\tau) : R_{12}(\tau) = E\{\hat{R}_{12}(\tau)\}$, where E{} denotes expectation. It is interesting to note that when the crosscorrelated signals are jointly stationary, $\hat{R}_{12}(\tau) \to R_{12}(\tau)$ when $T \to \infty$, and therefore the definition of equation 4.9 is consistent with equation 4.7. Conversely, when there are displacement gradients, echo signals are jointly nonstationary and therefore the above limit for infinite observation (integration) time does not hold. In fact, we will show that in the nonstationary case $E\{\hat{R}_{12}(\tau)\}$ vanishes as $T \to \infty$ for nonzero strain.

Thus, in the nonstationary case the expected value of the crosscorrelation function cannot be obtained by increasing the observation time T as proposed for stationary signals (Eq. 4.7). Alternatively, the expected value of the crosscorrelation can be approximated by considering an ensemble of crosscorrelation functions calculated from finite length echo-signal pairs, $r_1(t)$ and $r_2(t)$, viz.

$$E\{\hat{R}_{12}(\tau)\} = \frac{1}{T} \int_{-T/2}^{T/2} E\{r_1(t)\, r_2(t+\tau)\}\, dt = \frac{1}{T} \int_{-T/2}^{T/2} E\{s_1(t)\, s_2(t+\tau)\}\, dt \tag{4.10}$$

where the last expression above was obtained by taking into consideration that signals and noise are mutually uncorrelated. Equation 4.10 assumes stationarity within a short observation window of length T, a fact that is clearly an approximation that ultimately results in the dependence of the correlation function on ε and T. However, for short T, equation 4.10 yields reasonable estimates of the correlation function.

Following some algebraic steps, which were deferred to appendix B for clarity, equation 4.10 can be expressed as follows,

$$E\left\{\hat{R}_{12}(\tau)\right\} = R_{11}(\alpha\tau) * h(\tau) * \delta(\tau - t_0), \tag{4.11}$$

where

$$h(\tau) = \begin{cases} 1 & |\tau| \le \varepsilon T/2 \\ 0 & elsewhere \end{cases} \tag{4.12}$$

Inspection of equation 4.11 elucidates that the effect of the displacement gradient is equivalent to low-pass filtering the companded autocorrelation function; the impulse response of the filter, $h(t)$, is defined by the strain and the observation time (Eq. 4.12). It should be noted that this low-pass filter is not the integrating filter in the correlation operation of equation 4.10. It is effectively an additional low-pass filter that is introduced by assumption of stationarity within the observation window T, when in reality there is a displacement gradient (ε).

Alternatively, we can express equation 4.11 in the form of a convolution integral:

$$E\{\hat{R}_{12}(\tau)\} = \int_{-\infty}^{\infty} R_{11}(\alpha t)\, h(\tau - (t - t_o))\, dt = \int_{\tau - \varepsilon T/2 + t_o}^{\tau + \varepsilon T/2 + t_o} R_{11}(\alpha\tau)\, dt \tag{4.13}$$

Then, the mean correlation coefficient is given by

$$\begin{aligned} \rho_{12} &= E\{\hat{\rho}_{12}\} = \tfrac{E\{\hat{R}_{12}(t_o)\}}{E^2\{\sigma_r(0)\}} \\ &= \tfrac{1}{\sigma^2} \int_{-\varepsilon T/2 + t_o}^{\varepsilon T/2 + t_o} R_{11}(\alpha\tau - t_o)\, dt = \tfrac{1}{\sigma^2} \int_{-\varepsilon T/2}^{\varepsilon T/2} R_{11}(\alpha\tau)\, dt \end{aligned} \tag{4.14}$$

where we assume that $\sigma(0) = \sigma_1(0) = \sigma_2(0) = \sigma$.

Thus, the mean correlation coefficient is given by the average of the companded autocorrelation function over an interval of duration εT centered on the peak and normalised by the signal power. Equation 4.14 provides the decorrelation value as a function of T and ε, and $\rho_{12}(\varepsilon, T)$ is termed the decorrelation function.

It is interesting to consider some special cases. For zero strain ($\varepsilon = 0; \alpha = 1$), $h(t)$ is a delta function. Thus, from equation 4.11, the mean crosscorrelation function is

$$E\{\hat{R}_{12}(\tau)\} = R_{11}(\tau - t_0) \tag{4.15}$$

For any nonzero strain and $T \to \infty$, the time integration in equation 4.14 amounts to zero since the correlation function for our model is zero mean. Therefore, for the hypothetical situation of very long observation windows and nonzero strain, there is no correlation between the pre- and post-compression echo-signals due to nonstationarity.

For the relatively low displacement gradients of interest in this chapter, $\alpha \approx 1$. Therefore, the decorrelation function can be approximated by

$$\tilde{\rho}_{12} = \frac{1}{\sigma^2} \int_{-\varepsilon T/2}^{\varepsilon T/2} R_{11}(t)\, dt \tag{4.16}$$

where we assume that $R_{11}(t) \cong R_{11}(\alpha t)$. We will show later that in practice the above simplification results in small deviations from the exact decorrelation function (Eq. 4.14), particularly for strains below 1.5%.

4.3.3 The $|\varepsilon| T f_o$ bound

For a bandpass system with center frequency f_o, the correlation function is reminiscent of a sinc function. For a given center frequency and strain level, increasing the length of the observation window results in a decrease of the correlation coefficient. This can be observed from equation 4.14 where extending the limits of integration (e.g., increase T for fixed ε and f_o) beyond the first zero crossing of the autocorrelation function would incorporate negative correlation components. For a bandwidth limited signal centered on frequency f_o, the distance between zeros of the correlation function is $\frac{1}{2f_o}$. Therefore, to avoid including zero or negative correlation components in the estimate, we must satisfy the condition $|\varepsilon| T < \frac{1}{2f_o}$. This corresponds to limiting the effect of the displacement gradient over the extent of the observation window to less than one half the central period of the echo signal. Thus, desirable window lengths should satisfy the condition: $T < (2f_o |\varepsilon|)^{-1}$, which indicates that for small gradients the observation time can be several wavelengths long (e.g., for $|\varepsilon| = 0.02$, $T = 25 \times f_o^{-1}$).

Alternatively, we can define an upper bound for the product of strain, observation time and center frequency:

$$|\varepsilon| T f_o = \tfrac{1}{2} \tag{4.17}$$

which defines the desirable region of operation to avoid gradient-originated decorrelation. To first approximation, this formula can guide the selection of observation window length and applied strain (or pulse repetition interval in the flow case) for a given center frequency.

Interestingly, Bilgen and Insana (1997) have found that the minimum variance for displacement estimation in elastography occurs when $\alpha W = \sqrt{20}/\sqrt{1+Y^2}$ (in their notation $\alpha = \varepsilon, WL = T$ and $Y/L = 2\pi f_0$). Therefore, for bandpass signals ($Y >> 1$), the minimum displacement variance condition yields $\varepsilon T f_0 \approx 0.7$. Thus, and not surprisingly, a relationship between minimum displacement variance and minimum decorrelation is apparent.

4.3.4 Approximate decorrelation function.

The decorrelation function in equations 4.14 and 4.16 require knowledge of the mean autocorrelation function. Note that since our model assumes that the scattering function is random (white noise), the *mean* autocorrelation function of the echo signal is the autocorrelation function of the ultrasound pulse: $E\{R_{12}(\tau)\} = E\{R_{22}(\tau)\} = R(\tau)$. When this information is unavailable, we can approximate the autocorrelation function in the neighborhood of its peak by $R_a(\tau) = \cos(2\pi f_o \tau)$ where f_o is the center frequency of the echo signal. This is a reasonable first order approximation for Gaussian and flat spectra (Céspedes et al., 1995a; de Jong et al., 1990), which span a range of spectral shapes representative of most ultrasound instruments. The goodness of the approximation deteriorates with increasing bandwidth.

Applying equation 4.16 to $R_a(\tau)$, we obtain the approximate analytical expression of the decorrelation function:

$$\rho_a = sinc(T f_o \varepsilon) \tag{4.18}$$

where $sinc(x) = sin(\pi x)/(\pi x)$. This simple equation can be used to estimate decorrelation from measured strain. However, it does not yield a straightforward analytical tool to

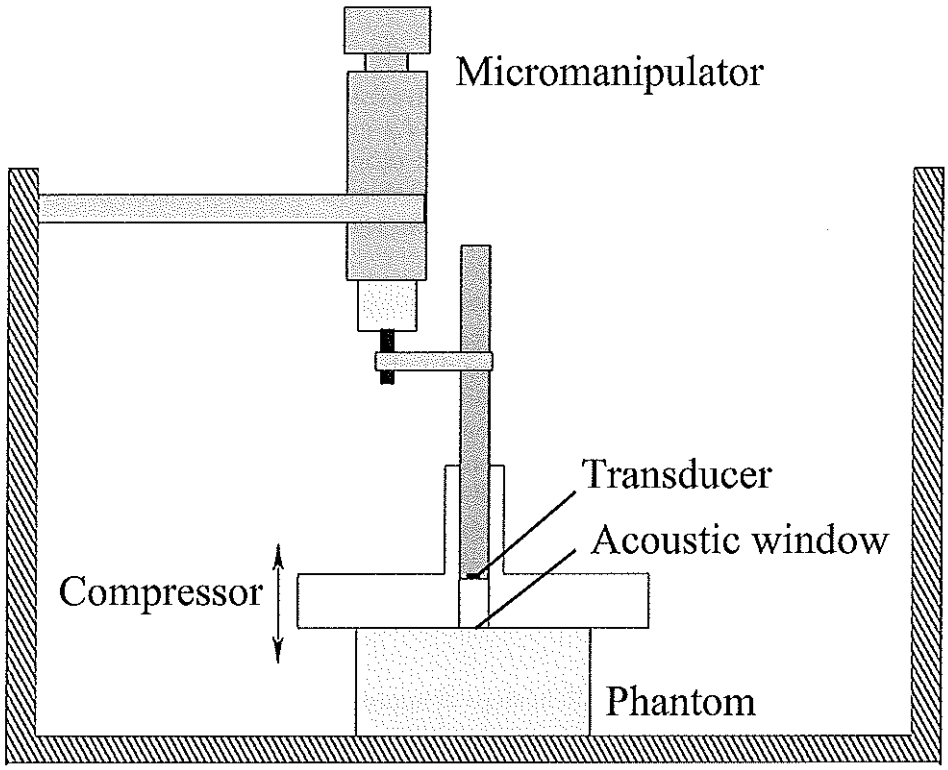

Figure 4.2 Illustration of the experimental set up.

estimate strain from measured decorrelation, which may be of practical interest. Series expansion of $sinc(x)$ around $x = 0$, with exclusion of higher order terms, yields

$$\rho_a = \sin c(T f_o \varepsilon) \cong 1 - \frac{(\pi \varepsilon T f_o)^2}{6} \tag{4.19}$$

(Bendat & Piersol, 1986, page 276), and therefore, we obtain

$$\hat{\varepsilon} \cong \frac{\sqrt{6(1-\rho)}}{\pi T f_o} \tag{4.20}$$

This simple equation allows estimation of strain from measured values of decorrelation. We will show below that these approximate decorrelation functions compare favorably to the exact decorrelation function for the conditions of interest in this study (i.e., small strains). The practical advantage of having an analytic expression for the decorrelation function may justify the approximation in some situations. Notably, the approximation in equation 4.19 yields an expression for the correlation coefficient which is equivalent to equation (21) in the development of Bonnefous for blood velocity gradients (Bonnefous, 1989).

4.4 Experimental methods

In order to test the theory, we conducted compression experiments using a tissue mimicking test object. The gel test object consists of a cylinder 38 mm in diameter and 20 mm high with uniform acoustic and mechanical properties. The test object was made with 8% by weight porcine skin gelatin (G-2500, Sigma Chemical, St Louis, MO), 2% agar-agarose, and 2% by weight carborundum (SiC) particles for scattering according to the method described in chapter 2.

A water tank with a micromanipulator (resolution 1 mm per division) fixed on a support bar was used for controlled compression of the test object. The experimental set up is illustrated in figure 4.2. The gel was subjected to uniaxial compression along the direction of the ultrasound beam. A 50 mm compression plate was securely attached to the transducer assembly to form a large compressing surface. The transducer assembly is attached to the compressor through a central opening which is covered at the level of the compressor surface by a thin, practically sonolucent layer (TPX film; 35 μm thick). The compression plate was designed to be larger than the test object to obtain a uniform distribution of strain (Ponnekanti et al., 1992). The water filled spacing between the transducer and the compressor surface was used to offset the near field. By insonifying the central part of the test object we minimised decorrelation components due to lateral and elevational motions.

Strains ranging from 0% to 2.5% in steps of approximately 0.25% were applied. Independent echo signals (N=9) were obtained by shifting the test object laterally to positions spaced approximately 1 mm around the center of the test object. The actual amount of compression and the sample were measured ultrasonically at each compression step from the travel time of the echo from the bottom of the tank and the acoustic window. The standard deviation of the applied strain was below 0.1%.

Without loss of generality, experimental corroboration was attained utilising intravascular ultrasound equipment and frequencies, and the results of this study can be generalised to general or cardiac ultrasound environments by virtue of frequency scale transformations. The test object was examined using a 28 MHz (30%, 10 dB bandwidth) unfocused piston transducer with an aperture of 1 mm. At the center frequency of the transducer, the wavelength is approximately $\lambda_0 = 50\ \mu m$. The pulse length is approximately 3.5 λ_o. Echo signals were recorded from the far field of the transducer at a starting depth of 15 mm. The analysis was performed on a total of 3 μs of RF data per line of sight. The transducer was pulsed using a modified intravascular ultrasound scanner (EndoSonics/Du-Med, Rijswijk, The Netherlands). Rf echo signals were digitised at 100 MHz and 8 bits with a LeCROY 9400 (LeCROY, Spring Valley, NY) digital oscilloscope; 10 rf signals obtained at a pulse repetition frequency of 200 Hz were averaged in each case to improve the signal-to-noise ratio.

Note that equation 4.14 predicts the value of the *mean* crosscorrelation coefficient. However, correlation coefficient estimates are not Normally distributed. Therefore, mean and confidence intervals of the correlation estimates were calculated utilising the Fisher-Z transform described in Appendix C, which transforms the skewed distribution to approximate Normality (Altman, 1994, page 293). This procedure allowed including all the available data without biasing the statistics.

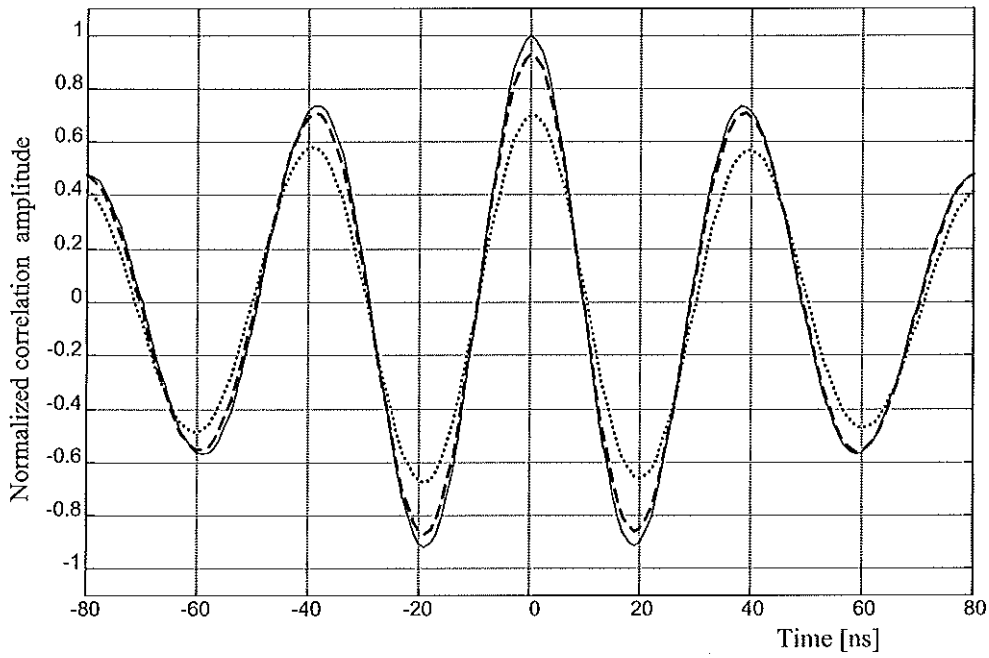

Figure 4.3 Mean crosscorrelation functions at zero, 1% (dashed line) and 2% (dotted line) strain (observation time $1\mu s$, center frequency 28 MHz).

4.5 Results and discussion

The mean crosscorrelation function at zero strain is shown in figure 4.3. This correlation function is an estimate of the autocorrelation function ($R_{11}(\tau) \cong R_{pp}(\tau)$) and was used to compute the theoretical decorrelation function as a function of strain and observation time. As discussed earlier, the distance to the first zero of the autocorrelation function is approximately 18 ns for a center frequency of 28 MHz. Figure 4.3 also shows the mean correlation coefficient functions for $|\varepsilon|Tf_o = 0.10$ (dashed line) and $|\varepsilon|Tf_o = 0.25$ (dotted line), which show the expected progressive decay of the peak values.

The exact (Eq. 4.14), approximate (Eq. 4.16) and sinc (Eq. 4.18) decorrelation functions are plotted in figure 4.4. The agreement between these suggests the possibility to use of the sinc approximation in some practical situations (i.e., for small $|\varepsilon|T$ product). The approximate decorrelation function is derived based on the center frequency and disregarding the bandwidth of the echo signal. This approximation can be expected to have a stronger effect for larger $|\varepsilon|T$ products. Note that a linear approximation to the decorrelation function (Varghese & Ophir, 1996; Alam & Ophir, 1997) would disagree with our estimates even for moderately low strains.

Experimental and theoretical decorrelation functions were appropriately normalised and are plotted in figure 4.5 for observation windows of 0.50 μs (14 λ_o or 4 pulse lengths), 0.75 μs (21 λ_o or 6 pulse lengths) and 1.00 μs (28 λ_o or 8 pulse lengths). The results (Fig. 4.5) show good general agreement between the experiment and the theory, with more significant deviations at higher $|\varepsilon|T$ products. Also, a generally increasing variance

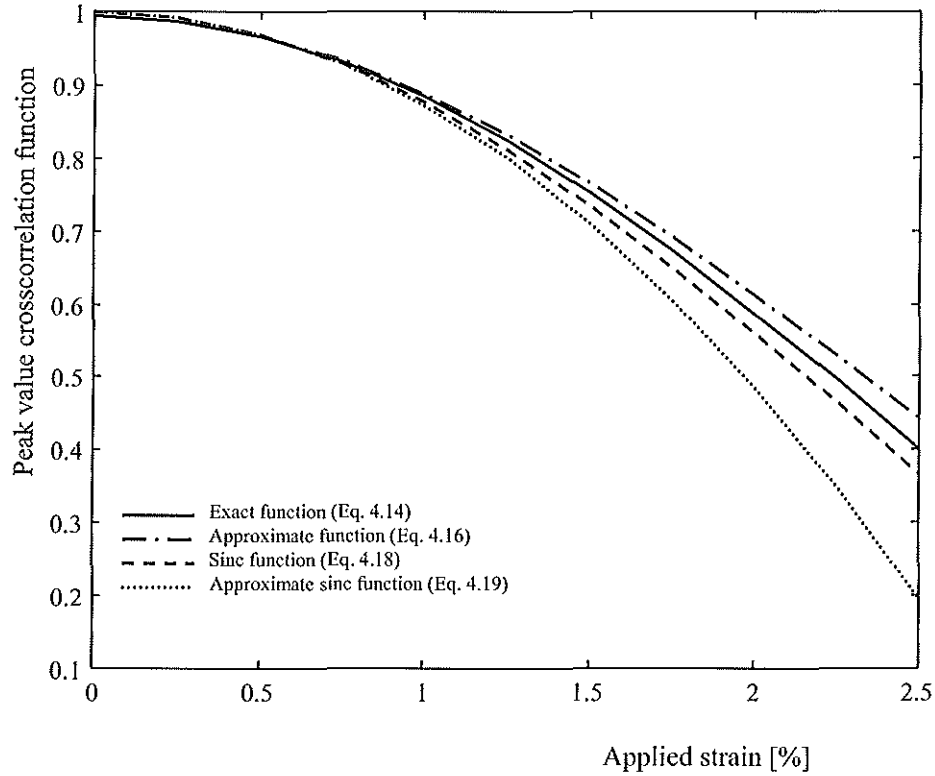

Figure 4.4 Exact and approximate theoretical decorrelation functions.

of the estimate can be observed for increasing values of the $|\varepsilon|T$ product. By analogy to the corresponding situation in stationary decorrelation (Bendat & Piersol, 1986, page 273), this is an expected result in the nonstationary situation as well.

We have introduced some approximate expressions that may be of advantage for practical purposes. The strain-frequency-time bound (i.e., the product $|\varepsilon|Tf_o$) provides an indication of the desirable region of operation where the correlation coefficient remains high ($\rho < 0.7$). The approximate analytical expressions of the decorrelation function can be used to quickly predict the expected decorrelation for a given gradient and vice versa, for given observation time and center frequency. For example, for an observation time of 1 μs, a strain of 1% and a center frequency of 28 MHz, equation 4.18 predicts a decorrelation of 0.87. And using equation 4.20, we can predict that a decorrelation of 0.85 corresponds to a strain of approximately 1.08%; in our experiment, the measured strain was 1.2%. These approximate, but quick, calculations can be a valuable tool for experimental design and data analysis.

Although our development was poised in terms of strain, the approximate expression in equation 4.20 is equivalent to the derivation of Bonnefous for blood flow gradients (Bonnefous, 1989). The validity of equation 4.20 was also verified by Bonnefous and by Li et al. by simulations (Bonnefous, 1989; Li et al., 1998a). However, figure 4.4 shows an increasing bias of this approximation from the exact model for higher gradients. In

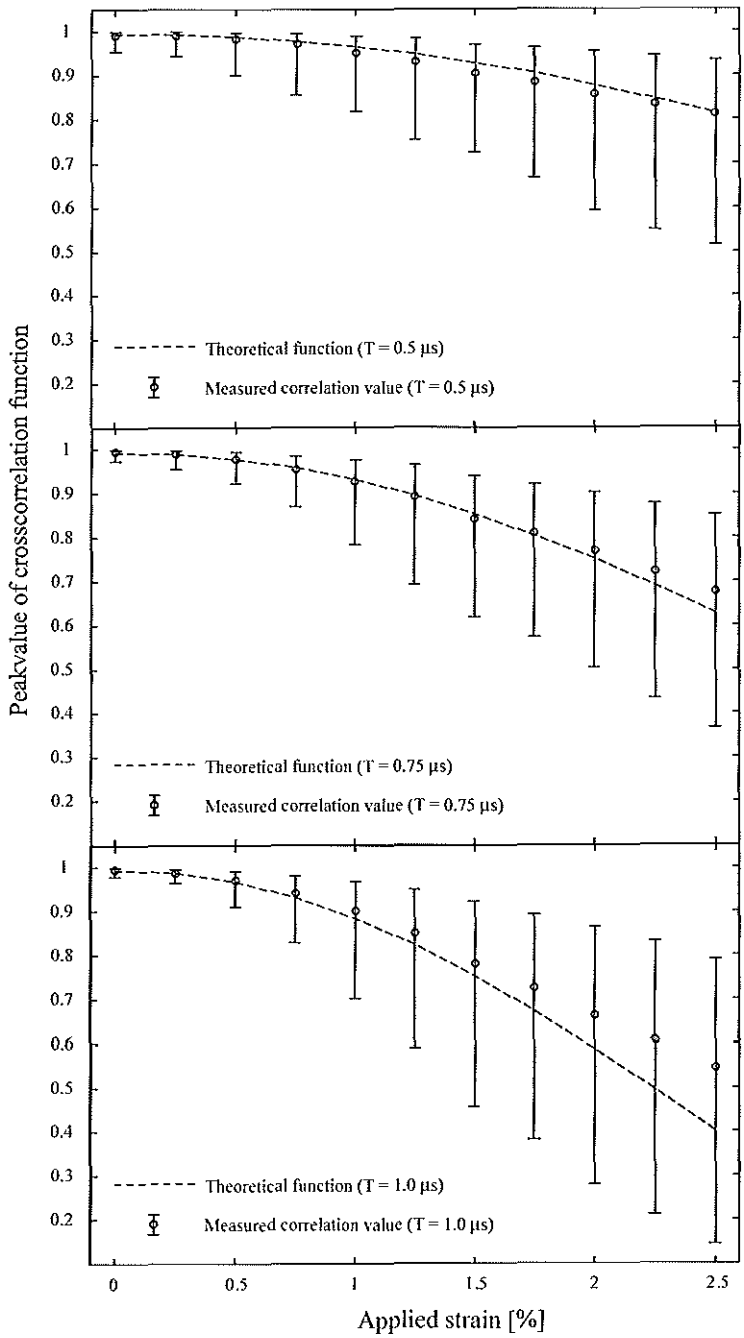

Figure 4.5 Theoretical and experimental correlation mean coefficient values as a function of strain for observation times $0.50\mu s$, $0.75\mu s$ and $1.00\mu s$. The error bars indicate 95% confidence intervals calculated using the Fisher-Z transform.

velocity gradients, the pulse repetition interval is the additional parameter that dictates the interval between the echo signal acquisitions, and thus the observed velocity gradient effect.

Although echo decorrelation has been presented so far as a deleterious effect, it carries information that can be rendered useful if appropriately utilised. Based on the relationship between the correlation coefficient and strain, decorrelation could be used for strain estimation within the constraints imposed by the variance of the estimate. Although direct use of decorrelation as a strain estimator remains unwarranted, averaging correlation coefficients may yield the required improvement. Consequently, the mean decorrelation over a number of compression steps may prove to be a useful indicator of strain in some situations. For example, decorrelation can be used as a subsidiary indicator of estimator quality in displacement estimation. In fact, we have shown that the criterion to achieve low gradient-originated decorrelation appears to be related to the criteria leading to minimum displacement variance as derived by Bilgen et al. (1997). This approach is currently being investigated for selection of acceptable strain estimates in intravascular elastography (Chapter 7) and for intravascular flow assessment (Li et al., 1997).

It is important to note that the theoretical axial decorrelation described here is the minimum level of decorrelation that can be expected since it represents the sole effect of an axial displacement gradient. In general, other decorrelation components from displacement and gradients across the ultrasound beam will contribute with additional decorrelation. Hence, the theory herein predicts minimum levels of decorrelation.

4.6 Summary and Conclusions

Displacement gradients appear in tissue due to compression and in blood due to velocity gradients. Both situations occur naturally in the human body. Additionally, compression can be used as a probing mechanism to measure the stiffness of tissues. Thus, gradient-originated echo decorrelation has an effect on techniques for the assessment of tissue parameters through displacement estimation. In this chapter, we investigated the decorrelation effect of displacement gradients on ultrasound echo signals.

We observed that the effect of a displacement gradient can be modeled as a low-pass filtering of the autocorrelation function of the system response. The impulse response of the filter is defined by the gradient and the observation time. Higher gradients and longer observation windows result in heavier filtering of the autocorrelation function and a reduction of the correlation coefficient (increased decorrelation).

In conclusion, we have developed theoretical models for the crosscorrelation function of echo signals from tissue obtained under the influence of displacement gradients and we have validated the theory experimentally. The general model can be applied to echo signals of arbitrary but known bandlimited spectra. Additionally, approximate decorrelation models appears to be adequate for small gradients, including the case of the experimental conditions of this work. Compression experiments corroborated the validity of our decorrelation model, which provides valuable insights into the mechanism underlying the decorrelation effect of displacement gradients.

Chapter 5

Influence of Catheter Position on Estimated Strain

abstract

In elastography, an erroneous strain estimate is obtained when the radial strain and the probing ultrasound beam are not properly aligned: the "strain projection artifact". In practice, an angle between the strain and the ultrasound beam will be present in most of the cases due to inhomogeneities or nonuniform compression.

In this study, a theoretical function describing the strain projection artifact is derived as a function of the angle between the radial strain and the ultrasound beam. Two main factors for an angle between strain and ultrasound beam in intravascular elastographic experiments are eccentricity and tilt of the transducer. The theoretical functions describing these errors are corroborated with strain estimates from an experiment with a circular, homogeneous gel-based vessel phantom. Comparison between the theoretical functions and the experimental results reveals that the strain projection artifact is well described by the theoretical findings.

As a result, the experimental data can be corrected for this artifact. The corrected elastograms reveal that correct strain estimates are obtained when the eccentricity of the intravascular catheter is less than 63%. An "off-the-wall" device may be required to advance intravascular elastography to in vivo implementation.

5.1 Introduction

Intravascular ultrasound (IVUS) elastography is a new imaging modality that obtains the local strain in the vessel wall and atherosclerotic plaque components from within the lumen using an IVUS catheter (Chapters 3 and 7), (Shapo et al., 1996b, 1996a; Ryan & Foster, 1997b). The strain may reveal important additional information as it is related to

based on the publication: "Influence of catheter position on estimated strain in Intravascular Elastography" by Chris L. de Korte; E. Ignacio Céspedes and Anton F.W. van der Steen. *IEEE Transaction on Ultrasound, Ferroelectrics and Frequency Control* 46(3): 616-625; 1999

two important parameters. First, the strain is related to the local mechanical properties. Knowledge of these properties is important for diagnosis and for guiding interventional procedures (Fitzgerald & Yock, 1993; Baptista et al., 1996; Gussenhoven et al., 1995; Mintz et al., 1996). Because interventional procedures are predominantly mechanical in nature, the outcome of the procedure is influenced by the mechanical properties of the vessel wall and plaque. Additionally, rupture of plaque is associated with elevated stress regions. These regions are an important indicator of plaque instability (Lee et al., 1993; Cheng et al., 1993).

In principle is the local strain obtained by compressing the tissue (Céspedes et al., 1993b; Ophir et al., 1991). The goal of elastography is to measure the radial component of the strain. The radial component of the strain can be determined accurately only when the direction of the radial stress and the ultrasound beam are aligned. However, an incorrect radial strain estimate is obtained when the acting stress and the ultrasound beam are not aligned. This misalignment of the stress and the beam results in bias errors and decreased precision of the strain estimate due to decorrelation effects of the echosignals. Heretofore, the strain error due to an angle between radial strain and the ultrasound beam is called *"strain projection artifact"*.

In intravascular elastography, the tissue is compressed by applying a force from within the lumen. Different levels of intraluminal pressure can be used as acting force. The source of this pressure can be the normal cardiac pulsation of the blood. Another potential source is a compliant percutaneous transluminal coronary angioplasty (PTCA) balloon (Shapo et al., 1996b). In a homogeneous circular vessel with an increased pressure from within the lumen (applied by balloon or blood pressure), the corresponding radial stress is perpendicular to the vessel wall. Therefore, the radial component of the strain and the ultrasound beam can be aligned only when the catheter is positioned parallel with the vessel-axis and in the centre of the lumen. During *in vitro* experiments, the catheter can be positioned in the centre of the lumen (Chapters 3 and 7). Conversely, in clinical practice the intravascular catheter will be positioned off-centre in most of the cases. In coronary applications, the position of the catheter will vary a lot due to the curved nature of these arteries. In most of the cases, the catheter will be close to the vessel wall and their axes not parallel. Thus, the concomitant error in the strain estimation needs to be studied and the feasibility of correction investigated.

In IVUS elasticity imaging, the problem of incorrect displacement estimation has been described by Shapo et al (Shapo et al., 1996b). In their study, a method called the Geometric Center (GC) algorithm is proposed to obtain the true displacement when the catheter is parallel with the vessel-axis but positioned off-centre in the lumen. The algorithm unifies the effect of eccentricity and catheter motion during compression. However, the strain errors that occur when this correction is not applied were not studied; therefore, the magnitude of the artifact and the need for correction were not evaluated.

In this chapter, we investigate the influence of an angle between the radial strain and the ultrasound beam on the estimated strain. The magnitude of the error is determined and the possibility for correction of this error is investigated. We consider two situations in IVUS imaging suitable for analysis of typical errors:

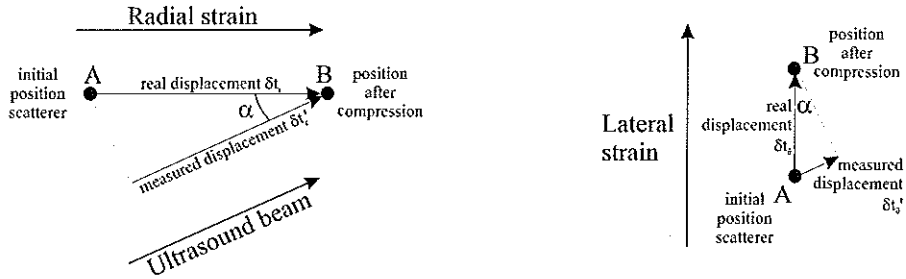

Figure 5.1 Schematic presentation of the error in the strain estimation due to the error in the displacement estimation. Due to an angle between the strain and the ultrasound beam a smaller displacement than the real displacement is measured.

1. The catheter is parallel to the vessel-axis but is not positioned in the centre of the lumen.

2. The catheter is centred but tilted with respect to the longitudinal axis of the vessel.

From geometrical analysis, theoretical descriptions for the strain projection artifact due to these situations are derived. Corroborative water-tank experiments were conducted using a vessel phantom. Finally, the derived theoretical expressions describing the *strain projection artifact* are used to correct the measured elastograms, thus demonstrating that partial correction for this artifact may be feasible.

5.2 Theory and error analysis

5.2.1 Strain estimation

In principle, the strain is determined from measured local displacements in the vessel-wall. The difference between the displacement in two windows is divided by the distance between these two windows (Ophir et al., 1991) to obtain the strain :

$$\varepsilon = \frac{\delta t_1 - \delta t_2}{\Delta} \tag{5.1}$$

$$\begin{aligned} with: \quad \varepsilon &= strain \\ \delta t_1 &= displacement\ in\ window\ 1 \\ \delta t_2 &= displacement\ in\ window\ 2 \\ \Delta &= Distance\ between\ two\ windows \end{aligned}$$

When the intraluminal pressure is used as the acting force to compress a homogeneous cylindrical vessel, the direction of the radial stress and the radial strain are perpendicular to the vessel wall. The radial component of the strain can be correctly measured when the intravascular catheter is positioned in the centre of the lumen and the direction of the ultrasound beam is perpendicular to the vessel wall (Fig. 5.2). An angle (α) between the ultrasound beam and the direction of the radial strain (furthermore identified as

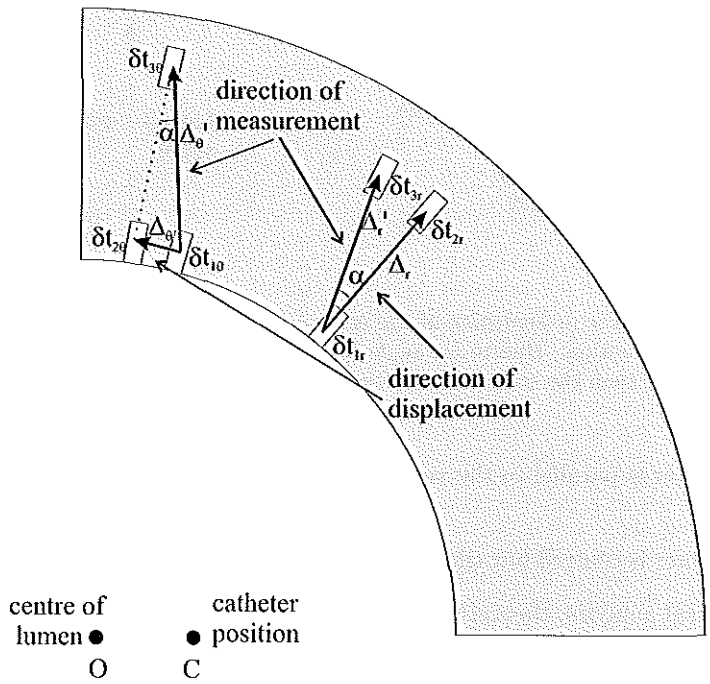

Figure 5.2 Schematic presentation of the error in the strain estimation due to the error in the distance between windows. Due to the angle the distance between δ_{t1} and δ_{t3} is measured and not the distance between δ_{t1} and δ_{t2}. This results in a larger distance between the two windows.

beam-strain angle) will result in underestimation of the radial strain. Additionally, due to the beam-strain angle α, the strain estimate will be influenced by the circumferential and longitudinal strain. In general, stress and strain are second ranked tensors containing 3 normal and 6 shearing components of the stress and strain. However, in a circular vessel with an uniformly thickened vessel wall containing homogeneous isotropic material, these 9 strain components can be diminished to strain components in the radial- (ε_r), circumferential- (ε_θ) and longitudinal-direction (ε_z) only (plane stress) (Appendix A),(Timoshenko & Goodier, 1970).

5.2.2 Bias error in strain estimate

The error in the local displacement is schematically visualised in figure 5.1. A scattering particle is displaced from its initial position A to the position B due to the compression of the tissue by the applied stress. Due to the beam-strain angle α between the ultrasound beam and the radial component of the strain, the measured displacement is smaller than the real displacement. From basic trigonometry we obtain (Fig. 5.1 *right*)

$$\begin{aligned} \delta t'_{1r} &= \delta t_{1r} \cdot \cos(\alpha) \\ \delta t'_{2r} &= \delta t_{2r} \cdot \cos(\alpha) \end{aligned} \tag{5.2}$$

An identical derivation can be performed for the circumferential component of the strain. From figure 5.1 *left* we can derive:

$$\begin{aligned} \delta t_{1\theta}^{'} &= \delta t_{1\theta} \cdot \sin(\alpha) \\ \delta t_{2\theta}^{'} &= \delta t_{2\theta} \cdot \sin(\alpha). \end{aligned} \tag{5.3}$$

The error in the distance Δ_r and Δ_θ between the two windows used for the displacement estimation δt_1 and δt_2 (Eq. 5.1) can be calculated using figure 5.2. Due to the angle, the differential displacement between estimation δt_{1r} and δt_{3r} is determined instead of estimation δt_{1r} and δt_{2r}. Since the path from δt_{1r} to δt_{3r} is different from the path from δt_{1r} to δt_{2r}, the distance Δ_r between the two windows is increased to

$$\Delta_r^{'} = \frac{\Delta_r}{\cos(\alpha).} \tag{5.4}$$

For Δ_θ this results in

$$\Delta_\theta^{'} = \frac{\Delta_\theta}{\sin(\alpha).} \tag{5.5}$$

From equation 5.1, when both local displacement (Eq. 5.2) and window distance (Eq. 5.3) errors are taken into account, the observed radial component of the strain $\hat{\varepsilon}_r$ will be

$$\hat{\varepsilon}_r = \frac{\cos(\alpha) \cdot \delta t_{1r} - \cos(\alpha) \cdot \delta t_{2r}}{\frac{\Delta_r}{\cos(\alpha)}} = \cos^2(\alpha) \cdot \varepsilon_r \tag{5.6}$$

and the observed circumferential component of the strain $\hat{\varepsilon}_\theta$ will be

$$\hat{\varepsilon}_\theta = \frac{\sin(\alpha) \cdot \delta t_{1\theta} - \sin(\alpha) \cdot \delta t_{2\theta}}{\frac{\Delta_\theta}{\sin(\alpha)}} = \sin^2(\alpha) \cdot \varepsilon_\theta. \tag{5.7}$$

The strain in the longitudinal direction ε_z can be obtained using a similar derivation as for the circumferential strain $\hat{\varepsilon}_\theta$:

$$\hat{\varepsilon}_z = \sin^2(\alpha).\varepsilon_z \tag{5.8}$$

The total observed strain is a combination of the radial, circumferential and longitudinal strain components. In a homogeneous isotropic material with a Poisson's ratio of 0.5, a compression ε_r of the material in the radial direction will result in a compression of the material in the circumferential direction ε_θ of -0.5 times ε_r and a compression in the longitudinal direction of -0.5 times ε_r. Note that a compression of -0.5 times ε_r means an expansion of 0.5 times ε_r.

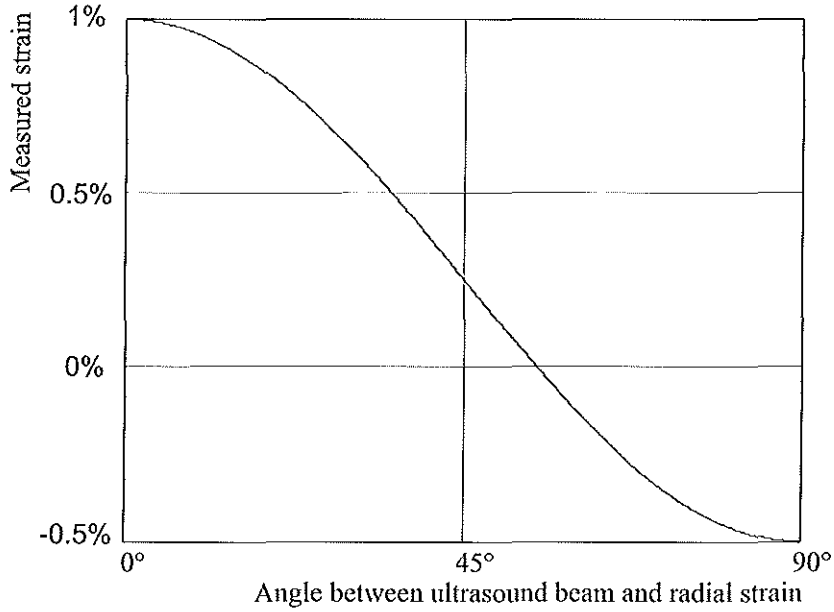

Figure 5.3 Measured strain as function of the beam-strain angle α (as determined using equation 5.9) while applying a radial strain of 1%.

When the imaging plain is perpendicular to the longitudinal axis, the influence of ε_z is negligible and the magnitude of the measured strain can be described by :

$$\begin{aligned} \hat{\varepsilon} &= \hat{\varepsilon}_r + \hat{\varepsilon}_\theta = \varepsilon_r \cos^2(\alpha) - 0.5 \cdot \varepsilon_r \sin^2(\alpha) \\ &= \varepsilon_r(\cos^2(\alpha) - 0.5 \cdot \sin^2(\alpha)) = \varepsilon_r(1.5 \cdot \cos^2(\alpha) - 0.5). \end{aligned} \tag{5.9}$$

The observed value of the strain is plotted as a function of the beam-strain angle α in figure 5.3. The direction of the measured strain is dependent on the angle α. If the angle is less than approximately 55°, the measured strain will be positive. At an angle of approximately 55°, the observed radial strain (compression of the tissue) will equal the observed circumferential strain (expansion of the tissue); thus the measured strain will be zero. A negative value of the strain (expansion) will be obtained for angles larger than approximately 55°.

A similar derivation can be performed to describe the observed strain when the circumferential strain is zero (catheter is centred in the vessel) but the influence of ε_z is not negligible (catheter is tilted):

$$\begin{aligned} \hat{\varepsilon} &= \hat{\varepsilon}_r + \hat{\varepsilon}_z = \varepsilon_r \cos^2(\alpha) - 0.5 \cdot \varepsilon_r \sin^2(\alpha) \\ &= \varepsilon_r(\cos^2(\alpha) - 0.5 \cdot \sin^2(\alpha)) = \varepsilon_r(1.5 \cdot \cos^2(\alpha) - 0.5). \end{aligned} \tag{5.10}$$

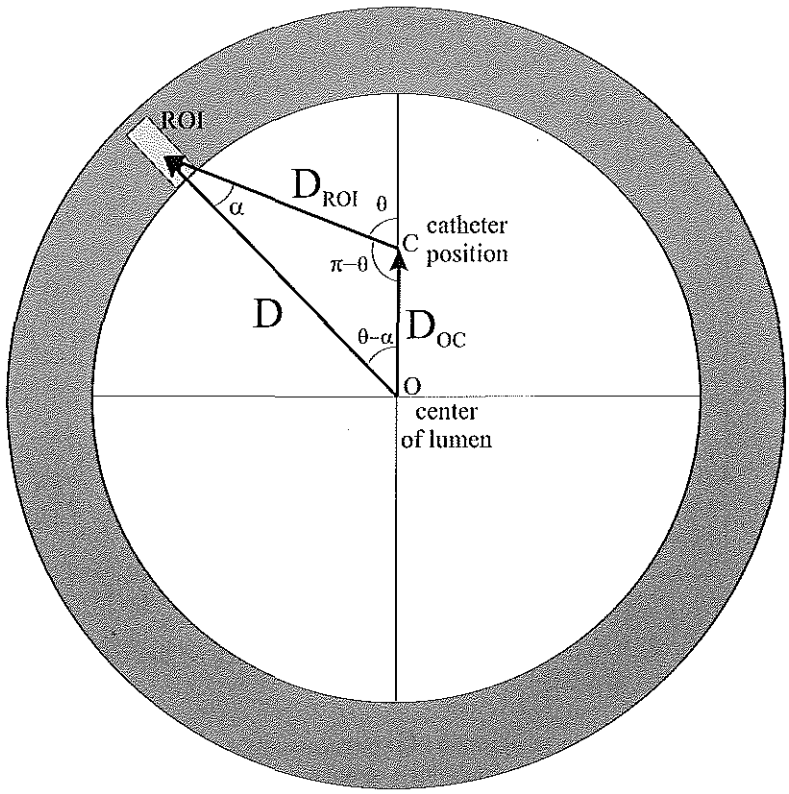

Figure 5.4 Schematic presentation an angle between the strain and the ultrasound beam α due to an eccentric position of the catheter. The angle α is dependent on the azimuth θ of the catheter and the position (D_{OC} and D) of the catheter in the lumen.

5.2.3 The effect of catheter position on the beam-strain angle

In practice, an angle between the radial component of the strain and the ultrasound beam can be caused by two main factors:

1. An eccentric position of the catheter in the lumen parallel with the vessel-axis (Fig. 5.4).
2. A catheter tilted with respect to the long axis of the vessel centred in the lumen (Fig. 5.6),

or a combination thereof. Both these examples are known sources of imaging artifacts in IVUS imaging (Chae et al., 1993; Nishimura et al., 1990; Schwarzacher et al., 1997; Potkin et al., 1990; Thompson & Wilson, 1996; Kearney et al., 1997). In both cases, the beam-strain angle α is a function of the angle of rotation (azimuth) θ of the ultrasound beam. The beam-strain angles due to tilt and eccentricity are examined separately, although in practice they may occur simultaneously and lead to a combined effect. Furthermore, it is assumed that the catheter position does not change during compression of the vessel wall. This assumption is justified due to the low compression levels of interest.

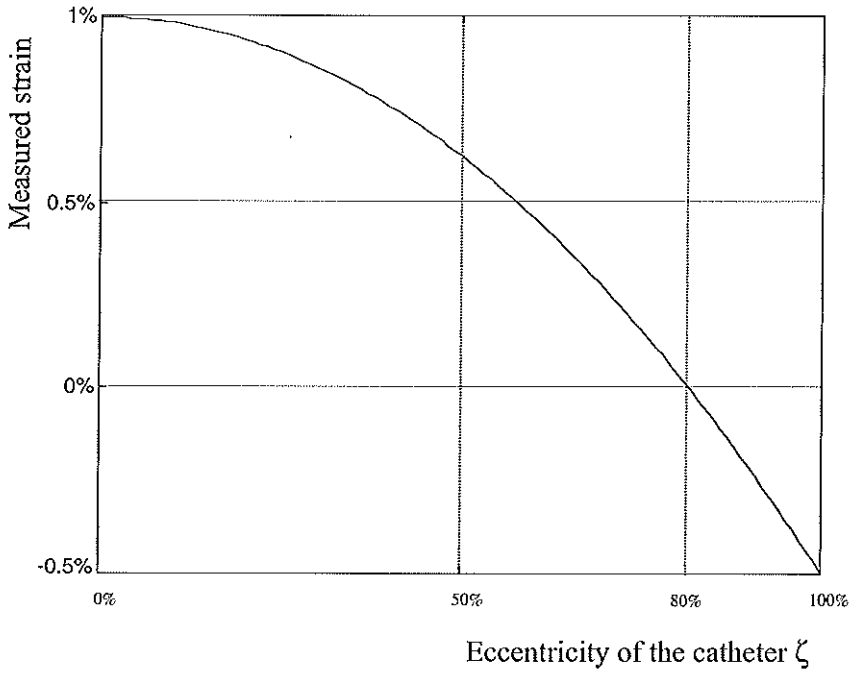

Figure 5.5 Measured strain as function of the eccentricity ξ of the catheter in the lumen (as determined using equation 5.8) while applying a radial strain of 1%. In practise, the eccentricity will always be less than 100% due to the physical dimensions of the catheter

Eccentric position of the catheter parallel with the vessel-axis: The beam-strain angle α is a function of the position of the catheter in the lumen. If the azimuth of the transducer θ, the distance of the catheter to the centre of the lumen D_{OC} and the diameter of the lumen D are known, the beam-strain angle α for regions at the lumen boundary interface can be determined using the sine rule :

$$\frac{\sin(\alpha)}{D_{OC}} = \frac{\sin(\pi-\theta)}{D} \Leftrightarrow$$
$$\alpha = asin(\frac{D_{OC}}{D} \cdot \sin(\pi - \theta)) = asin(\xi \cdot \sin(\pi - \theta)), \tag{5.11}$$

where the eccentricity ξ of the catheter in the lumen is defined as the ratio between D_{OC} and D. The beam-strain angle α is a function of the azimuth θ and the eccentricity ξ. This function is useful for correction if the strain palpogram is determined (the strain is determined only in the first part at the lumen vessel-wall boundary (Chapter 6),(Céspedes et al., 1997c; de Korte et al., 1998a)) and can be used to determine the maximum error in the strain as a function of the eccentricity. This function is plotted in figure 5.5 and reveals that, for eccentricities larger than 80%, strain values in the order of 0% or less are obtained. This makes eccentricities in the order of 80% unsuitable for elastography. Note that, per our definition, the maximum eccentricity of the catheter is always less than 100% due to the physical dimensions of the catheter.

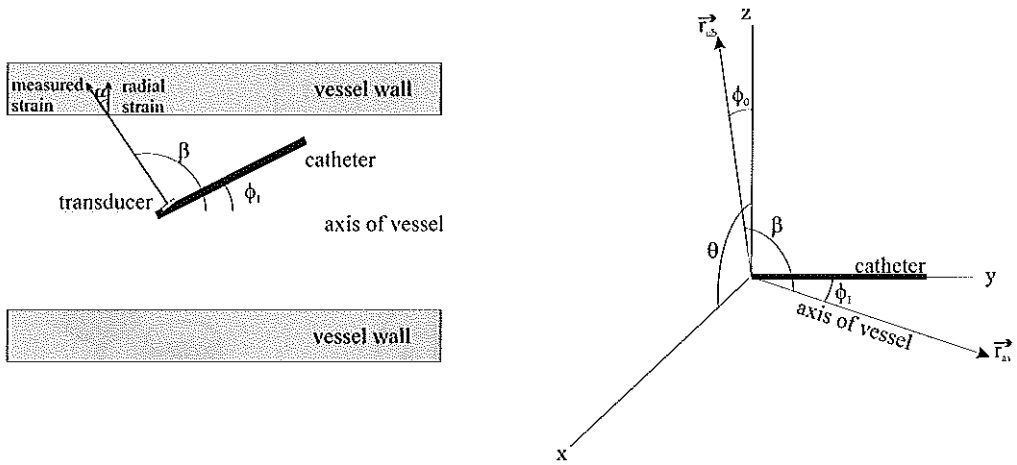

Figure 5.6 Schematic presentation an angle between the strain and the ultrasound beam α due to an tilted position of the catheter. A tilted transducer in the centre of the lumen causes an angle α dependent on the azimuth θ and the tilting angle ϕ_1.

For intravascular elastography of a thick-wall vessel, a depth-dependent correction is necessary. In this case, the beam-strain angle α is a function of the distance of the catheter to the centre of the lumen D_{OC} and the distance to the region of interest D_{ROI}. The angle α can be determined using the sine rule (Fig. 5.4):

$$\frac{\sin(\alpha)}{D_{OC}} = \frac{\sin(\theta - \alpha)}{D_{ROI}}. \tag{5.12}$$

Using the relation $sin(\theta - \alpha) = sin(\theta) \cdot cos(\alpha) - sin(\alpha) \cdot cos(\theta)$ and rearranging equation 5.12, we get:

$$\begin{aligned} \sin(\alpha)\left(\tfrac{D_{OC}}{D_{ROI}} + \cos(\theta)\right) &= \sin(\theta)\cos(\alpha) \Leftrightarrow \\ \alpha &= atan\left(\frac{\sin(\theta)}{\frac{D_{OC}}{D_{ROI}} + \cos(\theta)}.\right) \end{aligned} \tag{5.13}$$

Tilted catheter in centre of the lumen: The catheter is positioned in the centre of the lumen but the transducer is tilted over an angle of ϕ_1 degrees. Therefore, the beam-strain angle α is a function of the azimuth of the transducer θ (Fig. 5.6). The angle ϕ_0 between the ultrasound beam and the normal vector to the catheter is typical of mechanical IVUS catheters and designed to avoid reverberations from the catheter dome. For example, the ultrasound transducer of this Princeps® catheter is mounted at an angle of 10° with respect to the rotating axis. Note that the angle ϕ_0 will be zero for array IVUS catheters (O'Donnell et al., 1997).

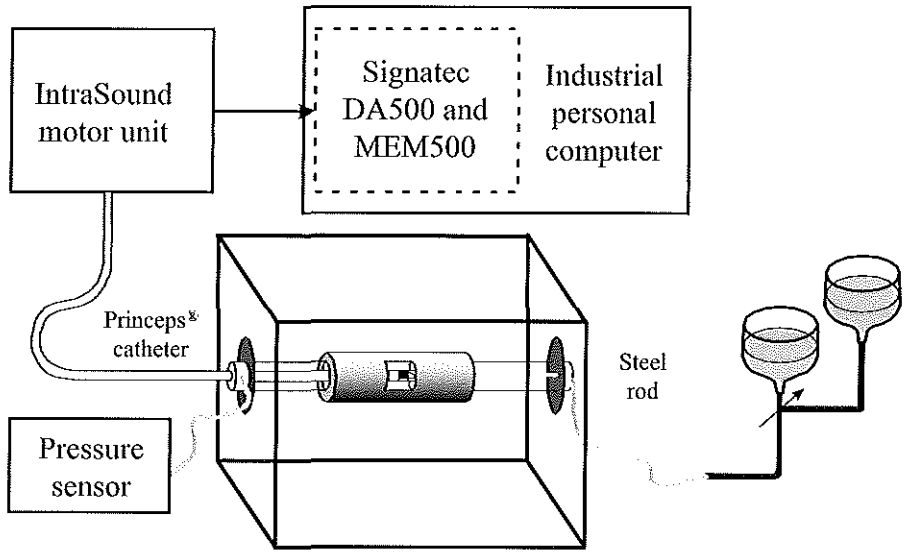

Figure 5.7 Experimental setup

In Cartesian coordinates, the direction of the ultrasound beam is described by the unity vector:

$$\vec{r}_{ub} = (\cos(\phi_0).\sin(\theta)\ ,\ -\sin(\phi_0)\ ,\ \cos(\phi_0)\cdot\cos(\theta)). \tag{5.14}$$

The direction of the long axis of the vessel is described by the unity vector:

$$\vec{r}_{av} = (0\ ,\ cos(\phi_1)\ ,\ -sin(\phi_1)). \tag{5.15}$$

The angle β between the ultrasound beam and the long axis of the vessel is given by the dot product of the two vectors:

$$(\vec{r}_{ub}\cdot\vec{r}_{av}) = |\vec{r}_{ub}|\cdot|\vec{r}_{av}|\cdot\cos(\beta). \tag{5.16}$$

Finally, the beam-strain angle due to tilt only is given by:

$$\alpha = \frac{\pi}{2} - \beta = \frac{\pi}{2} - acos(-sin(\phi_0)\cdot\cos(\phi_1) - \sin(\phi_1)\cdot\cos(\phi_0)\cdot\cos(\theta)). \tag{5.17}$$

Note that the observed strain in this situation is not influenced by the circumferential strain as the catheter is at the centre of the lumen, but only by the strain in the longitudinal direction. The observed strain can be described by equations 5.10 and 5.17. The beam-strain angle α due to the tilt only has no depth dependency.

5.3 Experimental methods

Phantom experiments were performed to investigate separately errors in strain estimate due to *(a)* eccentric position of the catheter parallel with the vessel-axis and *(b)* tilted transducer in the centre of the lumen. A gelatin based phantom (3% agar, 8% gelatin, and 1% carborundum (SiC), Chapter 2) with the morphology of a straight cylindrical vessel was prepared as described in chapter 3. The outer diameter of the vessel was 20 mm with a lumen diameter of 7 mm resulting in a vessel wall of 6.5 mm.

The vessel phantom was measured in a water tank (Fig. 5.7) and connected via two sheaths to a pressurising system. The sheath at the distal side was connected to the water column system and was used to insert the catheter. The sheath at the proximal side was used to monitor the intraluminal pressure. Experiments were performed for a range of eccentric positions of the catheter in the lumen (ξ = 0%, 32%, 63% and 84%, according to figure 5.4). The catheter was positioned in the lumen using a steel rod connected to the tip of the IVUS catheter, which was inserted using the proximal sheath. Although we intended to separate the two effects, a small tilt was unavoidable when positioning the catheter off-centre and relatively close to the vessel wall. Additionally, an experiment was performed with the catheter positioned in the centre of the lumen but tilted with an angle ϕ_1 of 30° between the long axis of the vessel and the catheter. The catheter was inserted through the vessel wall for this experiment. For each experiment, two frames of 400 steps per revolution were acquired at pressures of 50 mmHg and 57 mmHg. A differential pressure level of 7 mmHg was chosen to attain an average strain around 1%.

A Princeps® catheter was connected to a modified IntraSound® (EndoSonics Europe, Rijswijk, The Netherlands) motor unit (Chapter 7) containing the pulser and receiver. The transducer was rotated in 400 angles and at each angle, 10 μs long radio frequency (rf) signals were acquired at a sampling frequency of 200 MHz representing an echodepth of approximately 7.5 mm. The strain was calculated using successive windows of 100 samples (representing a depth range of 350 μm) with 50% overlap. The lumen-vessel boundary was determined using a threshold algorithm. This threshold algorithm determines the boundary by detecting the first echo that was above the noise level of the system. The time delay between corresponding windows of two gated rf signals acquired at different pressure levels was determined using the peak of the correlation coefficient function. To increase the resolution of the time delay estimation, the correlation coefficient function was upsampled 50 times (Chapter 7),(Céspedes et al., 1995a). Finally, strain elastograms of the first two millimetres of tissue were formed.

From the elastogram, the mean value of the strain in the inner first millimetre of tissue material was determined at each angle to form a strain profile. These measured strain profiles representing the strain as a function of the azimuth θ were compared to the theoretical strain profiles. The theoretical strain profiles were calculated using equations 5.9 and 5.11. The obtained elastograms were corrected using the depth dependent correction as determined using equations 5.9 and 5.13. Equation 5.17 was used to determine the beam-strain angle for the experiment with the tilted catheter in the centre of the lumen. Finally, the measured strain estimate was divided by the theoretic value as determined from equations 5.10 and 5.17 to correct for this artifact.

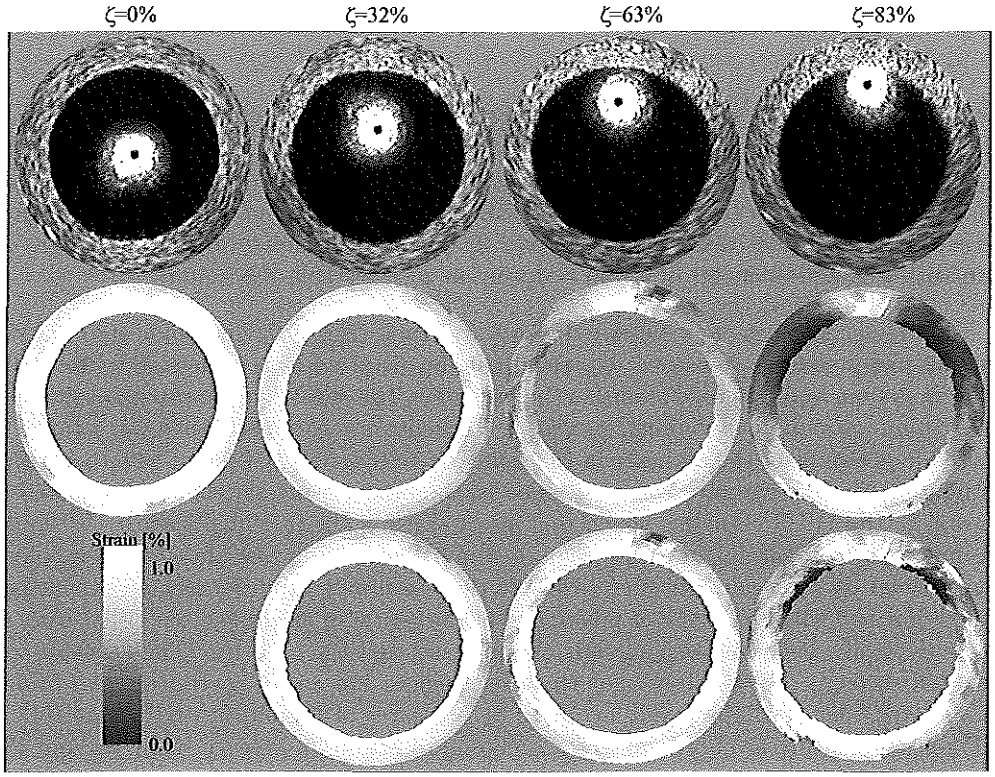

Figure 5.8 Echograms, elastograms and corrected elastograms *(upper, middle and lower row, respectively)* of a homogeneous circular vessel phantom with the catheter at various eccentric positions. The error in the elastograms is acceptable for eccentricities up to 30%. Corrections appear to be feasible for eccentricities up to 63%. For catheter positions adjacent to the vessel-wall (ξ=84%) correction does not seem feasible.

5.4 Results

Elastograms obtained with the catheter at various eccentric positions in the lumen are shown in figure 5.8. The vessel phantom is uniformly elastic, and therefore, a constant strain in the angular direction is expected with a progressive radial decay (Chapter 3). As can be observed, artifacts in the elastogram become more pronounced when the catheter is positioned away from the centre. When the catheter is at the centre (ξ=0%) or close to the centre (ξ=32%), the error in the strain is relatively small. However, when the catheter is close to the vessel wall (ξ=63% and 84%) the error in the strain increases within certain regions.

The experimentally measured strain profiles are compared to the theoretical descriptions (Eqs. 5.9 and 5.11) using the strain in the first layer of phantom material. Figure 5.9 shows that the error in the strain estimate increases with increasing eccentricity of the catheter and the vessel axis. The errors agree with the predicted theoretical values. When the catheter is positioned adjacent to the vessel wall (ξ=84%), in certain regions

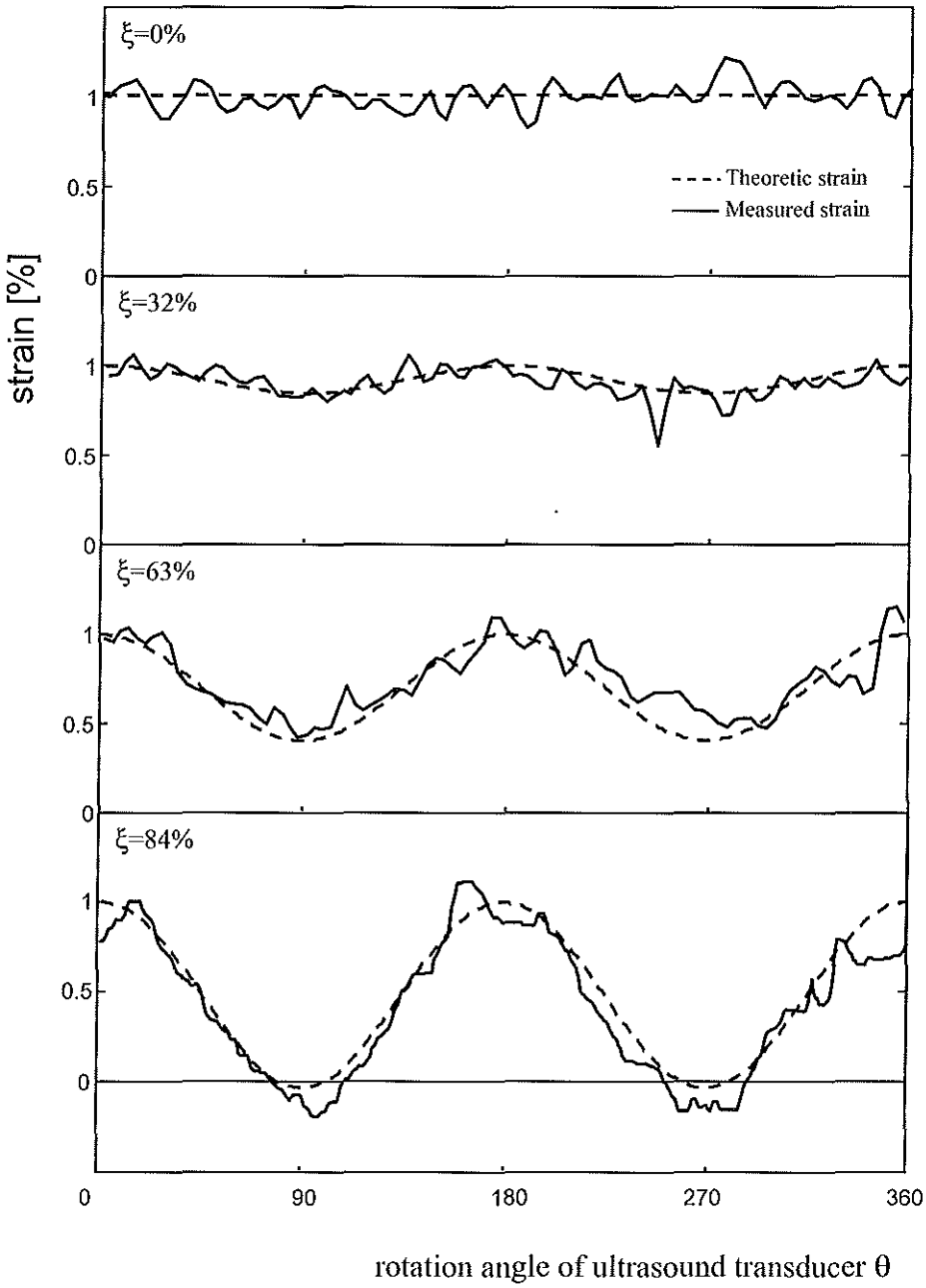

Figure 5.9 Strain profiles obtained from the first layer of the vessel wall for various eccentric positions of the catheter. The observed strain values are similar to the values derived with the theoretical description.

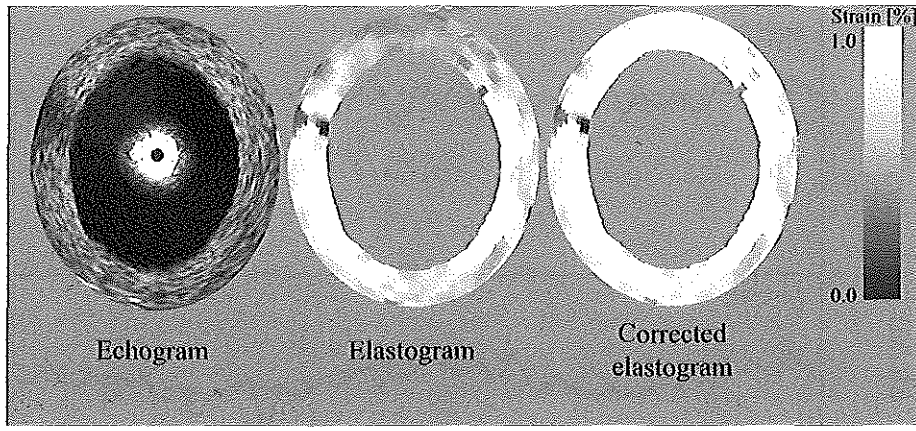

Figure 5.10 Echogram, elastogram and corrected elastogram obtained with a catheter positioned in the centre of the lumen but tilted over an angle of 30°. An elliptic lumen is obtained with an asymmetric error in the strain. The corrected elastogram reveals that correction for this artifact is feasible. Due to the low echogenicity at 1 o'clock, an artifact in the elastogram is obtained.

the strain becomes less than zero as predicted by equation 5.9 with the beam-strain angle $> 55°$. After correction with the theoretical depth dependent strain values (Eqs. 5.9 and 5.13), the 'debiased' elastograms show a more homogeneous strain estimate for all angles of rotation. However, correction is not feasible with the catheter at 84% eccentricity for regions in which the strain $\simeq 0\%$ ($\alpha \simeq 55°$).

Figure 5.10 shows the elastogram obtained with the catheter in the centre of the lumen but tilted with an angle of 30°. Due to the catheter tilt, an elliptically shaped lumen is obtained. A strong angle dependency of the strain estimate can be observed. The observed strain shows good agreement with the theoretical prediction from equations 5.10 and 5.17 (Fig. 5.11). An asymmetric strain profile is obtained because the element is mounted under an angle with respect to the long axis of the transducer and despite central position of the catheter. After correction, a more homogeneous elastogram is obtained.

5.5 Discussion

We investigated the influence of the position of the catheter on the strain estimation. Using a homogeneous phantom with a circular lumen, two sources of erroneous strain estimate were demonstrated separately: An off-centre position of the catheter in the lumen and an angle between the catheter and the long axis of the vessel. In both cases, the error in the strain estimate is a function of the azimuth θ of the intravascular catheter. The position of the catheter is assumed to be fixed during the compression. Because the strain is on the order of 1%, this assumption is justified.

The elastograms (Fig. 5.8) show that the error in the strain estimate increases with the distance of the catheter to the centre of the lumen D_{OC}, i.e. with increased "parallel"

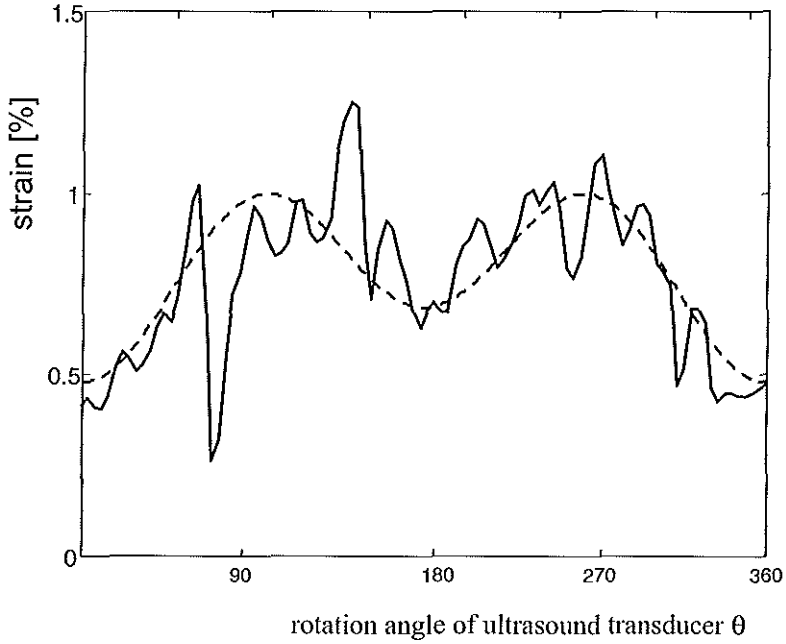

Figure 5.11 Strain profile obtained from the first layer of the vessel wall obtained with a tilted catheter (30°) in the centre of the lumen. The measured error in the strain is described by the error as derived with the theory.

eccentricity ξ. The measured strain profiles (Fig. 5.9) are similar to the theoretical strain profiles. This validates the described theory and supports its use to unbias the elastograms. The corrected elastograms are demonstrated in figure 5.8 (bottom row).

Quantitative comparison between the four elastograms, acquired at various eccentricities, reveals that the error in the strain is reasonable if the catheter is positioned near the centre; in this study, an eccentricity ξ of 32% of the catheter in the lumen induces a maximum error in the strain of 10%. This error is similar to the variation in the strain estimate in the first millimetre of tissue when the catheter is positioned in the centre (Fig. 5.7, $\xi = 0\%$). Since the compression modulus of vascular tissue spans a wide range (50kPa - 5MPa) (Lee et al., 1992, 1991), the expected strain values will span two orders of magnitude. An error of 10% in the strain estimation may be considered acceptable for the purpose of elasticity based detection of different vascular tissues. When the catheter is positioned closer to the vessel wall, the error in the strain increases (Figs. 5.8 and 5.9, $\xi = 63\%$). Because the bias error can be described theoretically, it can be corrected for. However, correction for the error in the strain is not possible when the catheter is adjacent to the vessel wall (Figs. 5.6 and 5.7, $\xi = 84\%$). In this case, the beam-strain angle α is larger than 55° in some regions. Correction for this error is not possible; the observed strain values have to be divided by theoretical strain values in the order of 0% but the variance in the strain estimate is too large to obtain proper results. In the theory, it was already derived that an eccentricity of 80% or more is unsuitable for elastography and this is demonstrated with this experiment.

Another source of error is present when the catheter is adjacent to the vessel wall, which leads to noisy strain estimates in the region close to the catheter. This effect can be explained by the rapidly fluctuating acoustic field in the near field of the ultrasound beam (Li et al., 1997). This fluctuating field introduces decorrelation errors.

A depth-dependent correction of the strain estimate is applied in figure 5.8. It can be noted that the depth dependency of the error in the strain estimate is weak for eccentricities up to 63% (Fig. 5.8, $\xi = 0\%$, 32% and 63%). However, a strong depth dependency is observed at 84% eccentricity. Because the additional complications of this position of the catheter makes it less favourable for elastographic imaging, no depth dependent correction is needed and a simple correction using equation 5.11 can be performed for eccentricities up to 63%.

To prevent eccentric catheter positions above 70%, an 'off-the-wall' device could be incorporated to the catheter. For example, this could be a small balloon that does not interrupt the blood flow or a steerable tip of the catheter. The overall quality of the IVUS echo image also will improve using such a device, because geometric distortion artifacts are reduced and the vessel wall is manoeuvred out of the near field of the ultrasonic beam (Potkin et al., 1990; Kearney et al., 1997).

The elastogram acquired with the catheter positioned in the centre of the lumen, but with an angle between the catheter and the long axis of the transducer shows a strong rotational angle dependency (Fig. 5.10). Due to the angle between the ultrasound beam and the normal to the vessel wall (and thus the strain), an elliptically shaped lumen is obtained (the cross-section of a cylinder with a surface under an angle is an ellipse). This is a well-known artifact in IVUS imaging (Chae et al., 1993; Nishimura et al., 1990; Schwarzacher et al., 1997).

The observed strain at an azimuth of 0° is different from the observed strain at 180° because the transducer is mounted under an angle of 10° with respect to the axis of the shaft in the Princeps catheter. A maximum error of 50% was predicted and measured with an angle of 30° between catheter and long axis of the vessel. An angle of 30° is at the high-end of typical maximal angles used for investigations on image distortion with IVUS echo imaging (Thompson & Wilson, 1996; Schwarzacher et al., 1997; Nishimura et al., 1990). Correction for the bias errors in the strain estimation appears to be feasible (Fig. 5.11) if the tilt-angle is known. Assuming a circular lumen, the tilt-angle could be calculated from the observed lumen shape. However, since the shape of the lumen is unknown for *in vivo* situations, the tilt-angle cannot be easily assessed from the IVUS image. However, the tilt-angle of the catheter may be reconstructed using biplane angiography (Slager et al., 1997), a method introduced for "true 3D" IVUS reconstruction.

In practice, an angle between the applied stress and the probing ultrasound beam can be present in intravascular applications due to reasons other than the catheter position. In intravascular and other applications of elastography, a beam-strain angle may occur due to tissue inhomogeneities and nonuniform compression. For example, when soft material (vessel wall) with a hard inclusion (fibrous plaque) is compressed by a transducer, the strain in the neighbourhood of the hard inclusion will be misaligned with the ultrasound beam (O'Donnell et al., 1994; Lubinski et al., 1996; Bilgen & Insana, 1996). Additionally, the strain and the ultrasound beam also will be misaligned when the tissue is nonuniformly compressed (compressor smaller than the tissue or irregular form (Ponnekanti et al., 1992; Konofagou et al., 1996)), even when the tissue is homogeneous.

Therefore, underestimation of the strain due to angle errors can be expected in vascular and nonvascular applications. The *strain projection* artifact due to catheter position is a special case of a generalised phenomenon in elastographic imaging.

5.6 Conclusions

The position of the intravascular catheter in the lumen affects the strain estimate. We derived theoretical expressions for the bias of the strain that agree well with experimental counterparts. For eccentricities smaller than 30%, the *strain projection* artifact is tolerable and does not impair interpretation of the elastographic image. An eccentricity between 30% and 70% results in a bias of the strain, but correction for this artifact appears to be feasible if the angle is known. For eccentricities larger than 70%, the artifact is readily recognisable and requires repositioning of the catheter. The *strain projection artifact* due to tilt-angles up to 30° can be corrected when the angle is known. In practise, little control over the catheter position is possible in cardiac catheterisations, so an 'off-the-wall' device would be highly advantageous to minimise angle errors associated with catheter position.

Chapter 6

Intraluminal Ultrasonic Palpation: Assessment of Local and Cross-sectional Tissue Stiffness

abstract

Many intravascular therapeutic techniques for the treatment of significant atherosclerotic lesions are mechanical in nature: angioplasty, stenting, atherectomy. The selection of the most adequate treatment would be advantageously aided by knowledge of the mechanical properties of the lesion and surrounding tissues. Based on the success of intravascular ultrasound (IVUS) in accurately depicting the morphology of atheromatous lesions, ultrasonic tissue characterisation has been proposed as a tool to determine the composition of atheroma.

We describe the addition of local compliance information to the IVUS image in the form of a colour coded line congruent with the lumen perimeter. The technique involves analysis of echo signals obtained at two or more states of incremental intravascular pressure. Using vessel phantoms and specimens we demonstrate the utility of intravascular compliance imaging. The palpograms are able to identify lesions of different elasticity, independently of the echogenicity contrast, since the information provided by the elastograms is generally independent of that obtained from the IVUS image.

Thus, the palpogram can complement the characterisation of lesion from the IVUS image. We also describe cross-sectional measures of elasticity that are based on the elastogram. Finally, natural extensions of intravascular palpation to other endoluminal ultrasound applications are proposed.

---

based on the publication: "Intraluminal Ultrasonic Palpation: Assessment of Local and Cross-sectional Tissue Stiffness" by E. Ignacio Céspedes; Chris L. de Korte and Anton F.W. van der Steen. *Ultrasound in Medicine and Biology*: submitted; 1999

6.1 Introduction

Technological advances in intravascular ultrasonography (IVUS) have made it possible to visualise the morphology and evolution of atherosclerotic lesions with great detail. IVUS imaging provides real-time, tomographic images of the arterial anatomy with accurate spatial representation of the vessel wall and atherosclerotic plaque morphology. However, distinction between plaque types from the IVUS echo image is at times difficult and leads to problems of interpretation particularly in the *in vivo* situation (di Mario et al., 1992). For example, using IVUS, fibrous and calcified plaques are correctly classified in most cases (Potkin et al., 1990); however, the discrimination of lipid-filled and mixed (fibrous, fatty, calcified) plaques is much more challenging (Yock & Linker, 1990).

The availability of IVUS has led to interest in the development of complementary ultrasonic characterisation techniques such as the assessment of the mechanical properties and/or the mechanical state of the vessel wall and atheroma. We will address two main potential clinical applications. First, knowledge of the mechanical properties of plaque may aid diagnosis and assist the identification of appropriate interventional procedures (Tobis et al., 1991). Plaques are treated using a variety of catheter-based techniques (e.g., balloon angioplasty, atherectomy, stents) that enlarge or recanalise the lumen to reinstate adequate blood flow (Yock & Linker, 1990; Waller, 1989; Serruys et al., 1996). Because these interventions are predominantly mechanical in nature, the outcome is likely to be influenced by both the structure and the composition of the atheromatous plaque.

Second, the mechanical stress-state of arteries containing vulnerable plaque has been linked to high risk of acute cardiac events (Davies, 1996; Lee & Libby, 1997). Vulnerable plaques, which are typically clinically silent, do not limit blood flow through the arteries significantly but are commonly responsible for severe ischemic attacks due to fracture or erosion with ensuing acute thromboembolism. Plaque rupture occurs in areas of mechanical stress concentration. Identification of these apparently harmless plaques is highly desirable (Davies, 1996; Lee & Libby, 1997) and presents a main hurdle in the management of cardiovascular disease for which a diagnostic tool remains unavailable. Thus, both the identification of mechanical stress concentration and the characterisation of plaque composition are of paramount importance and present areas where ultrasonic techniques may contribute.

6.2 Ultrasonic assessment of arterial wall elasticity

6.2.1 Prior related work

Techniques to assess the elasticity of arterial walls can be categorised according to their goal to measure *global* or *local* properties.

Global measurements of arterial stiffness have been of interest for decades. For example, a widely accepted measure of stiffness has been the "pressure-elastic modulus" or E_p, introduced by Peterson and co-workers (1960). Based on ultrasonic morphometry, this and other simple measures of arterial stiffness have been devised (Lee & Kamm, 1994; Reneman et al., 1986). For example, the diameter (or area) of the artery can be measured ultrasonically while the pressure is monitored. The ratio of a dimensional change and the pressure (e.g., compliance, distensibility or stress-strain elastic modulus) are related to the modulus of elasticity of the involved tissue. These non-imaging ultra-

sonic approaches have been applied extracorporeally to carotid arteries (Pignoli et al., 1986; Stadler et al., 1996) and intravascularly (Alfonso et al., 1994; Blankenhorn et al., 1988). For example, compliance has been utilised to assess coronary artery disease using IVUS (Alfonso et al., 1994) and significant differences in compliance were measured for hypoechogenic, fibrotic and calcified plaque types. A study of the stress-strain modulus of human carotid arteries with focal disease (Blankenhorn et al., 1988) concluded that the local mechanical properties of the plaque resulted in an overall change in vessel wall performance. Global measures of elasticity in diseased arteries will deviate from normal values as a result of focal disease.

Three prevailing measures of arterial elasticity are compliance, distensibility and stress-strain elastic modulus (Alfonso et al., 1994; Frobert et al., 1996; Hansen et al., 1995; Hoeks et al., 1992; Blankenhorn et al., 1988; Reneman et al., 1986; Yamamoto et al., 1993; Wilson et al., 1995; Stadler et al., 1996). All of these measurements provide a global measure of the stiffness of the arterial cross-section since they are based on the relationship between a pressure gradient and the resulting change in luminal area. By definition these measures of arterial stiffness do not take into consideration the thickness of the arterial wall or plaque. However, their prevalence implies that reasonably useful information on the elasticity of the artery can be obtained even when the thickness is ignored. An interesting advantage of these pragmatic approaches is that a single number is used as a global indicator of the stiffness of the arterial cross-section. The obvious disadvantage is the lack of information on local mechanical properties.

Local tissue elasticity assessment with ultrasound-based techniques has encountered increasing interest during the past two decades (Dickinson & Hill, 1982; Krouskop et al., 1987; Ophir et al., 1991; Parker et al., 1990; O'Donnell et al., 1994; Tristam et al., 1986; Wilson & Robinson, 1982; Yamakoshi et al., 1990). In principle, these techniques rely on mechanical stimulation of the tissue under examination and subsequent measurement of the resulting tissue displacement or velocity using 1- or 2-dimensional correlation (echo tracking), optical flow, or Doppler velocimetry techniques. Reviews of these techniques are available in the literature (Céspedes, 1993a; Ophir et al., 1996; Parker et al., 1996; Gao et al., 1996). More recently, variations and extensions of some elasticity imaging techniques have been developed for the intravascular ultrasound environment (Chapters 3 and 7), (Céspedes et al., 1997a; de Korte et al., 1998a; Ryan & Foster, 1997b; Shapo et al., 1996a, 1996b; Talhami et al., 1994). Two feasible sources of mechanical stimulus in the intravascular application are the arterial pressure (de Korte et al., 1998a) and the expansion of a compliant angioplasty balloon (Shapo et al., 1996b). Arterial pressure offers a source of biomechanical, differential deformation that can be controlled to some extent by timed acquisition of echo data. Alternatively, intravascular balloons offer a more controllable source of arterial deformation at the expense of an interruption of the blood flow, unless more sophisticated perfusion balloons are used (intraluminal balloons with a core allowing passage of blood during inflation). With either approach, the strain resulting from the elicited pressure (stress) can be assessed by ultrasonic means using IVUS.

Two IVUS techniques for the assessment of arterial elasticity information are closely related to the method proposed in this chapter:

(a) Intravascular elastography (Chapters 3),(Céspedes et al., 1997a) is an imaging technique based on the assessment of local tissue strain from crosscorrelation analysis of echo signals obtained at two or more stages of intraluminal pressure. First, local radial

displacements are computed using small ($< 400\mu m$) segments of the pre- and post-compression echo lines obtained from a beam direction. Strain profiles are computed by finite difference of the displacement along each beam. Strain profiles along adjacent beam positions within a scan plane are used to produce an image of elasticity, or elastogram. In IVUS elastography, strain is estimated locally within the vessel wall at all points in the cross-section for minute strains that are practically undetectable from analysis of IVUS images. Such strain sensitivity is well below the sensitivity of video-based analysis of cross-sectional compliance (The et al., 1995). IVUS palpation is derived from the concept of IVUS elastography.

(b) Talhami and co-workers (1994) described a technique termed Spectral Tissue Strain that superimposes a 1-dimensional representation of arterial strain on conventional IVUS images. The approach is based on indirect estimation of strain from the change in mean scatterer spacing as a result of arterial pulsation. Mean scatterer spacing was obtained from high resolution, chirp-Z transform based spectral analysis of the video information without range gating. Strain information was displayed as a colour coded ring positioned outside the arterial wall on the IVUS image. Although the method presented here has points in common with the technique of Talhami et al., substantial differences in the estimation method and data presentation will become evident throughout the following sections.

6.2.2 IVUS palpation

In this chapter, we introduce a compound imaging technique that merges stiffness information onto the IVUS image. More specifically, we propose a 1-dimensional method to measure and display local deformation of the inner layer of the arterial wall. Radial strain is measured from echo signals obtained at two stages of intraluminal pressure and displayed as a coloured profile coincident with the location of the lumen-vessel interface. The corresponding image is termed the strain palpogram. Alternatively, based on knowledge of the acting incremental pressure, the stress (pressure) to strain ratio can be calculated to obtain a quantity that resembles an elastic modulus. The corresponding image is termed the modulus palpogram. The method can be construed as minimum (radial) resolution version of IVUS elastography. In exchange for reduced spatial (axial) resolution, we expect IVUS palpation to be more robust and simpler to implement, particularly in relation to future use *in vivo*. Additionally, we propose to integrate the strain over the entire circumference of the artery to obtain a global indicator of cross-sectional arterial stiffness. In contrast to previous global elasticity estimates, our measure incorporates a finite thickness of tissue. Thus, both global (cross-sectional) and local elasticity information form part of IVUS palpation.

The objective of this chapter is to demonstrate feasibility of IVUS palpation *in vitro* in arterial phantoms and arterial specimens, and to illustrate some properties and the potential of this novel approach to elasticity assessment.

6.3 Theory

In 1961, Bergel expressed that while the mechanical properties of the arteries had been extensively studied in the past, precise quantitative knowledge of this subject was still lacking (Bergel, 1961). The fact that the same statement is still valid today is a manifestation that a full description of the mechanical properties of tissue is overwhelmingly complicated and involves a large number of elastic constants (Milnor, 1982) which are difficult or impossible to measure *in situ* or independently. In order to obtain realisable estimates of arterial elasticity, a number of simplifying assumptions are commonly accepted: the vessel wall is considered to be isotropic, homogeneous, incompressible and linearly elastic (Milnor, 1982; Bergel, 1961; Pagani et al., 1979). We wish not to dwell in the details of arterial biomechanics, that are already expertly described in the literature (Dobrin, 1978), but to pursue simple estimates of arterial elasticity with potential for application to the proposed clinical situations.

We define the local incremental stress-strain modulus (E_{SSM}) of elasticity as

$$E_{SSM} = \frac{\Delta P/2}{\varepsilon}, \tag{6.1}$$

where ΔP is the pressure change, $\Delta P/2$ is the mean radial stress in the wall (Dobrin, 1978) and ε is the resulting radial strain. Since in general the stress-strain ratio is nonlinear, E_{SSM} is a really function of the mean value of the stress. The local radial strain in the arterial wall is given by

$$\varepsilon = \frac{h - h_0}{h_0}, \tag{6.2}$$

where h is the wall thickness and h_0 is the wall thickness under additional intraluminal pressure. Strain is measured ultrasonically by tracking the displacement of a proximal layer of tissue (near the arterial lumen) and a more distal layer of tissue. These regions are selected so as to measure strain over a tissue thickness encompassing a substantial portion of the arterial wall (typically 0.5 to 1.5 mm). From a measurement point of view, the radial strain in the arterial wall is calculated from displacements as follows:

$$\varepsilon = \frac{\Delta R_2 - \Delta R_1}{R_2 - R_1} \tag{6.3}$$

where ΔR_1 is the displacement of the inner layer of wall tissue, ΔR_2 is the displacement at a deeper location in arterial wall, and $R_2 - R_1$ the tissue thickness entering the calculation. In an isotropic tube, the radial component of strain is given by

$$\varepsilon_r = \frac{1}{E}(\sigma_r - \nu\sigma_\theta - \nu\sigma_z), \tag{6.4}$$

where σ_r, σ_θ and σ_z are the stress components in the radial, circumferential and longitudinal directions, respectively, and ν is the Poisson's ratio. Notice that radial strain is compressive and circumferential and longitudinal stresses are tensile. This equation indicates that when any stress component increases, a corresponding increase in radial strain can be expected. Thus, although radial stresses are usually relatively small (Dobrin, 1978), the strain palpogram has the potential to be a good surrogate indicator of increased circumferential stress. This is an important association since it relates the strain palpogram to vulnerability of plaques. Studies have revealed that a thin cap overlying

fatty plaque may be unable to bear the circumferential stress imposed by the pulsatile systemic pressure (Loree et al., 1992; Lee & Libby, 1997; Richardson et al., 1989). As a global measure of cross-sectional stiffness, we define the integrated stress-strain modulus (E_{iSSM}) as

$$E_{iSSM} = \frac{\Delta P/2}{\varepsilon_{avg}}, \tag{6.5}$$

where

$$\varepsilon_{avg} = \frac{1}{2\pi} \int_{\theta} \varepsilon(\theta) d\theta. \tag{6.6}$$

The integrated stress-strain modulus E_{iSSM} does not directly correspond to any conventional measure of elasticity, but in the case of a uniform, isotropic, elastic artery it would equal the Young's modulus. In practice, most arteries requiring ultrasonic evaluation are abnormal to some extent and may contain focal or diffuse atherosclerotic disease. Except for few cases, the thin-walled tube approximation is not strictly valid and local stress and strain values can be disproportionally large. Nevertheless, the mechanical properties of a plaque can be expected to inflict a noticeable change in the cross-sectional arterial stiffness. Because E_{iSSM} is an overall measure of the local elastic modulus of the artery wall per se, while other mechanical measures such as compliance and distensibility refer to the stiffness of the artery as a hollow structure (Pagani et al., 1979), it may be a more reliable indicator of vessel mechanics.

6.4 Experimental methods

In order to evaluate the feasibility of intravascular ultrasonic palpation, we utilised an *in vitro* experimental framework based on clinical IVUS systems. The set-up was used to image gel-based vessel mimicking phantoms and artery specimens. These were scanned in the water tank at several states of static intraluminal pressure. In relation to future application of the method in vivo, these intraluminal pressures can be interpreted as the pressure state at specific time intervals during arterial pulsation or as the pressure state at different pressurisations of an intraluminal balloon.

6.4.1 Materials and experimental set-up

The experimental set-up, described in detail in chapter 3, consisted of a water tank equipped with sheaths (8 French) at two opposite sides to which the phantom or specimens could be securely attached. An IVUS catheter was inserted through one sheath and into the lumen of the phantom. This sheath was also connected to a variable water-column system for intraluminal pressurisation of the phantom.

We utilised two commercial IVUS systems. Phantoms and one specimen were studied utilising a 4.3 French (1.43mm diameter) mechanical catheter (Princeps, Endosonics/Dumed, Rijswijk, The Netherlands). Within the catheter, a 30 MHz piezoelectric transducer was rotated at 1600 rpm driven by a rotating flexible shaft. The catheter was connected to a modified IntraSound IVUS scanner (Endosonics/Dumed, Rijswijk, The Netherlands) with a stepper-motor unit that was set to scan the vessel at 400 steps/revolution. Other artery specimens were scanned using a coronary IVUS catheter

(Visions five-64, EndoSonics Inc., Rancho Cordova, CA) and coronary IVUS system (In-Vision, EndoSonics Inc., Rancho Cordova, CA) with a custom rf signal output. The 3.5 French (1.2mm diameter) solid-state IVUS catheter operates at a center frequency of 20 MHz and contains a 64-element transducer array. The change from a mechanical catheter to an array catheter took place to avoid motion artifacts: due to lack of moving parts, array catheters minimise strain estimation errors due to rotational artifacts commonly occurring in mechanical catheters.

Radiofrequency (rf) echo signals were digitised at 100 MHz, 8 bits using a digital oscilloscope (LeCROY 9400, LeCROY, Spring Valley, NY) and stored in a personal computer for off-line processing and display.

Vessel phantoms were constructed from solutions of agar and gelatin in water with carborundum (SiC) particles used for scattering. Combining plastic tubes of different diameters, gels were moulded into vessel-like structures. The phantom materials and construction method have been described recently elsewhere (Céspedes et al., 1997a),(Chapters 2 and 3). IVUS palpation was applied to two phantoms. First, a soft homogeneous phantom (E = 35 kPa) was used to identify the variance of the technique. Second, a soft vessel phantom (E = 35 kPa) with a hard lesion (E = 120 kPa) was constructed to investigate the possibilities of the technique to characterise soft and hard materials. Data was acquired at intraluminal pressures of 50 and 56 mmHg.

Two artery specimens were obtained at autopsy and scanned IVUS palpation.

- A 25-mm long segment of a human iliac artery specimen was dissected and frozen. After thawing,the specimen contained a plaque that was palpable externally. The iliac specimen was scanned in the water tank at room temperature using the mechanical IVUS catheter. Due to equipment failure, the specimen was scanned again two days later having remained in saline in a refrigerator. We applied static intraluminal pressures ranging from 95 to 98 mmHg in 1 mmHg increments. Histological analysis was obtained with Elastic van Gieson staining.

- A 40-mm long segment of diseased human femoral artery was dissected at autopsy and frozen. The specimen contained plaque of unspecified characteristics. Ultrasonic scanning was done in physiological saline, at room temperature, using the array IVUS catheter. We applied static intraluminal pressures of 100 and 120 mmHg. For histological analysis, picro Sirius red staining was used to counter-stain fibrous and fatty plaque components.

6.4.2 Estimation of radial strain and stress-strain modulus

Temporal shifts of the echo signals are related to corresponding displacements of the tissue originating the echoes. Under the effect of an intraluminal pressure differential, stiff tissues will deform less than softer tissues. This is illustrated in figure 6.1, where two IVUS images of the iliac artery specimen obtained at different intraluminal pressures are shown. On the echo images, we have identified two regions which correspond to relatively normal vessel wall (labelled A) and fibrous plaque (labelled B). It is clear that while the echoes from direction A appear compressed in time, those from direction B have suffered little change. These changes are not visible from the IVUS images.

Strain, stress-strain modulus (E_{SSM}) and the E_{iSSM} were calculated using Equations 6.2, 6.1 and 6.5, respectively. Two, non-overlapping, rf range gates sufficiently long to

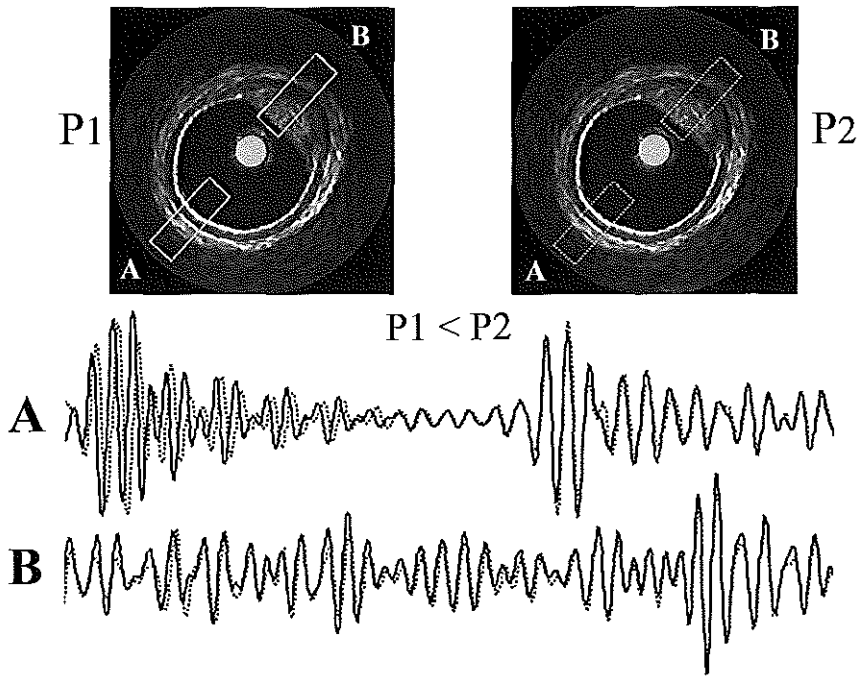

Figure 6.1 IVUS echo image of an iliac artery specimen obtained at two levels of intraluminal pressure (pressure change of 1 mmHg). The echo signals and their respective envelope show deformation (compression) of the tissue in angular position A, and little deformation in angular deformation B.

include the vessel wall or an equivalent part of the plaque were utilised to estimate the echo time-shift. Starting at the lumen, the default analysis thickness was 0.4 mm (two adjacent range gates of 0.2 mm each). The lumen-tissue boundary was readily detected *in vitro* since echo-free saline replaced blood. In this case, a simple amplitude thresholding algorithm could identify the lumen. Additionally, to investigate the dependence of the palpogram on the analysis thickness, rf data obtained from one phantom were processed using an analysis thickness of 0.4mm, 0.8 mm, and 1.2 mm (with adjacent range gates).

Rf data from iliac artery specimen was used to compute strain palpograms, E_{SSM} palpograms and E_{iSSM} at three pressure differentials to examine the dependence of these quantities on stress level. The analysis thickness was 0.4 mm with two adjacent 0.2mm range gates. The human femoral artery was scanned to demonstrate the feasibility of the technique using an array IVUS catheter. The analysis thickness was 0.4 mm with two adjacent 0.2mm range gates. The calculations based on the mechanical IVUS catheter required a beam matching procedure where, prior to strain estimation, the best match of a pre-compression rf signal was sought in the post-compression rf signal set. This was done to remove the effect of non-uniform rotation of the transducer in the mechanical catheter. The search was unnecessary when using the array IVUS catheter.

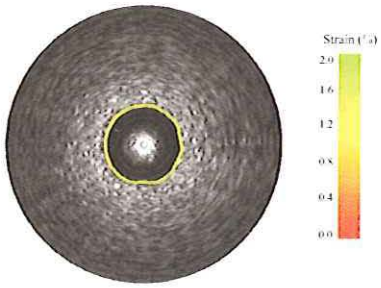

Figure 6.2 IVUS echogram and strain palpogram of a vessel phantom of uniform elasticity and echogenicity. No deformation abnormalities are shown in the palpogram.

6.5 Results

An endoluminal image with palpogram of a uniform vessel phantom void of lesions is presented in figure 6.2. The strain palpogram shows approximately constant strain all around in correspondence to the uniform stiffness of the phantom. An average strain of 1.25 % is measured, for an applied stress of approximately 400 Pa, yields an E_{iSSM} of 32 kPa. In this simple geometry, this would correspond to a Young's modulus of 32 kPa.

Figure 6.3 shows an IVUS image with a strain palpogram of the vessel phantom containing a stiff plaque. The palpogram demonstrates a region of increased strain from 1 to 5 o'clock, easily identifying the region of decreased stiffness. When analysis thicknesses of 0.4 mm, 0.8 mm and 1.2 mm are taken, a small, albeit noticeable change in strain palpogram can be observed. Note that since the strain decays radially from the lumen, a larger analysis thickness would include lower strains in the estimation process. Nevertheless, all strain palpograms correctly identify the plaque as stiffer than the rest of the phantom, thus satisfying the principal objective of the technique. The strain palpogram values corresponding to the plaque are 3 to 4 times lower than the strain in the soft vessel wall.

IVUS strain palpograms and histology of the iliac artery specimen are presented in figures 6.4 and 6.5, respectively. Note the clear identification of the plaque between 12

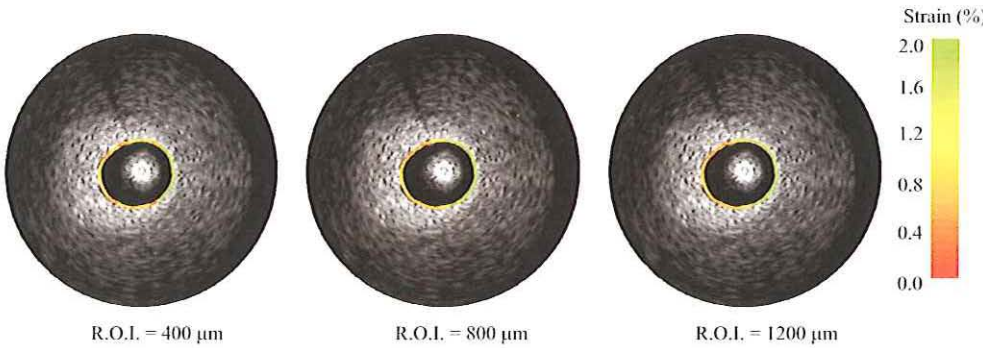

Figure 6.3 IVUS echogram and strain palpogram of a vessel phantom containing a hard plaque with echogenicity contrast. The plaque region can be readily identified in the palpogram. Increasing the region of interest influences the strain palpogram, but the soft vessel wall and hard plaque remain identifiable.

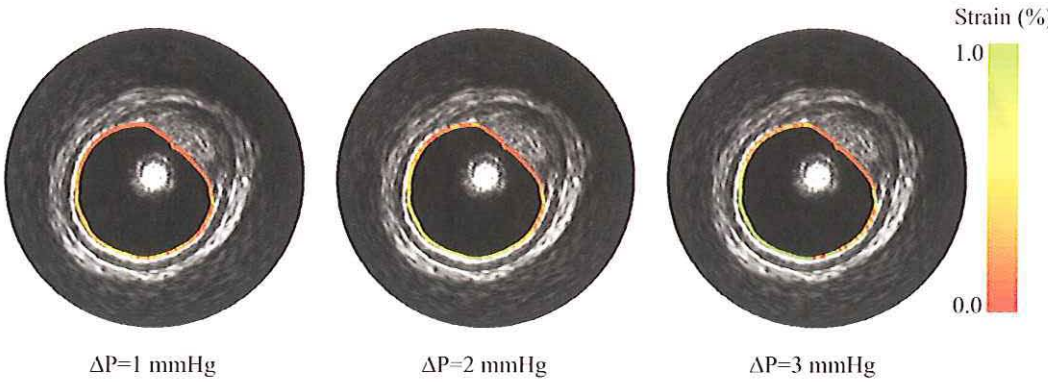

Figure 6.4 IVUS images and strain palpograms of an iliac artery specimen with a stiff plaque. The plaque is clearly visible in the echo image. The stiff nature of the plaque is indicated by the palpogram. Regions of increased strain are shown around the edges of the plaque. Strain increases with increased intraluminal pressure, particularly in the plaque-free region of the wall.

o'clock and 3 o'clock as markedly stiffer that the rest of the wall. Histological analysis confirmed the fibrous nature of this plaque, which clearly denotes increased stiffness. Although the plaque is also easily identified in the echo image, the palpogram incorporates biomechanical information without disturbing the original presentation of the IVUS image. With increasing pressure differentials (Fig. 6.4), the non-diseased part of the vessel wall shows increased strain; the average strains were 0.16%, 0.32% and 0.44%, respectively. At the junctions between the fibrous plaque and the normal vessel wall, increased strain (stress) levels can be observed. Such increased strain levels indicate stress concentration, which has been documented to occur at the junction of a plaque as discussed by Lee and co-workers (Lee et al., 1993; Loree et al., 1992). Finite element modelling of this particular cross-section revealed increased strain values at the junction between vessel wall and plaque. These were caused only by the geometry of this cross-section (de Korte et al., 1998b).

Stress-strain modulus palpograms of the iliac specimen are presented in figure 6.5. The elastic modulus palpogram offers a more absolute measure of the biomechanical characteristics, since the strain is normalised to the applied pressure differential. It can be noted, that the stress-strain modulus palpograms vary slightly between images. For pressure increments of 1, 2 and 3 mmHg the calculated E_{iSSM} are similar (80, 83 and 91 kPa, respectively), with a range of about 10%. Interestingly, the cross-section appears to stiffen for a larger applied pressure increment, an expected consequence of the non-linear elastic property of arterial tissue (Dobrin, 1978).

A strain palpogram of a diseased human femoral artery obtained with the array IVUS catheter is shown in figure 6.7. The IVUS image shows plaque all around the vessel wall. The strain palpogram reveals two soft regions (between 8 and 11 o'clock and between 3 and 6 o'clock) with two hard regions in between. The histology of this cross-section demonstrates that the main component in the soft regions is fatty material and the remaining two regions mainly contain fibrous material. The E_{iSSM} of this cross-section was 227 kPa.

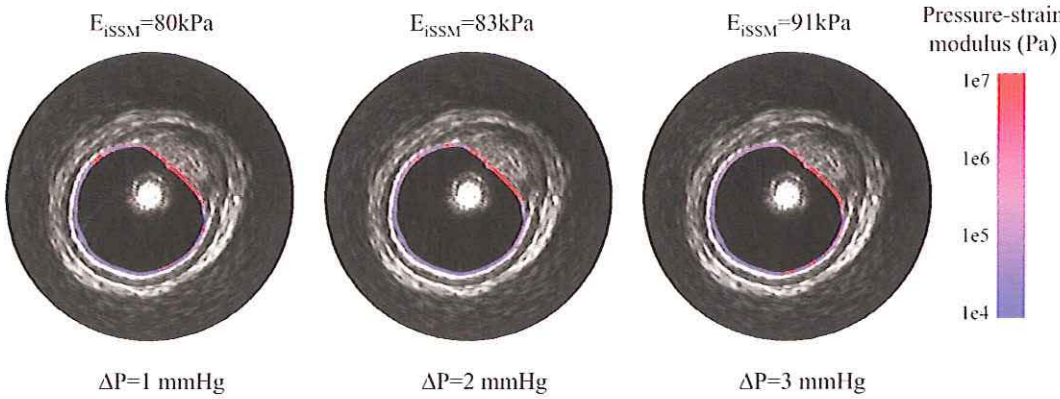

Figure 6.5 IVUS images and pressure-strain modulus palpograms of the iliac artery specimen at three levels of intraluminal pressure. Good correspondence is observed among the three measurements demonstrating a negligible change in the modulus palpogram for this small range of examined pressures.

6.6 Discussion

With an ambitious outlook, the ultimate goal of elasticity imaging should be to obtain local deformation and/or modulus of elasticity at high spatial resolution. In rigor, the true elasticity properties of tissue are fully characterised by several anisotropic elastic constants that can only be calculated with knowledge of the 3-dimensional state of stress and strain; furthermore, tissue is visco-elastic and non-linear (Ponnekanti et al., 1992; Fung, 1993). In practice, the internal stress in tissue cannot be measured and ultrasonic measurement of strain is limited to more or less precise estimation of the strain component along the direction of the ultrasound beam. Thus, a variety of realistic limitations would suggest taking a more pragmatic and simple approach. In this chapter, we have focused on a simple, yet practical approach: IVUS palpation.

Despite the complex nature of tissue biomechanics, significant information may be obtained from much-simplified mechanical models and measurements. The most popular measurements are the cross-sectional compliance and stress-strain modulus. In this chapter, we examine a novel 1-dimensional approach to the imaging of strain and local stress-strain elastic modulus which are computed over a layer of tissue of finite size. A

Figure 6.6 Histology of the human iliac artery. The elastin van Gieson stain reveals that the plaque is composed of fibrous material.

series of images emulate the acquisition of IVUS palpograms at subsequent time intervals during the pressure pulsation. Furthermore, incorporating the pressure into the measurement we obtain stress-strain modulus palpograms that are more closely related to the intrinsic mechanical properties of the surveyed tissue. While the strain palpograms are dependent on the pressure differential, the stress-strain modulus palpograms are similar for the three pressure differentials.

The strain palpogram of the femoral artery (Fig. 6.7) reveals that fibrous and fatty tissue can be clearly identified. The E_{iSSM} of this cross-section is 227kPa. This value is in the range of moduli measured by Lee and coworkers (Lee et al., 1993, 1992; Loree et al., 1992, 1994a). However, due to the complexity of the mechanical properties of arterial constituents and to the smallness of diseased arterial tissue samples, the independent, quantitative measurement of the mechanical properties of vessel wall and atheroma is an extremely difficult task. Although reported absolute values of arterial stiffness vary dramatically depending on the measurement method (static, dynamic, mechanical constraints, etc.), a several-fold stiffness difference exists between calcified, fibrous, and fatty plaques coworkers (Lee et al., 1993, 1992; Loree et al., 1992, 1994a).

Additionally, excision of specimens introduces additional complications for quantitative assessment of the mechanical properties. Gow and Hadfield (1979) clearly showed that both the static and dynamic elastic moduli of arteries were elevated after excision and that further increases may occur following cold storage. The only solution to measure representative quantitative mechanical parameters is to perform measurements *in vivo*. Preliminary evaluation of IVUS palpation in the catheterisation laboratory is currently underway.

In the past, strain imaging was performed as a practical substitute for elastic modulus imaging because the local stress components were unknown. However, modulus imaging was considered the optimal technique because it depicts a basic property of the tissue. In the cardiovascular environment, we have identified an important clinical application where the strain, rather than the modulus, is important. Therefore, in the context of imaging of vulnerable plaques, the strain palpogram is the desired result. For characterisation of plaque composition, the modulus palpogram may be more adequate.

Although we have described ultrasonic palpation based on rf processing, the robustness and decreased precision of time delay estimation with envelope processing (Céspedes, 1993a) may be well suited for this application. The trade-offs of envelope processing in IVUS palpation are currently under investigation.

A main aspect of IVUS palpation is the compound presentation of stiffness and echo information. The palpogram provides automatic registration of these information and assists in the definition of the lumen.

6.6.1 Limitations

Irregular rotation of the transducer at the tip of the IVUS catheter (in mechanical catheters) hinders the resolution of the system. For IVUS elastographic imaging, variations in the relative angular position of the beam in subsequent rf scans increases the need for 2-dimensional correlation, with concomitant increase in the computational demand of the technique.

An angle between the ultrasound beam and radial strain results in an underestimation of the strain due to 'projection' of the radial strain on the ultrasound beam and concomi-

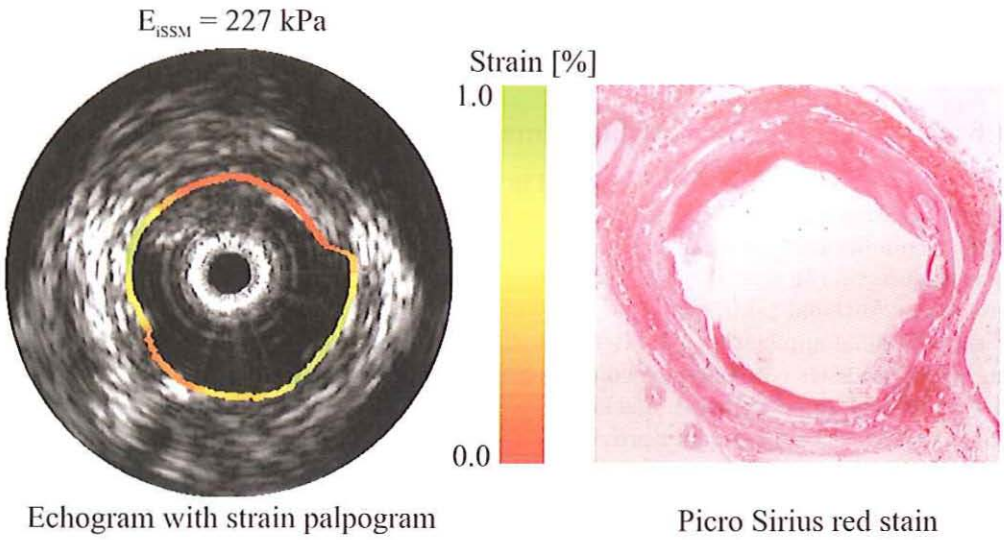

Figure 6.7 Palpogram of diseased human femoral artery with picro Sirius red stain. The palpogram reveals soft areas between 8 and 11 o'clock and between 3 and 6 o'clock. The remaining areas appear to be harder. The histology reveals that the main plaque component in the soft regions is fatty material (low amount of collagen) and the hard regions contain a large amount of collagen.

tant influence of the strain in the longitudinal and circumferential direction (Chapter 5). An angle between strain and beam will be present when the catheter is at eccentric positions or when the lumen shape is not round. Catheter eccentricity appears to have a small effect in the slightly eccentric position of the catheter in the palpogram of the iliac specimen. However a more significant effect, perhaps precluding strain estimation in extreme cases, has to be expected when the catheter is located next to the artery wall. In such circumstances, ad hoc expansion with a balloon, which automatically centres the catheter or a specialised IVUS catheter equipped with a centring device may be required. Interestingly, at the junctions of the fibrous plaque in the iliac artery (Fig. 6.4), an angle between radial strain and the ultrasound beam is present. This leads to an underestimation of the strain, which excludes the possibility that the projection artifact is the cause of the increased strain levels.

In vitro experiments are aided by simplified detection of the lumen boundary, since the blood can be replaced by anechoic saline. *In vivo*, however, detection of the lumen for ultrasonic palpation is slightly more complicated since echogenic blood is present. However, lumen detection (Li et al., 1994; Gronningsaeter et al., 1994), intravascular flow detection techniques (Li et al., 1997, 1998b), and blood noise reduction techniques (Pasterkamp et al., 1995; Gronningsaeter et al., 1995, 1996) are readily available and should not impose a severe limitation.

It has to be noted that strains of 1% and higher are obtained for very small pressure differentials in the iliac artery case. This was caused by the fact the iliac artery specimen remained in water for an extended period of time. Due to practical problems (pressurisation of the specimen, rotational artifacts of the transducer), reliable data was obtained

after three days of experiments. Partial deterioration of the tissue resulted in an E_{iSSM} smaller than could be expected.

6.6.2 Non-vascular applications

Endoluminal ultrasound is routinely used in several nonvascular applications, e.g., transrectal, endovaginal, endo-esophageal, transurethral. With advances in the miniaturisation of endoluminal devices, applications of ultrasound diagnosis from within the body are certainly on the rise (Djoa et al., 1996). Analogously to the situation in intravascular imaging, additional information on the stiffness of pathologies is useful in urologic and gastrointestinal applications. In fact, the phantoms presented which are intended to emulate blood vessels could also be construed to be scaled versions of other cavities such as the urethra or the esophagus. Lacking the pressure source provided by the pulsation of blood and the acoustic contact provided by blood, a fluid-filled balloon may be necessary to apply the probing deformation of the tissues and to provide acoustic coupling.

6.7 Conclusions

We describe a new method to image local tissue strain and stress-strain modulus using endoluminal ultrasound. We demonstrate that regions of different stiffness may be identified by this method independently of the ability to visualise the same lesion on the echo image. Thus, IVUS elasticity assessment may contribute with data complementary to the information obtained from IVUS imaging. Biomechanical information is displayed using a compound approach with automatic registration of mechanical and echo data.

Strain palpograms of an iliac artery specimen demonstrate the ability of IVUS palpation to measure local deformation of the vessel wall and atheroma. Regions of stress concentration can be identified at the shoulders of the plaque. In plaques with lipid contents, identification of areas of stress concentration is one main indicator of plaque vulnerability and no other method to obtain this information is presently available.

The simplicity and robustness associated with the ultrasonic palpation concept may allow advancement to a real-time implementation with which the true potential of the method can be adequately explored in the clinical environment.

Chapter 7

Initial Experience *in vitro* on Human Femoral Arteries

abstract

Intravascular elastography is a new technique to obtain the local mechanical properties of the vessel wall and its pathology using intravascular ultrasound (IVUS). Knowledge of these mechanical properties may be useful for guiding interventional procedures. An experimental set-up is described for assessment of the strain data of arteries. Using a 30 MHz IVUS catheter, radio frequency data are acquired with a custom made high performance data acquisition system. High resolution, local tissue displacement estimation by crosscorrelation is followed by computation of local strain. An algorithm that uses apriori knowledge of the correlation coefficient function was applied to filter the obtained strain data. With this experimental set-up, intravascular elastograms containing 400 angles/revolution with a radial resolution of $200\mu m$ *can be produced. The feasibility of intravascular elastography with this experimental set-up is demonstrated using two diseased human femoral arteries. Qualitative comparison of the elastograms with the echograms and the histology demonstrates the potential of intravascular elastography to obtain mechanical information from the vessel wall and from plaque.*

7.1 Introduction

Despite a significant decline in the last 25 years, atherosclerotic coronary disease remains the leading cause of death in the Western world. The physicians need to select the most appropriate technique for treating patients suffering from atherosclerotic disease. As the number of available interventional techniques for treatment of atherosclerotic luminal narrowing increases, the specific diagnostic information becomes increasingly important. Advances in high-frequency intravascular ultrasound (IVUS) have made it possible to study the morphology of the vessel wall and its pathology. Currently, IVUS is the only clinically available technique capable of providing real time cross-sectional images *in*

based on the publication: "Intravascular Ultrasound Elastography of Human Arteries: Initial experience *in vitro*" by Chris L. de Korte; Anton F.W. van der Steen; E. Ignacio Céspedes and Gerard Pasterkamp. *Ultrasound in Medicine and Biology* 24(3): 401-408; 1998

vivo, delivering information that is not available from x-ray angiography. For this reason, IVUS is more and more routinely used for guiding and selecting interventional procedures (Fitzgerald & Yock, 1993; Isner et al., 1991; Mintz et al., 1994) for investigation of the effectiveness of the procedure (Baptista et al., 1996; Gussenhoven et al., 1995) and for studying the mechanisms for restenosis (Mintz et al., 1996).

Since the outcome of the interventional procedure is determined not only by the morphology of the diseased vessel but also by the tissue components of the atheroma (Honye et al., 1992; Fitzgerald & Yock, 1993), knowledge of these properties is useful. Characterisation of the atherosclerotic plaques using IVUS is still limited. Using IVUS, calcified deposits can be identified in most cases due to the bright echo of this material and the distal acoustic shadow (Wolverson et al., 1983); However, identification of fatty, fibro-fatty and fibrous tissue is much more complex. Using the spectral information of the radio frequency (rf) signal, it is possible to discriminate between some types of atheroma *in vitro* (Barzilai et al., 1987; Bridal et al., 1997a, 1997b; Landini et al., 1986; Spencer et al., 1997; Wilson et al., 1994), but the feasibility *in vivo* has not been shown yet.

Knowledge of the mechanical properties of the vessel wall and the atherosclerotic lesions may be even more important than characterisation of the different plaque types. Lee and coworkers demonstrated the predictability of locations of plaque fracture as a result of balloon angioplasty (Cheng et al., 1993; Lee et al., 1993). They suggest that concentrations of stress can occur at junctions between hard material (plaque) and softer material (vessel wall). These high stress regions may predispose to plaque fracture.

IVUS can be used to study the mechanical properties of vascular tissue. Measuring the change in lumen area under application of a differential intraluminal pressure, the distensibility of the vessel can be determined from inside using IVUS (The et al., 1995). In some applications (*e.g.*, carotid artery), the distensibility can also be determined transcutaneously using echo-tracking techniques to determine the diameter of the vessel (Hoeks et al., 1992; Mozersky et al., 1972; Pagani et al., 1979) or echo-Doppler techniques (Reneman et al., 1986). In this chapter, an improved technique is described to determine the local mechanical properties of the vessel wall with atherosclerotic disease. This technique is based on the elastography principle proposed by Ophir et al. (1991) and applied *in vivo* by Céspedes et al. (1993b) for non-vascular applications. Using this technique, an elastogram (an image of strain or elastic modulus) is formed. Recent phantom studies revealed that this technique also may be applicable for intravascular purposes (Chapter 3),(Shapo et al., 1996b, 1996a; Ryan & Foster, 1997b). In gelatin-based vessel-mimicking phantoms with the morphology of vessels containing hard or soft plaques, regions with different elastic properties could be identified using the elastogram, independent of the corresponding echogenicity contrast. Although we were able to demonstrate the principle of intravascular elastography on slightly upscaled phantoms, the spatial resolution of the technique was not suitable for imaging in real vessels. Using phantoms with a wall thickness of 5 mm, strain estimates were obtained for each $400\mu m$. However, this resolution is insufficient to produce elastograms of real artery specimens with a wall thickness that is normally 1 mm or less. In this study, a technique with improved resolution is described. Using a new experimental set-up and custom-made data acquisition system, the signal-to-noise ratio was increased and motion artifacts were minimised. Additionally, new signal processing procedures were implemented to improve the quality of the strain values obtained. With these modifications, the resolution of the elasticity images is improved to a suitable level for elastography in arteries as demonstrated by the first elastograms of human femoral arteries *in vitro*. A qualitative comparison with conven-

tional echo images, histology and compression modulus values from literature is made to illustrate that intravascular elastography may be a useful technique to characterise mechanical properties of different plaque types.

7.2 Methods

7.2.1 Data acquisition

The experiments were performed in a water tank equipped with two insertion sheaths (8 F) at either side (Fig. 5.7), using a modified 4.3 F Princeps® 30 MHz catheter (DuMED (currently EndoSonics Europe), Rijswijk, The Netherlands). The original, flexible, drive shaft of the catheter was replaced by a rigid tube (diameter 0.85 mm, length 150 mm) to avoid motion artefacts due to non uniform rotation of the transducer (ten Hoff et al., 1989). The IVUS catheter was inserted via the proximal sheath. Intraluminal pressure was applied by a water column system containing degassed physiologic saline solution connected to a side arm of the proximal sheath. The intraluminal pressure was monitored using a pressure gauge (DTX/plus® Ohmeda, Bilthoven, The Netherlands) connected to a side arm of the distal sheath.

The catheter is connected to a modified IntraSound® motor unit (DuMED (currently EndoSonics Europe), Rijswijk, The Netherlands). This motor unit contains the pulser and receiver of the ultrasonic system and rotates the catheter in 400 angles/revolution using a stepper motor. At each angular position, 12 traces of 10.0 μs were acquired, representing an echo depth of 7.5 mm. The 12 traces were averaged to improve the signal-to-noise ratio (SNR): we measured an average SNR of 26 dB for the first 500 μm of tissue (calcified tissue excluded). Two scans were acquired: one at a pressure level of 80 mmHg and one at 100 mmHg.

The rf-data were stored in a custom-made acquisition system. This system contains an industrial grade Pentium® 133 MHz computer, equipped with two DA500A data acquisition boards (Signatec, Corona, CA, USA). The rf signals were digitised at 200 MHz in 8 bits and stored in a high-speed memory of 128 Mbytes. For phase-synchronous sampling, triggering of the ultrasonic system was synchronised with the external sampling clock output of the acquisition board. Using a low-frequency data acquisition board (ASO 1800, Keithley, USA), the electronic output of the pressure sensor was sampled at 100 kHz. The data were processed off-line.

7.2.2 Data processing

The portion of the signal containing data from the vessel wall were determined. The starting and ending point of the vessel wall for each trace were detected using a threshold value just above the noise level of the system. These starting and ending points values were filtered in the angular direction using a 15-point median filter.

Successive windows of 100 samples ($T = 0.5\ \mu s$) with 50% overlap were taken to determine the local time shifts between the traces acquired at the different pressure levels. The time shifts were determined using the peak of the correlation coefficient function. The correlation coefficient function was upsampled by a factor of 50 using a low-pass interpolation algorithm (IEEE, 1979) to achieve a time shift resolution of 100 ps. A value of 100 ps is on the order of the Cramér-Rao lower bound for time shift

estimation (Céspedes et al., 1995a) for the set-up used (80 ps with f_c=30 MHz, B=20 MHz T=500 ns and SNR=400).

Local radial strain $\hat{\varepsilon}$ was estimated using a 1-dimensional finite difference algorithm:

$$\hat{\varepsilon} = \frac{\delta t_2 - \delta t_1}{\Delta T} \tag{7.1}$$

where δt_1 is time the shift between the two echo signals observed through a window of duration T starting at a certain time t, and δt_2 is the time shift between the two echo signals observed through a window of the same duration T but starting at time $t + \Delta T$. The time between successive windows (ΔT) of 250 ps results in a strain estimate for each 200 μm.

Next, the strain data were filtered using the value of the peak of the correlation coefficient function as a figure of merit as follows. First, the location of the peaks of both correlation coefficient functions ($\hat{\rho}_1$ and $\hat{\rho}_1$) were determined and the strain value was calculated. Next, this strain value was used to determine the theoretical peak value $\hat{\rho}_{th}$ of the involved crosscorrelation functions as described by Céspedes et al. (chapter 5):

$$\rho_{th} = sinc\ (\varepsilon\ f_c T) \tag{7.2}$$

where ε = strain, f_c = center frequency and T = window length. Finally, the two measured values ($\hat{\rho}_1$ and $\hat{\rho}_2$) were compared to the theoretical peak value $\hat{\rho}_{th}$ and the strain estimate was rejected when the difference between the theoretical and one or both measured values was larger than 0.2. The threshold value of 0.2 was taken from the 65% confidence interval (1% strain and a time window of 0.5 ms) in the theoretical study (Chapter 5). Rejected strain values were replaced by the median value of the eight surrounding neighbours (the median of the 5 surrounding neighbours was taken at the border of the vessel wall).

7.2.3 Imaging

The rf signals were demodulated using the magnitude of the analytic signal to determine the envelope of the signal. Next, the 2000 samples in the radial direction of the envelope of each trace were downsampled to 100 points. The resulting values are converted to a linear grey scale and grey scales are plotted using a piece-wise bilinear interpolation.

The strain value is colour-coded using a "traffic light" notation: *i.e.*, from red for stiff material via yellow to green for compliant material. The lower bound for strain estimation error (Céspedes et al., 1995b) using this experimental set-up is 0.03% (f_c=30 MHz, B=20 MHz, T=500 ns, ΔT=250 ps and SNR=400). Strain estimates were clipped between 0.03% (coded in red) and 1% (coded in green) with only a few unreliable estimates above the 1% threshold.

7.2.4 Materials

Two atherosclerotic human femoral arteries obtained postmortem were used for illustration of the method. The femoral arteries were excised within 24 hours post mortem and stored at $-70°C$. The arteries were thawed at $4°C$ and measured at room temperature. The water tank of the experimental set-up was filled with a degassed physiological saline solution and the proximal and distal sides of the artery specimens were connected to the sheaths. Each specimen was scanned at three positions separated by 10 mm.

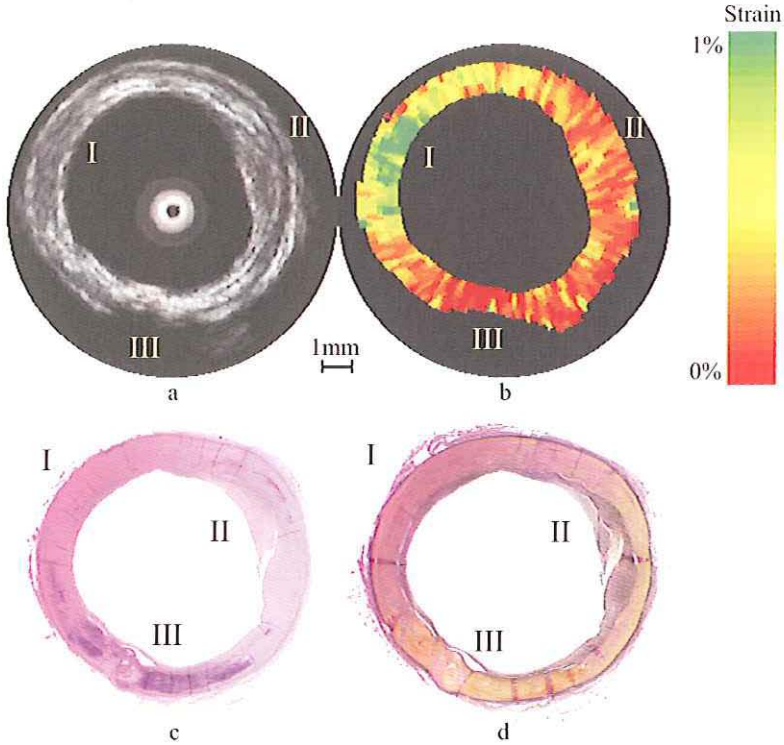

Figure 7.1 Corresponding echogram *(a)*, elastogram *(b)* and histologic counterparts with hematoxylin-eosin *(c)* and Verhoeff's elastic van Gieson *(d)* of a human femoral artery. In the four images a normal artery wall (I), fibrous plaque deposition (II) and a calcified region (III) are apparent.

After the intravascular experiments, the vessel specimens were fixed for 12 hours in a buffered (pH = 7) formaldehyde solution (3.6%). The specimens were decalcified in a standard RDO solution (Apex Inc., Plainfield, Illinois, USA). For histologic comparison, the arteries were processed for routine paraffin embedding. A pair of transverse sections of 5 μm perpendicular to the long axis of the vessel were cut at positions separated by 1 mm. One section of each pair was stained with hematoxylin-eosin to assess general structural features. The remaining section was stained with the Verhoeff's elastic van Gieson, which gives selective black staining of elastin fibres. The van Gieson technique was used to counterstain muscle and connective tissue.

7.3 Results

With the improved experimental set-up described in this chapter, we were able to obtain elastograms of diseased human arteries. The radial resolution of 200 μm is sufficient to obtain several strain values within a normal arterial wall. In the thickened wall up to 10 strain values are obtained.

The echogram and elastogram of a human femoral artery are shown in figure 7.1. The echogram (Fig. 7.1a) shows the three-layered structure of the femoral artery. A plaque deposition positioned towards the vessel wall is visible at region II. The composition of this plaque can not be obtained from the echogram. At region III, a bright echo with distal shadowing, indicating calcified material, is apparent. The elastogram of this

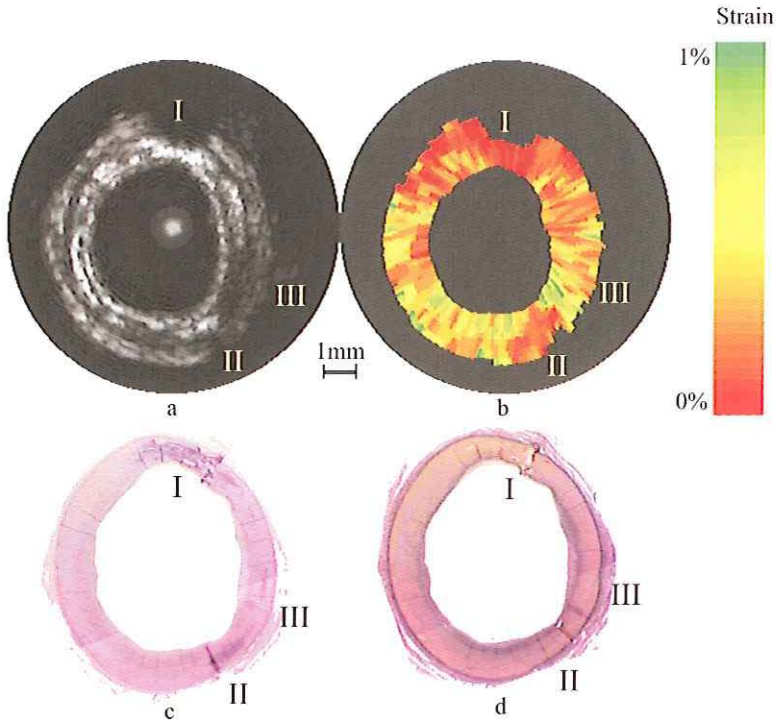

Figure 7.2 Corresponding echogram *(a)*, elastogram *(b)* and histologic counterparts with Hematoxylin Eosin *(c)* and Verhoeff's elastic van Gieson *(d)* of a human femoral artery. In the four images a severe calcified region (I) and a small calcified deposit (II) are apparent. An echolucent region in the echogram is visible at III.

section is shown in figure 7.1b. Regions with very small compression are coded in red, moderately compressed material is coded yellow and tissue compressed up to 1% in green. The elastogram shows small compression in region III, indicating stiff material. The strain in region I is around 1%, indicating compliant material. A moderate strain on the order of 0.25% is observed in region II.

The histologic section stained with hematoxylin-eosin (Fig. 7.1c) shows a plaque at region II. At region III, a calcified deposit can be found in the media. The rest of the vessel wall shows no plaque depositions with only a minor formation of intimal hyperplasia. The Verhoeff's elastic van Gieson stained section (Fig. 7.1d) shows that the main component of the plaque at region II is fibrous material. The result of the other femoral artery is shown in figure 7.2. The IVUS image shows calcified deposits (a bright echo with distal shadowing) at regions I and II. An echolucent media is apparent at region III. The elastogram clearly indicates the calcifications in regions I and II with moderate compression in other parts of the vessel wall. The strain in region III is similar to the strain in the other noncalcified parts of the vessel wall. The calcified deposits are also seen in the hematoxylin-eosin stained section where a calcified area is visible, located at the intima-media boundary in region I and the smaller calcified spot in region II is more distally located in the media. The elastogram adequately depicts the depth of the calcified deposits within the diseased wall. The histologic sections show no differences in tissue composition at region III as compared to the other normal vessel wall tissue.

7.4 Discussion

In this chapter, we present an improved elastographic data acquisition and signal processing method capable of obtaining elastograms of arteries *in vitro*. With respect to the earlier phantom study described in chapter 3, the flexible shaft of the Princeps® catheter was replaced by a rigid shaft to reduce motion artefacts. These motion artefacts introduce large noise components and preclude strain imaging in vessels. Rotational artefacts may be minimised by using array catheters such as the synthetic aperture phased array catheter as described by O'Donnell et al. (1997), and an interface to acquire rf signals from such devices is currently being developed.

Although the use of array catheters minimises rotational artefacts, 2-dimensional search algorithms will be necessary for *in vivo* experiments. The pulsation of the arterial system introduces a noncontrolled movement of the catheter in the lumen, resulting in a misalignment of successive frames. 2-dimensional search algorithms are currently being implemented in order to advance to *in vivo* intravascular elastography. An integrated catheter consisting of an imaging device and a compliant balloon (Shapo et al., 1996b) is another possibility to advance to *in vivo* elastography. Motion artefacts are minimised with this combined catheter, but blood flow is interrupted; thus a custom device is required.

Using the new data acquisition system and averaging of the signals, the signal-to-noise ratio is increased by 10dB. A better SNR allows the use of smaller time windows for the time shift estimation resulting in an increased radial resolution of $200\mu m$. Also, a filtering technique was applied that uses *a priori* knowledge of the expected correlation coefficient value (Chapter 5). Since the time shift is determined using crosscorrelation, the correlation coefficient can be compared to the theoretical correlation coefficient corresponding to that strain value and selectively discarded. When the theoretical peak value differs from the determined peak values, the strain value is rejected. In this way, 20% of the strain estimates were detected to be incorrect and consequently rejected.

It was shown that elastograms of human arteries can be obtained *in vitro*. Using the elastogram, regions with various pathological properties can be discriminated. In both arteries, the strain in the regions containing calcified material (Fig. 7.1, region III and Fig. 7.2, region I and II) is small, since these regions are very stiff. The strain in the normal vessel wall is up to 1%, indicating softer material. The region with the fibrous plaque deposition (Fig. 7.1, region II) has a moderate strain level. A radial resolution of $200\mu m$ is sufficient for adequate depiction of depth information. The elastogram (Fig. 7.2b) clearly shows a difference between a calcified deposits located at the intima-media interface (region I) and a deposit located in the media (region II).

In general, strain elastograms give an artifactual representation of the Young's modulus distribution. When soft material is covered by a cap of hard material, the strain in the soft material may be decreased (Céspedes et al., 1996). This mechanical shadowing is related not only to the hardness of the materials, but is dominated mainly by the geometry. In this study, the strain in the arterial wall distal to the fibrous plaque (Fig. 7.1, region II), is lower than the strain in the wall without plaque (Fig. 7.1, region I). This effect can be caused both by the radial decay of the strain (Chapter 3) and the mechanical shadowing by the fibrous plaque.

The Young's modulus is a function of the stress and the strain. Since the local strain is determined in this study, the local stress is needed for calculation of the local Young's

modulus. Using this method implies that only the applied stress at the lumen-vessel wall boundary is known. For a homogeneous material the stress and strain in the vessel wall can be calculated (Chapter 3), but this will in general not be the case for real artery specimens. In these cases, the use of finite element analysis can be helpful for a better understanding of the strain images (de Korte et al., 1996; Soualmi et al., 1997). Nevertheless, the values for the strain of the innermost layer of the vessel wall can be converted to approximate compression modulus values. The applied stress in this layer is the intraluminal pressure differential. An intraluminal pressure of 20 mmHg corresponds to an applied stress of 1.3 kPa (Chapter 6), (Dobrin, 1978). Using the relation $\sigma = E\varepsilon$ where σ is applied stress, E is the compression modulus and ε is the strain, the compression modulus for different tissue types can be calculated. This results in values of 150-300 kPa for normal vessel wall and approximately 500 kPa for fibrous plaque. Calcified material will have a compression modulus of several GPa. Quantitative comparison of compression moduli found in different studies is difficult, since the compression modulus is influenced by various measurement conditions (time after excision, temperature and amount of stretching). Nevertheless, the compression modulus of normal vessel wall found in this study is in the same range as values found in the literature for normal vascular tissue. Reported values range from 300 kPa to 700 kPa (Patel & Janicki, 1970a; Patel et al., 1970b; Gow & Taylor, 1968; Bergel, 1961). Values found for the compression modulus of atherosclerotic material span a wide range but studies of Lee et al. (1991, 1992) indicate that the stiffness of calcified material is about three times higher than that of fibrous material. This finding is similar to the results of this study. The echogram reveals the geometry of the plaque (Fig. 7.1, region II), but the composition of the plaque remains unknown. However, based on the mechanical properties, the elastogram reveals that this plaque may be composed of fibrous tissue. This finding is corroborated by the histology.

Although the elastographic results indicate good agreement with literature values for the compression modulus for the various pathologies, an *in vitro* study with a larger number of specimens needs to be conducted to evaluate the capabilities of intravascular elastography to quantify the mechanical properties of vessel wall and plaque. For this study, staining techniques specifically suited to identify fibrous, calcified and fatty tissue are required. Due to the preliminary nature of this work, we only used staining techniques for overall morphological analysis.

7.5 Conclusions

Based on improved experimental and processing conditions, we have obtained the first strain elastograms of diseased arteries *in vitro*. Preliminary elastograms demonstrate that quantification of mechanical properties and characterisation of regions with various pathologies may be feasible. Although additional information is required to determine the exact Young's moduli, the strain elastogram reveals useful information that is inconclusive from IVUS alone. The success of this study provides motivation to initiate a larger scale in vitro study to evaluate the capabilities of IVUS elastography to quantify the mechanical properties and characterise plaque constituents. Much additional work is required to advance this technique to *in vivo* imaging.

Chapter 8

IVUS Elastography: A Validation Study *in vitro*

abstract

Background. *The composition of the plaque is a major determinant of coronary related clinical syndromes. Intravascular ultrasound elastography has proven to be a technique capable of reflecting the mechanical properties of phantom material and the femoral arterial wall. The aim of this study is to investigate the capability of intravascular elastography to characterise different plaque components.*

Methods and results. *Diseased human femoral arteries (n=9) were measured in vitro. At each location (n=35), two IVUS images were acquired at different intraluminal pressures (80 and 100 mmHg). Using crosscorrelation analysis on the high frequency (rf-) ultrasound signal, the local strain in the tissue was determined. The strain was colour-coded and plotted as additional image to the IVUS echogram. The visualised segments were stained on the presence of collagen, smooth muscle cells and macrophages. Matching of elastographic data and histology was performed using the IVUS echogram. The cross-sections were segmented in regions (n=95) based on the strain value on the elastogram. The dominant plaque types in these regions (fibrous, fibro-fatty or fatty) were obtained from histology and correlated with the average strain and echo-intensity. The plaque types as determined by histology did not reveal echo-intensity differences in the IVUS echogram (p=0.992). However, the strain for the four tissue types differed significantly ($p < 0.001$). This difference was mainly evident between fibrous and fatty tissue (p=0.0012).*

Conclusion. *Different strain values are found between fibrous, fibro-fatty and fatty plaque components indicating the potential of intravascular elastography to identify vulnerable plaque.*

8.1 Introduction

Intravascular ultrasound (IVUS) currently is the only clinically available technique providing real-time cross-sectional images of the vascular wall. Although IVUS imaging reveals the geometry of the vessel wall and plaque, characterisation of the plaque com-

based on the publication: "Vascular plaque characterisation using Intravascular Ultrasound Elastography: A Validation study *in vitro*" by Chris L. de Korte, Gerard Pasterkamp, Anton F.W. van der Steen, Hein A. Woutman and Nicolaas Bom. *Circulation*: submitted; 1999

position remains difficult. Calcified and fibrous plaques can be identified in most of the cases (Potkin et al., 1990; Yock & Linker, 1990; Nishimura et al., 1990; Gussenhoven et al., 1996; Barzilai et al., 1987). Calcified areas are identified by their hyper-echoic appearance and distal shadowing and may be associated with acoustic reverberation. Fibrous lesions yield homogeneous echo reflections without distal shadowing. However, the compositions of lipid containing and mixed (fibrous, lipid calcified) plaques remain unknown in most of the cases (Potkin et al., 1990; Yock & Linker, 1990). Since the number of interventional techniques is large, knowledge about the plaque composition can assist the clinicians in choosing the proper technique. Moreover, since all interventional techniques are predominantly mechanical in nature (Waller, 1989), the outcome of the intervention may be influenced by the mechanical properties of vessel-wall and plaque (Hori et al., 1997).

The composition of the plaque is a major determinant of clinical syndromes (Fishbein & Sighel, 1996; Falk et al., 1995; Fuster et al., 1990). Additionally, vulnerability of plaque is influenced by the mechanical properties of the vessel wall and plaque. Studies revealed that a thin cap overlying fatty tissue may be unable to bear the stress imposed on it due to the pulsatile pressure of the blood (Lee & Libby, 1997; Loree et al., 1992; Richardson et al., 1989). Lipid rich lesions with a thin cap and local inflammatory response are considered rupture prone, which may lead to subsequent thrombosis and myocardial ischemia. Therefore, techniques that are capable of characterising the plaque may bear clinically relevant diagnostic, prognostic and aetiologic values (Lendon et al., 1991; Moreno et al., 1994). In IVUS imaging, the mechanical properties of the atherosclerotic plaque is not necessarily related to its echogenicity (Hori et al., 1997).

Intravascular elastography is a new technique based on IVUS. The technique is in principle able to discriminate between soft and hard material. The underlying principle is that soft material will strain more compared to hard material when a force is applied on the tissue (Ophir et al., 1991). The strain is determined using the ultrasound signal. The method was validated and applied *in vivo* for tumor detection in breast (Céspedes et al., 1993b). Currently, this technique is developed for intravascular purposes (Chapter 3), (Ryan & Foster, 1997b; Shapo et al., 1996b) and applied on human arteries in vitro (Chapter 7): preliminary experiments revealed that it is feasible to identify different tissue components using intravascular elastography. Since the images are based on

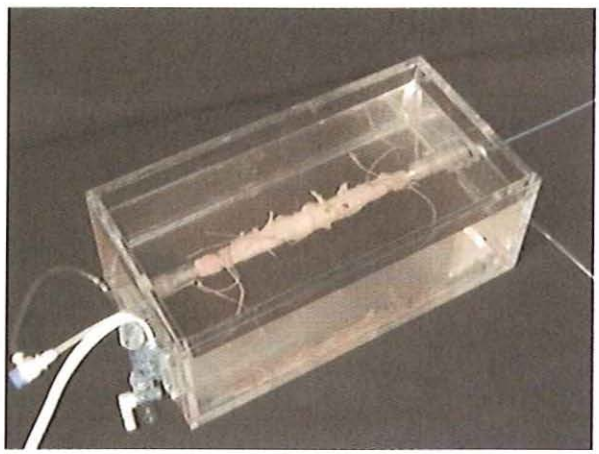

Figure 8.1 Water tank with artery specimen connected between two insertion sheaths. The side-branches are closed with suture. At the right side the Princeps® catheter is visible and at the left side the pressure sensor.

the radial strain, the technique has potential to detect regions with elevated stress: an increased circumferential stress will result in an increased radial strain of the material.

The aim of the present study is to investigate the capability of intravascular elastography to differentiate between different plaque components. We hypothesised that fibrous, fibro-fatty and fatty tissue could be discriminated using the elastogram with more strain in fatty lesions compared to fibrous lesions. Intravascular elastograms were obtained of diseased human femoral arteries *in vitro*. After the ultrasound experiments, the arteries were processed for histologic analysis. Regions with different elastographic values were correlated with the predominant plaque morphology as determined with histology. Additionally, the average echo intensity of the selected regions was correlated with histology.

8.2 Materials and Methods

8.2.1 Materials

Atherosclerotic human femoral artery segments (n=10) were excised within 24 hours post mortem and stored at $-70°C$. Next, the arteries were thawed at $4°C$ and sidebranches were closed using suture material. The arteries were connected to both the insertion sheaths of the experimental setup and tight with suture material (Figs. 5.7 & 8.1). Since the *in vivo* length of the specimens was unknown, the arteries were not stretched along the vessel axis. One artery was excluded since the data acquisition partly failed during this experiment. The arteries were scanned at different position with an interspacing of at least 10 mm. These cross-sections (n=54) were marked with a surgical needle, inserted in the peri-adventitia which is clearly visible in the echogram. After the ultrasound experiment, a suture was used to connect a marker to the outside of the vessel-wall at the position of the needle.

8.2.2 IVUS experiments

The ultrasound experiments were performed in a physiological saline solution in a water tank at room temperature $21 \pm 2°C$ (Chapter 7). The intraluminal pressure was adjusted using a water column system connected to the proximal sheath. Using this water column system, containing a degassed physiological saline solution, pressures of 80 and 100 mmHg were applied from within the lumen. This sheath was also used to insert a Princeps® 30 MHz IVUS catheter (EndoSonics, Rijswijk, The Netherlands). The pressure was monitored using a pressure gauge (DTX/plus®, Ohmmeda, Bilthoven, The Netherlands) connected to the distal sheath.

The catheter was connected to a modified IntraSound® (EndoSonics, Rijswijk, The Netherlands) motor unit. This unit contains the pulser and receiver of the echographic system and a stepper motor to rotate the single element transducer. The transducer was rotated in 400 steps per revolution. At each angle, 12 traces of 10.0 μs radio frequency (rf-) data were acquired. These 12 traces were averaged to increase the signal to noise ratio. The data were stored in an industrial grade Pentium^{TM} computer, equipped with a 200 MHz sampling frequency acquisition board (Signatec, Corona, CA, USA)(Chapter 7).

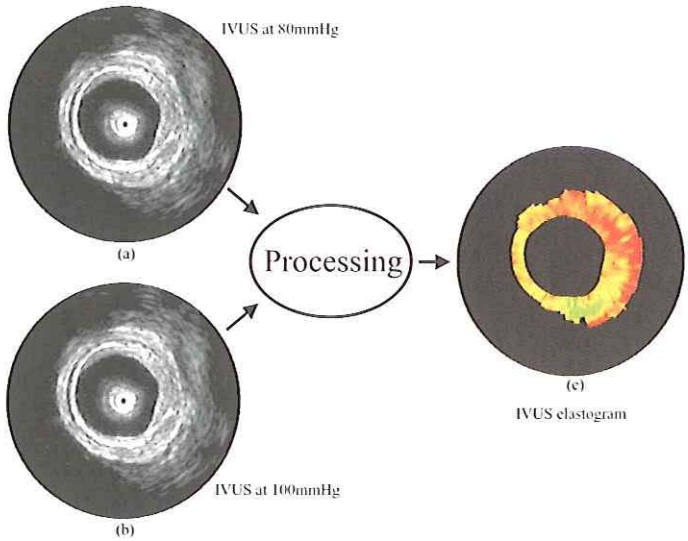

Figure 8.2 Principle of forming an intravascular elastogram. An IVUS echogram is acquired at an intraluminal pressure of 80 mmHg (a). Next, another IVUS echogram is acquired at 100 mmHg intraluminal pressure (b). Using crosscorrelation analysis on the radio frequency signal, the local strain is determined. The strain is colour-coded and plotted in a complimentary image called intravascular elastogram (c).

Elastograms were calculated as described in chapter 7. First, an IVUS frame was acquired at 80 mmHg intravascular pressures (Fig. 8.2a). After 2 seconds, an IVUS frame was acquired at 100 mmHg (Fig. 8.2b) to achieve different strain levels of the material. Using crosscorrelation techniques, the local strain was calculated from the gated rf-traces. First, the displacement of the tissue at increasing depths was determined. Next, the differential displacement of the tissue is directly converted to strain (ε). The strain values were colour-coded from red for low strain via yellow to green for 1% strain (traffic-light notation) and plotted as complementary image to the IVUS echogram (Fig. 8.2c). The resolution of the strain in the radial direction is 200 μm.

8.2.3 Histology

After the *in vitro* ultrasound experiments and subsequent fixation, the marked arterial segments (0.5 cm) were dissected. The segments were decalcified in EDTA and subsequently processed for routine paraffin embedding. Sections of 4 μm thickness were sliced near the center of the marked segment. For each segment, cross-sections were stained for collagen with picro Sirius red stain, for smooth muscle cells with anti Alpha-actin stain (Sigma, clone 1a4, 8mg/ml) and for macrophages with anti CD-68 stain (DAKO, kp1, 3mg/ml). The immunoreactivity of Alpha-actin and CD-68 stain were enhanced with 10 mmol/L citrate and buffered at pH 6.0 for 15 minutes at $100°C$. In addition, a streptavidine-biotine complex/horseradish technique was used. The picro Sirius red stain was used in combination with polarised microscopy to estimate the amount of fatty tissue within the plaque.

8.2.4 Matching IVUS and histology

The alignment of the ultrasound data and histologic cross-sections was performed using the IVUS echogram and histology. Many groups already demonstrated the relation between IVUS echograms and histologic sections, especially the geometry of the vessel wall and plaque (Nishimura et al., 1990; Potkin et al., 1990; van der Lugt et al., 1995). Only cross-sections with an exact match between histology and IVUS echogram were taken for the statistical analysis (n=35). The matching was performed without knowledge of the elastographic results.

The cross-sections were segmented into regions based on the strain. Regions were selected with a similar strain value in the elastogram (see Figs. 8.3 and 8.4). Regions with unreliable strain information were rejected. In these regions the estimated strain was not in accordance with the peak value of the crosscorrelation function used for the strain estimation as described in previous chapters (4 and 7). Next, the average strain (ε_{avg}) in this region was determined. Finally, in the corresponding region in the echogram, the average echo intensity was calculated. Since the echointensity is taken from the envelope that is calculated from the rf-signal (digitised in 8 bits), the values will be between 0 and 128. For correlation with histology, the dominant tissue types in the selected regions were determined by two researchers unaware of the elastographic results (HAW and GP). The regions were subdivided in five tissue types:

1. Fibrous tissue. More than 80% of the area consists of fibrous material.
2. Fibro-fatty tissue. If 20%-50% of the area was fatty material and the remaining area contained fibrous material the dominant tissue type was fibro/fatty.
3. Fatty tissue. More than 50% of the area consists of fatty material.
4. Fibro-calcified tissue. If 20%-50% of the area was calcified material and the remaining area contained fibrous material the dominant tissue type was fibro/calcified.
5. Vessel wall. If the echogram revealed no plaque in the region and the main content was fibrous material the region was classified as vessel wall.

8.2.5 Statistical analysis

Since only in two cross-sections fibro-calcified material was found, this tissue type was excluded from the statistical analysis. First, the distribution of the average strain and average echo-intensity were tested for normality. These test revealed that the strain ($p < 0.01$) and the echo-intensity ($p < 0.01$) were not normally distributed. Next, the median, upper and lower quartiles of the average strain value and the echo-intensity in the regions was determined for the four groups. The incremental pressure strain modulus was calculated using the relation $E_{ps} = \Delta P/2\varepsilon_{avg}$ (Dobrin, 1978),(Chapter 6). Since in general the stress strain ratio is non-linear, this elastic modulus is a function of the mean of the stress.

A Kruskall-Wallis test between the three plaque types and the strain was performed using SAS (SAS Institute Inc., Cary, NC, USA) to investigate if the strain in the three plaque groups was different. Finally, the differences between two plaque groups (fibrous versus fibro-fatty, fibrous versus fatty and fibro-fatty versus fatty) were tested using a Wilcoxon test. Values of $p < 0.0166$ were considered significant (Bonferroni correction). A Kruskall-Wallis test was also performed to test the difference of the echo-intensity for the three plaque types.

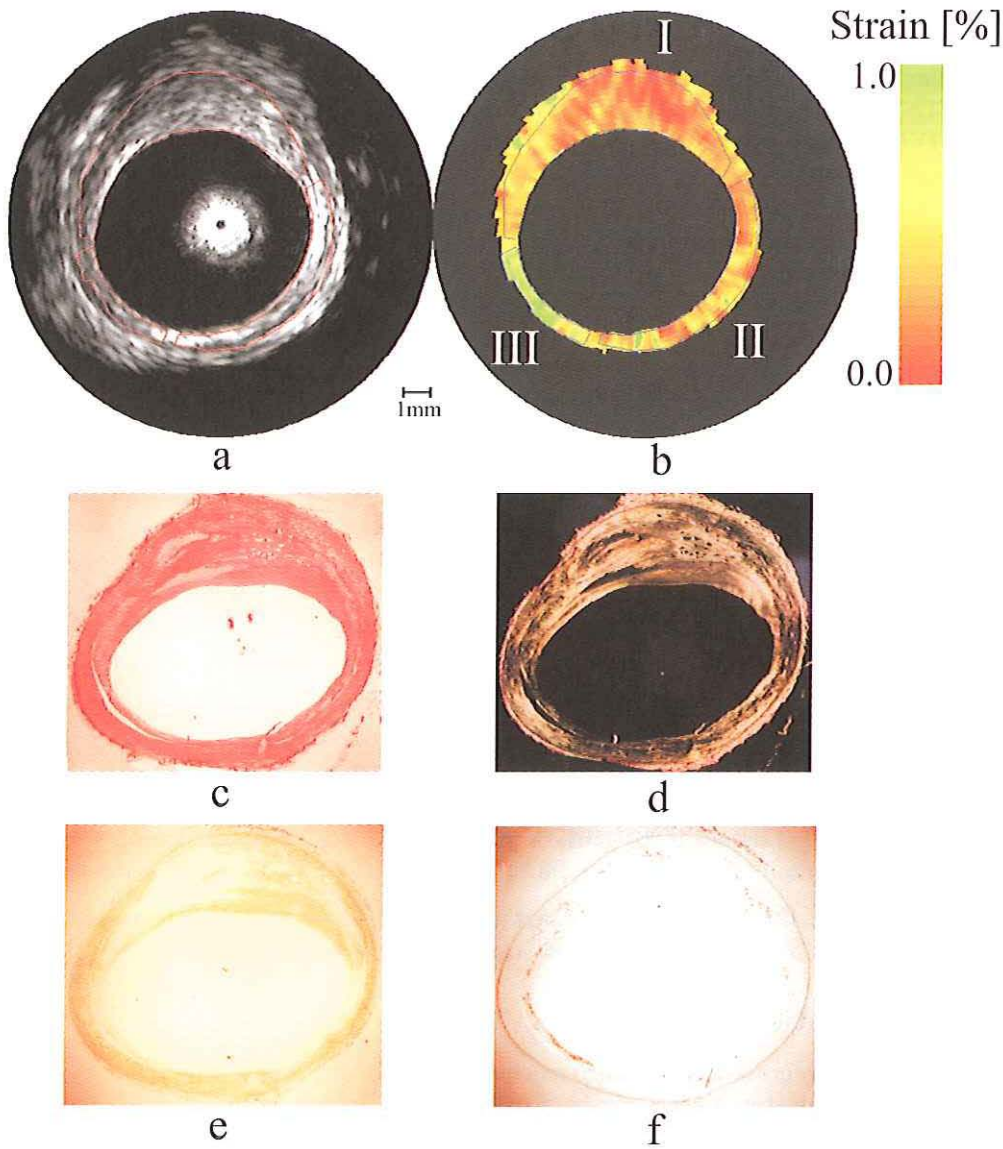

Figure 8.3 Intravascular echogram (a) and elastogram (b) of a diseased human femoral artery with the corresponding histology: (c) Picro-Sirius-red, (d) polarised light microscopy of picro-Sirius red (e) anti-Alpha actin and (f) anti CD-68 antibody. The echogram reveals an eccentric plaque between 9 and 3 o'clock. The elastogram reveals low strain in the plaque (0.24%), a similar strain in the non-diseased vessel wall between 3 and 7 o'clock (0.32%) and a high strain in the vessel wall between 7 and 9 o'clock (0.96%). The histology reveals a fibrous composition of the plaque (c,d & e). The region with high strain contains fatty foam cells at the lumen-vessel wall boundary and an increased macrophage activity (f) indicating this region as an erosive plaque region.

Table 8.1 Strain and Pressure strain modulus for the different plaque types and normal vessel wall.

	Strain [%] Median	Pressure-Strain modulus [kPa]	Number
Fibrous tissue	0.27	493	48
Fibro-fatty tissue	0.41	324	25
Fatty tissue	0.66	202	7
Normal vessel wall	0.44	302	16
		Total number of regions	95

8.3 Results

In this study, 35 cross-sections were analysed from 9 arteries. The cross-sections were segmented in regions (n=95). The majority of regions (Table 8.1) contained fibrous material (51%), the minority fatty material (7%). 26% was mixed fibro-fatty material and 17% of the regions contained non-diseased vessel wall material.

An IVUS echogram and elastogram are presented in figure 8.3. The echogram reveals an eccentric plaque between 9 and 3 o'clock (region I). The elastogram shows that the strain in the plaque is low. The strain in the vessel wall was similar to the strain in the plaque except for the region between 7 and 9 o'clock (region III): increased strain values were found in this region. The histology revealed that the dominant plaque component was fibrous material. The vessel wall with increased strain values has fatty tissue components at the lumen vessel-wall boundary with fibrous tissue components more distally. Additionally, an increased macrophage concentration was found identifying this region as an erosive plaque region. Note that the echogenicity among these regions was similar implying that the difference in composition between this region and the remaining arterial wall could not be made using the IVUS echogram.

Another example is presented in figure 8.4. The IVUS echogram (Fig. 8.4a) shows a concentric plaque with different echogenicities. The elastogram reveals two regions with low strain values and two regions with increased strain values. The histology reveals that the regions with increased strain correspond to lipid rich regions and the regions with low strain values to fibrous plaque components. The difference between the different regions could not be observed using the echogram since the echointensity between region III and region IV is similar but the dominant tissue type is not.

The box-and-whisker plot shows the median, lower and upper quartiles and the extend of the data for the four tissue types (Fig. 8.5). The strain in fibrous tissue is lower than the strain in fibro-fatty tissue. Fatty tissue components are softer than fibro-fatty and fibrous tissue components. A highly significant difference for the strain among the four groups is observed ($p < 0.001$). Table 8.2 reveals that differences between fibrous and fatty and between fibrous and fibro-fatty are significant. Table 8.3 reveals that there is no difference in echogenicity for the three different plaque types (p=0.922). The echo

Table 8.2 Differences between strain values (p-values from Wilcoxon test)

	Fibrous - FibroFatty	Fibrous - Fatty	FibroFatty - Fatty
p-value	0.012	0.0012	0.024

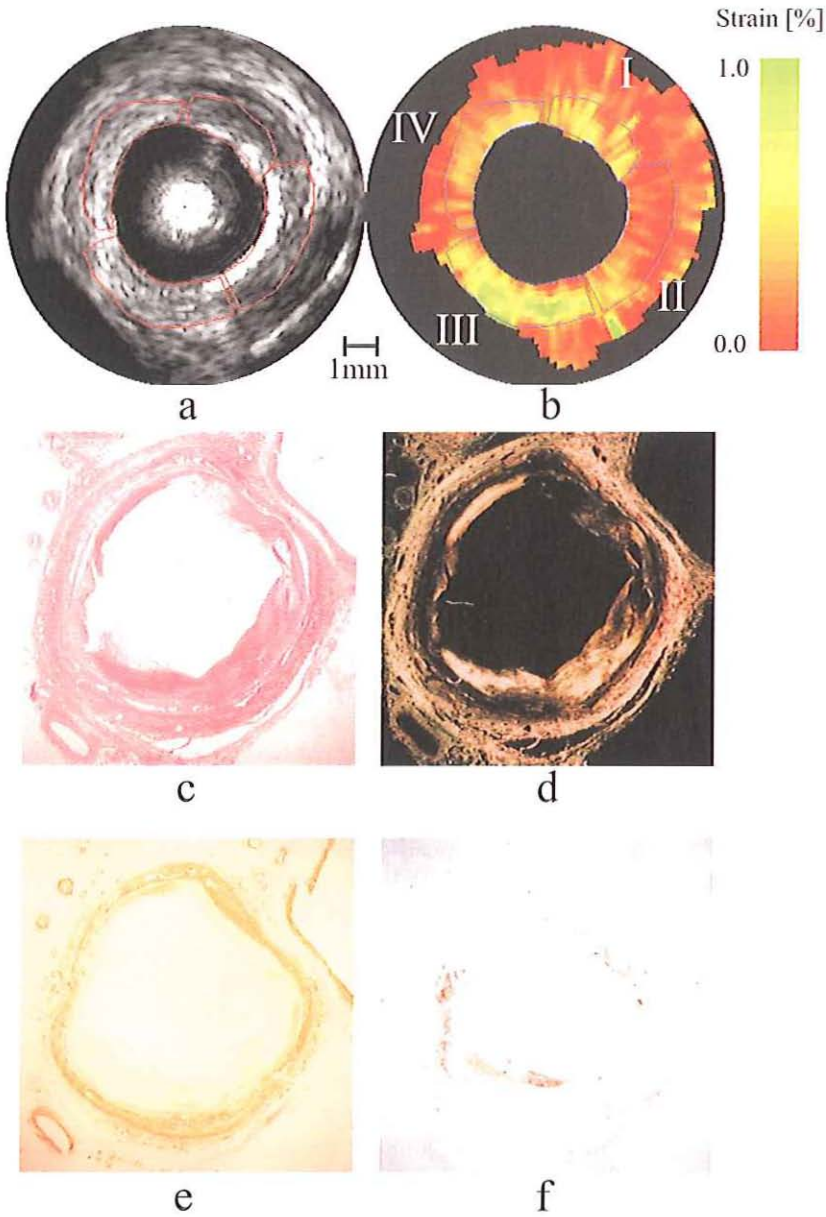

Figure 8.4 Intravascular echogram (a) and elastogram (b) of a diseased human femoral artery with the corresponding histology: (c) Picro-Sirius-red, (d) polarised light microscopy of picro-Sirius red (e) anti-Alpha actin and (f) anti CD-68 antibody. The echogram shows a concentric plaque with different echogenicities for the regions. The elastogram reveals two soft regions (Region I and region III) and two harder regions (region II and IV). The histology reveals that the two soft regions contain fatty material and the two harder regions mainly contain fibrous material (c,d & e). The macrophage concentration is also increased in the soft regions (f).

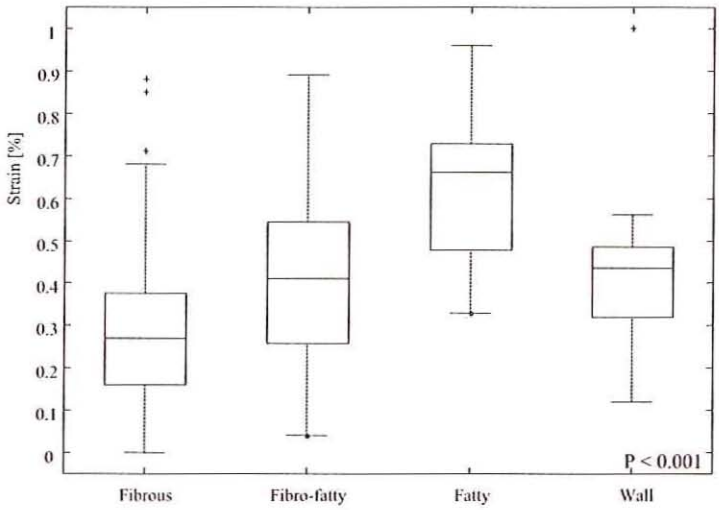

Figure 8.5 Box and whisker plot of the four tissue types. The boxes have lines at the lower quartile, median, and upper quartile values. The whiskers are lines extending from each end of the box to show the extend of the data. The plot reveals a difference between the three plaque types. A highly significant difference between the groups is found using the Kruskall-Wallis test.

intensity did not differ between fibrous and lipid rich tissue implying that regions that could be demarcated within the elastogram could not be identified in the still frame IVUS echogram by eyeballing. A tendency for higher echogenicity within the normal arterial wall is observed.

8.4 Discussion

The composition and morphology of the atherosclerotic lesion rather than the degree of stenosis is currently considered an important determinant for clinical complications (Lee & Libby, 1997; Richardson et al., 1989; Loree et al., 1992; Lendon et al., 1991; Moreno et al., 1994). Imaging modalities capable of characterising the tissue of the atherosclerotic lesion may help us to understand its natural history and detect lesions with high risk for acute events. The increased desire for knowledge on the course and mechanism of acute coronary occlusion has emerged since pharmaceutical lipid lowering strategies have shown to impair the incidence of cardiac related events (Jukema et al., 1996; Cobbaert et al., 1997).

Table 8.3 Echo intensity for the different plaque types and normal vessel wall.

	Echo-intensity	Upper & Lower quartiles	Number
Fibrous tissue	22.6	17.8-32.3	48
Fibro-fatty tissue	26.4	17.4-31.9	25
Fatty tissue	23.0	13.6-42.1	7
Normal vessel wall	33.8	27.0-39.1	16
	test p= 0.992	total number of regions	95

In this study, the characterisation capabilities of intravascular elastography were investigated. 95 regions were selected from 35 cross-sections in 9 arteries based on their elastographic (strain) values. After ultrasound imaging, the dominant tissue type in these regions was determined by immuno-staining. The principal findings in this study were:

1. In human femoral artery specimen, the elastogram is capable of demarcating regions within the plaque representing differences in strain whereas in the still frame IVUS image these regions could not be discriminated.

2. These differences in strain as observed within the elastogram were associated with differences in tissue types: lipid rich regions revealed significant higher strain values compared with fibrous rich regions.

The result of this study demonstrates that characterisation of different plaque components is feasible with intravascular elastography. A great advantage of this technique is that it is based on clinical available instruments. This in contrast to other imaging techniques capable of characterising plaques such as optical coherence tomography (Brezinski et al., 1997), angioscopy (Feld et al., 1996; Thieme et al., 1996) and Raman spectroscopy (Römer et al., 1998) that still have to be developed for *in vivo* applications. The data processing now performed off-line still has to be implemented in the echo apparatus. For an elastogram, only two IVUS echograms are required, obtained at two different intraluminal pressures. *In vivo*, different pressures are already present due to the pulsation of blood. This implicates that with only a pressure sensor and an IVUS catheter all tools for *in vivo* intravascular elastography are available. Thus, IVUS imaging is a technique capable of providing both qualitative as well as quantitative information of the atherosclerotic lesion.

The information in the elastogram is in principle independent of the echographic information (de Korte et al., 1998c),(Chapter 3). This is an important feature, since characterisation of fibrous, fibro-fatty and fatty plaques based on the echogram only is limited (Potkin et al., 1990; Yock & Linker, 1990). In this study, no significant difference between the average echointensity for the three tissue types was observed. In figure 8.4, region III and IV have similar echointensities but the elastogram reveals that region IV is hard and region III is soft. The histology corroborates these elastographic findings since region III is mainly fatty and region IV is fibrous.

The measured average strain values were converted to a pressure strain modulus (Chapter 6). The pressure-strain modulus of fibrous tissue (493 kPa) is approximately two times the pressure-strain modulus of fatty tissue (202 kPa). The pressure-strain modulus of mixed plaques has a value in between these two values (324 kPa). Although these values are higher than the static stiffness as measured by Lee et al. (1992), the ratio between the modulus of the two groups is similar. It has to be noted that the different elastic moduli are highly dependent on the different measuring techniques (static, dynamic, circumferential, tangential etc) and experimental methods. For fatty tissue, the mechanical properties are related to the cholesterol monohydrate concentration (Loree et al., 1994b).

8.4.1 Detection of vulnerable plaque

The primary aim of this study was to evaluate the capability of intravascular elastography to characterise different plaque components. In patients suffering from cardiovascular disease, plaque morphology is related with clinical presentation. Atherosclerotic plaques observed in patients suffering from unstable angina and myocardial infarction have features associated with local thrombus formation due to plaque rupture. The classical vulnerable plaque consists of a thin fibrous cap overlying a large atheroma with local inflammatory response beneath the surface of the cap. The present study shows that IVUS elastography is able to differentiate between lipid rich and fibrous tissues within the plaque. In addition, a thin fibrous cap is less able to bear the circumferential stress applied on it with subsequent strain increase on the elastogram. Destruction of the collagen fibers by local inflammation may further weaken the cap and reflect additional strain increase on the elastogram. Thus, theoretically not only the lipid mass but also cap thickness and local inflammatory response (Figures 8.3 and 8.4) may be reflected within the elastogram which makes it potentially a powerful tool to visualise the vulnerable lesion. Future validation studies are necessary to support this postulation.

8.4.2 Limitations of the study

The elastographic experiments are performed in a watertank at room temperature. The intraluminal pressure is applied with a water column system connected to the proximal side of the arteries. The pressure is monitored at the distal side. A stable pressure was only achieved if all sidebranches of the arteries were perfectly closed. In some specimen, a total closure of all branches was not possible. Leakage of the intraluminal saline solution resulted in a pressure drop and finally in a pressure differential less than 20 mmHg. A pressure differential smaller than 20 mmHg leads to smaller strains. This increases the variance of the strain estimate for all three plaque type groups.

The elastographic measurements have been performed in a watertank at $21°C$ whereas *in vivo* measurements are being performed at $37°C$. Since the mechanical properties of the tissue in the arterial wall is likely to be different at $21°C$ as compared with $37°C$, which is particularly the case for lipid cores, this temperature drop may bring forth inaccuracy of the measurements presented. However, above $20°C$ fatty tissues tend to melt (Lundberg, 1985) and this will increase the difference between this tissue type and fibrous tissues.

The elastograms were matched to the histology using the IVUS echogram. Although the correlation between histology and IVUS echograms was already demonstrated by many studies (Nishimura et al., 1990; Potkin et al., 1990; van der Lugt et al., 1995; Gussenhoven et al., 1996, 1989), matching of the IVUS and histologic sections was not possible in all cases. Especially matching of cross-sections with concentric plaque with a lack of calcified areas was impossible in some cases. In the staining process, the position of the marker was not always identifiable in the histologic sections. However, exclusion of segments occurred without knowledge of the elastogram. Thus the present observations may not be a result of selection bias.

This study was performed on excised femoral arteries. The specimens were frozen after excision and thawed just before the ultrasound measurements. Freezing and thawing tissue has no significant influence on the acoustical properties of the tissue (van der Steen et al., 1991). Gow and Hadfield (1979) clearly showed that both the static and dynamic

elastic moduli of arteries were elevated after excision and that further increases may occur following cold storage. However, excision of the arteries and freezing the specimens before the ultrasound experiments will effect the results badly when it has different influence on the different tissue components. Since this method will be evaluated *in vivo*, the effect of excision and freezing can be investigated.

The study was performed in atherosclerotic femoral arteries. It is unknown whether these findings are applicable to the coronary circulation. However, previous studies showed that plaque morphology within the femoral artery resembles atherosclerotic lesion types as observed in coronary arteries (Pasterkamp et al., 1998, 1999).

8.4.3 Advancing intravascular elastography to *in vivo* applications

As already discussed, different pressure levels are normally present in human circulatory system. In this study, the two echograms are acquired at 80 and 100 mmHg. These pressures are in the range of the normal coronary pressure. Using time gated data acquisition, datasets at different pressure levels can be acquired, which can be used to determine elastograms.

Especially in coronary arteries, IVUS catheters will move in the lumen due to the contraction of the heart. Not only movements in the plane of the cross-sections will occur but also movements along the long axis of the vessel. This movement along the axis of the vessel will introduce errors that can not be corrected for since data from different parts of the artery will be acquired. However, initial measurements in human coronary arteries *in vivo*, revealed that the motion of the catheter in the lumen is minimal near end diastole while maintaining a pressure differential large enough to strain the tissue.

8.5 Conclusions

Intravascular elastography is a new technique that assesses the local mechanical properties of the vessel wall and plaque. The three plaque components fibrous, fibro-fatty and fatty tissue result in different mean strain values. Fibrous tissue has lower strain values than fibro-fatty tissue and the latter one has lower strain levels than fatty tissue. Identification of the three tissue types based on the average echo intensity was not possible. These results demonstrate the potential of IVUS elastography to identify rupture prone plaques.

Chapter 9

IVUS Elastography of Human Coronary Arteries *in vivo*

abstract

Background. *The composition of the plaque is a major determinant of coronary related clinical syndromes. In vitro experiments on human femoral arteries have demonstrated that different plaque types were detectable with intravascular ultrasound elastography. The aim of this study is to investigate the feasibility to apply intravascular elastography during interventional procedures in the catheterisation laboratory.*

Methods and results. *Data were acquired in three patients with stable (n=2) and unstable (n=1) angina pectoris with an EndoSonics InVision echoapparatus equipped with an rf-output. The systemic pressure was used to strain the tissue. This strain was determined using crosscorrelation analysis of sequential frames. A likelihood function was determined to obtain the frames with minimal motion of the catheter in the lumen. Motion of the catheter prevents reliable strain estimation. Minimal motion was observed near end-diastole. Reproducible strain estimates were obtained within one pressure cycle and over several pressure cycles. Validation of the results was limited to the information provided by the echogram.*

Conclusion. *In vivo intravascular elastography is feasible. Additional signal processing and acquisition schemes are required to correct the artefacts due to the motion of the catheter.*

9.1 Introduction

There is a great variation in stability of coronary atherosclerotic plaques. When coronary flow is limited by plaque, patients develop angina, which can be stable for years. However, disruption of coronary plaques with superimposed thrombosis is the main cause of acute coronary events, such as unstable angina pectoris, sudden coronary death and acute myocardial infarction (Falk, 1991; Fuster et al., 1992; Fuster, 1994; Kragel et al., 1991). There are two major mechanisms underlying plaque disruption (Burke et al., 1997; Davies, 1996): rupture of a fibrous cap of a lipid-rich plaque (Falk et al., 1995) and

based on the publication: "Combined assessment of morphologic and mechanic information of coronary ateries: a feasibility study *in vivo*" by Chris L. de Korte, Stephane G. Carlier, Frits Mastik, Anton F.W. van der Steen, Patrick W. Serruys and Nicolaas Bom. *Circulation*: to be submitted; 1999

denudation and erosion of the endothelial surface (Farb et al., 1996; Fishbein & Sighel, 1996).

It is now widely accepted that the propensity of a lesion to rupture is poorly predicted by coronary angiography (Lee & Libby, 1997; Falk et al., 1995). A major problem is that vulnerability of plaque is not directly related to plaque size (Topol & Nissen, 1995; Ambrose et al., 1988; Fishbein & Sighel, 1996) but that the plaque composition is a major determinant (Davies, 1996; Lee & Libby, 1997). Using intravascular ultrasound, the geometry of lumen, plaque and vessel-wall can be obtained and is closely correlated to clinical angina (Hodgson et al., 1993). However, identification of the different plaque components is still limited (di Mario et al., 1992; Potkin et al., 1992) although some promising ultrasound based techniques are currently being developed (Barzilai et al., 1987; Bridal et al., 1997a, 1997b; Landini et al., 1986; Spencer et al., 1997; Wilson et al., 1994).

There is a wide range of techniques that have potential to visualise or characterise the plaque. Using scintigraphy, detection of plaque instability remained confined (Vallabhajosula et al., 1988; Lees et al., 1988; Miller et al., 1991). Other potential techniques may be magnetic resonance imaging (Merickel et al., 1993) or optical coherence tomography (Brezinski et al., 1997; Tearney et al., 1997). With spectroscopy, certain plaque components may be detectable (Toussaint et al., 1994) as well as with angioscopy (Feld et al., 1996; Thieme et al., 1996) and Raman spectroscopy (Brennan III et al., 1997; Römer, 1999). Promising new techniques are electrical impedance imaging (Bouma, 1998) and thermal examination (Casscells et al., 1996) of plaque surfaces since positive correlation between plaque vulnerability and parameters obtained using these techniques were found.

The main disadvantage of the techniques described above is that plaque vulnerability is associated to indirect parameters like plaque geometry, content, colour or temperature although plaque vulnerability is mainly a mechanical phenomenon: using computer simulations, concentrations of circumferential tensile stress were more frequently found in unstable plaque than in stable plaques (Cheng et al., 1993; Richardson et al., 1989). For example, a thin fibrous cap shielding a lipid core from the blood may rupture since it is unable to bear the high circumferential stress due to the pulsating blood pressure. These high stress regions can be caused by the geometry of the plaque (Loree et al., 1992; Richardson et al., 1989) or by local weakening of the plaque due to macrophage infiltration (Lendon et al., 1991).

In 1991, a new technique was proposed to directly measure mechanical properties of tissue by ultrasound called elastography (Ophir et al., 1991). This technique was developed using phantom studies (Céspedes, 1993a) and evaluated *in vivo* (Céspedes et al., 1993b). The underlying principle is that tissue is strained and that the strain rate is related to the local mechanical properties. The local strain of the material is obtained by means of comparing several ultrasound images. Currently, this technique is developed for intravascular purposes (Chapters 3 and 7),(Ryan & Foster, 1997b; Shapo et al., 1996b) and was recently applied on human femoral arteries *in vitro* (Chapter 8). These experiments revealed that the local strain as measured with intravascular elastography is significantly different for fibrous and fatty plaque components. Furthermore, this technique showed potential to identify plaque vulnerability. Since the radial strain is obtained, the technique may detect regions with elevated stress: an increased circumferential stress will result in an increased radial strain of the material (de Korte et al.,

1998b).

In this study, the feasibility to obtain elastographic images *in vivo* has been investigated. Using data obtained from coronary arteries, elastograms were determined. The pulsatile intracoronary pressure was used to obtain different levels of strain in the arterial wall. Since the catheter was moving in the lumen due to the contraction of the heart, an algorithm to determine the echo frames with minimal motion arterfacts was applied on the data.

9.2 Patient description

Intravascular ultrasound (IVUS) data was obtained in three patients referred for percutaneous coronary intervention with stable (n=2) or unstable angina pectoris (n=1). All the patients signed an informed consent. The culprit lesions to be treated were situated in the left anterior descending artery (n=2) and the right coronary artery (n=1). After intravenous administration of 10,000 IU heparin and 250 mg acetylsalicylic acid, a 6 Fr. guiding catheter was advanced up to the ostium of the involved artery. After coronary injection of a bolus of 3 mg isosorbide dinitrate, pre-intervention IVUS assessment of the lesion was performed with a MegaSonics® (EndoSonics, Rijswijk, The Netherlands), a combination device consisting of an angioplasty balloon (3.5 mm diameter, length 20.0mm) and a 64 F/X array IVUS transducer proximal to the balloon. Lesions were crossed and imaged without complication. While the non-inflated balloon was crossing the lesions, the absence of ischemia and angina permitted the search for a stable position of the transducer in the center of the lumen offering the visualisation of a significant plaque. The rf data were acquired as described below. The pressure was measured at the level of coronary ostium via the guiding catheter connected to a standard fluid-line system (Ohmeda, Bilthoven, The Netherlands). (Ohmeda).

9.3 Methods

The 64 element phased array catheter with balloon was connected to an EndoSonics InVision system. The system is equipped with an analog radio frequency (rf) data output. This output provides the data used for making a ChromaFlo^{TM} flow mode image. In this mode, the catheter operates in linear instead of phase array mode thus providing low resolution images (Borsboom et al., 1999). Each frame contained 64 angles containing an rf-signal of $10\mu s$ (corresponding to 7.5 mm). These data were digitised in a custom-made acquisition system, containing a Pentium computer with a acquisition board (Signatec, Corona, CA, USA) with 128Mbyte to store the rf data at a sampling rate of 200 MHz in 8 bits.

10 frames per second were acquired at cross-sections where the IVUS echogram revealed diseased vessel wall and plaque. For determination of the strain, crosscorrelation techniques were applied to the data. First the movement of the tissue along the ultrasound beam was determined. The local strain was obtained from this displacement. Due to the contraction of the heart, the catheter will move in the lumen. For large motion, the frames acquired at the different intraluminal pressures may be misaligned thus hindering adequate displacement estimates.

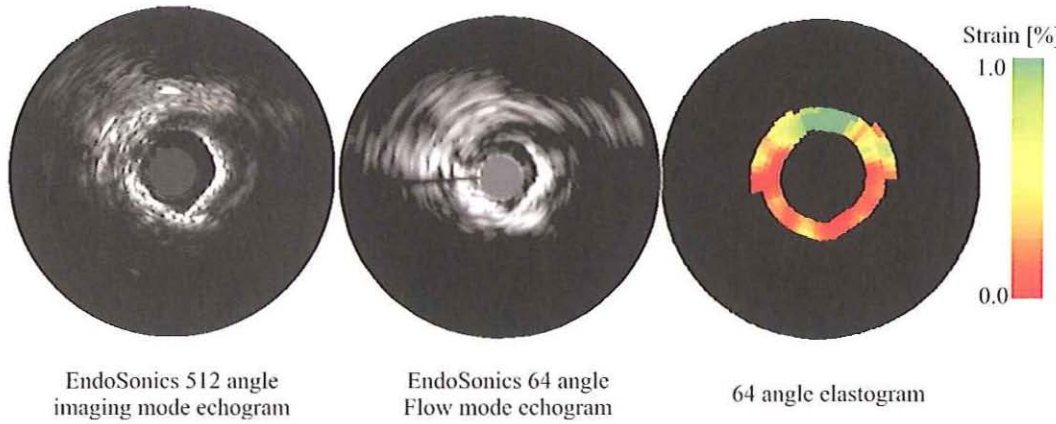

Figure 9.1 Echogram (acquired in image and ChromaFlo mode) and elastogram of cross-section in the LAD. The echogram *(left)* reveals calcified material between 1 and 9 o'clock. The elastogram shows low compression in this area and high compression in the remaining region (between 9 and 1 o'clock).

An algorithm to determine the similarity between sequential echo frames is used as a figure of merit for the motion of the catheter in the lumen. The normalised absolute difference between two sequential echo frames is determined using the likelihood between the frames. Next these values were scaled between 0 and 100%. 0% corresponds to no similarity between the frames and 100% means that both frames were exactly the same. Sequential frames with a high likelihood and a pressure differential large enough to results in strain levels on the order of 1% are taken to calculate the elastograms.

9.4 Results

In figure 9.1, two echograms and an elastogram are presented. The data is acquired near end-diastole from patient 1. The left echogram is the original echogram as produced using the EndoSonics InVision system. The echogram reveals a highly calcified wall between 1 and 9 o'clock. The region between 9 and 1 o'clock contains no calcified material. The low resolution echogram in the middle is the echogram determined directly from the rf-data. Since the rf-data is acquired in ChromaFlo^{TM} mode, only 64 angles are available at low resolution. The elastogram (Fig. 9.1 *left*) shows very low strain values between 1 and 9 o'clock corresponding to the calcified area. The region between 9 and 1 o'clock has high strain levels, indicating soft material in this region.

The reproducibility of the technique *in vivo* is illustrated in figure 9.2. The echogram of this cross-section of patient 2 shows a eccentric plaque between 3 and 9 o'clock. At 8 o'clock, a calcified deposit is visible in the plaque. The pressure curve is plotted together with the likelihood curve. Relating the likelihood curve to the pressure curve reveals that the sequential frames have the best match near end-diastole which corresponds well to the absence of movement and contraction in this phase of the heart cycle. As can be appreciated, the pressure differential between frames at this point in the pressure curve is in the order of 5 mmHg. This pressure differential is large enough to strain the vessel wall and plaque between 0 and 1%. Over the five cycles the elastograms have a

similar appearance. The arterial wall between 9 and 3 o'clock has moderate to high strain levels. At 3 o'clock, erroneous strain estimates can be observed caused by not properly working transducer elements. This artifact was also visible when the ChromaFlo mode was activated. The plaque area between 3 and 7 o'clock has low strain estimates. The region corresponding to the calcified spot (as identified with the IVUS echogram), has very low strain values.

Data from patient 3 is presented in figure 9.3. The pressure curve shows a diastolic pressure of 105 mmHg and systolic pressure of 135 mmHg. The pressure curve is plotted together with the curve representing the resemblance between the sequential echo-frames. Again it can be observed, that during systole the resemblance between the frames is small and that near end diastole the similarity between frames is high.

The IVUS echogram (upper right corner) reveals a concentric plaque in this artery. The echogenicity of the plaque is lower than the echogenicity of the wall distal to it. A strong reflection of the lumen - plaque boundary is observed between 4 and 8 o'clock. Between 11 and 1 o'clock the echogenicity is low and the thickness of the plaque is small.

Three frames near end diastole were taken to determine two elastograms. The pressure differential between sequential frames is 3 - 4 mmHg. Both images indicate that the region between 11 and 2 o'clock has high strain values indicating soft tissue. The region at 3 o'clock is relatively hard. The region between 3 and 6 o'clock has intermediate strain values at the lumen vessel wall boundary and high strain levels distal to this region. The region between 6 and 11 o'clock has low strain values. The similarity between the 2 frames is high, indicating that the determination of the strain values in one pressure cycle is reproducible.

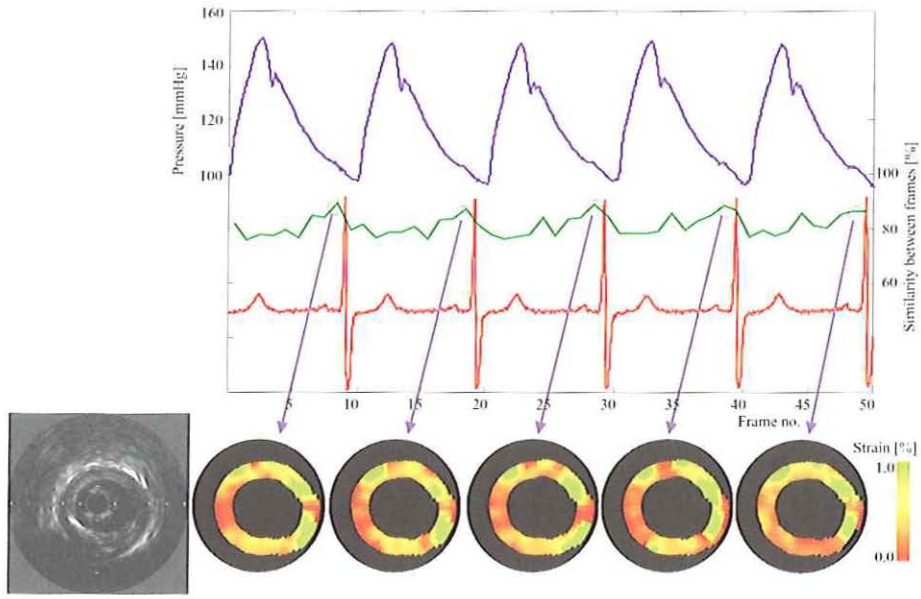

Figure 9.2 Reproducibility of the elastographic acquisition over several pulsations. The likelihood curve reveals that the catheter motion is minimal near end diastole. At this phase of the heart cycle there is still a pressure differential between sequential frames. The region at 3 o'clock produces erroneous strain estimates due to malfunctioning catheter elements.

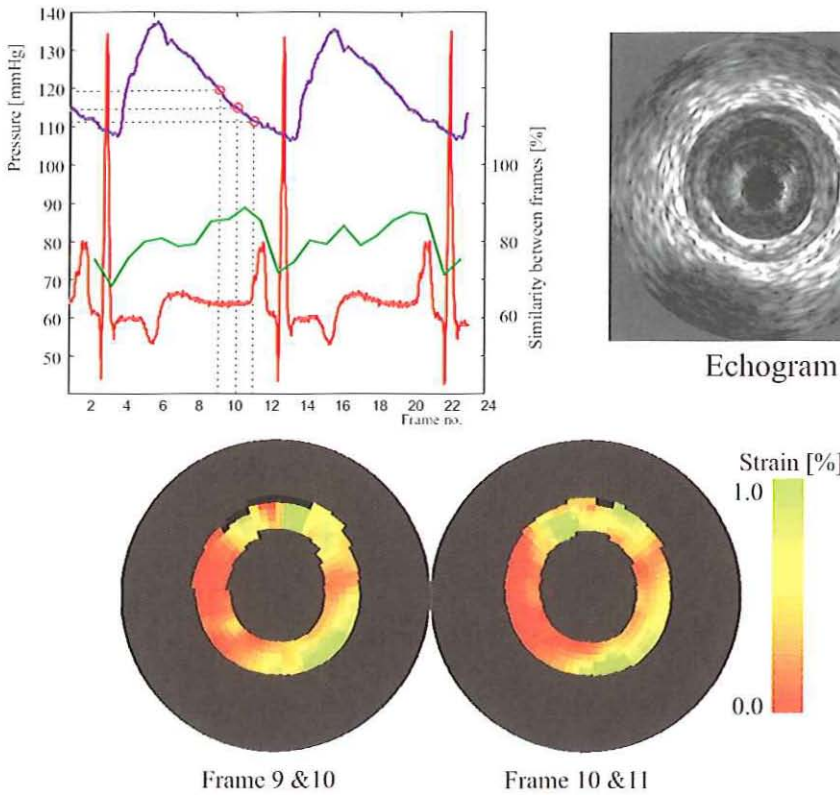

Figure 9.3 Reproducibility of the elastographic acquisition in one pressure cycle. 3 frames near end-diastole with a large likelihood were taken. The pressure differential between sequential frames is 3 to 4 mmHg. The IVUS echogram reveals a concentric plaque. The elastogram reveals soft regions between 12 and 2 o'clock and between 4 and 6 o'clock. This information was not found from the echogram.

9.5 Discussion

Identification of plaque vulnerability is crucial. Currently, there is no clinically available tool for a reliable detection of vulnerable plaque. Elastography is a promising technique, capable of assessing the local mechanical properties of the vessel wall and plaque (Chapter 8): *in vitro* experiments demonstrated that strain values obtained with intravascular elastography differ significantly for fibrous and fatty plaque components. It was even shown that fatty regions with an increased macrophage activity could be identified using the elastogram.

In this study, *in vivo* elastograms of diseased human coronary arteries are presented. Contrary to a previous *in vitro* study (Chapter 8), a dynamic instead of static pressure differential is used to strain the tissue. The advantage is that this excitation source is already present in the arterial system. Using gated acquisition, different levels of intravascular pressure were obtained. These preliminary results indicate that reproducible elastograms can be obtained using this acquisition scheme.

Compared to the *in vitro* study, the pressure differential between the two frames is

smaller: 3-4 mmHg instead of 20 mmHg. A smaller pressure differential will immediately result in lower strain values. However, the strain values found in this *in vivo* study were in the same range as the strain values found in the *in vitro* study indicating that the tissue in this study is softer. A possible explanation is that the elastic moduli of tissue will be elevated after the tissue is excised (Gow & Hadfield, 1979) and may even further increase after cold storage. Additionally, since the *in vitro* study was performed at room temperature, fatty tissues will be harder than at body temperature (Lundberg, 1985) resulting in decreased strain values.

Another potential source to strain the tissue is a compliant angioplasty type of balloon with the transducer in the balloon as proposed by Shapo et al. (1996b). Although the motion artifacts due to the contraction of the heart are minimised, this technique has several disadvantages (interruption of the blood flow, non-radial expansion of the artery when the lumen is not circular, movement of the transducer in the balloon due to inflation of the balloon).

Contrary to the *in vitro* validation study, a phased array transducer, used every day in our catheterisation laboratory for clinical purposes, was used for the data acquisition. This monorail catheter presents better manageability than a single element catheter and no artifact from the guide wire. Moreover, the use of an array catheter removes the artifacts due to non-uniform rotation. Therefore, 2-dimensional instead of 1-dimensional crosscorrelation techniques might be applied to determine the strain values. These techniques are currently being implemented. In principle 2-dimensional crosscorrelation technique are more robust and should lead to more reliable strain estimates.

9.5.1 Limitations

A major problem of advancing intravascular elastography to cardiac *in vivo* applications is the acquisition of data in a pulsating artery located near a contracting muscle of the heart. The catheter will move in the lumen and this will result in a mismatch of the data acquired at the low and high pressure. Correct strain estimates are only obtained when the two echoframes (at low and high pressure) image the same cross-section. This study revealed that the motion of the catheter is minimal near end-diastole in the relaxed phase of the cardiac cycle. However, useful data was not obtained during all measurements. In some cases the motion was still to large even near end-diastole. A possible solution for this problem is to obtain data during the inflation of the angioplasty balloon at the tip of this newly available catheter containing an IVUS transducer proximally. By inflating the balloon the position of the transducer is fixed in the artery. Additionally, improved signal processing tools can be applied to increase the robustness of the method.

The elastograms presented in this study could not be validated using histology. Therefore, the elastographic findings were compared with the echographic findings. For detection of calcified regions and revealing the geometry of the plaque and vessel wall, IVUS echograms has proven to be a useful tool (Nishimura et al., 1990; Potkin et al., 1990; van der Lugt et al., 1995). However recent studies revealed that the correlation between echogenicity and fibrous, fibro-fatty or fatty plaque components is low. (Potkin et al., 1990; Yock & Linker, 1990),(Chapter 8). Additionally, IVUS echograms present limited information for the detection of microcalcification accumulation (Friedrich et al., 1994). Therefore, no validation of the high strain regions in the elastograms was performed. Validation of the elastographic findings could be performed using a directional atherec-

tomy device. However, the resolution of such a device is low, implicating that only large plaque areas could be validated. Validation of small spots would need a system that is able to determine the tissue type with a higher resolution. The current developments in optical coherence tomography (OCT) (Brezinski et al., 1997) and Raman spectroscopy (Römer et al., 1998) may allow to perform such validation of intravascular elastography *in vivo*.

9.6 Conclusions

It is feasible to apply intravascular elastography *in vivo*. Using the pulsatile pressure as a mechanical stimulus, different strain levels were measured for different tissue components. Additional signal processing techniques and validation are needed to improve the reliability of the technique

Chapter 10

Discussion and Conclusions

10.1 Discussion

Intravascular ultrasound elastography is a new imaging technique that allows visualisation of the mechanical properties of vascular tissues. The technique is based on the principle that the response of tissue to a mechanical excitation is a function of its mechanical properties (Ophir et al., 1991). During intravascular experiments, the mechanical stimulus can be applied from within the lumen. The systemic pressure continuously strains the tissue and thus can act as mechanical stimulus. Another potential source can be an angioplasty type balloon (Shapo et al., 1996b). The latter source has the advantage that the stimulus is more controllable, however, the blood flow is interrupted by this device.

For intravascular experiments, the radial component of the strain (i.e., the component along the ultrasound beam) is measured. The softer the tissue under investigation, the higher the strain will be. This strain is measured using ultrasound. Pressures applied on the tissues are in the range between 80 and 140 mmHg and are large enough to strain the tissues on the order of 0 to 5%. It is extremely challenging to measure these strain levels using conventional echograms. Therefore, high frequency rf-signals are used to determine the strain.

10.1.1 Phantoms

As an initial phase of this study, the feasibility of the technique was investigated by phantom studies. In ultrasound imaging, agar and gelatin based materials are often used since these materials have similar acoustic properties to biological tissue. However, little knowledge was present of the mechanical properties of these materials. Therefore, a study was performed to determine these properties. It was concluded that the compression modulus of these materials could be easily adjusted by varying the agar concentration. The gelatin concentration was fixed since increasing this concentration increased the acoustic attenuation of the material dramatically. The compression modulus of these materials was highly dependent on the temperature and age. Since the temperature is of large influence, it has to be well controlled during the experiments.

The feasibility of intravascular elastography was tested using vessel-mimicking phan-

toms. The results of these experiments revealed that hard and soft material could be identified independently of the echogenicity contrast. In other words, lesions that could not be detected in the echogram were identifiable in the elastogram. Although the results of this study demonstrated that intravascular elastography is feasible, some limitations became apparent. The strain in a vessel wall decays radially. Since this decay can be described theoretically, correction for this artifact is possible. Another phenomenon that was found is the "mechanical shadow". Soft tissue distal to hard tissue is difficult to detect using the elastogram. Correction for this type of artifact could be feasible using finite element modelling.

10.1.2 Femoral arteries *in vitro*

The first intravascular elastograms of human femoral arteries *in vitro* were acquired with a modified IVUS catheter: the original flexible axis was replaced by a rigid tube to minimise rotational artifacts. These experiments revealed that the strain in fibrous plaque was smaller than the strain in calcified plaque. This finding was in accordance with literature, since reported compression modulus values for calcified tissue are 3 to 4 times higher than the compression modulus of fibrous material.

Encouraged by the results of this preliminary study, an *in vitro* study on a larger scale was performed. This time, the original DuMED Princeps® catheter with flexible axis was used since the performance of the motor unit responsible for the rotation of the transducer was increased. This study revealed that significant differences for the strain are present in fibrous, fibro-fatty and fatty plaque components ($p < 0.001$). The echointensity in this three plaque types was not different ($p = 0.992$). Although differentiation between fibrous and fatty materials seems feasible with elastography, the sensitivity and specificity of the technique have not been tested yet. These results indicate that intravascular elastography has the potential to detect plaque vulnerability since vulnerability of plaque is highly associated with a large lipid core and a thin fibrous cap. Furthermore, vulnerability of plaque is highly related to high stress concentrations: a thin or locally weakened cap is unable to bear the stress of the pulsatile pressure imposed on it and will rupture. A high stress concentration results in increased strain values that may be detectable with elastography.

10.1.3 Coronary arteries *in vivo*

The technique was advanced to *in vivo* coronary applications. In these experiments the systemic pressure was used as the mechanical stimulus. Using time gated acquisition, frames at different intraluminal pressures were acquired. Dedicated algorithms were developed to overcome motion artifacts that were associated with the contraction of the heart. Preliminary results demonstrate that the developed acquisition scheme gives reproducible strain estimates. Validation of these *in vivo* elastograms was performed using the IVUS image that could only identifies regions as being calcified or non-calcified.

10.2 Limitations

This study revealed the potential of intravascular elastography to characterise different plaque components *in vitro*. Additionally, the technique *in vivo* was demonstrated. However, the results identified several limitations of this study.

10.2.1 Motion artifacts

A major problem to be solved during the whole project was to minimise motion artefacts. The described technique correlates two frames, acquired at different intraluminal pressures. Reliable strain estimates are only obtained when signals from the same region of tissue are correlated. During the *in vitro* studies and especially during the preliminary *in vivo* studies, motion related phenomena were always present. The first phantom experiments used the Princeps® catheter. A single element transducer in this catheter is rotated by means of a flexible axis. This axis consists of two counter-winded springs. Due to the resistance of this axis in the catheter, rotational artifacts at the transducer can be present (ten Hoff et al., 1989). These rotational artifacts resulted in a misalignment of the echoframes and concomitant decorrelation effects. Angle matching algorithms had to be developed to cope with this artifact. During the *in vitro* studies on diseased femoral arteries, motion artifacts occurred with the pressurisation of the specimen. An increasing intraluminal pressure often resulted in a rotation and/or translation of the artery with respect to the transducer. Again, angle matching algorithms were applied to correct for the rotation artifact. However, correction was only partly feasible when a combined translation and rotation artifact was present. In these cases, the tissue moved to another part of the beam resulting in decorrelation effects.

Especially during the *in vivo* experiments in human coronary arteries, motion artifacts were present. Due to the contraction of the heart, the catheter was moving along the long axis of the vessel. Since different cross-sections were acquired due to this motion, correlation of the signals was not possible. Therefore, echo frames representing the same cross-section had to be identified while still having a sufficient large pressure differential. Preliminary experiments revealed that useful frames could be acquired near end-diastole. In this phase of the heart cycle, the catheter is at a relatively stable position while the pressure differential between frames is in the order of 5 mmHg. However, not in all experiments sequential frames, imaging the same cross-sections, were found. Additional experiments and dedicated signal processing techniques have to be developed to advance intravascular elastography to a more robust and reproducible technique.

10.2.2 Real-time implementation

Intravascular elastography is still an off-line technique. Currently it takes 5 to 10 minutes to compute an *in vivo* elastogram. For evaluation of the technique, this time is reasonable but for clinical evaluation the processing time has to be reduced. Intravascular palpation determines the strain in a significant part of the vessel wall and plots the strain information at the lumen vessel wall boundary. Since only 1 strain value per angle is determined, the technique is computationally less demanding and due to the limited information is also more robust. In other words, the technique has more potential to be implemented in real-time on short notice. The use of a phased array transducer diminishes rotational

artifacts and allows the use of 2-dimensional correlation techniques. Although these techniques are computationally more intensive, the robustness of the technique will increase significantly. As a result, the need for correction algorithms is reduced. Since the algorithms used for calculating the strain information are closely related to the algorithms to determine the flow, real-time implementation should be possible. Currently, InVision echo equipment (EndoSonics, Rijswijk, The Netherlands) is already equipped with real-time flow imaging (ChromaFlo^{TM}), although this technique is computationally less demanding.

10.2.3 Quantification of mechanical properties

Using the strain values measured with the presented technique, the compression modulus of the tissue can be determined. However, the compression modulus is highly dependent on excision of the tissue, method of storage (freezing or at $4°C$) and the temperature ($20°C$ or $37°C$). In this way, it is difficult to determine accurately quantitative values for the compression modulus using *in vitro* experiments. The *in vitro* study was performed at room temperature on excised tissue after freezing of the specimens. The only way to measure the true compression modulus is measuring *in vivo*. Since validation of the preliminary *in vivo* experiments is not performed yet, quantitative values of the compression modulus of vascular tissue are still unknown

Additionally, the compression modulus is dependent on the way it is measured. The static compression modulus is different from the dynamic modulus. Since the *in vitro* experiments were performed using a static pressure differential and the *in vivo* experiments used the dynamic systemic pressure, different values for the compression modulus were expected. According to studies of Lee and co-workers (1992, 1991), higher values for the dynamic compression modulus (measured in the frequency range 0.5 to 2 Hz) than for the static compression modulus were expected. In the experiments described in this thesis, similar strain values were found in the static and dynamic experiments, although the pressure differential was 4 to 5 times lower during the dynamic experiments. This indicates that in our experiments the dynamic compression modulus has lower values than the static compression modulus. However, since excision and freezing the specimens increases the compression modulus (Gow & Hadfield, 1979), quantitative comparison between the compression moduli acquired during *in vivo* and *in vitro* experiments remains limited. The dynamic compression modulus also depends on the frequency of the force applied on the tissue: Lee and co-workers (Lee et al., 1991) found a significant positive correlation between frequency and storage modulus of atherosclerotic lesion lipid pools. The storage modulus increased 10% when the frequency went up from 0.1 to 3 Hz. This in contrast to our phantom experiments (Fig. 2.2) where we found no dependence of the compression modulus on the frequency of vibration. This contrast may be associated with tissue viscosity.

However, in all studies (Lee et al., 1992, 1991), the ratio between the compression modulus of fibrous and calcified tissue had the same value, independent of static or dynamic excitation and independent of the excitation frequency. The different moduli measured with elastography are useful since the ratio between different materials can be used to characterise different plaque components.

10.2.4 Inverse problem

In principle, a strain elastogram gives a artifactual image of the Young's modulus distribution. Therefore, the elastogram cannot directly be converted to an image representing the Young's modulus. Especially in intravascular applications were boundary conditions are sparsely defined (for example the moving and contracting heart), reconstruction of the Young's modulus is challenging. However, since the thickness of the arterial wall is relatively small, reconstruction of the Young's modulus may not be necessary.

A difficult geometry is soft tissue behind hard material: mechanical shadowing will occur (de Korte et al., 1996). The hard material is bearing all the stress that is applied on the tissue and, consequently, the soft tissue will strain less than expected. Additionally, imaging behind hard tissue like calcified material is already difficult since normally the ultrasound signal can hardly penetrate through calcified material. When fatty tissue is covered by a fibrous plaque, the strain in the fatty tissue is lower than expected. However, in relation to plaque vulnerability this mechanical shadow may reveal important information. If the fibrous cap is able to bear the stress, low strain values will be measured. If the cap is unable to bear the stress, high strain spots will appear. This information can be useful for the detection of vulnerable plaque.

10.3 Future directions

10.3.1 Minimising motion artifacts

Intravascular elastography has proven to be a technique capable of characterising different plaque components. However, the sensitivity and specificity of the technique have not been identified yet. An *in vitro* study on a large scale has to be performed to investigate these parameters. A phased array catheter would be the best choice for such a study since rotational artifacts are precluded and 2-dimensional crosscorrelation algorithms can be applied. The use of 2-dimensional crosscorrelation algorithms will improve the robustness of the technique.

For *in vivo* applications, motion artifacts can be minimised by using a balloon catheter. When the balloon is inflated, the position of the transducer is fixed with respect to the arterial wall. The MegaSonics catheter (EndoSonics, Rijswijk, The Netherlands) is a combined catheter with the balloon distal to the transducer. While the balloon is inflated, the systemic pressure is still straining the tissue, making this catheter suited especially for elastographic purposes. Additionally, inflation of the balloon results in a less eccentric position of the transducer in the lumen. This position will reduce the number of erroneous strain estimates. It has to be noted that the balloon only needs to be inflated with a low pressure to stabilise the position of the transducer.

In this study, the balloon was not inflated to stabilise the position of the catheter. The experiments revealed that motion of the catheter is minimal near end-diastole. Additional studies are required to investigate the use of these frames to obtain reproducible strain estimates. An advantage of a phased array transducer catheter as compared to a mechanical IVUS catheter is the possibility to use different firing schemes. In this way, scanning schemes can be adjusted to minimise the influence of motion of the catheter.

10.3.2 Potential clinical applications

The technique described in this thesis is evaluated *in vitro* and preliminary experiments were performed *in vivo*. Although the technique has proven its potential to identify different plaque components, the clinical usefulness *in vivo* was not demonstrated yet. In the future, IVUS elastography may be useful with regard to the following phenomena.

- **Elastography to choose the proper interventional technique.** The initial goal of this study was to determine the feasiblity of intravascular elastography to identify different plaque components. Knowledge of the composition and the mechanical properties of the plaque may be useful for the physician to choose the proper interventional technique (Baptista et al., 1996; Linker et al., 1991; Tobis et al., 1991). Moreover, since all interventional techniques are predominantly mechanical in nature, the outcome of the intervention is not only determined by the chosen technique but also by the mechanical properties of the vessel wall and plaque. Until now, mechanical information was not available. Studies have to reveal the usefulness of this information during catheterisation interventions.

- **Elastography in relation to vulnerable plaque.** Elastography certainly has potential to visualise vulnerability of plaque. A vulnerable plaque can be described by a large fatty pool with a thin fibrous cap overlying the fatty material or erosion of the intima by macrophage infiltration (Davies, 1996; Lee & Libby, 1997). Both these morphologies may be detectable with elastography as already demonstrated in chapter 8. The power of elastography is that the strain is measured and not a parameter related to the size (OCT, (Brezinski et al., 1997)), chemical composition of the material (Raman spectroscopy, (Römer et al., 1998)) etc. For example, it may not be necessary to know the thickness of the cap to determine if a plaque is vulnerable or not. The strain may be a direct indicator of the possibility of a plaque to bear a stress imposed on it. The potential of elastography to identify plaque vulnerability *in vivo* still has to be determined.

- **Strain imaging during PTCA.** A major problem of angioplasty and stenting is the development of restenosis in the artery: the arterial wall is responding to the intervention by forming new plaque that is obstructing the free lumen area. 6 months after the angioplasty, 20-40 % of patients develop restenosis and clinical angina (Serruys et al., 1998). 6 months after stent placement, 10-30 % of the patients develop restenosis (Serruys et al., 1998). Elastography may be a useful tool to investigate the relation between the chances for restenosis and the applied strain in the tissue during angioplasty and stent placement. For this application the transducer has to be placed in the balloon (Shapo et al., 1996b). Consequently, the balloon material must be transparent for ultrasound. Additionally the influence of the circular balloon on geometries with a non-circular lumen has to be investigated.

- **Elastography to guide brachytherapy interventions.** In brachytherapy (King III et al., 1998), the radiation interaction and the radioactive decay is related to the mechanical properties of the tissue. The attenuation of the radiation depends on the density of the material, and its composition (Coursey et al., 1998). Using intravascular elastography, the dose could be adjusted to the mechanical properties of the material.

10.4 Conclusions

Intravascular elastography is a new technique capable of providing cross-sectional images of strain within the vessel wall. From this information, it is possible to identify tissue stiffness: soft and hard materials. Since tissue stiffness is generally independent of tissue echogenicity, this new information is unavailable or inconclusive from the IVUS echogram alone.

Different strain values are found for fibrous, fibro-fatty and fatty plaque components. Consequently, identification of different plaque types could be performed using IVUS elastography. Furthermore, IVUS elastography has the potential to identify vulnerable plaques. Initial trials in the catheterisation laboratory demonstrate the feasibility of intravascular elastography *in vivo*. Additional signal processing techniques and validation are needed to improve the robustness of the technique *in vivo*.

Appendix A

Stress, Strain and Displacement in a Tube

Expressions for the stress and the strain (radial strain ε_r and circumferential strain ε_θ) in a long, cylindrical, isotropic and homogeneous tube, when submitted to a uniform pressure on the inner and outer surfaces, were first derived by Lamé (1866) (Fig. A.1). In discussing stresses, strains and displacement in a tube, it is advantageous to use polar co-ordinates (σ_r , σ_θ and σ_z for the stress in the radial, circumferential and longitudinal direction resp. and ε_r , ε_θ and ε_z for the strain in the radial, circumferential and longitudinal direction resp.). The stress-strain relationship for polar co-ordinates are given by (Noordergraaf, 1969) ;

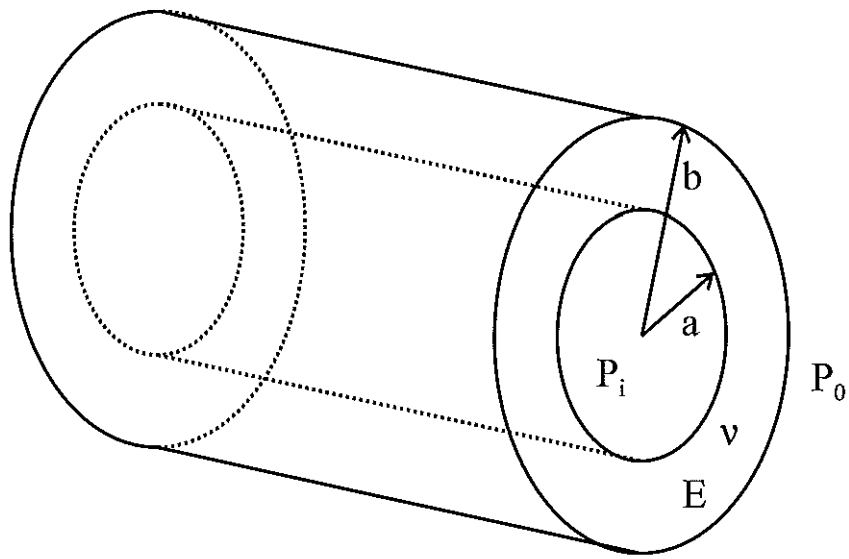

Figure A.1 Schematic drawing of tube with inner pressure P_i and outer pressure P_o. a and b are the inner and outer radius, respectively. E = Young's modulus; ν = Poisson's ratio

$$\begin{aligned} \varepsilon_r &= \frac{1}{E}(\sigma_r - \nu(\sigma_\theta + \sigma_z)) \\ \varepsilon_\theta &= \frac{1}{E}(\sigma_\theta - \nu(\sigma_r + \sigma_z)) \\ \varepsilon_z &= \frac{1}{E}(\sigma_z - \nu(\sigma_r + \sigma_\theta)) \end{aligned} \tag{A.1}$$

$$\begin{aligned} \textit{where} \quad E &= \textit{Youngs modulus} \\ \nu &= \textit{Poisson's ratio} \end{aligned}$$

The expressions for the stress in a thick walled tube are derived in Timoshenko and Goodier (1970), considering the stress functions are only dependent on r ;

$$\begin{aligned} \sigma_r &= \frac{a^2b^2(p_0 - p_i)}{b^2 - a^2} \cdot \frac{1}{r^2} + \frac{p_i a^2 - p_0 b^2}{b^2 - a^2} \\ \sigma_\theta &= -\frac{a^2b^2(p_0 - p_i)}{b^2 - a^2} \cdot \frac{1}{r^2} + \frac{p_i a^2 - p_0 b^2}{b^2 - a^2} \end{aligned} \tag{A.2}$$

$$\begin{aligned} \textit{where} \quad P_i &= \textit{pressure inside the vessel} \\ P_0 &= \textit{pressure outside the vessel} \\ a &= \textit{inner diameter} \\ b &= \textit{outer diameter} \end{aligned}$$

A.1 Plane stress

In this case, the stress in the longitudinal direction (σ_z) is assumed to zero. Considering plane stress in the tube wall, the stress-strain relations are given by,

$$\begin{aligned} \varepsilon_r &= \frac{1}{\mathrm{E}}(\sigma_r - \nu\sigma_\theta) \\ \varepsilon_\theta &= \frac{1}{\mathrm{E}}(\sigma_\theta - \nu\sigma_r). \end{aligned} \tag{A.3}$$

With the above equations, the displacement in the tube can be calculated, since the strain is related to the displacement (assuming only a radial displacement u_r in the tube) by (Timoshenko & Goodier, 1970)

$$\begin{aligned} \varepsilon_r &= \frac{\delta u_r}{\delta r} \\ \varepsilon_\theta &= \frac{u_r}{r}. \end{aligned} \tag{A.4}$$

The radial displacement u_r can be obtained using one of the above equations A.4, leading to

$$u_r = \frac{r}{\mathrm{E}(b^2 - a^2)}((p_i a^2 - p_0 b^2)(1-\nu) - a^2 b^2 (p_0 - p_i)(1+\nu) \cdot \frac{1}{r^2}) \tag{A.5}$$

In this study strain profiles are determined using two different levels of endoluminal expansion. The differential displacement in the tube due to the low pressure p_l and the high pressure p_h can be obtained by subtraction of the displacements. The displacement and strain expressions for a differential pressure are given by

$$\begin{aligned} u_{r,diff} &= \frac{a^2(p_h - p_l)}{\mathrm{E}(b^2 - a^2)}(\frac{b^2(1+\nu)}{r} + (1-\nu) \cdot r) \\ \varepsilon_{r,diff} &= \frac{a^2(p_h - p_l)}{\mathrm{E}(b^2 - a^2)}((1-\nu) - \frac{b^2(1+\nu)}{r^2}). \end{aligned} \tag{A.6}$$

A.2 Plane strain

In this case, the stress in the z-direction is not zero. By eliminating σ_z in equation A.1, the stress-strain relations are given by

$$\begin{aligned} \varepsilon_r &= \frac{1+\nu}{\mathrm{E}}((1-\nu)\sigma_r - \nu\sigma_\theta - \frac{\nu}{1+\nu}\mathrm{E}\varepsilon_z) \\ \varepsilon_\theta &= \frac{1+\nu}{\mathrm{E}}((1-\nu)\sigma_\theta - \nu\sigma_r - \frac{\nu}{1+\nu}\mathrm{E}\varepsilon_z). \end{aligned} \tag{A.7}$$

Using the boundary condition for plane strain (ε_z is 0) and the equations A.2 and A.4, the expression for the displacement as a function of r becomes

$$u_r = \frac{r}{\mathrm{E}(b^2 - a^2)}((p_i a^2 - p_0 b^2)(1+\nu)(1-2\nu) - a^2 b^2 (p_0 - p_i)(1+\nu) \cdot \frac{1}{r^2}). \tag{A.8}$$

Next, the relation for the radial displacement and strain as a function of two levels of endoluminal expansion can be derived

$$\begin{aligned} u_{r,diff} &= \frac{a^2(p_h - p_l)}{\mathrm{E}(b^2 - a^2)}(\frac{b^2(1+\nu)}{r} + (1+\nu)(1-2\nu) \cdot r) \\ \varepsilon_{r,diff} &= \frac{a^2(p_h - p_l)}{\mathrm{E}(b^2 - a^2)}((1+\nu)(1-2\nu) - \frac{b^2(1+\nu)}{r^2}). \end{aligned} \tag{A.9}$$

Appendix B

Derivation of the Low-Pass Filtered Autocorrelation Function

Using the signal model of equations 4.5 and 4.6 and equation 4.10, the crosscorrelation function is obtained from the expected value of the estimates for finite observation time T as

$$E\{\hat{R}_{12}(\tau)\} = \frac{1}{T}\int_{-T/2}^{T/2} E\{s_1(t)s_2(t+\tau)\}dt \tag{B.1}$$

Expressing the crosscorrelation function as the inverse Fourier transform of the crossspectrum (Bendat & Piersol, 1986, page 120), we obtain

$$E\{\hat{R}_{12}(\tau)\} = \frac{1}{T}\int_{-T/2}^{T/2}\int_{-\infty}^{\infty} G_{12}(f)e^{j2\pi f\tau}dfdt \tag{B.2}$$

where the cross-spectrum $G_{12}(f)$ is given

$$G_{12}(f) = \int_{-\infty}^{\infty} E\left\{s_1(t)s_2(t+\tau)\right\}e^{-j2\pi f\tau}d\tau \tag{B.3}$$

Using the definitions of $s_2(t)$ in equation 4.6, we can write the cross-spectrum expressing $s_2(t)$ in terms of its components, that is

$$G_{12}(f) = E\{s_1(t)\int_{-\infty}^{\infty} s(\alpha(t+\tau)-t_0) * p(t)e^{-j2\pi f\tau}d\tau\}. \tag{B.4}$$

We can express the delayed scattering function in equation B.4 as

$$s(\alpha(t+\tau)-t_0) = s[(t+\alpha\tau)+(\alpha-1)t-t_0] \tag{B.5}$$

and rewrite the Fourier transform of the scattering function as

$$\int_{-\infty}^{\infty} s(\alpha(t+\tau)-t_0)e^{-j2\pi f\tau}d\tau \rightarrow e^{j2\pi f[(\alpha-1)t-t_0]}\int_{-\infty}^{\infty} s(t+\alpha\tau)e^{-j2\pi f\tau}d\tau \tag{B.6}$$

Substituting equation B.6 into equation B.4 and with the change of variable $\tau' = \alpha\tau$, we obtain

$$G_{12}(f) = E\{s_1(t)e^{j2\pi f[(\alpha-1)t-t_0]}\int_{-\infty}^{\infty} \alpha^{-1}s(t+\tau')*p(t)e^{-j2\pi f\tau'/\alpha}d\tau' \tag{B.7}$$

From equation 4.3, $\alpha - 1 = \varepsilon$ and rearranging the integral and expectation operators in the above equation, we obtain

$$G_{12}(f) = e^{j2\pi f[\varepsilon t-t_0]}\int_{-\infty}^{\infty} \alpha^{-1}E\{s_1(t)s(t+\tau')\}e^{-j2\pi f\tau'/\alpha}d\tau' \tag{B.8}$$

and,

$$G_{12}(f) = e^{j2\pi f\varepsilon t}e^{-j2\pi ft_0}\alpha^{-1}G_{11}(f/\alpha) \tag{B.9}$$

where $G_{11}(f)$ is the autospectrum (auto spectral density function). Equation B.9 demonstrates the nonstationary nature of the cross-spectrum of the signals in equations 4.5 and 4.6, since the cross-spectrum is a function of the autospectrum and a function of time. Replacing equation B.9 in equation B.2 yields

$$E\{\hat{R}_{12}(\tau)\} = \frac{1}{T}\int_{-T/2}^{T/2}\int_{-\infty}^{\infty} \alpha^{-1}G_{11}(f/\alpha)e^{j2\pi f\varepsilon t}e^{-j2\pi ft_0}e^{j2\pi f\tau}df\,dt\,d\tau \tag{B.10}$$

Exchanging the order of the two integration operators, we obtain

$$E\{\hat{R}_{12}(\tau)\} = \int_{-\infty}^{\infty} \alpha^{-1}G_{11}(f/\alpha)e^{-j2\pi ft_0}e^{j2\pi f\varepsilon\tau}\left[\frac{1}{T}\int_{-T/2}^{T/2} e^{j2\pi f\varepsilon t}dt\right]df \tag{B.11}$$

where the term in square brackets reduces to a sinc function yielding

$$E\{\hat{R}_{12}(\tau)\} = \frac{1}{T}\int_{-\infty}^{\infty} \alpha^{-1}G_{11}(f/\alpha)e^{-j2\pi ft_0}\,sinc(f\varepsilon T)\,e^{j2\pi f\tau}df \tag{B.12}$$

Using the convolution theorem and the scaling property of the Fourier transform, the spectral product in equation B.12 can be expressed in the time domain as the following convolution,

$$E\left\{\hat{R}_{12}(\tau)\right\} = R_{11}(\alpha\tau) * h(\tau) * \delta(\tau - t_0), \tag{B.13}$$

where

$$h(\tau) = \begin{cases} 1, & |\tau| \leq \frac{T_\varepsilon}{2} \\ 0, & elsewhere \end{cases} \tag{B.14}$$

Appendix C

The Fisher-Z Transform

The distribution of correlation coefficient estimates deviates from Normal when ρ is not zero. To better describe the statistics of such skewed estimates, Fisher (1970, page 185) proposed the transformation

$$z = 0.5 \times [\ln(1+\rho) - \ln(1-\rho)], \tag{C.1}$$

a transformation that leads to approximately Normal distributed estimates. This transformation is well suited for our application where the region of interest is $0.5 < \rho < 1$. Mean and standard deviations are computed in the transformed variable z. Then, the inverse transform,

$$\rho = \frac{e^{2z} - 1}{e^{2z} + 1} \tag{C.2}$$

is applied to obtain the average decorrelation, and lower and upper bounds, which are expectedly asymmetric, corresponding to the 95% confidence interval.

Bibliography

Adams, W. B., Kuhn, J. P. & Whyland, W. P. (1980). Correlator compensation requirements for passive time-delay estimation with moving source or receivers. *IEEE Transactions on Acoustics, Speech, and Signal Processing, 28*, 158-168.

Adler, R. S., Rubin, J. M., Fowlkes, J. B., Carson, P. L. & Pallister, J. E. (1995). Ultrasonic estimation of tissue perfusion: a stochastic approach. *Ultrasound in Medicine and Biology, 21*(4), 493-500.

Alam, S. K., & Ophir, J. (1997). On the use of envelope and rf signal decorrelation as tissue strain estimators. *Ultrasound in Medicine and Biology, 23*, 1427-1433.

Alfonso, F., Macaya, C., Goicolea, J., Hernandez, R., Segovia, J., Zamorano, J., Banuelos, C. & Zarco, P. (1994). Determinants of coronary compliance in patients with coronary artery disease: an intravascular ultrasound study. *Journal of the American College of Cardiology, 23*(4), 879-884.

Altman, D. C. (1994). *Practical statistics for medical research.* London, UK: Chapman and Hall.

Ambrose, J. A., Tannenbaum, M. A., Alexopoulos, D., Monsen, C. S., Weiss, M., Borriw, S., Gorlin, R. & Fuster, V. (1988). Angiographic progression of coronary artery disease and the developmant of myocardial infarction. *Journal of the American College of Cardiology, 12*, 56-62.

Armitage, P. (1973). *Statistical methods in medical research.* Oxford, United Kingdom: Blackwell Scientific publications.

Baptista, J., di Mario, C., Ozaki, Y., Escaned, J., Gil, R., de Feyter, P. J., Roelandt, J. R. T. C. & Serruys, P. W. (1996). Impact of plaque morphology and composition on the mechanisms of lumen enlargement using intracoronary ultrasound and quantitative angiography after balloon angioplasty. *American Journal of Cardiology, 77*, 115-121.

Barzilai, B., Saffitz, J. E., Miller, J. G. & Sobel, B. E. (1987). Quantitative ultrasonic characterization of the nature of atherosclerotic plaques in human aorta. *Circulation research, 60*, 459-463.

Becker, A. E. (1988). Atherosclerose- een dynamisch-morfologische beschouwing. In T. van der Werf & A. C. Arntzenius (Eds.), *Atherosclerose en coronaire insufficientie* (p. 33-57). Utrecht: Wetenschappelijke uitgeverij Bunge.

Bendat, J. S., & Piersol, A. C. (1986). *Randon data: analysis and measurement* (2nd ed.). New York, USA: Wiley and Sons.

Bergel, D. H. (1961). The static elastic properties of the arterial wall. *Journal of Physiology, 156,* 445-457.

Betz, J. W. (1984). Comparison of the deskewed short-time correlator and the maximum likelihood correlator. *IEEE Transactions on Acoustics, Speech, and Signal Processing, 32,* 285-294.

Betz, J. W. (1985). Effects of uncompensated relative time companding on a broad-band crosscorrelator. *IEEE Transactions on Acoustics, Speech, and Signal Processing, 33,* 505-510.

Bilgen, M., & Insana, M. F. (1996). Deformation models and correlation analysis in elastography. *Journal of the Acoustic Society of America, 99*(5), 3212-3225.

Bilgen, M., & Insana, M. F. (1997). Error analysis in acoustic elastography 1: displacement estimation. *Journal of the Acoustical Society of America, 101*(2), 1139-1146.

Blankenhorn, D. H., Chin, H. P. & Conover, D. J. (1988). Ultrasound observation of pulsation in human carotid artery lesions. *Ultrasound in Medicine and Biology, 14*(7), 583-587.

Bom, N., Lancée, C. T., Honkoop, J. & Hugenholtz, P. G. (1971). Ultrasonic viewer for cross-sectional analyses of moving cardiac structures. *Biomedical Engineering, 6*(11), 500-503.

Bom, N., Lancée, C. T., Rijsterborgh, H., ten Hoff, H. & Roelandt, J. R. T. C. (1993). From idea to clinical application. In J. R. T. C. Roelandt, E. J. Gussenhoven & N. Bom (Eds.), *Intravascular ultrasound* (p. 1-13). Dordrecht, The Netherlands: Kluwer academic publishers.

Bom, N., Lancée, C. T. & van Egmond, F. C. (1972). An ultrasonic intracardiac scanner. *Ultrasonics, 10,* 72-76.

Bonnefous, O. (1989). Statistical analysis and time correlation processes applied to velocity measurement. *IEEE Ultrasonics Symposium Proceedings,* 887-892.

Borsboom, J. M. G., Céspedes, E. I., Steen, A. F. W. van der & Lancée, C. T. (1999). Simulation of phased array ultrasound transducers for intravascular applications. *Journal of Acoustic Society of America,* accepted.

Bouma, C. (1998). *Lipid detection in atherosclerotic lesions by intravascular impedance imaging.* Phd dissertation, Utrecht University, The Netherlands.

Brennan III, J. F., Römer, T. J., Lees, R. S., Tercyak, A. M., Kramer, J. R. & Feld, M. S. (1997). Determination of human coronary artery composition by raman spectroscopy. *Circulation, 96,* 99-105.

Brezinski, M. E., Tearney, G. J., Weissman, N. J., Boppart, S. A., Bouma, B. E., Hee, M. R., Weyman, A. E., Swanson, E. A., Southern, J. F. & Fujimoto, J. G. (1997). Assessing atherosclerotic plaque morphology: comparison of optical coherence tomography and high frequency ultrasound. *Heart, 77*, 397-403.

Bridal, S. L., Fornes, P., Bruneval, P. & Berger, G. (1997a). Correlation of ultrasonic attenuation (30 to 50 MHz) and constituents of atherosclerotic plaque. *Ultrasound in Medicine and Biology, 23*(5), 691-703.

Bridal, S. L., Fornes, P., Bruneval, P. & Berger, G. (1997b). Parametric (integrated backscatter and attenuation) images constructed using backscattered radio frequency signals (25-56 MHz) from human aortae in vitro. *Ultrasound in Medicine and Biology, 23*(2), 215-229.

Burke, A. P., Farb, A., Malcolm, G. T., Liang, Y., Smialek, J. & Virmanu, R. (1997). Coronary risk factors and plaque morphology in men with coronary disease who died suddenly. *New England Journal of Medicine, 336*(18), 1276-1282.

Casscells, W., Hathorn, B., David, M., Krabach, T., Vaughn, W. K., McAllister, H. A., Bearman, G. & Willerson, J. T. (1996). Thermal detection of cellular infiltrates in living atherosclerotic plaques: possible implications for plaque rupture and thrombosis. *Lancet, 347*, 1447-1449.

Céspedes, E. I. (1993a). *Elastography: imaging of biological tissue elasticity.* Phd dissertation, University of Houston, USA.

Céspedes, E. I., de Korte, C. L. & van der Steen, A. F. W. (1997c). Intravascular ultrasonic palpation: assessment of local wall compliance. *IEEE Ultrasonics Symposium Proceedings*, 1079-1082.

Céspedes, E. I., de Korte, C. L., van der Steen, A. F. W., Norder, B. & te Nijenhuis, K. (1996). Tissue mimicking material and artifacts in intravascular elasticity imaging. *IEEE Ultrasonics Symposium Proceedings*, 1181-1184.

Céspedes, E. I., de Korte, C. L., van der Steen, A. F. W., von Birgelen, C. & Lancée, C. T. (1997a). Intravascular elastography: principle and potentials. *Seminars in Interventional Cardiology, 2*(1), 55-62.

Céspedes, E. I., Huang, Y., Ophir, J. & Spratt, S. (1995a). Methods for estimation of subsample time delays of digitized echo signals. *Ultrasonic Imaging, 17*, 142-171.

Céspedes, E. I., Insana, M. F. & Ophir, J. (1995b). Theoretical bounds on strain estimation in elastography. *IEEE Transactions on Ultrasonics, Ferroelectrics, and Frequency Control, 42*(5), 969-972.

Céspedes, E. I., Ophir, J. & Alam, S. K. (1997b). The combined effect of signal decorrelation and random noise on the variance of time delay estimation. *IEEE transactions on Ultrasound, Ferroelectrics and Frequency Control, 44*(1), 220-225.

Céspedes, E. I., Ophir, J., Ponnekanti, H. & Maklad, N. (1993b). Elastography: elasticity imaging using ultrasound with application to muscle and breast in vivo. *Ultrasonic Imaging, 17*, 73-88.

Chae, J. S., Brisken, A. F., Maurer, G. & Siegel, R. J. (1993). Geometric accuracy of intravascular ultrasound imaging. *Journal of American Society of Echocardiology, 5*(6), 577-587.

Chan, Y. T., Riley, J. M. & Plant, J. B. (1981). Modeling of time delay and its applications to estimation of nonstationary delays. *IEEE Transactions on Acoustics, Speech, and Signal Processing, 29*, 5577-581.

Chen, E. J., Novakofski, J., Jenkins, W. K. & O'Brien, W. D. (1996). Young's modulus measurements of soft tissues with application to elasticity imaging. *IEEE Transactions on Ultrasonics, Ferroelectrics, and Frequency Control, 43*(1), 191-194.

Cheng, G. C., Loree, H. M., Kamm, R. D., Fishbein, M. C. & Lee, R. T. (1993). Distribution of circumferential stress in ruptured and stable atherosclerotic lesions. a structural analysis with histopathological correlation. *Circulation, 87*, 1179-1187.

Cobbaert, C., Jukema, J. W., Zwinderman, A. H., Withagen, A. J., Lindemans, J. & Bruschke, A. V. (1997). Modulation of lipoprotein(a) atherogenicity by high density lipoprotein cholesterol levels in middle-aged men with symptomatic coronary artery disease and normal to moderately elevated serum cholesterol. regression growth evaluation statin study (REGRESS) study group. *Journal of American College of Cardiology, 30*(6), 1491-1499.

Constantinides, P. (1990). Cause of thrombus in human atherosclerotic arteries. *American Journal of Cardiology, 66*, 37G-40G.

Cortis, B. S., Hussein, H., Khandekar, C. S. & Principe, J. (1984). Angioscopy in vivo. *Catheterization and Cardiovascular Diagnosis, 10*, 493-500.

Coursey, B. M., Seltzer, S. M., Soares, C. S. & Zimmerman, B. E. (1998). Glossary of radiation physics for vascular radiation therapy. In R. Waksman & P. W. Serruys (Eds.), *Handbook of vascular brachytherapy* (p. 5-10). London: Martin Dunitz Ltd.

Curie, J., & Curie, P. (1880). Sur l'electricite polaire dans les cristaus hemiedres a facer inclinees. *Compt. Rend. Seances Acad. Sci., 91*, 383-389.

Davies, M. J. (1996). Stability and instability: two faces of coronary atherosclerosis. *Circulation, 94*(8), 2013-2020.

de Groot, E., Zwinderman, A. H., van der Steen, A. F. W., Ackerstaff, R. G. A., Montauban van Swijndregt, A. D., Bom, N., Lie, K. I. & Bruschke, V. G. (1998). Variance components analysis of carotid and femoral intima-media thickness measurements. *Ultrasound in Medicine and Biology, 24*, 825-832.

de Jaegere, P. P., de Feyter, P. J., van der Giessen, W. J. & Serruys, P. W. (1994). Intracoronary stents: A review of the experience with five different devices in clinical use. *Journal of Interventional Cardiology, 7*, 117-128.

de Jong, N., Djoa, K. K., van der Steen, A. F. W., Lancée, C. T., Kasprzak, J. D., Breburda, C. & Bom, N. (1999). Real-time three dimensional data acquisition. *IEEE Ultrasonics Symposium Proceedings, Sendai, Japan*, 1843-1846.

de Jong, P. G. M., Arts, T., Hoeks, A. P. G. & Reneman, R. S. (1991). Experimental evaluation of the correlation interpolation technique to measure regional tissue velocity. *Ultrasonic Imaging, 13*, 145-161.

de Jong, P. G. M., Hoeks, A. P. G. & Reneman, R. S. (1990). Determination of tissue motion velocity by correlation interpolation of pulsed ultrasonic echo signals. *Ultrasonic Imaging, 12*, 84-98.

de Korte, C. L., Céspedes, E. I., Carlier, S. G., van der Steen, A. F. W., Pasterkamp, G., Thompson, D., Thomas, J. D. & Bom, N. (1998b). Assessment of stiffness and elevated mechanical stress in atherosclerotic plaques by intravascular ultrasound: in vitro experience. *European Heart Journal, 19*(Abstr.Suppl.), 620.

de Korte, C. L., Céspedes, E. I., van der Steen, A. F. W. & Lancée, C. T. (1996). Image artifacts in intravascular elastography. *IEEE EMBS Symposium Proceedings, Amsterdam, The Netherlands*, paper no. 685.

de Korte, C. L., Céspedes, E. I., van der Steen, A. F. W., Pasterkamp, G. & Bom, N. (1998a). Intravascular ultrasound elastography: Assessment and imaging of elastic properties of diseased arteries and vulnerable plaque. *European Journal of Ultrasound, 7*(3), 219-224.

de Korte, C. L., van der Steen, A. F. W., Dijkman, B. H. J. & Lancée, C. T. (1997). Performance of time delay estimation methods for small time shifts in ultrasonic signals. *Ultrasonics, 35*(4), 263-274.

de Korte, C. L., van der Steen, A. F. W., Thijssen, J. M., Duindam, J. J., Otto, C. & Puppels, G. J. (1994). Relation between local acoustic parameters and protein distribution in human and porcine eye lenses. *Experimental Eye Research, 59*, 617-627.

de Korte, C. L., Woutman, H., van der Steen, A. F. W., Pasterkamp, G. & Céspedes, E. I. (1998c). IVUS elastography: a potential identifier of vulnerable atherosclerotic plaque. *IEEE Ultrasonics Symposium Proceedings, Sendai, Japan*, 1729-1732.

del Grosso, V. A., & Mader, C. W. (1972). Speed of sound in pure water. *Journal of the Acoustic Society of America, 52*, 1442-1446.

di Mario, C., The, S. H. K., Madrestma, S., Suylen, R. J. van, Wilson, R. A., Bom, N., Serruys, P. W., Gussenhoven, E. J. & Roelandt, J. R. T. C. (1992). Detection and characterization of vascular lesions by intravascular ultrasound: an in vitro study correlated with histology. *Journal of American Society Echocardiography, 5*(2), 135-146.

Dickinson, R. J., & Hill, C. R. (1982). Measurement of soft tissue motion using correlation between A-scans. *Ultrasound in Medicine and Biology, 8*(3), 263-271.

Djoa, K. K., de Jong, N., Cromme-Dijkhuis, A. H., Lancée, C. T. & Bom, N. (1996). Two decades of transesophageal phased array probes. *Ultrasound in Medicine and Biology, 22*(1), 1-9.

Djoa, K. K., de Jong, N., van Egmond, F. C., Kasprzak, J. D., Vletter, W. B., Lancée, C. T., van der Steen, A. F. W., Bom, N. & Roelandt, J. R. T. C. (1999). Real time three-dimensional echo data acquisition with a fast rotating scanning unit. *Ultrasound in Medicine and Biology*, accepted.

Dobrin, P. B. (1978). Mechanical properties of arteries. *Physiological Reviews*, *58*(2), 397-460.

Dussik, K. T., Dussik, F. & Wyt, L. (1947). Auf dem Wege zum Hyperphonographie des Gehirnes. *Wien. Med. Woch.*, *38/39*, 425.

Edler, I., & Hertz, C. H. (1954a). Application of echo ranging techniques to the determination of structures of biological tissues. *K. Fysiogr. Sallst. Lund Forshung*, *24*, 1-19.

Edler, I., & Hertz, C. H. (1954b). The use of the reflectoscope for the continuous recording of the movement of heart walls. *K. Fysiogr. Sallst. Lund Forshung*, *24*, 40-58.

Emelianov, S. Y., Lubinski, M. A., Skovoroda, A. R., Erkamp, R. Q., Leavey, S. F., Wiggins, R. C. & O'Donnell, M. (1997). Reconstructive ultrasound elasticity imaging for renal pathology detection. *IEEE Ultrasonics Symposium Proceedings, Toronto, Canada*, 1123-1126.

Emelianov, S. Y., Lubinski, M. A., Weitzel, W. F., Wiggins, R. C., Skovoroda, A. R. & O'Donnell, M. (1995). Elasticity imaging for early detection of renal pathology. *Ultrasound in Medicine and Biology*, *21*(7), 871-883.

Falk, E. (1991). Coronary thrombosis: pathogenesis and clinical manifestations. *The American Journal of cardiology*, *68*, 28B-35B.

Falk, E., Shah, P. & Fuster, V. (1995). Coronary plaque disruption. *Circulation*, *92*(3), 657-671.

Farb, A., Burke, A. P., Tang, A. L., Liang, Y., Mannam, P., Smialek, J. & Virmani, R. (1996). Coronary plaque erosion without rupture into a lipid core: a frequent cause of coronary thrombosis in sudden coronary death. *Circulation*, *93*(7), 1354-1363.

Feld, S., Ganim, M., Carell, E. S., Kjellgern, O., Kirkeeide, R. L., Vaughn, W. K., Kelly, R., McGhie, A. I., Kramer, N., Loyd, D., Anderson, H. V., Schroth, G. & Smalling, R. W. (1996). Comparison of angioscopy, intravascular ultrasound imaging and quantitative coronary angiography in predicting clinical outcome after coronary intervention in high risk patients. *Journal of American College of Cardiology*, *28*(1), 97-105.

Ferrara, K., & DeAngelis, G. (1997). Color flow mapping. *Ultrasound in Medicine and Biology*, *23*(3), 321-345.

Ferrara, K. W., Zagar, B., Sokil-Melgar, J. & Algazi, V. R. (1996). High resolution 3D color flow mapping: applied to the assessment of breast vasculature. *Ultrasound in Medicine and Biology*, *22*(3), 293-304.

Firestone, F. A. (1945). The supersonic reflectoscope for interior inspection. *Metal Prog., 48*, 505-512.

Fishbein, M. C., & Sighel, R. J. (1996). How big are coronary atherosclerotic plaques that rupture. *Circulation, 94*(10), 2662-2666.

Fisher, R. A. (1970). *Statistical methods for research workers* (4th ed.). Edinburgh: Oliver and Boyd.

Fitzgerald, P. J., & Yock, P. G. (1993). Mechanisms and outcomes of angioplasty assessed by intravascular ultrasound imaging. *Journal of Clinical Ultrasound, 21*, 579-588.

Foster, F. S., Ryan, L. K. & Lockwood, G. R. (1993). High frequency ultrasound scanning of the arterial wall. In J. R. T. C. Roelandt, E. J. Gussenhoven & N. Bom (Eds.), *Intravascular ultrasound* (p. 91-108). Norwell, MA, USA: Kluwer Academic Publishers.

Foster, F. S., Strban, M. & Austin, G. (1984). The ultrasonic macroscope: initial studies of breast tissue. *Ultrasonic Imaging, 6*, 243-261.

Foster, S. G., Embree, P. M. & O'Brien, W. D. (1990). Flow velocity profile via time-domain correlation: error analysis and computer simulation. *IEEE Transactions on Ultrasonics, Ferroelectrics, and Frequency Control, 37*(2), 164-175.

Friedrich, G. J., Moes, N. Y., Muhlberger, V. A., Gabl, C., Mikuz, G., Hausmann, D., Fitzgerald, P. J. & Yock, P. G. (1994). Detection of intralesional calcium by intracoronary ultrasound depends on the histologic pattern. *American Heart Journal, 128*(3), 435-41.

Friemel, B. H. (1994). *Real-time ultrasonic two-dimensional vector velocity estimation utilizing speckle-tracking algorithms: implementation and limitations.* Phd dissertation, Duke University, USA.

Frobert, O., Gregersen, H. & Bagger, J. P. (1996). Mechanics of porcine coronary arteries ex vivo emplying impedance planimetry: a new intravascular technique. *Annals of Biomedical Engineering, 24*, 148-155.

Fung, Y. C. (1993). *Biomechanics: mechanical properties of living tissues* (2nd ed.). New York: Springer-Verlag.

Fuster, V. (1994). Mechanisms leading to myocardial infarction: Insights from studies of vascular biology. *Circulation, 90*(4), 2126-2146.

Fuster, V., Badimon, L., Badimon, J. J. & Chesebro, J. H. (1992). The pathogenesis of coronary artery disease and the acute coronary syndromes. *New English Journal of Medicine, 326*(4), 242-250.

Fuster, V., Stein, B., Ambrose, J., Badimon, L., Badimon, J. J. & Chesebro, J. H. (1990). Atherosclerotic plaque rupture and thrombosis: evolving concepts. *Circulation, 82*(suppl II), II.47-II.59.

Gao, L., Parker, K. J., Lerner, R. M. & Levinson, S. F. (1996). Imaging of the elastic properties of tissue - a review. *Ultrasound in Medicine and Biology, 22*(8), 959-977.

Garra, B. S., Insana, M. F., Shawker, T. H. & Russell, M. A. (1987). Quantitative estimation of attenuation and echogenicity: normal state versus diffuse liver disease. *Radiology, 162*, 61-67.

Gow, B. S., & Hadfield, C. D. (1979). The elasticity of canine and human coronary arteries with reference to post-mortem changes. *Circulation research, 45*(5), 588-594.

Gow, B. S., & Taylor, M. G. (1968). Measurement of viscoelatic properties of arteries in the living dog. *Circulation Research, 23*, 111-122.

Greenleaf, J. F., Duck, F. A., Samayo, W. F. & Johnson, S. A. (1974). Ultrasonic data acquisition and processing system for atherosclerotic tissue characterisation. *IEEE Ultrasonics Symposium Proceedings*, 738-743.

Gronningsaeter, A., Angelsen, B. A. J., Gresli, A., Torp, H. G. & Linker, D. T. (1995). Blood noise reduction in intravascular ultrasound imaging. *IEEE Transactions on Ultrasonics, Ferroelectrics, and Frequency Control, 42*(2), 200-209.

Gronningsaeter, A., Angelsen, B. A. J., Heimdal, A. & Torp, H. G. (1994). Vessel wall detection and blood noise reduction in intravascular ultrasound imaging. *IEEE Ultrasonics Symposium Proceedings, Cannes, France*, 1609-1612.

Gronningsaeter, A., Angelsen, B. A. J., Heimdal, A. & Torp, H. G. (1996). Vessel wall detection and blood noise reduction in intravascular ultrasound imaging. *IEEE Transactions on Ultrasonics, Ferroelectrics, and Frequency Control, 43*(3), 359-369.

Gussenhoven, E. J., Essed, C. E., Frietman, P., Mastik, F., Lancée, C. T., Slager, C., Serruys, P. W., Gerritsen, P., Pieterman, H. & Bom, N. (1989). Intravascular echographic assessment of vessel wall characteristics: a correlation with histology. *International Journal of Cardiac Imaging, 4*, 105-116.

Gussenhoven, E. J., Lugt, A. van der, Pasterkamp, G., van den Berg, F. G., Sie, L. H., Vischjager, M., The, S. H. K., Li, W., Pieterman, H. & van Urk, H. (1995). Intravascular ultrasound predictors of outcome after peripheral balloon angioplasty. *European Journal of vascular and Endovascular Surgery, 10*, 279-288.

Gussenhoven, E. J., Lugt, A. van der, van der Steen, A. F. W. & Ligtvoet, K. M. (1996). What have we learned from in vitro intravascular ultrasound. *American Heart Journal, 132*(3), 702-710.

Hamburger, J. N., Gijsbers, G. H. M., Ozaki, Y., N, R. P., de Feyter, P. J. & Serruys, P. W. (1997). Recanalization of chronic total coronary occlusions using a laser guidewire: a pilot-study. *Journal of the American College of Cardiology, 30*, 649-656.

Hansen, F., Mangell, P., Sonesson, B. & Lanne, T. (1995). Diameter and compliance in the human common carotid artery - variations with age and sex. *Ultrasound in Medicine and Biology, 21*(1), 1-9.

Hehrlein, C., & Kubler, W. (1997). Advantages and limitations of radioactive stents. *Seminars in Interventional Cardiology, 2*(2), 109-13.

Hein, I. A., & O'Brien, W. D. (1993). Current time-domain methods for assessing tissue motion by analysis from reflected ultrasound echoes - a review. *IEEE transactions on Ultrasound, Ferroelectrics and Frequency Control, 40*(2), 84-102.

Hodgson, J. M. B., Reddy, K. R., Suneja, R., Nair, R. N., Lesnefsky, E. J. & Sheehan, H. M. (1993). Intracoronary ultrasound imaging: correlation of plaque morphology with angiography, clinical syndrome and procedural results in patients undergoing angioplasty. *Journal of American College of cardiology, 21*(1), 35-44.

Hoeks, A. P. G., Brands, P. J. & Reneman, R. S. (1992). Assessment of arterial distension waveform using doppler signal processing. *Journal of Hypertension, 10*(6), S19-S22.

Honye, J., Mahon, D. J., Jain, A., White, C. J., Ramee, S. R., Wallis, J. B., Al-Zarka, A. & Tobis, J. M. (1992). Morphological effects of coronary balloon angioplasty in vivo assessed by intravascular ultrasound imaging. *Circulation, 85*(3), 1012-1025.

Hori, T., Leung, C. Y., De Guzman, S., Caiozzo, V. J., Farvid, A. R., Karimi, H., Helfant, R. H. & Tobis, J. M. (1997). Are soft echoes really soft? intravascular ultrasound assessment of mechanical properties in human atherosclerotic tissue. *American Heart Journal, 133*(1), 1-7.

IEEE. (1979). *Programs for digital signal processing.* IEEE Press, John Wiley & Sons.

Isner, J. M., Rosenfield, K., Losordo, D. W., Rose, L., Langevin, R. E., Razvi, S. & Kosowsky, B. D. (1991). Combination of balloon -ultrasound imaging catheter for percutaneous transluminal angioplasty. *Circulation, 84*(2), 739-754.

Jukema, J. W., van Boven, A., Groenemeijer, B., Zwinderman, A., Reiber, J., Bruschke, A., Henneman, J., Molhoek, G., Bruin, T., Jansen, H., Gagne, E., Hayden, M. & Kastelein, J. (1996). The ASP9 ASN mutation in the lipoprotein lipase gene is associated with increased progression of coronary atherosclerosis. regress study group, interuniversity cardiology institute, utrecht, the netherlands. regression growth evaluation statin study. *Circulation, 94*(8), 1913-1918.

Kallel, F., Varghese, T., Ophir, J. & Bilgen, M. (1997). The nonstationary strain filter in elastography: part 2. lateral and elevational decorrelation. *Ultrasound in Medicine and Biology, 23*, 1357-1369.

Kearney, P. P., Ramo, M. P., Spencer, T., Shaw, T. R. D., Starkey, I. R., McDicken, N. & Sutherland, G. R. (1997). A study of the quantitative and qualitative impact of catheter shaft angulation in a mechanical intravascular ultrasound system. *Ultrasound in Medicine and Biology, 23*(1), 87-93.

King III, S. B., Williams, D. O., Chougule, P., Klein, J. L., Waksman, R., Hilstead, R., MacDonald, J., Andersberg, K. & Crocker, I. R. (1998). Endovascular β-radiation to reduce restenosis after coronary balloon angioplasty: results of the beta energy restenosis trial (BERT). *Circulation, 97*, 2025-2030.

Knapp, C. H., & Carter, G. C. (1976). The generalized correlation method for estimation of time delay. *IEEE Transactions on Acoustics, Speech, and Signal Processing, 24*, 320-327.

Konings, M. K., Mali, W. P. & Viergever, M. A. (1997). Development of an intravacular impedance catheter for detection of fatty lesions in arteries. *IEEE Transactions on Medical Imaging, 16*(4), 439-446.

Konofagou, E., Dutta, P., Ophir, J. & Céspedes, E. I. (1996). Reduction of stress nonuniformities by apodization of compressor displacement in elastography. *Ultrasound in Medicine and Biology, 22*(9), 1229-1236.

Kornet, L., Lambregts, J., Hoeks, A. P. & Reneman, R. S. (1998). Differences in near-wall shear rate in the carotid artery within subjects are associated with different intima-media thicknesses. *Arteriosclerosis, Thrombosis, and Vascular Biology, 18*(12), 1877-84.

Kragel, A. H., Gertz, S. D. & Roberts, W. C. (1991). Morphologic comparison of frequency and types of acute lesions in the major epicardial coronary arteries in unstable angina pectoris, sudden coronary death and acute myocardial infarction. *Journal of American College of Cardiology, 18*(3), 801-808.

Krams, R., Wentzel, J. J., Oomen, J. A., Vinke, R., Schuurbiers, J. C., de Feyter, P. J., Serruys, P. W. & Slager, C. J. (1997). Evaluation of endothelial shear stress and 3D geometry as factors determining the development of atherosclerosis and remodeling in human coronary arteries in vivo. combining 3D reconstruction from angiography and IVUS (ANGUS) with computational fluid dynamics. *Arteriosclerosis, Thrombosis, and Vascular Biology, 17*(10), 2061-5.

Krouskop, T. A., Dougherty, D. R. & Levinson, S. F. (1987). A pulsed doppler ultrasonic system for making noninvasive measurements of the mechanical properties of soft tissue. *Journal of Rehabilitation Res. Dev., 24*, 1-8.

Kuc, R., & Schwartz, M. (1979). Estimating the acoustic attenuation coefficient slope for liver from reflected ultrasound signals. *IEEE Transactions on Sonics and Ultrasonics, 26*, 353-362.

Lamé, M. G. (1866). *Lecons sur la théorie mathématique de l'élasticité des corps solides.* Paris: Gautiers-Villars.

Lancée, C. T., Bom, N. & Rijndorp, H. H. (1975). Construction of a circular ultrasonic array with miniature elements for cardiac application. In E. Kazner (Ed.), *Ultrasonics in medicine* (p. 49-53). Excerpta Medica.

Landini, L., Sarnelli, R., Picano, E. & Salvadori, M. (1986). Evaluation of frequency dependence of backscatter coefficient in normal and atherosclerotic aortic walls. *Ultrasound in Medicine and biology, 12*(5), 397-401.

Lee, R. T., Gordzinsky, A. J., Frank, E. H., Kamm, R. D. & Schoen, F. J. (1991). Structure-dependent dynamic mechanical behavior of fibrous caps from human atherosclerotic plaques. *Circulation, 83*, 1764-1770.

Lee, R. T., & Kamm, R. D. (1994). Vascular mechanics for the cardiologist. *Journal of the American College of Cardiology, 23*(6), 1289-1295.

Lee, R. T., & Libby, P. (1997). The unstable atheroma. *Arteriosclerosis, Thrombosis, and Vascular Biology, 17*(10), 1859-1867.

Lee, R. T., Loree, H. M., Cheng, G. C., Lieberman, E. H., Jaramillo, N. & Schoen, F. J. (1993). Computational structural analysis based on intravascular ultrasound imaging before in vitro angioplasty: prediction of plaque fracture locations. *Journal of American College of Cardiology, 21*, 777-782.

Lee, R. T., Richardson, G., Loree, H. M., Gordzinsky, A. J., Gharib, S. A., Schoen, F. J. & Pandian, N. (1992). Prediction of mechanical properties of human atherosclerotic tissue by high-frequency intravascular ultrasound imaging. *Arteriosclerosis and Thrombosis, 12*, 1-5.

Lees, A. M., Lees, R. S., Scoen, F., Isaacsohn, J. S., Fischman, A. J., McKusick, K. A. & Strauss, H. W. (1988). Imaging human atherosclerosis with 99m Tc-labeled low density lipoproteins. *Arteriosclerosis, 8*(5), 461-470.

Lendon, C. L., Davies, M. J., Born, G. V. R. & Richardson, P. D. (1991). Atherosclerotic plaque caps are locally weakened when macrophage density is increased. *Atherosclerosis, 87*, 87-90.

Lerner, R. M., Huang, S. R. & Parker, K. J. (1990). Sonoelasticity images derived from ultrasound signals in mechanically vibrated tissues. *Ultrasound in Medicine and Biology, 16*, 231-239.

Li, W., Lancée, C. T., Céspedes, E. I., van der Steen, A. F. W. & Bom, N. (1997). Potentials of volumetric blood-flow measurement. *Seminars in Interventional Cardiology, 2*(1), 49-54.

Li, W., Lancée, C. T., Céspedes, E. I., van der Steen, A. F. W. & Bom, N. (1998a). Decorrelation properties of intravascular echo signals. *Journal of the Acoustical Society of America, 102*(6), 3785-3794.

Li, W., van der Steen, A. F. W., Lancée, C. T., Cespedes, E. I. & Bom, N. (1998b). Blood flow imaging and volume flow quantitation with intravascular ultrasound. *Ultrasound in Medicine and Biology, 24*(2), 203-214.

Li, W., von Birgelen, C., di Mario, C., Boersma, E., Gussenhoven, E. J. & van der Putten, N. (1994). Semi-automatic contour detection for volumetric quantification of intracoronay ultrasound. In *Computers in cardiology* (p. 277-280). Los Alamitos, CA: IEEE Computer Society Press.

Linker, D. T., Klever, A., Gronningsaeter, A., Yock, P. G. & Angelsen, B. A. J. (1991). Tissue characterization with intra-arterial ultrasound: special promise and problems. *International Journal on Cardiac Imaging, 6*, 255-263.

Lockwood, G. R., Ryan, L. K., Hunt, J. W. & Foster, F. S. (1991). Measurement of the ultrasonic properties of vascular tissues and blood from 35-65 MHz. *Ultrasound in Medicine and Biology, 17*, 653-666.

Loree, H. M., Grodzinsky, A. J., Park, S. Y., Gibson, L. J. & Lee, R. T. (1994a). Static circumferential tangential modulus of human atherosclerotic tissue. *Journal of Biomechanics, 27*(2), 195-204.

Loree, H. M., Kamm, R. D., Stringfellow, R. G. & Lee, R. T. (1992). Effects of fibrous cap thickness on peak circumferential stress in model atherosclerotic vessels. *Circulation Research, 71*, 850-858.

Loree, H. M., Tobias, B. J., Gibson, L. J., Kamm, R. D., Small, D. M. & Lee, R. T. (1994b). Mechanical properties of model atherosclerotic lesion lipid pools. *Arteriosclerosis and Thrombosis, 14*(2), 230-234.

Loupas, T., Powers, J. T. & Gill, R. W. (1995). An axial velocity estimator for ultrasound blood flow imaging, based on a full evaluation of the doppler equation by means of a two-dimensional autocorrelation approach. *IEEE Transactions on Ultrasonics, Ferroelectrics, and Frequency Control, 42*(4), 672-688.

Lubinski, M. A., Emelianov, S. Y., Raghavan, K. R., Yagle, A. E., Skovoroda, A. R. & O'Donnell, M. (1996). Lateral displacement estimation using tissue incompressibility. *IEEE Transactions on Ultrasonics, Ferroelectrics, and Frequency Control, 43*(2), 247-256.

Ludwig, G. D., & Struthers, F. W. (1949). *Considerations underlying the use of ultrasound to detect gallstones and foreign bodies in tissues* (Tech. Rep. No. Project 004 001 Report no 4). Naval Med. Res. Inst. Reports.

Lundberg, B. (1985). Chemical composition and physical state of lipid deposits in atherosclerosis. *Atherosclerosis, 56*, 93-110.

Madsen, E. L., Zagzebski, J. A., Banjavie, R. A. & Jutila, R. E. (1978). Tissue mimicking materials for ultrasound phantoms. *Medical Physics, 15*(5), 391-394.

Madsen, E. L., Zagzebski, J. A. & Frank, G. R. (1982a). Oil-in-gelatin dispersions for use as ultrasonically tissue-mimicking materials. *Ultrasound in Medicine and Biology, 8*(3), 277-287.

Madsen, E. L., Zagzebski, J. A., Insana, M. F., Burke, T. M. & Frank, G. R. (1982b). Ultrasonically tissue- mimicking liver including the frequency dependence of backscatter. *Medical Physics, 9*(5), 703-710.

Merickel, M. B., Berr, S., Spetz, K., Jackson, T. R., Snell, J., Gillies, P., Shimshick, E., Hainer, J., Brookeman, J. R. & Ayers, C. R. (1993). Noninvasive quantitative evaluation of atherosclerosis using MRI and image analysis. *Arteriosclerosis and Thrombosis, 13*(8), 1180-1186.

Meunier, J., & Bertrand, M. (1995). Ultrasonic texture motion analysis: theory and simulation. *IEEE Transactions on Medical Imaging, 14*(2), 293-300.

Miller, D. D., Rivera, F. J., Garcia, O. J., Palmaz, J. C., Berger, H. J. & Weisman, H. F. (1991). Imaging of vascular injury with 99m Tc-labeled monoclonal antiplatelet antibody S12: Preliminary experience in human percutaneous transluminal angioplasty. *Circulation, 85*(4), 1354-1363.

Miller, J. G., Pérez, J. E. & Sobel, B. E. (1985). Ultrasonic characterization of the myocardium. *Progres. Cardiovasc. Dis., 28*, 85-110.

Miller, M. A., & Leavell, L. C. (1972). *Kimber-gray-stackpole's anatomy and physiology* (16th ed.). New York: The Macmillan Corporation.

Milnor, W. R. (1982). *Hemodynamics.* Baltimore, MD: Williams & Wilkins.

Mintz, G. S., Pichard, A. D., Kovach, J. A., Kent, K. M., Satler, L. F., Javier, S. P., Popma, J. J. & Leon, M. B. (1994). Impact of preintervention intravascular ultrasound imaging on transcatheter treatment strategies in coronary artery disease. *American Journal of Cardiology, 73*(7), 423-430.

Mintz, G. S., Popma, J. J., Kent, K. M., Satler, L. F., Wong, S. C., Hong, M. K., Kovach, J. A. & Leon, M. B. (1996). Arterial remodeling after coronary angioplasty. a serial intravascular ultrasound study. *Circulation, 94*(1), 35-43.

Moreno, P. R., Falk, E., Palacios, I. F., Newell, J. B., Fuster, V. & Fallon, J. T. (1994). Macrophage infiltration in acute coronary syndromes: implcations for plaque rupture. *Circulation, 90*(2), 775-778.

Mozersky, D. J., Sumner, D. S., Hokanson, D. E. & Strandness, D. E. (1972). Transcutaneous measurement of the elastic properties of the human femoral artery. *Circulation, 46*, 948-955.

Nishimura, R. A., Edwards, W. D., Warnes, C. A., Reeder, G. S., Holmes, D. R., Tajik, A. J. & Yock, P. G. (1990). Intravascular ultrasound imaging: in vitro validation and pathologic correlation. *Journal of American College of Cardiology, 16*(1), 145-154.

Nissen, S. E., & Gurley, J. C. (1991). Application of intravascular ultrasound for detection and quantitation of coronary atherosclerosis. *International Journal of Cardiac Imaging, 6*, 165-177.

Noordergraaf, A. (1969). Hemodynamics. In P. Schwan (Ed.), *Biological engineering.* New York, USA: McGraw-Hill.

O'Donnell, M., Eberle, M. J., Stephens, D. N., Litzza, J. L., San Vicente, K. & Shapo, B. M. (1997). Synthetic phased arrays for intraluminal imaging of coronary arteries. *IEEE Transactions on Ultrasonics, Ferroelectrics, and Frequency Control, 44*(3), 714-721.

O'Donnell, M., Emelianov, S. Y., Skovorada, A. R., Lubinski, M. A., Weitzel, W. F. & Wiggins, R. C. (1993). Quantitative elasticity imaging. *IEEE Ultrasonics Symposium Proceedings*, 893-903.

O'Donnell, M., Skovoroda, A. R. & Shapo, B. M. (1991). Measurement of arterial wall motion using fourier based speckle tracking algorithm. *IEEE Ultrasonics Symposium Proceedings, Orlando, Fl, USA*, 1101-1103.

O'Donnell, M., Skovoroda, A. R., Shapo, B. M. & Emelianov, S. Y. (1994). Internal displacement and strain imaging using ultrasonic speckle tracking. *IEEE Transactions on Ultrasonics, Ferroelectrics, and Frequency Control, 41*, 314-325.

O'Donnell, M., & Thomas, L. J. (1992). Efficient synthetic aperture imaging from a circular aperture with possible application to catheter based imaging. *IEEE Transactions on Ultrasonics, Ferroelectrics, and Frequency Control, 39*(3), 366-380.

Oosterveld, B. J., Thijssen, J. M., Hartman, P. C. & Rosenbusch, G. J. E. (1991). Detection of difuse liver disease by quantitative echography. *Ultrasound in Medicine and Biology, 19*, 21-25.

Ophir, J., Céspedes, E. I., Garra, B., Ponnekanti, H., Huang, Y. & Maklad, N. (1996). Elastography: ultrasonic imaging of tissue strain and elastic modulus in vivo. *European Journal Ultrasound, 3*, 49-70.

Ophir, J., Céspedes, E. I., Ponnekanti, H., Yazdi, Y. & Li, X. (1991). Elastography: a method for imaging the elasticity in biological tissues. *Ultrasonic Imaging, 13*, 111-134.

Pagani, M., Mirsky, I., Baig, H., Manders, W. T., Kerkhof, P. & Vatner, S. F. (1979). Efffects of age on aortic pressure-diameter and elastic stiffness-stress relationships in unanesthesized sheep. *Circulation Research, 44*, 420-429.

Parker, K. J., Gao, L., Lerner, R. M. & Levinson, S. F. (1996). Techniques for elastic imaging: a review. *IEEE Engineering in Medicine and Biology, November/December*, 52-59.

Parker, K. J., Huang, S. R., Musulin, R. A. & Lerner, R. M. (1990). Tissue response to mechanical vibrations for "sonoelasticity imaging". *Ultrasound in Medicine and Biology, 16*(3), 241-246.

Parker, K. J., & Lerner, R. M. (1992). Sonoelasticity of organs, shear waves ring a bell. *Journal of Ultrasound in Medicine, 11*, 387-392.

Pasterkamp, G., Schoneveld, A. H., van der Wal, A. C., Haudenschild, C. C., Clarijs, R. J., Becker, A. E., Hillen, B. & Borst, C. (1998). Relation of arterial geometry to luminal narrowing and histologic markers for plaque vulnerability: the remodeling paradox. *Journal of the American College of Cardiology, 32*(3), 655-662.

Pasterkamp, G., Schoneveld, A. H., van der Wal, A. C., Hijnen, D. J., van Wolveren, W. J., Plomp, S., Teepen, H. L. & Borst, C. (1999). Inflammation of the atherosclerotic cap and shoulders of the plaque is a common and locally observed feature in unrupted plaques of femoral and coronary arteries. *Arteriosclerosis, Thrombosis and Vascular Research, 19*(1), 54-58.

Pasterkamp, G., van der Heiden, M. S., Post, M. J., Borst, C., Gussenhoven, E. J., Pieterman, H., van Urk, H. & Bom, N. (1995). Discrimination of intravascular lumen and dissections in single intravascular ultrasound images using subtraction, conventional averaging and saline flush. *Ultrasound in Medicine and Biology, 21*(2), 149-156.

Patel, D. J., & Janicki, J. S. (1970a). Static elastic properties of the left coronary circumflex artery and the common carotid artery in dogs. *Circulation research, 27*, 149-158.

Patel, D. J., Tucker, W. K. & Janicki, J. S. (1970b). Dynamic elastic properties of the aorta in radial direction. *Journal of Applied Physiology, 28*(5), 578-582.

Pérez, J. E., Miller, J. G., Barzilai, B., Wickline, S., Mohr, G. A., Wear, K., Vered, Z. & Sobel, B. E. (1988). Progress in quantitative ultrasonic characterization of the myocardium: From the laboratory to the bedside. *Journal of the American Society of Echocardiology, 1*, 294-305.

Peterson, L. H., Jenssen, R. E. & Parnell, J. (1960). Mechanical properties of arteries in vivo. *Circulation Research, 8*, 622-639.

Pignoli, P., Tremoli, E., Poli, A., Oreste, P. & Paoletti, R. (1986). Intimal plus medial thickness of the arterial wall: a direct measurement with ultrasound imaging. *Circulation, 74*(6), 1399-1406.

Ponnekanti, H., Ophir, J. & Céspedes, E. I. (1992). Axial stress distribution between coaxial compressors in elastography: an analytical model. *Ultrasound in Medicine and Biology, 18*, 667-673.

Potkin, B. N., Bartorelli, A. L., Gessert, J. M., Neville, R. F., Almagor, Y., Roberts, W. C. & Leon, M. B. (1990). Coronary artery imaging with intravascular high-frequency ultrasound. *Circulation, 81*(5), 1575-1585.

Potkin, B. N., Keren, G., Mintz, G. S., Douek, P. C., Pichard, A. D., Satler, L. F., Kent, K. M. & Leon, M. B. (1992). Arterial responses to balloon coronary angioplasty: an intravascular ultrasound study. *Journal of American College of Cardiology, 20*, 942-951.

Quazi, A. H. (1981). An overview of the time delay estimate in acitve and passive systems for target localization. *IEEE Transactions on Acoustics, Speech, and Signal Processing, 29*, 527-533.

Raman, C. V. (1928a). A change of wavelength in light scattering. *Nature, 121*, 618.

Raman, C. V., & Krishnan, K. S. (1928b). A new type of secondary radiation. *Nature, 121*, 501-502.

Remley, W. R. (1963). Correlation of signals having a linear delay. *Journal of the Acoustical Society of America, 35*, 65-69.

Reneman, R. S., van Merode, T., Hick, P., Muytjens, A. M. M. & Hoeks, A. P. G. (1986). Age-related changes in carotid artery wall properties in men. *Ultrasound in Medicine and Biology, 12*(6), 465-471.

Rhea, M. R., Walker, I. C. & Cutler, E. C. (1924). The surgical treatment of mitral stenosis: experimental and clinical studies. *Archives of Surgery, 6*, 689-690.

Richardson, P. D., Davies, M. J. & Born, G. V. R. (1989). Influence of plaque configuration and stress distribution on fissuring of coronary atherosclerotic plaques. *The Lancet, 21*, 941-944.

Rijsterborgh, H., Mastik, F., Lancée, C. T., Verdouw, P. D., Roelandt, J. R. T. C. & Bom, N. (1993). Ultrasound myocardial intergrated backscatter signal processing: frequency domain versus time domain. *Ultrasound in Medicine and Biology, 19*, 211-219.

Römer, T. J. (1999). *Raman spectroscopy of arterial wall.* Phd dissertation, Rijksuniversiteit, Leiden, The Netherlands.

Römer, T. J., BrennanIII, J. F., Fitzmaurice, M., Feldstein, M. L., Deinum, G., Myles, J. L., Kramer, J. R., Lees, R. S. & Feld, M. S. (1998). Histopathology of human coronary atherosclerosis by quantifying its chemical composition with raman spectroscopy. *Circulation, 97*, 878-885.

Romijn, R. L., Thijssen, J. M., Oosterveld, B. J. & Verbeek, A. M. (1991). Ultrasonic differentiation of intra-ocular melanomas: parameters and estimation methods. *Ultrasonic Imaging, 3*, 27-55.

Rubens, D. J., Hadley, M. A., Alam, S. K., Gao, L., Mayer, R. D. & Parker, K. J. (1995). Sonoelasticity imaging of prostate cancer: in vitro results. *Radiology, 195*, 379-383.

Ryan, L. K., & Foster, F. S. (1997a). Tissue equivalent vessel phantoms for intravascular ultrasound. *Ultrasound in Medicine and Biology, 23*(2), 261-273.

Ryan, L. K., & Foster, F. S. (1997b). Ultrasonic measurement of differential displacement and strain in a vascular model. *Ultrasonic Imaging, 19*, 19-38.

Ryan, L. K., Lockwood, G. R., Bloomfield, T. S. & Foster, F. S. (1993). Speckle tracking in high frequency ultrasound images with applications to intravascular imaging. *IEEE Ultrasonics Symposium Proceeedings*, 889-892.

Ryan, L. K., Lockwood, G. R., Staskoski, B. G. & Foster, F. S. (1992). A high frequency intravascular ultrasound imaging system for investigation of vessel wall properties. *IEEE Ultrasonics Symposium Proceeedings, Tucson, AZ, USA*, 1101-1105.

Sagar, K. B., Rhyne, T. L., Warltier, D. C., Pelc, L. E. & Wann, L. S. (1987). Intramyocardial variability in intergrated backscatter: effects of coronary occlusion and reperfusion. *Circulation, 75*, 436-442.

Sarvazyan, A. P., Emelianov, S. Y. & Skovorada, A. R. (1993). Intracavity device for elasticity imaging. Patent application 5,265,612, November 39.

Schwarzacher, S. P., Honda, Y., Metz, J. A., Asvar, C. A., Fitzgerald, P. J. & Yock, P. G. (1997). Impact of curve distortion errors on intravascular ultrasound measurements and three-dimensional reconstructions. *The American Journal of Cardiology, 79*, 384-387.

Serruys, P. W., Emanuelsson, H., van der Giessen, W., Lunn, A. C., Kiemeney, F. & et al. (1996). Heparin-coated Palmaz-Schatz stents in human coronary arteries. early outcome of the BENESTENT-II pilot study. *Circulation, 93*, 412-22.

Serruys, P. W., Hout, B. van, Bonnier, H., Legrand, V., Garcia, E., Macaya, C., Sousa, E., Giessen, W. van der, Colombo, A., Seabra-Gomes, R., Kiemeneij, F., Ruygrok, P., Ormiston, J., Emanuelsson, H., Fajadet, J., Haude, M., Klugmann, S. & Morel, M. A. (1998). Randomised comparison of implantation of heparin-coated stents with balloon angioplasty in selected patients with coronary artery disease (BENESTENT II). *Lancet, 352*(9129), 673-81.

Shapo, B. M., Crowe, J. R., Erkamp, R., Emelianov, S. Y., Eberle, M. & O'Donnell, M. (1996a). Strain imaging of coronary arteries with intraluminal ultrasound: experiments on an inhomogeneous phantom. *Ultrasonic Imaging, 18*, 173-191.

Shapo, B. M., Crowe, J. R., Skovoroda, A. R., Eberle, M., Cohn, N. A. & O'Donnell, M. (1996b). Displacement and strain imaging of coronary arteries with intraluminal ultrasound. *IEEE Transactions on Ultrasonics, Ferroelectrics, and Frequency Control, 43*(2), 234-246.

Siegel, R. J., Ariani, M., Fishbein, M. C., Chae, J., Park, J. C., Maurer, G. & Forrester, J. S. (1991). Histopathologic validation of angioscopy and intravascular ultrasound. *Circulation, 84*(1), 109-117.

Skovoroda, A. R., Emelianov, S. Y. & O'Donnell, M. (1995). Tissue elasticity reconstruction based on ultrasonic displacement and strain images. *IEEE Transactions on Ultrasonics, Ferroelectrics, and Frequency Control, 42*, 747-765.

Slager, C. J., Essed, C. E., Schuurbiers, J. C. H., Bom, N., Serruys, P. W. & Meester, G. T. (1985). Vaporization of atherosclerotic plaques by spark erosion. *Journal of the American College of Cardiology, 5*, 1382-1386.

Slager, C. J., Wentzel, J. J., Oomen, J. A. F., Schuurbiers, J. C. H., Krams, R., von Birgelen, C., Tjon, A., Serruys, P. W. & de Feyter, P. J. (1997). True reconstruction of vessel geometry from combined X-ray angiography and intracoronary ultrasound data. *Seminars in Interventional Cardiology, 2*(1), 43-47.

Somer, J. C. (1968). Electronic sector scanning for ultrasonic diagnosis. *Ultrasonics, 6*(3), 153-159.

Soualmi, L. (1998). *Caracterisation des proprietes elastiques de la paroi arterielle par ultrasonographie endovasculaire.* Phd dissertation, Ecole polytechnic de Montreal, Canada.

Soualmi, L., Bertrand, M., Mongrain, R. & Tardif, J. C. (1997). Forward and inverse problems in endovascular elastography. In S. Lees & L. A. Ferrari (Eds.), *Acousical imaging* (Vol. 23, p. 203-209). New York, USA: Plenum.

Spencer, T., Ramo, M. P., Salter, D. M., Anderson, T., Kearney, P. P., Sutherland, G. R., Fox, K. A. A. & McDicken, W. N. (1997). Assessment of regional vascular distensibility in deceased iliofemoral arteries by intravascular ultrasound. *Ultrasound in Medicine and Biology, 20*(6), 529-542.

Stadler, R. W., Karl, W. C. & Lees, R. S. (1996). The application of echo-tracking methods to endothelium-dependent vasoreactivity and arterial compliance measurements. *Ultrasound in Medicine and Biology, 22*(1), 35-42.

Talhami, H. E., Wilson, L. S. & Neale, M. L. (1994). Spectral tissue strain: a new technique for imaging tissue strain using intravascular ultrasound. *Ultrasound in Medicine and Biology, 20*(8), 759-772.

te Nijenhuis, K. (1981a). Investigation into the aging process in gels in gelatin/water systems by measurement of their dynamic moduli. part 1- phenomenology. *Colloid & Polymer Science, 259*(5), 522-535.

te Nijenhuis, K. (1981b). Investigation into the aging process in gels in gelatin/water systems by measurement of their dynamic moduli. part 2- mechanisms of the aging process. *Colloid & Polymer Science, 259*(10), 1017-1026.

Tearney, G. J., Brezinski, M. E., Bouma, B. E., Boppart, S. A., Pitris, C., Southern, J. F. & Fujimoto, J. G. (1997). In vivo endoscopic optical biopsy with optical coherence tomography. *Science, 276*, 2037-2039.

ten Hoff, H., Korbijn, A., Smit, T. H., Klinkhamer, J. F. F. & Bom, N. (1989). Imaging artefacts in mechanically driven ultrasound catheters. *International Journal of Cardiac Imaging, 4*, 195-199.

The, S. H. K., Gussenhoven, E. J., Pieterman, H., van Bortel, L. M. A. B., Li, W., Roelandt, J. R. T. C., de Feyter, P. & van Urk, H. (1995). Assessment of regional vascular distensibility in diseased iliofemoral arteries by intravascular ultrasound. *Ultrasound in Medicine and Biology, 21*, 17-24.

Thieme, T., Wernecke, K. D., Meyer, R., Brandenstein, E., Habedank, D., Hintz, A., Felix, S. B., Baumann, G. & Kleber, F. X. (1996). Angioscopic evaluation of atherosclerotic plaques: validation by histomorphologic analysis and association with stable and unstable coronary syndromes. *Journal of American College of Cardiology, 28*(1), 1-6.

Thijssen, J. M., Oosterveld, B. J., Hartman, P. C. & Rosenbusch, G. J. E. (1993). Correlations between acoustic and texture parameters from rf and B-mode liver echograms. *Ultrasound in Medicine and Biology, 19*, 13-20.

ThomasJr, G. J., & Agard, D. A. (1984). Quantitative analysis of nucleid acids, proteins, and viruses by raman band deconvolution. *Biophysical Journal, 46*, 763-768.

Thompson, R. S., & Wilson, L. S. (1996). The effect of variations in transducer position and sound speed in intravascular ultrasound: a theoretical study. *Ultrasound in Medicine and Biology, 22*(6), 719-734.

Thurstone, F. L., & von Ramm, O. T. (1974). A new ultrasound imaging technique employing two dimensional electronic beam steering. In P. S. Green (Ed.), *Acoustical holography and imaging* (Vol. 5, p. 249-259). Plenum Press.

Timoshenko, S. P., & Goodier, J. N. (1970). *Theory of elasticity.* Singapore: McGraw-Hill.

Tobis, J. M., Mahon, D. J., Moriuchi, M., Honye, J. & McRae, M. (1991). Intravascular ultrasound imaging following balloon angioplasty. *International Journal of Cardiac Imaging, 6*, 191-205.

Topol, E. J., & Nissen, S. E. (1995). Our preoccupation with coronary luminology: the dissociation between clinical and angiographic findings in ischamic heart disease. *Circulation, 92*, 2333-2442.

Toussaint, J. F., Southern, J. M., Fuster, V. & Kantor, H. L. (1994). 13 C-NMR spectroscopy of human atherosclerotic lesions: relation between fatty acid saturation, cholesteryl ester content and luminal obstruction. *Circulation, 14*(12), 1951-1957.

Trahey, G. E., Allison, J. W. & von Ramm, O. T. (1988). Angle independent ultrasonic detection of blood flow. *IEEE Transactions on Biomedical Engineering, 34*, 965-967.

Tristam, M., Barbosa, D. C., Cosgrove, D. O., Bamber, J. C. & Hill, C. R. (1988). Application of Fourier analysis in clinical study of patterns in tissue movement. *Ultrasound in Medicine and Biology, 14*(8), 695-707.

Tristam, M., Barbosa, D. C., Cosgrove, D. O., Nassiri, D. K., Bamber, J. C. & Hill, C. R. (1986). Ultrasonic study of in vivo kinetic characteristics of human tissues. *Ultrasound in Medicine and Biology, 12*(12), 927-937.

Tsuda, H., Ruben, J. & Arends, J. (1996). Raman spectra of human dentin mineral. *European Journal of Oral Science, 104*, 123-131.

Vallabhajosula, S., Paidi, M., Badimon, J. J., Le, N., Goldsmith, S. J., Fuster, V. & Ginsberg, H. N. (1988). Radiotracers for low density lipoprotein biodistribution studies in vivo: technetium-99m low density lipoprotein versus radioiodinated low density lipoprotein preparations. *Journal of Nuclear medicine, 29*(7), 1237-1245.

van Beusekom, M. M. M., Serruys, P. W., Post, J. C., Verdouw, P. D. & van der Giessen, W. J. (1994). Stenting or balloon angioplasty of stenosed autologos saphenous vein grafts in pigs. *American Heart Journal, 127*, 273-281.

van den Aarssen, M., Verhoef, W. A. & Thijssen, J. M. (1989). Influence of absorbing and scattering media on the propagation of ultrasound. *Journal of the Acoustic Society of America, 85*(2), 145-161.

van der Lugt, A., Gussenhoven, E., Stijnen, T., van Strijen, M., van Driel, E., van Egmond, F. C., van Suylen, R. J. & van Urk, H. (1995). Comparison of intravascular ultrasonic findings after coronary balloon angioplasty evaluated in vitro with histology. *Journal of the American College of Cardiology, 76*, 661-666.

van der Steen, A. F. W., Cuypers, M. H. M., Thijssen, J. M. & de Wilde, P. C. M. (1991). Influence of histochemical preparation on acoustical parameters of liver tissue, a 5 MHz study. *Ultrasound in Medicine and Biology, 17*, 879-891.

van der Steen, A. F. W., Rijsterborgh, H., Lancée, C. T., Mastik, F., Krams, R., Verdouw, P. D., Roelandt, J. R. T. C. & Bom, N. (1997). Influence of data processing on cyclic variation of intergrated backscatter and wall thickness in stunned porcine myocardium. *Ultrasound in Medicine and Biology, 23*, 405-414.

van der Steen, A. F. W., Thijssen, J. M., van der Laak, J. A. W. M., Ebben, G. P. J. & de Wilde, P. C. M. (1994). A new method for correlation of acoustical spectroscopy microscopy (30 MHz) and light microscopy. *Journal of Microscopy, 175*, 21-33.

van Leeuwen, T. G., Meertens, J. H., Velema, E., Post, M. J. & Borst, C. (1993). Intraluminal vapour bubble induced by excimer laser pulse causes microsecond arterial dilation and invagination leading to extensive wall damage in the rabbit. *Circulation, 83*, 1258-1263.

van Leeuwen, T. G., Veen, M. J. van der, Verdaasdonk, R. M. & Borst, C. (1991). Noncontact tissue ablation by holmium: YAGG laser pulses in blood. *Lasers in Surgery and Medicine, 11*, 26-34.

Varghese, T., & Ophir, J. (1996). Estimating tissue strain from signal decorrelation using the correlation coefficient. *Ultrasound in Medicine and Biology, 22*(9), 1249-1254.

von Ramm, O. T., & Bashford, G. (1991). High speed ultrasound volumetric imaging system. part 2: parallel processing and image display. *IEEE Transactions on Ultrasonics, Ferroelectrics, and Frequency Control, 38*, 109-115.

Walker, W. F., & Trahey, G. E. (1994). A fundamental limit on the accuracy of speckle signal alignment. *IEEE Ultrasonics Symposium Proceedings*, 1787-1791.

Walker, W. F., & Trahey, G. E. (1995). A fundamental limit on delay estimation using partially correlated speckle signals. *IEEE Transactions on Ultrasonics, Ferroelectrics, and Frequency Control, 42*, 301-308.

Waller, B. F. (1989). Crackers, breakers, stretchers, drillers, scrapers, shavers, burners, welders and melters. the future treatment of atherosclerotic coronary artery disease. *Journal of the American College of Cardiology, 13*, 969-987.

Wear, K. A., & Popp, R. L. (1987). Theoretical analysis of a technique for the characterization of myocardium contraction based upon temporal correlation of ultrasonic ehoes. *IEEE Transactions on Ultrasonics, Ferroelectrics, and Frequency Control, 34*.

Wells, P. N. T. (1966). Developments in medical ultrasonics. *World Med Electron, 66*, 272-277.

Wells, P. N. T. (1977). *Biomedical ultrasonics*. London: Academic Press.

White, C. J., Ramee, S. R., Collins, T. J., Escobar, A. E., Karsan, A., Shaw, D., Jain, S. P., Bass, T. A., Heuser, R. R., Teirstein, P. S., Bonan, R., Walter, P. D. & Smalling, R. W. (1996). Coronary thrombi increase PTCA risk: angioscopy as clinical tool. *Circulation, 93*, 253-258.

Wild, J. J., & Reid, J. M. (1952). Application of echo ranging techniques to the determination of structures of biological tissues. *Science, 115*, 226.

Wild, J. J., & Reid, J. M. (1954). Echographic visualisation of lesions of the living intact human breast. *Cancer Research, 14*, 277-283.

Wilson, L. S., Neale, M. L., Talhami, H. E. & Appleberg, M. (1994). Preliminary results from attenuation-slope mapping of plaque using intravascular ultrasound. *Ultrasound in Medicine and Biology, 20*(6), 529-542.

Wilson, L. S., & Robinson, D. E. (1982). Ultrasonic measurement of small displacements and deformations of tissues. *Ultrasonic Imaging, 4*, 71-82.

Wilson, R. A., di Mario, C., Krams, R., Soei, L. K., Wenguang, L., Laird, A. C., The, S. H. K., Gussenhoven, E., Verdouw, P. & Roelandt, J. R. T. C. (1995). In vivo measurement of regional large artery compliance by intravascular ultrasound under pentovarbital anesthesia. *Angiology, 46*(6), 481-488.

Wolverson, M. K., Bashiti, H. M. & Peterson, G. J. (1983). Ultrasonic tissue characterization of atheromatous plaques using a high resolution real time scanner. *Ultrasound in Medicine and Biology, 9*(6), 599-609.

Yamakoshi, Y., Sato, J. & Sato, T. (1990). Ultrasonic imaging of internal vibrtation of soft tissue under forced vibration. *IEEE Transactions on Ultrasonics, Ferroelectrics, and Frequency Control, 17*, 45-53.

Yamamoto, K., Shikutani, M., Amano, T. & Okamoto, E. (1993). An intravascular ultrasonic imaging technique for measurement of elastic properties of the artery. *Acoustical Imaging, 20*, 433-440.

Yaroslavsky, I. V., Yaroslavsky, A. N. & Otto, C. (1994). Combined elastic and raman light scattering of human lenses. *Experimental Eye Research, 59*, 393-399.

Yock, P. G., & Linker, D. T. (1990). Intravascular ultrasound. looking below the surface of vascular disease. *Circulation, 81*(5), 1715-1718.

Summary

Intravascular ultrasound (IVUS) is a technique that provides real-time cross sectional images *in vivo* of the geometry of the vessel wall, plaque and lumen. However, characterisation of different plaque components still remains a problem. Although other new imaging techniques show promising results, characterisation of atherosclerotic plaques *in vivo* remains difficult. An even more challenging problem is identification of plaque vulnerability.

Elastography is a new imaging technique that visualises mechanical properties of tissue. The underlying principle is that the response of tissue to a mechanical excitation is a function of its mechanical properties. The technique was evaluated *in vitro*, and experiments *in vivo* demonstrated the potential to apply elastography in a clinical environment. In this thesis, the usefulness and additional diagnostic value of the technique for intravascular purposes is investigated.

In intravascular applications, the intraluminal pressure can act as the mechanical stimulus to strain the tissue. Using the systemic pressure that is already present in the body, different strain levels can be achieved. The strain is determined using data obtained with an intravascular catheter. Since the strain levels are on the order of 1%, analysis of high frequency rf-signals was used. *In vitro* experiments on vessel-mimicking phantoms and diseased artery specimens were performed in a watertank. A water column system was used to pressurise the vessels at different levels. A modified IntraSound (DuMED/EndoSonics, Rijswijk, The Netherlands) and a commercial InVision (EndoSonics, Rijswijk, The Netherlands) echoapparatus with custom rf-data output were used to acquire the data. The data was digitised and processing of the data was performed offline. First, the time delay between gated signals was determined using cross-correlation analysis. Next, the finite difference of the time delay was used to determine the strain.

The potential of the technique to identify soft and hard plaques in a vessel wall was investigated by phantom studies. First, the mechanical properties of agar-gelatin based phantom materials were determined. These materials are often used as tissue mimicking material in ultrasound experiments. The hardness of these materials was directly related to the agar concentration. By adjusting the concentration of Carborundum (SiC) particles, which were acting as scattering particles, hyper- and hypo-echoic materials could be constructed. The experimental results on phantoms, with the geometry of a vessel wall with a soft or hard plaque, revealed that characterisation of the different plaques was feasible. Identification of hard and soft materials was independent on the echogenicity contrast between the vessel wall and plaque.

The vessel phantoms were up-scaled versions of human femoral and coronary arteries. As a consequence, the resolution of the technique had to be improved. The signal-

to-noise ratio of the system was increased by improving the data acquisition system. Additionally, the mechanical scanning mechanism was upgraded. Finally, a filter was developed to determine the reliability of the estimated strain values. This filter uses the peak of the correlation function as a figure of merit for the strain estimate. It is based on decorrelation properties of compressed tissue. When tissue is compressed, the peak value of the correlation function decreases. The peak value can be determined theoretically and is a function of the center frequency of the transducer, the window length and the rate of compression. Since the strain is determined using the cross correlation function, the peak value can directly be used to check if the determined strain value is in accordance with the peak value.

The influence of the position of the catheter on the strain was also investigated. Theoretical relations between the position in the lumen and the measured strain were derived: the measured strain decreased in certain regions in the vessel wall when the catheter was not positioned in the center of the lumen. The error in the measured strain increased with the distance of the catheter to the center. Since this error could be described theoretically, correction for this artifact is feasible. However, for catheter positions close to the vessel wall correction is not possible. Also the influence of a tilted catheter in the lumen was determined. For known tilt-angles correction for the resulting artifact is possible.

A robust compound imaging technique was developed that will be easier to implement for *in vivo* applications: intravascular ultrasound palpation. This compound imaging technique presents the mechanic and acoustic information in one image. The strain information is plotted as a colour coded line congruent with the lumen vessel wall boundary. In this way, the mechanical information can directly be linked to the conventional IVUS echogram information. Since only one strain estimate per angle is determined corresponding to a substantial portion of the vessel wall, this method is faster and more robust than elastography. The technique was validated using vessel phantoms and diseased human arteries: soft and hard material were identified using the strain palpogram. Additionally, fibrous and fatty plaque components could be differentiated with the information provided by the palpograms.

Diseased human femoral arteries were measured with the upgraded elasticity imaging system. Data was obtained at intraluminal pressures of 80 and 100 mmHg. Preliminary experiments revealed the feasibility to obtain elastograms from diseased and normal parts of the vessel wall. The resolution of the technique (300 μm) was sufficient to determine several strain estimates per angle in the vessel wall and plaque. Calcified regions were identifiable on the elastogram by their low strain. Normal vessel wall regions had moderate to high strain levels where fibrous regions showed strain values in between these two.

Encouraged by the preliminary results, a larger scale *in vitro* study was performed. 35 cross-sections in 9 diseased human femoral arteries were scanned. Elastograms were determined and the IVUS cross-sections were segmented based on the strain value. The specimens were processed for histology and staining techniques to identify fibrous, fatty and calcified material were performed. Additionally, a staining technique to indicate the presence of macrophages was performed. The presence of macrophages is a marker for plaque vulnerability. Correlation of the elastographic results with the dominant tissue type present in the plaque, revealed a significant difference between the strain values for the plaque types ($p < 0.001$). Especially, the strain value in fibrous and fatty material was

significantly different (p=0.0012). The results of this study demonstrated the potential of the technique to characterise different plaque components and to identify vulnerability of plaque.

Finally, the feasibility of the technique to be applied *in vivo* was investigated. During *in vivo* experiments the systemic pressure was used as mechanical stimulus. However, due to the contraction of the heart, the catheter is moving in the lumen. Especially motion along the long axis of the vessel wall is a problem since data from different cross-sections are acquired. In this case, the strain in the tissue cannot be determined. The results of the experiments revealed that motion of the catheter in minimal near end diastole. Two frames could be acquired at this point in the pressure cycle with a pressure differential in the order of 5 mmHg. Preliminary results indicate that reproducible elastograms can be obtained in one and over several pressure cycles.

In conclusion, intravasular elastography is a technique capable of providing cross-sectional images of the mechanical properties of the vessel wall and plaque. Soft and hard material can be identified independently of the echogenicity of the materials. The potential to characterise different plaque components using this information was demonstrated *in vitro*. Additionally, the potential to identify the vulnerability of the plaque was shown. Preliminary experiments demonstrated the feasibility of the technique to be applied *in vivo*.

Samenvatting

Intravasculair ultrageluid (IVUS) is een techniek waarmee real-time dwarsdoorsneden van vaten gemaakt worden zodat de geometrie van de vaatwand, het lumen en de laesie afgebeeld kunnen worden. Met deze techniek is het echter moeilijk om de verschillende soorten laesies te karakteriseren. Hoewel er nieuwe technieken worden ontwikkeld blijft vooral de *in vivo* karakterisatie van de verschillende laesies moeilijk. Een nog grotere uitdaging vormt de detectie van instabiele laesies.

Elastografie is een nieuwe afbeeldingstechniek, waarmee de mechanische eigenschappen van weefsel kunnen worden bepaald. Deze techniek is gebaseerd op het principe dat de vervorming van weefsel, als gevolg van een mechanische stimulus, een functie is van de mechanische eigenschappen van het weefsel. De techniek is gevalideerd aan de hand van *in vitro* experimenten. *In vivo* experimenten hebben aangetoond dat elastografie van toegevoegde waarde kan zijn in een klinische omgeving. In dit proefschrift wordt de toepasbaarheid en bruikbaarheid van deze techniek in intravasculaire applicaties beschreven.

Voor intravasculaire toepassingen kan de pulsatie van de bloeddruk gebruikt worden als mechanische stimulus. De vervorming wordt bepaald aan de hand van data die wordt verkregen met een intravasculaire echocatheter. Omdat de vervorming van het weefsel klein is (in de orde van 1%), wordt gebruik gemaakt van de radio frequentie (rf-) signalen. *In vitro* experimenten met vaatfantomen en aangetaste arteriën werden uitgevoerd in een waterbak. Een waterkolom systeem werd gebruikt om verschillende druk niveaus in de vaten aan te brengen. Een gemodificeerd IntraSound echoapparaat (DuMED/EndoSonics, Rijswijk) en een commercieel verkrijgbaar InVision echoapparaat (EndoSonics, Rijswijk), met een speciale rf-signaal uitgang, werden gebruikt om de data te verkrijgen. De data werd vervolgens gedigitaliseerd en off-line verwerkt. Allereerst werd de tijdsvertraging tussen segmenten van het rf-signaal bepaald met behulp van cross-correlatie technieken. Vervolgens werd aan de hand van de afgeleide van deze tijdsvertragings functie de mate van vervorming van het weefsel bepaald.

Met behulp van een vaatfantoom studie werd de mogelijkheid van de techniek om harde en zachte laesies in een vaatwand te identificeren onderzocht. Eerst werden de mechanische eigenschappen van materialen, gemaakt van agar en gelatine, onderzocht. Deze materialen worden in ultrageluids experimenten vaak gebruikt als weefsel nabootsende materialen. De hardheid van de materialen bleek direct gerelateerd te zijn aan de agar concentratie. Carborundum (SiC) deeltjes werden gebruikt om het geluid te reflecteren. Door de concentratie van deze deeltjes te varieren konden, hyper en hypo echogene materialen worden gemaakt. De resultaten van de experimenten met de vaatfantomen, toonden aan dat identificatie van harde en zachte laesies met elastografie

mogelijk was. Deze resultaten waren onafhankelijk van een al dan niet aanwezig contrast in echo-eigenschappen van de vaatwand en de laesie.

De gebruikte vaatfantomen waren vergrote versies van humane femoraal en coronair arteriën. Om de techniek toe te kunnen passen op humaan materiaal moest de resolutie verbeterd worden. De signaal ruisverhouding van het systeem werd vergroot door het data acquisitie systeem te verbeteren. Verder werd het mechanische scan mechanisme verbeterd. Als laatste werd een filter ontwikkeld om de betrouwbaarheid van de berekende vervormingswaarden te bepalen. Aan de hand van de piekwaarde van de correlatie functie wordt de betrouwbaarheid van de vervormingswaarde bepaald. Dit filter is gebaseerd op decorrelatie eigenschappen van gecomprimeerd weefsel. Wanneer het weefsel gecomprimeerd is zal de piekwaarde van de correlatie functie afnemen. De piekwaarde kan theoretisch worden bepaald en is een functie van de centrale frequentie van de transducent, de segmentgrootte en de mate van compressie. Omdat de vervorming wordt bepaald met behulp van de correlatie functie kan de piekwaarde direct worden gebruikt om te controleren of de bepaalde vervorming in overeenkomst is met de waarde van de piek.

Vervolgens is de invloed van de positie van de catheter in het lumen op de berekende vervorming onderzocht. Theoretische relaties tussen de positie in het lumen en de gemeten vervorming werden afgeleid: de vervorming werd in bepaalde gebieden in de vaatwand onderschat. De onderschatting van de deformatie nam toe naar mate de afstand van de catheter tot het middelpunt toenam. Met behulp van een theoretisch beschrijving kan voor deze onderschatting worden gecorrigeerd. Echter, wanneer de catheter tegen de vaatwand ligt is correctie niet meer mogelijk. De invloed van een gekantelde transducer werd ook onderzocht. Wanneer de kantelhoek bekend is kan deze fout worden gecorrigeerd.

Een afbeeldingstechniek die eenvoudiger geïmplementeerd kan worden werd ontwikkeld: intravasculaire ultrageluids palpografie. Deze gecombineerde afbeeldingstechniek presenteert de mechanische en echo informatie in 1 afbeelding. De mate van vervorming wordt in de echoafbeelding weergegeven als een kleurgecodeerde lijn op de overgang tussen lumen en vaatwand. Op deze manier kan direct een relatie tussen de mechanische informatie en het klassieke IVUS echogram worden gelegd. Omdat per hoek maar 1 waarde voor de vervorming wordt weergegeven, is deze methode sneller en robuuster dan elastografie. De techniek is gevalideerd aan de hand van vaatfantomen en aangetaste humane arteriën: zachte en harde materialen konden worden geïdentificeerd met het palpogram. Verder konden met behulp van deze informatie vette en fibreuze laesie componenten worden geidentificeerd.

Aangetaste humane femoraal vaten werden gemeten met een verbeterde opstelling. Data werd verkregen bij intraluminale drukken van 80 en 100 mmHg. De eerste resultaten lieten zien dat het mogelijk is om elastogrammen van aangetaste en normale vaten te maken. De resolutie van de techniek (300 μm) was voldoende om een aantal vervormingswaarden per hoek in de vaatwand en laesie te bepalen. Gekalcificeerde regio's werden met het elastogram geïdentificeerd door de lage vervormingswaarden. Niet aangetaste gebieden in de vaatwand hadden een gemiddelde tot hoge vervormingswaarde en fibreuze gebieden een vervormingswaarde tussen die van normaal en gekalcificeerd weefsel in.

Een *in vitro* validatie studie met een groter aantal vaten is uitgevoerd. 35 dwarsdoorsneden werden opgenomen in 9 aangetaste humane femoraal vaten. Elastogrammen

werden bepaald en de IVUS echogrammen werden verdeeld in gebieden, gebaseerd op de vervormingswaarden. Histologische analyse van de vaten werd verricht waarbij specifieke kleuringstechnieken werden gebruikt om fibreus, vet en gekalcificeerd weefsel te identificeren. Tevens werd een kleuringstechniek gebruikt om de aanwezigheid van macrofagen aan te tonen. De aanwezigheid van macrofagen is een kenmerk van instabiele laesies. Correlatie tussen de elastografische resultaten en het dominante weefseltype in de laesie toonde aan dat er een significant verschil tussen de vervormingswaarde van de verschillende weefsel typen bestaat ($p < 0.001$). Vooral de vervormingswaarden in fibreus en vet weefsel waren significant verschillend ($p = 0.0012$). De resultaten van deze studie tonen aan dat elastografie mogelijk een techniek is om verschillende laesie componenten te karakteriseren en instabiele plaque te detecteren.

Als laatste werd intravasculaire elastografie in het catheterisatie laboratorium toegepast. Voor deze experimenten werd de pulserende bloeddruk als mechanische stimulus gebruikt. Door de samentrekking van het hart had de catheter geen vaste positie in het lumen. Vooral bewegingen langs de lengteas van vat veroorzaakten problemen omdat dan data van verschillende dwarsdoorsneden wordt opgenomen. Daardoor kan de vervorming van het weefsel moeilijk worden bepaald. De resultaten toonden aan dat de beweging van de catheter minimaal is aan het einde van de diastolische cyclus. In dit deel van de hartslag konden twee opeenvolgende dwarsdoorsneden worden opgenomen met een drukverschil van ongeveer 5 mmHg. De eerste resultaten laten zien dat reproducerende elastogrammen worden verkregen in 1 en over meerdere hartslagen.

Concluderend is aangetoond dat intravasculaire elastografie een techniek is waarmee afbeeldingen van de locale mechanische eigenschappen van de vaatwand kunnen worden gemaakt. Zachte en harde materialen konden, onafhankelijk van een verschil in echo-eigenschappen, worden geïdentificeerd. Aan de hand van een *in vitro* studie werd aangetoond dat verschillende laesie componenten kunnen worden gekarakteriseerd. Verder werd de mogelijkheid van de techniek om instabiele laesies te detecteren aangetoond. Voorlopige experimenten laten zien dat de techniek ook in het catheterisatie laboratorium kan worden toegepast.

Dankwoord

Tijdens mijn studie elektrotechniek kwam ik op het Biofysisch Laboratorium van Dr.ir. J.M. Thijssen in aanraking met biomedische techniek. Vanaf het eerste moment voelde ik me in deze omgeving thuis. Han, ik wil je bedanken voor de kans die je me hebt gegeven het positioneringssysteem van de akoestische microscoop van het project "acoustical imaging of ocular melanomas" te verfijnen. Ook wil ik de motiverende begeleiding van Rien Cuypers niet onvermeld laten. Deze stage was zo goed bevallen dat ik mijn afstudeeropdracht op het bifi-lab wilde doen. Onder leiding van Han Thijssen en Ton van der Steen werden de akoestisch eigenschappen van verschillende oogweefsels gemeten. Han en Ton wil ik bedanken voor de begeleiding en het wegwijs maken in de wetenschappelijke wereld. Dankzij jullie had ik aan het einde van mijn studie geroken aan het geven van presentaties en het schrijven van abstracten en wetenschappelijke publicaties. Tevens wil ik de discussies met Henk-Jan Huisman over de basis principes van medisch ultrageluid vermelden. Speciaal voor de uurtjes in de zon die we spendeerden om Morse and Ingard en Kinsler and Frey te doorgronden.

Begin 1993 was ik aanwezig bij een vergadering van het Nederlands akoestisch genootschap. Daar hield Prof.dr.ir. N. Bom een voordracht over cardiologische toepassingen van ultrageluid. Ik was zo onder de indruk van al deze toepassingen dat ik via Ton van der Steen contact heb gelegd om een promotie plaats in Rotterdam te bemachtigen. Na een gesprek met Charles Lancée mocht ik beginnen aan het project Intravasculaire Elastografie.

Het eerste jaar heb ik intensief samen gewerkt met Bart Dijkman. Bart, samen wisten we niet waar we heen moesten en aan het eind zagen we het project ook niet meer zo zitten. De samenwerking en de steun in dat eerste jaar hebben me goed gedaan. Inmiddels was een oude bekende op het lab komen werken, namelijk Ton van der Steen. Hij had in Washington Dr. E.I. Céspedes, een expert op het gebied van elastografie, ontmoet en stelde hem voor om een aantal maanden in Rotterdam te komen werken.

Ignacio, since you started in Rotterdam, the whole elastography project changed. Your drive to work things out, your brilliant and never stopping stream of new ideas and, especially, your friendly and stimulating personality made intravascular elastography a promising project. We switched from the dynamic to the static approach and when you left after half a year we had performed phantom experiments and the mechanical testing of the phantom materials. After a while you returned to work on the flow-project but still you found time to look at my papers, to discuss things and to provide me with new ideas. Thanks for all your comments to improve the manuscripts, the tips to improve my presentations and last but not least to teach me how to do scientific work.

Ton, ik wil je bedanken voor de begeleiding in de afgelopen 8 jaar (eigenlijk 7 om-

dat je het eerste en laatste half jaar van mijn Rotterdamtijd niet aanwezig was). Als co-promotor heb je me vooral de management kant van wetenschappelijk onderzoek bijgebracht. Je leerde me de waarde van publiceren, presenteren en het schrijven van projectaanvragen inzien. Daarnaast wist je goed de vinger op cruciale problemen in mijn onderzoek te leggen. Tevens wist je makkelijk kontakt met het catheterisatie laboratorium en andere groepen te leggen waardoor we in staat waren gezamelijke studies uit te voeren.

Klaas, ik wil je bedanken voor het vertrouwen en het aanbieden van een werkplek. Naast mijn promotor ben je de afgelopen jaren ook een promotor van intravasculaire elastografie geweest. Dit ging samen met gezellige maaltijden en terrasjes tijdens congressen. Vooral daar heb ik veel geleerd van je brede kijk op medisch ultrageluid.

Charles was altijd bereid problemen op te lossen die voor mij te moeilijk waren. De manier waarop jij je vastbijt in een probleem totdat je de oplossing hebt gevonden is voor ieder een voorbeeld. Ook tijdens de lunch hadden we gezellige kritische gesprekken: jouw kritische kijk op alles wat Nederlands is (o.a. het Nederlands elftal en weersvoorspellingen) maakt je een typische Hollander.

Frits Mastik wil ik bedanken voor het vele malen oplossen van mijn computerproblemen. Dankzij jouw inzet beschikte ik altijd over een systeem met de juiste software. Veel belangrijker was je inbreng in het acquisitie systeem. Door jouw inzet waren we instaat de *in vitro* en niet in de laatste plaats de *in vivo* studies te volbrengen. Bij deze laatste studies was de inzet van Stephane Carlier van onmisbare waarde. Je technische en klinische kennis hebben de introductie van elastografie daar tot een succes gemaakt.

Gerard Pasterkamp wil ik bedanken voor het vertrouwen in elastografie. Ondanks dat je van te voren niet wist waar wij met elastografie toe in staat waren, heb je materiaal en histologische kennis verschaft. Daarbij wil ik ook Hein Woutman bedanken voor de inzet om de histologische coupes te snijden, te kleuren en te interpreteren.

Ben Norder en Dr.ir K te Nijenhuis wil ik bedanken voor de medewerking om de mechanische eigenschappen van de verschillende fantoom-materialen te meten. Dankzij Carola Janssen werd het beste zoekalgorithme gevonden om de kwaliteit van elastogrammen te verbeteren. Bedankt dat je je met zoveel energie hebt ingezet voor dit project.

Frans van Egmond wil ik bedanken voor de broodnodige orde op het lab. Dankzij jouw inzet is het lab nog net niet veranderd in een beestenstal. Bedankt voor de moderne computersystemen, je steken onder water en je collegialiteit. Dankzij Jan Honkoop werden alle grote en kleine technische problemen geen obstakels. Jouw inzicht om electrotechnische problemen snel en praktisch op te lossen hebben er toe geleid dat er sneller en beter gemeten kon worden.

Peter Frinking wil ik bedanken dat hij ook de klappen van de promotiezweep kent. Bedankt voor het luisterend oor (zeker die week tussen 45 spaans sprekende Argentijnen) en voor de hotelservice wanneer er een cathlab sessie om 08.00 uur gepland stond. Ook het corrigeren van dit boekje wil ik niet onvermeld laten.

I'd like to thank Li Wenguang, Ignacio Céspedes, Ayache Bouakaz, Fermin Lupotti, Marvin Doyley, Peggy Pallanchon and Stephane Carlier for making the lab an international lab. Thanks for improving my English and the taste of the international kitchen. I'd like to thank Jane Thulis for the energy that she put in arranging catheters, handling the system in the cathlab and last but not least for the brownies and other cookies.

Corrie Eefting, Yvonne van der Steen en Trude Matla wil ik bedanken voor alle secretariële ondersteuning. Daarbij wil ik Yvonne van der Steen mede bedanken voor de

koffie en de gezellige uurtjes vroeg in de morgen.

Oh, ja Nico, bedankt dat je een Feijenoord fan bent. De afgelopen jaren was het een feest om maandag op het werk te verschijnen (dat incident van afgelopen 25 april vergeten we maar even, al is mijn band nog steeds niet geplakt).

Verder was het merendeel van de studies onmogelijk geweest zonder de medewerking van Patrick Serruys, Pim de Feyter, Wim van der Giessen, David Foley en Jurgen Ligthart van het Cath-Lab, de mechanische hulpstukken vervaardigd door Leo Bekkering en Wim van Alphen van de CID en de dia's van Rene Frowijn.

Als laatste wil ik degenen bedanken die niet direct tot het onderzoek hebben bijgedragen maar wel van groot belang zijn geweest. Pa en Ma wil ik bedanken voor hun interesse in het onderzoek en dat ze mij de kans hebben gegeven om te studeren. Kees en Peter wil ik bedanken dat zij mijn paranimfen willen zijn. Als laatste wil ik Pé bedanken voor het creëren van een rustgevende sfeer thuis. Daardoor kon ik me thuis altijd ontspannen en heb ik niet het idee dat een promotieonderzoek altijd gepaard moet gaan met stress.

Curriculum Vitae

Christoffel Leendert de Korte was born on May 18, 1969 in Sint Maartensdijk. After 6 years on "Het Christelijk Lyceum" in Zeist, he went to Eindhoven Technical University were he studied Electrical Engineering. His master project, at the section of Medical Electrical engineering headed by Prof.dr.ir. J.E.W Beneken, was carried out at the Biophysics Laboratory, Department of Ophthalmology of the Radboud University Hospital in Nijmegen, The Netherlands. Dr.ir. J.M Thijssen gave him the opportunity to participate in the project "acoustical imaging of ocular melanomas". During this project, he studied the acoustic properties of eye tissues and developed strong interest in medical ultrasound.

In September 1993, he started at the Experimental Echocardiography Laboratory of the Erasmus University Rotterdam, The Netherlands headed by Prof.dr.ir. N Bom. His main interest was to develop elastography for intravascular applications. From 1995 to 1998 he was participating in the Dutch Technology Foundation project "High frequency signal analysis for intravascular ultrasound" and Interuniversity Cardiology Institute of the Netherlands (ICIN) project 18. Currently he is employed by the Erasmus University Rotterdam on a grant from the Janivo Foundation, The Netherlands.

List of Publications

Papers

- de Korte, C.L.; van der Steen, A.F.W.; Thijssen, J.M. Acoustic velocity and attenuation of eye tissues at 20 MHz. *Ultrasound in Medicine and Biology* 20(5): 471-480; 1994
- van der Steen, A.F.W.; de Korte, C.L.; Thijssen, J.M. Ultrasonic spectroscopy of the porcine eye lens. *Ultrasound in Medicine and Biology* 20(9): 967-974; 1994
- de Korte, C.L.; van der Steen, A.F.W.; Thijssen, J.M.; Duindam, J.J.; Otto, C.; Puppels, G.J. Relation between local acoustic parameters and protein distribution in human and porcine eye lenses. *Experimental Eye Research* 59: 617-627; 1994
- Thijssen, J.M.; de Korte, C.L.; van der Steen, A.F.W.; Duindam, J.J.; Otto, C.; Puppels, G.J. Acoustic characteristics of the eye lens. *Documenta Ophtalmologica* 61: 483-496; 1997
- de Korte, C.L.; Céspedes, E.I.; van der Steen, A.F.W.; Lancée C.T. Intravascular elasticity imaging using ultrasound: feasibility studies in phantoms. *Ultrasound in Medicine and Biology* 23(5): 735-746; 1997
- de Korte, C.L.; van der Steen, A.F.W.; Dijkman B.H.J.; Lancée C.T. Performance of time delay estimation methods for small time shifts in ultrasonic signals. *Ultrasonics* 35: 263-274; 1997
- Céspedes, E.I.; de Korte, C.L.; van der Steen, A.F.W.; Von Birgelen, C.; Lancée C.T. Intravascular elastography: principle and potentials. *Seminars in Interventional Cardiology* 2(1): 55-62; 1997
- de Korte, C.L.; Céspedes, E.I.; van der Steen, A.F.W. Norder, B. te Nijenhuis K. Elastic and acoustic properties of vessel mimicking material for elasticity imaging. *Ultrasonic Imaging* 19(2): 112-126; 1997
- de Korte, C.L.; van der Steen, A.F.W.; Céspedes, E.I.; Pasterkamp G. Intravascular ultrasound elastography of human arteries: initial experience in vitro. *Ultrasound in Medicine and biology* 24(3): 401-408; 1998
- Bom, N. Li, W. van der Steen, A.F.W. Lancée, C.T.; Céspedes, E.I.; Slager, C.J.; de Korte, C.L. New developments in intravascular imaging. *European Journal of Ultrasound* 7(1): 9-14; 1998

- Céspedes E.I.; de Korte C.L.; van der Steen A.F.W. Echo decorrelation from displacement gradients. *Ultrasonics* 36(1-5): 661-661; 1998
- Bom N. Li W. van der Steen A.F.W. Lancée C.T.; Céspedes E.I.; de Korte C.L. Intravascular Imaging. *Ultrasonics* 36(1-5): 625-628; 1998
- de Korte, C.L.; Céspedes, E.I.; van der Steen, A.F.W.; Pasterkamp G. Intravascular ultrasound elastography: Assessment and imaging of elastic properties of diseased arteries and vulnerable plaque. *European Journal of Ultrasound* 7(3): 219-224; 1998
- van der Steen, A.F.W.; de Korte, C.L.; Céspedes, E.I. Intravascular ultrasound elastography. *Ultraschall in Medizine* 19: 196-201; 1998
- de Korte, C.L.; Céspedes, E.I.; van der Steen, A.F.W. Influence of catheter position on strain estimation in intravascular elastography. *IEEE transactions on Ultrasonics, Ferroelectrics and Frequency Control* 46(3): 616-625; 1999
- Céspedes, E.I.; de Korte, C.L.; van der Steen, A.F.W. Echo decorrelation from displacement gradients in elasticity and velocity estimation. *IEEE transactions on Ultrasonics, Ferroelectrics and Frequency Control* 46(4): in press; 1999
- Céspedes, E.I.; de Korte, C.L.; van der Steen, A.F.W. Intraluminal ultrasonic palpation: assessment of local and cross-sectional tissue stiffness. *Ultrasound in Medicine and Biology*: submitted; 1999
- de Korte, C.L.; Woutman H.A.; van der Steen, A.F.W.; Pasterkamp G.; Bom N. Characterization of plaque components with intravascular ultrasound elastography: a validation study in vitro. *Circulation*: submitted; 1999
- de Korte, C.L.; Carlier, S.G.; Mastik, F.; van der Steen, A.F.W.; Serruys, P.W.; Bom, N. Combined assessment of morphologic and mechanic information of coronary ateries: a feasibility study *in vivo*. *Circulation*: to be submitted; 1999

Award

- de Korte C.L.; Céspedes E.I.; van der Steen A.F.W.; Pasterkamp G. Intravascular ultrasound elastography: assessment and imaging of elastic properties of diseased arteries and vulnerable plaques. *EUROSON 1998 Young Investigator Award of the European Federation of Societies for Ultrasound in Medicine and Biology, Tours, France.*

Patent

- Céspedes, E.I.; de Korte, C.L.; van der Steen, A.F.W. Intravascular Ultrasonic Palpation. *European Patent application no. 97203072.0*

Book Chapters

- Bom N.; Li W.; van der Steen A.F.W.; de Korte C.L.; Gussenhoven E.J.; von Birgelen C.; Lancée C.T. Intravascular ultrasound possibilities of image enhancement by signal processing. *In: Marwick T.H.; Reiber J.H.C.; van de Wall E.E. (eds) Advances in imaging techniques in ischemic heart disease.* Kluwer academic press, Dordrecht: 113-125; 1995

- Bom N.; Li W.; van der Steen A.F.W.; de Korte C.L.; Gussenhoven E.J.; von Birgelen C.; Lancée C.T.; Roelandt J.R.T.C. Intravascular ultrasound: technical update 1995 *In: de Feyter P.J.; di Mario C.; Serruys P.W. (eds) Quantitative coronary imaging.* Barjesteh, Meeuwes & Co, Rotterdam: 89-106; 1995

- Li W.; Bom N.; von Birgelen C.; van der Steen A.F.W.; de Korte C.L.; Gussenhoven E.J.; Lancée C.T.. State of the art in ICUS quantitation. *In: Reiber J.H.C.; van der Wall E.E. (eds) Cardiovascular Imaging.* Kluwer Academic Publishers, Dordrecht: 79-92; 1996

Proceedings

- de Korte C.L.; Céspedes E.I.; van der Steen A.F.W.; Lancée C.T. Image artifacts in intravascular elastography. *IEEE EMBS conference proceedings, Amsterdam, The Netherlands*: CD-rom paper no. 685;1996

- de Korte C.L.; Céspedes E.I.; van der Steen A.F.W.; Norder B.; te Nijenhuis K. Tissue mimicking material for intravascular elasticity imaging. *IEEE EMBS conference proceedings, Amsterdam, The Netherlands*: CD-rom paper no. 487; 1996

- Céspedes E.I.; de Korte C.L.; van der Steen A.F.W.; Lancée C.T. Crossambiguity and wavelet processing in ultrasonic elasticity imaging. *IEEE Ultrasonics Symposium Proceedings, San Antonio, TX, USA*: 1135-1138; 1996

- Céspedes E.I.; de Korte C.L.; van der Steen A.F.W.; Norder B.; te Nijenhuis K. Tissue mimicking material and artifacts in intravascular elasticity imaging. *IEEE Ultrasonics Symposium Proceedings, San Antonio, TX, USA*: 1181-1184; 1996

- de Korte C.L.; van der Steen A.F.W.; Céspedes E.I.; Pasterkamp G. Intravascular elastography of human femoral arteries: an in vitro study. *IEEE Ultrasonics Symposium Proceedings, Toronto, Canada*: 1075-1078; 1997

- Céspedes E.I.; de Korte C.L.; van der Steen A.F.W. Intravascular ultrasonic palpation: assessment of local wall compliance. *IEEE Ultrasonics Symposium Proceedings, Toronto, Canada*: 1079-1082; 1997

- de Korte C.L.; Woutman H.A.; van der Steen A.F.W.; Pasterkamp G.; Céspedes E.I. IVUS elastography: a potential identifier of vulnerable plaque. *IEEE Ultrasonics Symposium Proceedings, Sendai, Japan*: 1729-1732; 1998

- van der Steen A.F.W.; Céspedes E.I.; de Korte C.L.; Carlier S.G.; Li W.;Mastik F.; Lancée C.T.; Eberle M.; Serruys P.W.; Bom N. Novel developments in intravascular imaging. *IEEE Ultrasonics Symposium Proceedings, Sendai, Japan*: 1733-1724; 1998

Abstracts

- van der Steen, A.F.W.; de Korte, C.L.; Thijssen, J.M. De akoestische eigenschappen van de ooglens. *Gemeenschappelijke vergadering NOG-BOG-IOI, Gent, Belgium*: p.D2; 1993
- Thijssen, J.M.; van der Steen, A.F.W.; de Korte, C.L.; Deutman, A.F. Ultrasonic characterization of the eye lens. *First Annual Meeting of the European community Ophtalmic Research Association, Bonn*: p.30; 1993
- van der Steen, A.F.W.; de Korte, C.L.; Thijssen, J.M. Acoustic spectography of the porcine eye lens. 18^{th} *International Symposium on Ultrasonic Imaging and Tissue Characterization, Washington DC, USA* Ultrasonic Imaging 15: 160; 1993
- de Korte, C.L.; van der Steen, A.F.W.; Thijssen, J.M.; Duindam, J.J.; Otto, C.; Puppels, G.J. Acoustic characteristics of the eye lens. *International Ophtalmology*; 1994
- van der Steen, A.F.W.; de Korte, C.L.; Thijssen, J.M.; Deutman A.F. Ultrasonic characterization of the eye lens. 8^{th} *Congress of the European Federation of Societies for Ultrasound in Medicine and Biology, Innsbruck* European Journal of Ultrasound 1(S1): S55; 1994
- Thijssen, J.M.; de Korte, C.L.; van der Steen, A.F.W.; Duindam, J.J.; Otto, C.; Puppels, G.J. Acoustic characteristics of the eye lens. *SIDUO*: 15; 1994
- de Korte, C.L.; van der Steen, A.F.W.; Thijssen, J.M.; Duindam, J.J.; Otto, C.; Puppels, G.J. Acoustic characteristics of the eye lens (human, porcine) and relation to protein distribution. 7^{th} *congress of World Federation of Ultrasound in Medicine and Biology, Sapporo, Japan* Ultrasound in Medicine and Biology 20(S1): s73; 1994
- Céspedes E.I.; de Korte C.L.; van der Steen A.F.W.; Lancée C.T. Intravascular ultrasound system for characterization of atherosclerotic plaque hardness. *Fourteenth annual Houston conference on biomedical research 1996, Houston, TX, USA*: p.147; 1996
- de Korte C.L.; Céspedes E.I.; van der Steen A.F.W.; Lancée C.T. Local compressibility assessment using a 20 kHz sound excitation. 21^{st} *International Symposium on Ultrasonic Imaging and Tissue Characterization, Washington DC, USA* Ultrasonic Imaging 18: 67-68; 1996.
- Céspedes E.I.; de Korte C.L.; van der Steen A.F.W.; Lancée C.T. Imaging atherosclerotic plaque hardness using intravascular ultrasound. 21^{st} *International Symposium on Ultrasonic Imaging and Tissue Characterization, Washington DC, USA* Ultrasonic Imaging 18: 47; 1996.

- de Korte C.L.; Céspedes E.I.; van der Steen A.F.W.; Norder B.; te Nijenhuis K. Tissue mimicking material for intravascular elasticity imaging. 18^{th} *Annual International Conference of IEEE/EMBS, Amsterdam, The Netherlands*: p.78; 1996

- de Korte C.L.; Céspedes E.I.; van der Steen A.F.W.; Lancée C.T. Image artifacts in intravascular elastography. 18^{th} *Annual International Conference of IEEE/EMBS, Amsterdam, The Netherlands*: p.78; 1996

- Céspedes E.I.; de Korte C.L.; van der Steen A.F.W.; Lancée C.T. Crossambiguity and wavelet processing in ultrasonic elasticity imaging. *IEEE Ultrasonics Symposium, San Antonio, TX, USA*: p. 279; 1996

- Céspedes E.I.; de Korte C.L.; van der Steen A.F.W.; Krams R. Artifacts in intravascular elasticity imaging. *IEEE Ultrasonics Symposium, San Antonio, TX, USA*: p.295; 1996

- de Korte C.L.; Céspedes E.I.; van der Steen A.F.W. Intravascular elastography: experimental studies of blood vessels. 12^{th} *symposium on echocardiology, Rotterdam, The Netherlands* Thoraxcentre J 9(3): 17; 1997

- Céspedes E.I.; de Korte C.L.; Ophir J.; van der Steen A.F.W. The decorrelation of echosignals from compressed tissues. *Ultrasonics International '97, Delft, The Netherlands*: p.50; 1997

- de Korte C.L.; Céspedes E.I.; van der Steen A.F.W.; Lancée C.T. Intravascular elasticity imaging of the arterial wall. *VIII Congress of World Federation for Ultrasound in Medicine and Biology, Buenos Aires, Argentina* Ultrasound in Medicine and Biology 23(S1): s71; 1997

- de Korte C.L.; van der Steen A.F.W.; Céspedes E.I.; Pasterkamp G. Intravascular elastography of human femoral arteries: an in vitro study. *IEEE Ultrasonics Symposium, Toronto, Canada*: p.113; 1997

- Céspedes E.I.; de Korte C.L.; van der Steen A.F.W. Intravascular ultrasonic palpation: assessment of local wall compliance. *IEEE Ultrasonics Symposium, Toronto, Canada*: p.114; 1997

- de Korte C.L.; Céspedes E.I.; van der Steen A.F.W. Dependence of strain estimation on catheter position in intravascular elastography. 23^{rd} *International Symposium on Ultrasonic Imaging and Tissue Characterization, Washington DC, USA* Ultrasonic Imaging 20(1): 47-48; 1998

- de Korte C.L.; Céspedes E.I.; van der Steen A.F.W.; Pasterkamp G. Vascular plaque characterisation using intravascular elastography. 23^{rd} *International Symposium on Ultrasonic Imaging and Tissue Characterization, Washington DC, USA* Ultrasonic imaging 20(1): 48; 1998

- Céspedes E.I.; de Korte C.L.; van der Steen A.F.W.; Pasterkamp G.; Bom N. Assessment of stiffness and elevated mechanical stress in atherosclerotic plaque by intravascular ultrasound: in vitro experience. *Sixteenth annual Houston conference on Biomedical Engineering Research, Houston, TX, USA*: p.160; 1998

- van der Steen A.F.W.; de Korte C.L.; Céspedes E.I. Intravascular elastography. 2^{nd} *Symposium on Quantitative Sonography in Clinic and Research and* 3^{rd} *bilateral German-Polish Symposium on Ultrasound Measurement Methods in Science and Technique, Halle, Germany*: p.19; 1998

- de Korte C.L.; Céspedes E.I.; Carlier S.; van der Steen A.F.W.; Pasterkamp G.; Thompson D.; Thomas J.D.; Bom N.; Serruys P.W. Assessment of stiffness and elevated mechanical stress in atherosclerotic plaques by intravascular ultrasound: in vitro experience. 20^{th} *congress of the European Society of Cardiology, Vienna, Austria* European Heart Journal 19(Abstr.Suppl.): 620; 1998

- de Korte C.L.; Woutman H.A.; van der Steen A.F.W.; Pasterkamp G.; Céspedes E.I. IVUS elastography: a potential identifier of vulnerable plaque. *IEEE Ultrasonics Symposium, Sendai, Japan*: p.129-130; 1998

- van der Steen A.F.W.; Céspedes E.I.; de Korte C.L.; Carlier S.G.; Li W.;Mastik F.; Lancée C.T.; Eberle M.; Serruys P.W.; Bom N. Novel developments in intravascular imaging. *IEEE Ultrasonics Symposium, Sendai, Japan* p.131-132; 1998

- Janssen C.R.M.; de Korte, C.L.; van der Heiden M.S.; Wapenaar C.; van der Steen A.F.W. Angle matching in intravascular elastography. *Ultrasonics International '99 & WCU'99, Copenhagen, Denmark*: accepted

- de Korte, C.L.; Woutman H.A.; van der Steen A.F.W.; Pasterkamp G.; Céspedes E.I. Vascular tissue characterisation with IVUS elastography. *Ultrasonics International '99 & WCU'99, Copenhagen, Denmark*: accepted